universität wien

DISSERTATION | DOCTORAL THESIS

Titel | Title

Sensorimotor transformation in the brain of *C. elegans*

verfasst von | submitted by

Anton Parinov M.Sc.

angestrebter akademischer Grad | in partial fulfilment of the requirements for the degree of

Doctor of Philosophy (PhD)

Wien | Vienna, 2025

Studienkennzahl lt. Studienblatt | Degree programme code as it appears on the student record sheet:	UA 794 685 490
Dissertationsgebiet lt. Studienblatt | Field of study as it appears on the student record sheet:	Molekulare Biologie
Betreut von | Supervisor:	Univ.-Prof. Dr. Manuel Zimmer

Table of Contents

1. Acknowledgements *4*

2. Summary *5*

2.1 Abstract **5**

2.2 Zusammenfassung **6**

2. Introduction *8*

2.1 Sensorimotor transformation **8**

2.1.1 Fundamental questions in sensorimotor transformation 8
2.1.2 Input-output vs. Coordination View perspectives on brain functionality organization 9
2.1.3 Theories on the interaction of motor-related and sensory-related information in the brain 11
2.1.4 Response variability as a crucial element in sensorimotor processing 14

2.2 C. elegans as a model organism for sensorimotor transformation studies **16**

2.2.1 Principal characteristics of *C. elegans* as a model for neuroscience research 16
2.2.2 Core aspects of nervous system organization in *C. elegans* 16
2.2.3 Characteristics of *C. elegans* neuronal activity and calcium (Ca^{2+}) imaging 17
2.2.4 Overview of chemosensory systems in *C. elegans* 18
2.2.5 Ethological role of the oxygen sensation in *C. elegans* 18
2.2.6 Morphological and functional characteristics of the oxygen sensory neurons 20
2.2.7 Functions of interneurons in the oxygen perception circuit 21
2.2.8 Premotor interneurons control forward and reverse locomotion in *C. elegans* 22

2.3 Aims of current research **24**

3. Results *26*

3.1 Periodic oxygen stimulation elicits reversal behavior in populations of *C. elegans* **26**

3.2 Revealing the profile of oxygen stimuli in behavioral and imaging assays with oxygen dye recordings **31**

3.3 Single-neuron resolution whole-brain imaging allows for the investigation of the brain activity in the oxygen stimulation assay **33**

3.4 Oxygen sensory neurons reliably encode periodic oxygen stimulus in the whole-brain imaging experiments **36**

3.5 Motor response is significantly entrained by the oxygen stimulus in the whole-brain imaging assay **42**

3.6 Analysis of control dataset confirms 21% [O_2] entrainment in the periodic oxygen shift experiments **46**

3.7 Reliable sensory encoding and variable motor response reveal the probabilistic nature of the sensorimotor transformation **49**

3.8 Intrinsic AVA state and its history partially explain the probabilistic nature of sensorimotor transformation in response to the oxygen stimulus **50**

3.8 "Hit-Miss; Evoked-Spontaneous"-triggered average analysis approach for exploring neuronal mechanisms behind the probabilistic nature of sensorimotor transformation **51**

3.9 Role of the oxygen sensory neurons in sensorimotor transformation **53**

3.9.1 Oxygen sensory neurons detecting the increase in the environmental oxygen concentration reveale distinct activity for the "Hit" and "Miss" trials 53
3.9.2 Inhibition of BAG neurons by elevated environmental oxygen concentration precedes AVA activation 57

3.9.3 Activation timing and response variability of the oxygen sensory neurons do not account for the motor response variability 58

3.10 Role of the primary interneurons in sensorimotor processing of the environmental oxygen stimulus 61

3.10.1 Stimulus-triggered average analysis identifies primary interneurons in the whole-brain imaging recordings 62

3.10.2 The "Hit-Miss; Evoked-Spontaneous"-triggered average analysis shows that primary interneurons exhibit activity indicative of the reversal motor response decision-making process....64

3.10.2 Primary interneurons demonstrate activation preceding the AVA activity onset 66

3.10.3 Primary interneurons show activity suppression at "Spontaneous" AVA-triggered trials 67

3.10.4 RMG interneurons demonstrated trial-to-trial response variability interrelated with the reversal motor command 69

3.11 The intrinsic state of AVA preceding the 21% [O_2] stimulus exerts minimal impact on the response of oxygen sensory neurons and primary interneurons to the stimulus 72

3.12 Head motor neurons demonstrated activity with opposite modalities on "Hit" and "Miss" trials 73

3.12.1 "Hit-Miss"-triggered average analysis of the HMN and RID neurons 75

3.12.2 "Evoked-Spontaneous" AVA-triggered average analysis of the HMN and RID neurons 76

3.13 Neurons encoding forward locomotion exhibit activity that may be predictive for sensorimotor transformation....78

3.13.1 RIB interneurons show activity down-modulation to oxygen stimulus in both 'Hit' and 'Miss' trials 79

3.13.2 RIB down-modulation events exhibit higher trial reliability compared to AVA and show timing variations with sensorimotor transformation outcomes 81

3.13.3 AVA-triggered average analysis reveals different RIB activity pattern at "Evoked" versus "Spontaneous" trials 82

3.13.4 Variations in relative timing of oxygen sensory and RIB neuron activity with sensorimotor transformation outcome....84

4. Discussion 87

4.1 The principal objectives of the research project 87

4.2 Reversal motor response to the oxygen stimulus in freely moving worms....88

4.3 Multiple classes of sensory neurons encode oxygen stimulus....89

4.3.1 Different classes of sensory neurons are involved in the oxygen perception....89

4.3.2 Potential role of multiple neuronal classes in sensory processing....90

4.3.3 Constraints and future outlooks in exploring the functional role of various oxygen sensory neuron classes in *C. elegans* 92

4.4 Reversal motor response in the whole-brain imaging experiments....93

4.4.1 Premotor interneuron AVA entrains the oxygen stimulus in the whole-brain imaging experiments 93

4.4.2 Characterization of the reversal response for the individual animals reveals inter-individual variability....95

4.4.3 Discrepancy between behavioral and imaging reversal response might be explained by the difference in the stimulus profile and restrained animal's conditions....96

4.5 The comparison of sensory and motor responses reveals the phenomenon of response variability 97

4.6 AVA intrinsic state history as a factor affecting the response variability 99

4.7 A "Hit-Miss; Evoked-Spontaneous"-triggered average analysis pipeline allows for a thorough exploration of the whole-brain imaging datasets 101

4.8 Overview of the results of the "Hit-Miss; Evoked-Spontaneous"-triggered average analysis 103
4.8.1 The activity profiles of sensory neurons and primary interneurons are predominantly associated with the stimulus 103
4.8.2 Sensory neurons and primary interneurons activity suppression suggests several alternative neuronal mechanisms 104
4.8.3 Sensory neurons and primary interneurons activity modulation reflects the sensorimotor transformation 105
4.8.4 The onset timing analysis highlights the motor response resilience to fine-scale sensory modulations and further supports the suppressive corollary discharge hypothesis 106
4.8.5 Neuronal activity prior to the 21% [O_2] stimulus may contribute to the reversal response decision-making mechanism 107
4.8.6 Head motor neurons might function as a gating mechanism in the sensorimotor transformation chain 108
4.9 Forward locomotion signal potentially provides a phasic framework gating the system response 108
4.10 Conclusion and further perspectives 111
5. Methods 114
5.1 Worm culture and strain 114
5.2 Behavioral experiments 114
5.3 Oxygen dye recordings 117
5.4 Whole-brain Ca^{2+} imaging 118
5.5 AVA neuron activity analysis 122
5.6 "Hit-Miss; Evoked-Spontaneous"-triggered average analysis 125
5.7 "Hit-Miss" neuron's activity onsets timing analysis for the oxygen sensory neurons and RMG neuron analysis 127
5.8 RIB neuron analysis methods 128
6. Supplementary Materials 130
7. References 140

1. Acknowledgements

I would like to acknowledge the contributions of the following people to my doctoral research:

First of all, my supervisor, Manuel Zimmer, for his scientific guidance and for encouraging my development as an independent researcher throughout this project.

Members of my thesis committee, Prof. Gasper Tkacik and Prof. Wulf Haubensak, for their valuable expertise, and Christopher Robinson, the administrator of the VBC PhD program, for his continuous support.

The PhD programs of the Vienna Biocenter and the Vienna Doctoral School of Cognition, Behaviour and Neuroscience for making my PhD research possible.

All the members of the Zimmer lab, with whom I had the pleasure of working. In particular, I would like to thank Susanne Skora, Annika Nichols, Julia Riedl, Harris Kaplan, Kerem Uzel, Mara Andrione, Lukas Hille, and Richard Latham for generously sharing their expertise and knowledge with me.

My sincere gratitude to Ulises Ray for the constant moral support throughout the timespan of my PhD.

I would also like to acknowledge Jalaja Madhusudhanan for continuing and further developing this research project.

Of course, I am deeply grateful to my parents, Julia and Pavel Parinov, and to my grandparents, Elena and Mikhail Parinov, and Ludmila Yarmal, who were always there for me.

Finally, my heartfelt thanks to my friends Aleksandr Liapichev and Hooram Nam for all the many things they did to support me.

2. Summary

2.1 Abstract

Sensorimotor transformation refers to the complex neural processes that convert sensory input into motor commands, enabling organisms to effectively coordinate their actions and movements in response to external stimuli, thereby facilitating interaction with and adaptation to their dynamic surroundings. Importantly, emerging perspectives in neuroscience, such as the Coordination View, highlight the intricate flow of information within sensorimotor circuits and emphasize the crucial role of internal system activity in these processes.

In this project, we utilized the ethologically relevant behavior of the soil nematode worm *C. elegans*, which involves reversal crawling to avoid high environmental oxygen concentrations, to study sensorimotor transformation in its nervous system. The main objectives were to identify and thoroughly describe the specific neuronal circuits involved in this process and uncover the neural activity patterns driving sensorimotor transformation and understand their functional roles. Throughout the project, we designed an effective experimental paradigm to investigate sensorimotor transformation in *C. elegans*, utilizing the advantages of whole-brain Ca^{2+} imaging. This included the development of a complementary analysis algorithm that enables unbiased identification of neurons involved in information processing, distinguishing between sensory and motor processing content. This approach led to significant findings, revealing key principles of sensorimotor transformation in the nervous system of the worm.

Our study unveiled multiple indicators of neuronal activity that support the Coordination View hypothesis in neuroscience. In particular, we discovered response variability and revealed the pivotal role of the internal state of the system in this phenomenon. Moreover, multiple sensory and interneurons identified in this sensorimotor circuit demonstrated activity signatures indicating their role in the response variability. Further, we made a compelling finding about the second-layer interneuron RIB, which is known to play a role in controlling forward locomotion. Our data indicate that the phase of low-amplitude spontaneous activity modulations in the RIB neuron might set the timing window for triggering a reversal locomotion response to the oxygen stimulus. Finally, we uncovered numerous signatures in sensory and interneuron activity profiles implying potential feedback mechanisms that could modulate their responsiveness based on the current internal state of the circuit. Overall, we characterized and provided new insights into the intricate dynamics of sensorimotor transformation, including the response variability observed in the brain of *C. elegans*.

2.2 Zusammenfassung

Die sensorimotorische Transformation bezieht sich auf die komplexen neuronalen Prozesse, die sensorische Eingaben in motorische Befehle umwandeln und es Organismen ermöglichen, ihre Handlungen und Bewegungen effektiv auf äußere Reize abzustimmen. Dadurch wird die Interaktion mit und die Anpassung an ihre dynamische Umgebung erleichtert. Wichtige neue Perspektiven in der Neurowissenschaft, wie beispielsweise die „Coordination View“, betonen den komplexen Informationsfluss innerhalb sensorimotorischer Schaltkreise und die entscheidende Rolle der Aktivität interner Systeme in diesen Prozessen.

In diesem Projekt nutzten wir das ethologisch relevante Verhalten des Bodenfadenwurms *C. elegans*, das darin besteht, durch Rückwärtskriechen hohe Sauerstoffkonzentrationen in der Umwelt zu vermeiden, um die sensorimotorische Transformation in seinem Nervensystem zu untersuchen. Die Hauptziele bestanden darin, die spezifischen neuronalen Schaltkreise zu identifizieren und gründlich zu beschreiben, die an diesem Prozess beteiligt sind, sowie die neuronalen Aktivitätsmuster aufzudecken, die die sensorimotorische Transformation steuern, und ihre funktionalen Rollen zu verstehen. Im Verlauf des Projekts entwickelten wir ein effektives experimentelles Paradigma zur Untersuchung der sensorimotorischen Transformation bei *C. elegans*, wobei wir die Vorteile des Ganzhirn-Ca^{2+}-Imagings nutzten. Dies umfasste die Entwicklung eines ergänzenden Analysealgorithmus, der eine unvoreingenommene Identifizierung der an der Informationsverarbeitung beteiligten Neuronen ermöglicht und zwischen sensorischen und motorischen Verarbeitungsinhalten unterscheidet. Dieser Ansatz führte zu bedeutenden Erkenntnissen, die wesentliche Prinzipien der sensorimotorischen Transformation im Nervensystem des Wurms offenbarten.

Unsere Studie enthüllte mehrere Indikatoren neuronaler Aktivität, die die „Coordination View“-Hypothese in der Neurowissenschaft unterstützen. Insbesondere entdeckten wir eine Variabilität der Reaktionen und zeigten die entscheidende Rolle des internen Zustands des Systems in diesem Phänomen auf. Darüber hinaus zeigten mehrere sensorische Neuronen und Interneuronen, die in diesem sensorimotorischen Schaltkreis identifiziert wurden, Aktivitätsmuster, die auf ihre Rolle in der Reaktionsvariabilität hinweisen. Ferner machten wir eine überzeugende Entdeckung über das zweite interneuronale Schichtneuron RIB, das dafür bekannt ist, eine Rolle bei der Steuerung der Vorwärtsbewegung zu spielen. Unsere Daten deuten darauf hin, dass die Phase von niederamplitudigen, spontanen Aktivitätsmodulationen im RIB-Neuron das Zeitfenster für das Auslösen einer Rückwärtsbewegungsreaktion auf den Sauerstoffreiz festlegen könnte. Schließlich entdeckten wir zahlreiche Signaturen in den Aktivitätsprofilen von sensorischen Neuronen und Interneuronen, die auf potenzielle Feedback-Mechanismen hinweisen, die ihre Reaktionsfähigkeit basierend auf dem aktuellen internen Zustand des Schaltkreises modulieren könnten. Insgesamt charakterisierten wir die komplexen

Dynamiken der sensorimotorischen Transformation und lieferten neue Einblicke in die Reaktionsvariabilität, die im Gehirn von *C. elegans* beobachtet wurde.

2. Introduction

2.1 Sensorimotor transformation

2.1.1 Fundamental questions in sensorimotor transformation

The concept of "sensorimotor transformation" classically refers to the intricate series of neural processes responsible for converting sensory input into motor commands, enabling living organisms to effectively react and respond to their surrounding environment. These processes play a fundamental role in directing and coordinating actions and movements in response to external stimuli, facilitating the interaction and adaptation of biological organisms to their ever-changing surroundings. Therefore, the exploration of sensorimotor transformation is of paramount importance in comprehending the functioning and interaction of organisms with their environment (Flanders, 2011; Huston & Jayaraman, 2011).

The study of sensorimotor transformation entails the exploration of two primary research questions. Firstly, it involves the investigation of the neural pathways involved in this process, necessitating the identification and characterization of specific brain regions and neuronal circuits that participate in sensorimotor transformation of every specific type, as well as an understanding of their interplay and functional connectivity. Secondly, researchers seek to uncover patterns of neural activity underlying sensorimotor transformation and their functionality.

Further, the process of understanding how the brain generates behavior in response to sensory stimuli can be divided into three main steps, which involve linking stimuli, behavior, and neural activity. The first step, known as psychophysics, involves identifying the specific features of sensory stimuli that drive behavior. This requires understanding how different sensory inputs lead to specific behavioral responses. The second step, called encoding, involves linking sensory stimuli to neural codes to determine how the brain represents behaviorally relevant sensory features. This step involves identifying the patterns of neural activity that correspond to particular sensory inputs and understanding how these patterns of activity are generated. The final step, known as decoding, involves linking neural codes to behavior to understand how neuronal activity is transformed into behavior. This involves identifying how the brain translates patterns of neural activity into specific motor commands and how these commands lead to the observed behavior (Clemens & Murthy, 2017).

2.1.2 Input-output vs. Coordination View perspectives on brain functionality organization

The classical view on the brain function and sensorimotor transformation as an input-output computational mechanism with a feed-forward information flow was build up during the first half of the XX century based on several theories and discoveries. First, the Reticular Theory of nervous system which assumed that the nervous system is organized as single continuous network (Raviola & Mazzarello, 2011) was replaced by the Neuron Doctrine of Santiago Ramón y Cajal. The Neuron Doctrine postulates that nervous system consists of individual discrete neuronal cells connected to each other with synapses main function of which is to transmit the information in unidirectional fashion (Bennett, 1999; De Robertis & Bennet, 1955; De Felipe, 2009; López-Muñoz et al., 2006). On the other hand, profound work of Charles Scott Sherrington on the neurological basis of the reflex (Sherrington, 2012) and evolutionary approach of the George Howard Parker (Parker, 1919) led to the fact that the reflex arc became seen as the basic organizational principle of nervous systems and became the functional representative of the input–output mechanism framework (Zeigler & Gallistel, 1981).

Further, these biological findings were reinforced by the notion of information processing in the nervous system originated from the Claude Elwood Shannon's Information Theory (Burock, 2008; Nizami, 2019), which has become closely linked with concepts like computation and representation and linked to the analogy of the nervous system with a logical electronic circuitry (McCulloch & Pitts, 1943). Thus, neurons became seen as discrete entities that transmit and receive electrical signals from each other through synapses, operating in an all-or-none manner akin to electrical switches.

This framework got a further contribution from a Feature-detector Theory of the brain function (Barlow, 1972, 2013; K. A. C. Martin, 1994) which suggests a prevalence of the feed-forward information flow where upon extracting an invariant representation from sensory input, the brain's sensory systems transfer this information to a distinct neural region responsible for the executing appropriate actions based on the acquired representation. This approach was further developed in the work of David Hunter Hubel and Torsten Nils Wiesel which strongly contributed to the model of the feed-forward hierarchy in the brain with a notion of neuronal function as a serial extraction of relevant features in the sensory processing flow (Hubel & Wiesel, 1959, 1998).

Overall, described scientific framework considers nervous system as an input-output computational mechanism which connects sensors to effectors at a fundamental level as interpreted in the Braitenberg's vehicles (Braitenberg, 1984). In this approach information flows in a feed-forward manner from the sensory neurons layer through the layers of interneurons which preforms computations to the motor neurons which encode behavioral motor activity as an ultimate response to the stimulus.

However, lately the Neuronal Doctrine has been revised in the light of the appeared knowledge of various phenomena such as: a) gap junction which allow direct electrical communication between neighboring neurons, b) neuromodulatory substances, such as amines and neuropeptides, which add a complexity in the way neurons can modulate activity of other neurons, c) retrograde propagation of action potentials from the axon and cell body back towards the dendrites which challenges the traditional view of unidirectional information flow within neurons, d) employment of the graded electrical events by neurons in addition to the all-or-none spike event, undermines the view of the neurons as a pure electrical switches and assumes potential complexity of the information processing by a single neuron, e) dynamism of the nervous system related to the plasticity of the synapses (Bullock, 1993, 1997; Bullock et al., 2005; Guillery, 2007; Smythies, 2002). Collectively, these facts challenge the established Neuronal Doctrine and the traditional Input-output View of the brain. Therefore, it becomes necessary to consider an alternative perspective on how the brain is organized and functions.

An alternative to the Input-output View is the Coordination View, originating from Carl Frederick Abel Pantin's research on nervous system evolution. This perspective suggests that the development of early nervous systems was driven primarily by the need for muscle coordination to facilitate mobility and allow organisms to function as cohesive multicellular units (Pantin, 1956; Passano & Hutchinson, 1963; Keijzer et al., 2013). The Coordination View was further elaborated into the Skin Brain Thesis (SBT) and related Animal Sensorimotor Organization (ASMO) frameworks (Keijzer, 2014, 2015; Keijzer et al., 2013; Keijzer & Arnellos, 2017), which propose progressive emergence of functional coordination structures, starting from simple contractile tissues and evolving toward complex nervous systems. In this perspective the reflex arc should be seen not as evolutionary primary building block of the nervous system but rather as a secondary simplification of initially complex nervous system (Horridge, 1968; Passano & Hutchinson, 1963; Pantin, 1956; Pavans De Ceccatty, 1974). Importantly, this view highlights the role of the endogenously generated spontaneous activity in the brain functionality (Lichtneckert & Reichert, 2007; Passano & Hutchinson, 1963).

Further, the SBT and ASMO frameworks align with the broader theory of Embodied Cognition, which holds that cognitive processes are deeply shaped by the body's interactions with the environment (Barrett, 2011; Brooks, 1999; Chemero, 2009; Clark, 2008; Gelder, 1995; Pfeifer & Bongard, 2007; Thompson, 2007), as well as with the related Sensorimotor Perception approach (Buhrmann et al., 2013; Hurley, 2001; O'Regan, 2011; O'Regan & Noë, 2001), which emphasizes that perception arises through active movement and the structured relationships between actions and sensory changes.

Recent advances in large-scale brain activity recordings have resulted in a vast pool of new experimental data, challenging the classical Input-output View of brain function. Notably, it has become evident that behavior-related information persists across various brain regions, including those traditionally

classified as primary sensory areas, in different model organisms. This suggests that the widespread distribution of behavior-related information across different brain regions is a fundamental principle of brain organization. In particular, in mice it was found that significant portion of brain activity is associated with the ongoing behavior of animals, encompassing both cortical regions, including primary sensory areas, and subcortical areas (Musall et al., 2019; Niell & Stryker, 2010; Salkoff et al., 2020; Steinmetz et al., 2019; Stringer et al., 2019). Similarly, it was shown that in drosophila a walking behavior is reflected in the increase of the global brain activity across multiple regions (Aimon et al., 2019, 2023; Brezovec et al., 2024; Schaffer et al., 2023). Finally, research in *C. elegans* acquired findings which also goes along with this concept: it was found that the global brain activity is dominated by the motor command signal and a large portion of neurons including those traditionally categorized as interneurons exhibit motor representation (Gordus et al., 2015; Kaplan et al., 2020; Kato et al., 2015; Z. Li et al., 2014; Luo et al., 2014). However, it should be also mentioned that research on *Zebrafish* larvae provides opposite observation with clearly segregated regions encoding sensory and motor behavior related information (Ahrens et al., 2012; Dunn et al., 2016; Portugues et al., 2014).

Overall, the Coordination View and the accumulating experimental data suggest that the brain's functionality involves extensive coordination and integration of motor behavior related information across multiple brain regions rather than only sequential sensory input processing and motor output generation. This alternative perspective offers valuable insights into the evolutionary origins and functional organization of nervous systems, paving the way for further exploration and understanding of brain function.

2.1.3 Theories on the interaction of motor-related and sensory-related information in the brain

Multiple non-mutually exclusive theories have been proposed to elucidate the organization of information within the brain, particularly regarding the presence of motor-related information in diverse regions, including primary sensory areas. By incorporating these theories, we can achieve a more comprehensive understanding of the brain's intricate functional organization, surpassing the traditional Input-output View of information processing in the brain.

Sensory gain modulation theory suggests that motor-related activity serves to modulate processing of sensory information in relation to the current behavioral state. In particular, there are numerous evidences that global activity state (e.g. sleep versus awake state) (Raizen et al., 2008; Stephenson & Lewis, 2011; Vorster & Born, 2015), locomotion state (Chiappe et al., 2010; Niell & Stryker, 2010) and the attention state (Buschman & Miller, 2007; De Bivort & Van Swinderen, 2016; Engel et al., 2016; Noudoost et al., 2010; Reynolds & Chelazzi, 2004; Schröder et al., 2019) can modulate sensory processing across different species from invertebrates to mammals. Overall, sensory gain modulation

theory establishes a reciprocal bridge between the sensory processing and motor-related information in the nervous system.

Corollary discharge theory suggests that internally generated motorrelated timing signal is translated into the other regions of the brain including the sensory areas to coordinate its activity by inhibition, facilitation, or modulation (Crapse & Sommer, 2008; Fukutomi & Carlson, 2020; Sperry, 1950; Straka et al., 2018). The corollary discharge concept encompasses the theory of the efference copy (von Holst & Mittelstaedt, 1950) as its particular case. The efference copy principle proposes that the nervous system generates a duplicate of the motor command signals which is then sent to the sensory regions of the brain to make predictions of the expected sensory input resulting from the organism's own actions (re-afference input). This should allow the brain to differentiate between the anticipated sensory input and the sensory input arising from external changes in the environment (ex-afference input) (Fukutomi & Carlson, 2020) .

A substantial body of experimental evidence from different model organisms highlights the significant role of corollary discharge and efference copy concepts in sensorimotor transformation, which has been extensively reviewed in the literature (Busse, 2020; Busse et al., 2017; Crapse & Sommer, 2008; Cullen, 2004; Fukutomi & Carlson, 2020; Poulet & Hedwig, 2007). Several notable historical examples include the inhibition of the auditory sensory system in crickets during singing, which prevents the saturation of central auditory pathways (Poulet & Hedwig, 2002, 2003, 2006; Straka et al., 2018), and a similar mechanism supporting echolocation in bats (Suga & Schlegel, 1972; Suga & Shimozawa, 1974). Moreover, extensive experimental evidence from studies on electric perception in weakly electric fish reveals that corollary discharge adjusts the perception of their self-generated electric field (C. C. Bell, 1989; C. C. Bell & Grant, 1989; Fukutomi & Carlson, 2020; Requarth & Sawtell, 2011; Zipser & Bennett, 1976). Next, research on flies provides abundant examples of corollary discharge mechanisms, such as the integration of walking motor information into the visual system (Fujiwara et al., 2017, 2022), canceling of the visual flow detection during flight (Collett & Land, 1975; Kim et al., 2017) , and the suppression of visual processing during saccadic turns in flight (Kim et al., 2015; Schnell et al., 2014). Interestingly, an analogous mechanism has been also detected in the primate visual system where saccadic eye moments are accompanied by a suppression in the visual sensory system (Goldberg & Wurtz, 1972). Finally, it is important to mention that recent advances from *C. elegans* research detected similar mechanism in the worm's nervous system where it was found that extrasynaptic tyramine signal suppresses perception of the self-generated CO_2 trace during the reversal locomotion (Riedl et al., 2022). Overall, it is evident from the experimental findings that the corollary discharge and efference copy play an important role in the sensorimotor transformation mechanisms of the brain across phyla and encompasses an important fundamental principle of the brain organization.

Generative internal model theory: on a larger scale the efference copy and corollary discharge mechanisms are hypothesized to be a part of the generative internal models generated by the brain. This concept originates from the Control Theory (Kawato, 1999; Todorov, 2004, 2006; Webb, 2004) and was applied to the neuroscience field where it was proposed by multiple authors as a comprehensive framework for understanding the brain circuitry involved in cognition (Barsalou, 1999; A. Clark & Grush, 1999; Cruse, 2003; Reviewed, 2004). In a nutshell, generative internal model is a mechanism that predicts the future state of a system given the current state and the control signals (Webb, 2004). In the neuroscience framework, internal model is a brain mechanism that employs the information of the current state of the organism and efference copies of the motor commands to anticipate the results of movements. Further, these predictions can be refined by detecting any deviations from the expected outcomes, allowing for further optimization (Kawato, 1999; Wolpert & Miall, 1996). Thus, on the conceptually level, internal models are equivalent to a simulation of the external world and function to make predictions of sensory input, thus, allowing the brain to distinguish between self-generated and externally generated input (Keller & Mrsic-Flogel, 2018).

There are multiple variations of the concept that the brain utilizes an internal model to anticipate sensory information by considering past sensory experience and movements which include predictive coding, hierarchical temporal memory, and Bayesian inference, all of which revolve around the notion of a generative model of the world that helps predict sensory input (Friston, 2005; Körding & Wolpert, 2004; Rao & Ballard, 1999; Spratling, 2010). Together, these theories fall under the so-called Predictive Coding Theory (Clark, 2013). According to the Predictive Coding Theory, sensory input is processed by comparing it with the internal models in order to update them when their predictions do not match the sensory signals. The sensory cortex plays a crucial role in this process by comparing expected and actual sensory input permitting the transmission of bottom-up input to other brain regions in cases where it contradicts the internal model. Thus, communication between brain regions primarily focuses on prediction and prediction error signals. The computations involved are centered on comparing these signals and updating the internal model, rather than extracting features to create increasingly specific representations. These errors are corrected within a cascade of cortical processing events in which higher-level systems attempt to predict the inputs to lower-level ones on the basis of their own emerging models of the causal structure of the world (Clark, 2013).

Further, the motor control theories proposed that internal models can be either forward, which can predict sensory consequences from efference copies of issued motor commands, or inverse, which can calculate necessary feedforward motor commands from desired trajectory information (Kawato, 1999; Lalazar & Vaadia, 2008). Numerous pieces of evidence from the motor control field in neuroscience research support the existence of internal models. These include studies on adaptation to force fields, posture control, grip-load force coupling, oculo-manual coordination, and the vestibular system

(Kawato, 1999). In particular, the cerebellum is considered to be a crucial brain region for the acquisition and storage of internal models, which are important for the coordination and execution of motor movements (C. C. Bell, 1995; Ito, 1970; Miall et al., 1996). Additionally, research on invertebrates provides abundant evidence supporting the existence of internal models as a brain mechanism (Webb, 2004).

In summary, these theories aim to offer more detailed explanations of how sensory information processing and motor-related information interact in the brain. They also explain why motor-related information is distributed across extensive brain regions, extending beyond traditional "motor" areas. Fundamentally, these theories challenge the classical view of brain function as a hierarchical input-output information processing system, proposing instead more complex forms of information processing within the brain.

2.1.4 Response variability as a crucial element in sensorimotor processing

An essential characteristic of the sensorimotor transformation processes in the brain, which fundamentally distinguishes it from the Input-output model and underscores the importance of endogenous activity, is the variability in responses. Response variability of the individual organism across the repetitions of a certain stimulus can be observed even under the well-controlled laboratory experimental conditions at the different level from individual synapses up to the whole-organism behavior level (H. C. Bell, 2014; Maye et al., 2007).

From one point of view, this phenomenon might simply reflect the intrinsic chaotic properties of the network's behavior (Sabarathinam et al., 2013) and thus be considered a result of the inevitable inaccuracy in the functioning of the nervous system. However, an alternative hypothesis posits that this variability could play an ethological role in the animal's adaptation to environmental conditions. It may introduce a creative element into behavioral strategies, which could be crucial for various specific behaviors (Brembs, 2011b). For example, in a prey organisms response variability of the escape trajectories was shown to facilitate evasion of predators by increasing the unpredictability of the escape trajectory (Driver and Humphries 1988; Domenici and Blake 1993; Domenici et al. 2008; Eaton, Lavender, and Wieland 1981). Next, the behavioral variability, might allow the organism to effectively explore the surrounding environment which was demonstrated in both biological experiment (Brembs, 2011a; Charnov, 1976; Humphries et al., 2010) and computer simulation studies which also demonstrated the necessity of the randomness for the effective exploration behavior (Powers, 1989). Finally, from the neurophysiological perspective the element of randomness might enhance the learning processes (Chaisanguanthum et al., 2014; Ölveczky et al., 2005; Tumer & Brainard, 2007). Overall, numerous pieces of evidence point to the beneficial effects of variability in the nervous system. Some

perspectives even propose that this variability is deliberately introduced by the nervous system to endow the organism with above-described adaptability traits (Beck et al., 2012; Brembs, 2011a; Maye et al., 2007; Neuringer, 2004).

Response variability might originate from different sources in the nervous system. On the first, place it can originate from the level of the sensory system where the stochastic noise can improve the perception of a weak signals by the costs of the precision. Next, it can be introduced at the level of synaptic transmission or neuronal level at any subsequent stage of the information flow in a sensorimotor circuit. Finally, the current internal state of the system at the moment of the stimulus presentation can be decisive for the systems response (Barlow, 1972; Barlow et al., 1971; Benzi et al., 1981; Bialek, 2003; Lillywhite & Laughlin, 1979; Longtin et al., 1991). In line with this theory, it was found that fluctuations in the default network activity (Fox et al., 2007; Iemi et al., 2019) and the state of alertness (Goodale et al., 2021) predicts the response variability in humans. Similarly, the ellipsoid body in fruit flies exhibits the spontaneous activity (J. R. Martin et al., 2007) reminding the mammals default-mode network which explains variability in the fly's walking behavior (J. R. Martin et al., 2001; Sorribes et al., 2011).

Research in *C. elegans* also provided examples of the response variability. Importantly, due to the relatively simplistic neural architecture it was possible to track the variability down to the individual neurons. A prominent example is a study in which scientists investigated the neuronal circuit mediating the worm's response to the odor stimulus. The circuit involves the olfactory neuron AWC which provides an input into the reversal premotor interneuron AVA. Importantly, besides the direct synapses from the AWC to AVA neurons the circuit contains connections transitioning through the AIB and RIM interneurons. The main finding is that the activity of the AIB and RIM neurons introduced a significant variability in the motor response to the attractive odors reliably detected by the AWC neuron. The authors argue that the inclusion of RIM and AIB neurons in the reversal circuit is crucial for introducing necessary response variability. Without this, the reversal circuit would be overly deterministic and potentially maladaptive (Gordus et al., 2015). Further, research in our laboratory revealed that the intrinsic activity of the AVA premotor interneuron itself can influence the responsiveness of the worm in a similar odor stimulation paradigm. Therefore, it was suggested that the internal state of the system should be considered during the analysis of the experimental results to achieve the proper interpretation of the response rate in the sensorimotor transformation paradigm (Kaplan et al., 2018).

In summary, response variability serves as a critical element in the domain of sensorimotor processing. This variability can emerge from a diverse array of sources as was described above. Regardless of its origin, response variability plays a significant role in shaping the sensorimotor processing pathway, potentially modifying the response outcomes and thus influencing behavior. Therefore, understanding

and accounting for response variability is of paramount importance in the accurate modeling and interpretation of sensorimotor processing.

2.2 C. elegans as a model organism for sensorimotor transformation studies

2.2.1 Principal characteristics of *C. elegans* as a model for neuroscience research

Caenorhabditis elegans is a small reaching 1mm length, free-living nematode worm that is commonly used as a model organism in laboratory research. In natural environment it lives in soil and rotten plants material and supposedly feeds on bacteria (Frézal & Félix, 2015). In laboratory conditions, *C. elegans* can be conveniently cultivated on agar plates, utilizing *Escherichia coli* as a food source. Additionally, the hermaphrodite *C. elegans* are reproducing through self-fertilization, while the species exhibits a brief reproductive cycle of 3-4 days during which it progresses through four larval stages (L1-L4) before reaching adult organism stage. Moreover, *C. elegans* elegans possesses a comparatively uncomplicated anatomy, as it consists of only 959 stereotyped somatic cells with a well-defined developmental trajectory throughout ontogenesis (Sulston & Horvitz, 1977). Further, the hermaphrodites worm's nervous system consists of 302 neurons with completely mapped connectome (Cook et al., 2019; Varshney et al., 2011; White et al., 1986). Collectively, these attributes contribute to the practicality of *C. elegans* as a laboratory model organism.

Despite possessing a relatively simple nervous system and bodily anatomy, *C. elegans* exhibits a diverse range of behaviors, including foraging, avoidance behavior, nictation, mating, egg-laying, and sleep, among others (Croll, 1975; H. Lee et al., 2012; Raizen et al., 2008) . These behavioral repertoire equips the worm with the capacity to adapt to its environment. In terms of locomotion, *C. elegans* employs several fundamental modes, such as forward and reverse crawling, as well as ventral and dorsal turns, achieved through undulatory body movements regulated by the ventral and dorsal groups of body muscles (Chalfie et al., 1985; De Bono & Maricq, 2005; Gray et al., 2005).

2.2.2 Core aspects of nervous system organization in *C. elegans*

The nervous system of *C. elegans* hermaphrodites consists of 302 neurons, classified into 118 classes. Notably, the *C. elegans* nervous system is comprised of two nearly independent pharyngeal and somatic modules that are linked solely by a pair of RIP neurons. The pharyngeal nervous system consists of 20 neurons responsible for regulating the feeding behavior, while the somatic nervous system, comprising 279 neurons, governs all other behaviors (White et al., 1986).

The somatic nervous system of *C. elegans* is divided into head and tail ganglia, connected by a ventral nerve cord. The head ganglion comprises the anterior, dorsal, ventral, lateral, and retrovesicular ganglia,

while the tail ganglion is composed of the pre-anal, dorso-rectal, and lumbar ganglia. Both ganglia contain sensory neurons, interneurons, and a subset of motor neurons. The ventral nerve cord, on the other hand, encompasses most of the motor neurons, which innervate the body wall muscles, and regulate the undulatory movements necessary for locomotion (White et al., 1986).

The nervous system of *C. elegans* displays a predominantly bilateral symmetric arrangement, with the majority of neurons arranged into left-right pairs (Hobert et al., 2002; White et al., 1986). Neurons within a pair typically exhibit similarities in morphology, connectome, and function. However, some exceptions to this rule exist, such as the ASE sensory neurons, which demonstrate functional asymmetry. Specifically, the left and right ASE neurons respond differently to variations in salt concentration and mediate opposing behavioral responses, as documented in prior research (S. Chang et al., 2004; Cochella & Hobert, 2012; Hobert et al., 2002).

2.2.3 Characteristics of *C. elegans* neuronal activity and calcium (Ca^{2+}) imaging

To date, the *C. elegans* genome analysis has revealed the absence of voltage-gated sodium channels. Thus, the traditional assumption has been that *C. elegans* neurons are isopotential and use gradual neural transmission without classical action potentials that depend on sodium currents (Bargmann, 1998; Goodman et al., 1998; Lindsay et al., 2011). However, recent research has identified several exceptions to this concept. For example, the AWA sensory neuron and enteric motor neurons AVL and DVB involved in defecation are believed to generate all-or-none action potentials (Liu et al., 2018). Additionally, Mellem et al. (2008) demonstrated that the RMD neuron produces bistable plateau potentials (Mellem et al., 2008). Therefore, it is now suggested that the nematode's neurons encode information using a combination of gradual and active currents, some of which fulfill the stricter criteria for action potentials. Importantly, both mechanisms rely on calcium (Ca^{2+}) and potassium (K^{+}) ion currents. Furthermore, Ca^{2+} is required for synaptic vesicle release, which regulates synaptic information transmission. Thus, we expect a correlation between intracellular Ca^{2+} concentration and neuronal membrane potential, as well as with synaptic release.

The aforementioned characteristics of *C. elegans* combined with its tractable genome, as well as the transparency of its body, enable the use of genetically encoded Ca^{2+} indicators (GECIs) as a viable means of measuring neuronal activity. Many studies in neuroscience, including the present research, have utilized a type of GECI known as GCaMP. GCaMP is a fusion protein composed of calmodulin (CaM), a calcium-binding protein, a sequence from myosin light-chain kinase (M13), and green fluorescent protein (GFP). When intracellular Ca^{2+} bind to the CaM, a series of conformational changes occur that ultimately result in increased fluorescence of the GFP molecule which can be detected by means of various microscopy techniques (Akerboom et al., 2012; Chen et al., 2013; Nakai et al., 2001).

In particular, previous studies in our laboratory utilized a method to record neuronal activity in *C. elegans* by specifically localizing GCaMP to neuronal nuclei in combination with a spinning disk confocal microscope recording. We also employed microfluidic devices to immobilize the animals and deliver sensory stimuli in an acute manner. Importantly, under the experimental conditions described, a significant proportion of neurons within the head ganglion of *C. elegans* display a coordinated and spontaneous activity, as demonstrated by our previous studies (Kato et al., 2015; Prevedel et al., 2014; Schrödel et al., 2013; Uzel et al., 2022).

2.2.4 Overview of chemosensory systems in *C. elegans*

C. elegans has several sensory systems that allow it to detect and respond to different environmental stimuli. These include: chemosensation, thermosensation, mechanosensation, nociception and photoreception. Chemosensation is essential for *C. elegans* to locate food sources, avoid predators and toxins, and locate conspecific during mating behavior (Allen et al., 2015; Altun & Hall, 2011; White et al., 1986).

Chemosensation is achieved through the use of specialized chemosensory neurons that penetrate the cuticle, exposing their sensory cilia to the external environment. These neurons are located in the amphid, phasmid, and inner labial organs, with a total of 32 neurons responsible for detecting chemicals. The chemosensory neurons are exposed to the environment either directly or indirectly through openings created by socket and sheath glial cells (Bargmann, 2006).

Further, chemosensation in *C. elegans* includes detection of water-soluble (gustation) and volatile (olfaction) attractants and repellents which are mediated by different classes of primary sensory neurons. Additionally, *C. elegans* has specialized sensory systems responsible for the detection of environmental gases concertation such as carbon dioxide (CO_2) and oxygen (O_2) (Bargmann, 2006).

2.2.5 Ethological role of the oxygen sensation in *C. elegans*

Environmental oxygen concentration ($[O_2]$) is an important sensory cue for the *C. elegans* navigation in its natural environment of the soil and rotten plants material. Due to the poor solubility and low diffusion rate of O_2 in water, $[O_2]$ in soil can rapidly fluctuate at short distances varying from 0% to 21% (Bamgartl et al., 1994; Denny, 1993; Drew, 1992). From an ethological perspective, low $[O_2]$ may signal the presence of potential food, such as *E. coli* bacteria, which are substantial consumers of O_2 (Gray et al., 2004). On the other hand, high environmental $[O_2]$ close to 21% might signal the vicinity of the soil surface which should be a repellent factor for the nematode (Cheung et al., 2005). From the physiological perspective, environmental O_2 can influence the metabolic state of the nematode as the O_2 rapidly diffuses through the cuticle to the pseudocoelomic fluid; thus, altering animals internal $[O_2]$

level (D. L. Lee, 1965; Shen & Powell-Coffman, 2003). Consequently, *C. elegans* can maintain normal metabolism under the environmental [O_2] conditions from 3.6 to 21% (Shen & Powell-Coffman, 2003; van Voorhies & Ward, 2000).

Consistent with this *C. elegans* tend to avoid both hypo- and hyperoxia environment and locate in the preferred [O_2] range of 5-11% (Gray et al., 2004). However, in the presence of food *C.elegan* reveals two different phenotypes of behavior with relation to oxygen stimulus: solitary and social types. Solitary strains feed individually and disperse on a bacterial food surface. On the contrary, social feeding phenotype is characterized by the worms forming social aggregates ("aggregation behavior") on the food surface and worms tending to locate on the thicker bacteria layer at the boarders of the food lawn ("bordering behavior"). These phenotypes are explained by the variation in the *npr-1* gene which encodes for the FMRFamide-like peptide (FLP) NPR-1 receptor. A standard laboratory strain N2 (Bristol) accumulated a gain-of-function mutation in the *npr-1* gene and the hyper-expression of NPR-1 receptors leads to the dampened reaction to the hyperoxia in the presence of food and consequent solitary on-food behavior. On the opposite, Hawain wild strain (HW) and *npr-1* knocked out mutants with a low *npr-1* expression preserve strong hyperoxia avoidance behavior in the presence of food and exhibit the above-described social behavior (Weber et al. 2010; De Bono and Bargmann 1998; Gray et al. 2004; Cheung et al. 2005; Rogers et al. 2006).

Interestingly, it was found that social aggregates of *C. elegans* create a steep [O_2] gradient with [O_2] being substantially lower inside of the aggregate compared to the ambient one (Rogers et al., 2006). Also, [O_2] at boarders of the bacterial food lawn is lower comparing to the central area (Gray et al., 2004). Moreover, the decrease in the ambient [O_2] reduces aggregation behavior (Rogers et al., 2006). Additionally, NPR-1 receptors were found to be expressed and act in the oxygen sensory neurons URX, AQR, PQR and their synaptic targets - primary interneurons RMG and AUA which are promoting aggregation behavior (Carrillo et al., 2013; Coates & De Bono, 2002; Macosko et al., 2009; Zimmer et al., 2009). Altogether, these observation points to the assumption that social feeding behaviors can be part of the hyperoxia avoidance strategy. Consistent with this in the same study it was shown that nematodes elicit reversal crawling when the head of the worm leaves the aggregate, and this behavior presumably contributes to the maintaining of the aggregate (Rogers et al., 2006).

To avoid high [O_2] conditions *C. elegans* exhibit an avoidance behavior reaction which consists of two phases. At the initial stage, worms respond to elevated [O_2] with a transient increase in the probability of reversal crawling and omega turns - behavioral patterns aimed at reorienting the worms (Busch et al., 2012; Cheung et al., 2005; Persson et al., 2009; Rogers et al., 2006). This phase corresponds to the time period of the [O_2] rise. The second phase of hyperoxia avoidance reaction consists of a prolonged period of the accelerated forward locomotion (Busch et al., 2012; Laurent et al., 2015). Importantly, our

current research focused on the phase of the transient reversal response in the *npr-1* social strain in the presence of food, which was intended to mimic the animals' natural conditions.

2.2.6 Morphological and functional characteristics of the oxygen sensory neurons

Environmental [O_2] is detected by a specialized set of primary sensory neurons that can sense relative changes in [O_2]. This includes a group of neurons that detect increases in environmental [O_2], specifically the URX and IL2 neurons, along with a single AQR neuron located in the head and a single PQR neuron in the tail of the animal. Additionally, SDQ, BDU, ALN, and PLN neurons are also believed to contribute to the detection of increased environmental [O_2] and the associated behavioral responses (Chang et al. 2006; Zimmer et al. 2009; Gray et al. 2004). Conversely, a pair of BAG neurons in the worm's head detects reductions in [O_2].

URX, AQR and PQR are body cavity neurons with unique property (together with CEP neurons) to be in a direct contact with pseudocoelomic fluid by their cell body or dendrites (Coates & De Bono, 2002; White et al., 1986). It is estimated that the environmental O_2 should reach AQR and PQR dendrites in the pseudocoelomic fluid by diffusion in less than a second (Gray et al., 2004). At the same time, URX projects its dendrite to the tip of the nose within a labial process bundle and PQR projects dendrite within a phasmid sensilla structure (Doroquez et al., 2014; Gray et al., 2004; White et al., 1986). IL2 neurons send dendrites within the inner labial sensilla which are exposed to environment. BAG neurons send their processes within the lateral labial process bundles and like URX neurons they are not open to the outside. These suggests that overall, these neurons can monitor [O_2] within the pseudocoelomic fluid and in the external environment.

The above-described oxygen sensory neurons possess sensory cilia at the tip of their dendrites which are rich with microtubule and contain sensory transduction molecules (Ward et al., 1975; Ware et al., 1975). Numerous experimental studies point toward the fact that soluble guanylate cyclase homologs (sGCs) enzymes serve as the O_2 molecular receptors in *C. elegans*. It was found that mutations or altered expression of sGCs genes can affect oxygen related behavioral reactions (A. J. Chang et al., 2006; Cheung et al., 2005; Gray et al., 2004).

It was also shown that URX and BAG neurons require specific sGC homologues to sense increases and decreases in environmental oxygen levels [O_2], respectively (Zimmer et al., 2009). Next, it is known that sGCs can bind O_2 via oxygen heme binding (H-NOX) domain (Denninger & Marletta, 1999; Gray et al., 2004) which leads to the reaction where the 3′,5′-cyclic guanosine monophosphate (cGMP) is synthetized from GTP (Gray et al., 2004). Finally, cGMP can depolarize neurons by activating cyclic nucleotide-gated channels (Finn et al., 1996).

Importantly, previous Ca^{2+} imaging studies using microfluidic chip devices and in freely moving animals have demonstrated that the oxygen sensory neurons URX, AQR, PQR, and IL2 are activated in response to changes in ambient [O_2], as it shifts from preferred low levels to non-preferred levels of 15% or 21% [O_2]. (Busch et al., 2012; Kato et al., 2015; Kazatskaya et al., 2020; Nichols et al., 2017; Oda et al., 2017; Persson et al., 2009; Zimmer et al., 2009). On the other hand, BAG neuron is activated by the decrease in the environmental [O_2] (Kato et al., 2015; Zimmer et al., 2009).

Importantly, URX, AQR, and PQR neurons are known to exhibit a bi-component response. First response component ("phasic" component) is characterized by a sharp peaking activation that corresponds to the time period when the [O_2] stimulus rises. Next, as the [O_2] stimulus reaches the higher-level setting point, the neuronal activity drops to a plateau level exceeding the baseline ("tonic" component) which lasts as long as [O_2] stays at the elevated level. The magnitude of the phasic response component depends on the past history of the [O_2] stimulus, amplitude of a step-change stimulus and d[O_2]/dt of the ramp-stimulus (Busch et al., 2012; Zimmer et al., 2009). Il2 neuron exhibits similar initial sharp peaking activation, however, the following response component has more complex structure with a mixture of tonic activations and secondary activity rise peaks (Nichols et al., 2017).

2.2.7 Functions of interneurons in the oxygen perception circuit

On the next stage the information from the oxygen sensory neurons flows to the primary interneurons which implement further information processing and decision making. Connectome organization suppose three pairs of the candidate interneurons which might serve this function: RMG, AUA and PVP neurons. In particular, RMG neurons are recurrently connected with URX sensory neurons via chemical synapses and gap junctions. Similarly, AUA neurons receive major chemical synapses inputs from the URX neurons. PVP neuron has gap junctions with AQR and PQR sensory neurons. On the other hand, AUA, RMG and PVP interneurons each send chemical synapses to one or more of the reverse premotor interneurons AVA, AVD and AVE. Overall, this connectome arrangement puts AUA, RMG and PVP interneurons in the position where they could potentially be involved in the information transfer between the layer of the oxygen sensory neurons and premotor interneurons (White et al. 1986; Macosko et al. 2009).

This assumption was further supported by the Ca^{2+} imaging studies which revealed that the AUA and RMG neurons demonstrate activation in response to the elevated environmental [O_2], reflecting the URX response. (Busch et al., 2012; Laurent et al., 2015; Nichols et al., 2017; Oda et al., 2017). Moreover, it was shown that the URX ablation (Laurent et al., 2015) or GCY-35 guanylate cyclase mutation which disrupts oxygen sensation in the oxygen sensory neurons (Busch et al., 2012), lead to

the disruption of the response in the RMG and AUA neurons. These findings testify to the hypothesis that the Ca^{2+} response in the RMG and AUA neurons are driven by the oxygen sensory neurons input. Thus, it was experimentally proven that the oxygen sensory neurons transmit the information about the rise in the environmental [O_2] to the AUA and RMG interneurons.

On the other hand, ablation studies demonstrated that RMG and AUA contribute to the change of the behavioral state in response to the changes in the environmental [O_2]. Importantly, in the same study it was shown that ablating RMG interneurons also reduced the transient reversals and turns elicited during the [O_2] rise (Busch et al., 2012). Additionally, optogenetic stimulation studies demonstrated that RMG is activity is sufficient for inducing up-modulation of the forward locomotion (Laurent et al., 2015). Additionally, it was shown that the RMG neuron serves as a hub center in the distributed neuronal circuit which regulates oxygen related aggregation behavior (Macosko et al., 2009);

Additionally, a second-layer interneuron RIB might be potentially involved in the information processing from the oxygen sensory neurons. RIB neuron receives a large fraction of input from the AUA interneuron which as mentioned above receives inputs from the URX oxygen sensory neuron (White et al., 1986). Another substantial fraction of inputs RIB receives from the BAG neuron (White et al., 1986) which is known to detect the environmental [O_2] decrease. Numerous imaging, ablation and stimulation studies testify that the RIB neuron is involved in forward locomotion (Gray et al., 2005; Kato et al., 2015; Li et al., 2014; Tsalik & Hobert, 2003; Wang et al., 2020); on the other hand, RIB neuron send a major fraction of synapses to the AVE and AVA reversal premotor interneurons and increases the probability of reversal locomotion during the local search state of the worm (Gray et al., 2005; White et al., 1986). Overall, RIB neuron might receive information about the increase in the ambient [O_2] from the URX neuron via the AUA neuron and other hand, can influence motor state of the worm.

2.2.8 Premotor interneurons control forward and reverse locomotion in *C. elegans*

C. elegans demonstrates two main locomotion states, forward and reverse crawling, mediated by five pairs of premotor interneurons. From a connectome perspective, these interneurons are uniquely positioned as they gather synaptic inputs from sensory neurons and first- and second-layer interneurons, and serve as the primary source of input to the A and B motor neuron classes along the ventral cord (Chalfie et al., 1985; Varshney et al., 2011; White et al., 1986). The AVB and PVC interneurons drive forward locomotion by innervating B class motor neurons, whereas reverse locomotion is driven by AVA, AVD, and AVE interneurons that target A class motor neurons.

Ca^{2+} imaging studies shows that each of two premotor interneurons pools is active without oscillations during locomotion in the corresponding direction (Chronis et al., 2007; Faumont et al., 2011; Kawano et al., 2011). The activity of premotor interneurons is both correlated within their respective pools and reciprocal between different pools. This activity spontaneously switches, reflecting spontaneous switch between forward and reverse locomotion typically observed in *C. elegans* behavior (Gray et al., 2005; Kato et al., 2015; Pierce-Shimomura et al., 1999). Experimental ablation of one of the premotor neuronal pools reduces initiation of locomotion in the associated direction (Chalfie et al., 1985; Kawano et al., 2011; Wicks & Rankin, 1996). Next, ablation of all premotor interneurons does not eliminate rhythmic undulatory muscle activity, however it substantially affects undulatory coordination and speed (Gao et al., 2018; Kawano et al., 2011; Zheng et al., 1999). Altogether, these findings indicate that premotor interneurons are involved in the drive of the forward and reversal locomotor state but are not part of the central pattern generator.

Further, multiple studies point to the key role of the AVB and AVA neuron within the corresponding pools for the forward locomotion and reversal locomotion respectively. In particular, AVB and AVA activity rises coincide with the onset of forward and reverse movement respectively (Ben Arous et al., 2010; Chronis et al., 2007; Faumont et al., 2011; Gordus et al., 2015; Kato et al., 2015; Kawano et al., 2011; Larsch et al., 2013; Laurent et al., 2015). Moreover, ablation of AVA and AVB neurons severely impairs forward and reverse locomotion respectively (Chalfie et al., 1985; Gray et al., 2005; Piggott et al., 2011; Zheng et al., 1999) and the optogenetic activation of the AVA evokes reversal locomotion (Gordus et al., 2015; Schmitt et al., 2012). Thus, the traditional framework to explain the mechanism of the transiting between forward and reverse motor states relies on a reciprocal inhibition circuit pattern operating between two distinct neuronal modules (Roberts et al., 2016).

However, recent research has revealed novel insights indicating that AVA serves dual roles, both promoting and inhibiting reverse locomotion (Kawano et al., 2011), and additionally playing a crucial part in facilitating forward locomotion (Meng et al., 2022). This suggests a more intricate mechanism governing the dynamics of locomotion states, with AVA acting as a central controller of locomotion state by applying bidirectional control over AVB activity across different time scales. A strong transient depolarization of AVA results in phasic inhibition during reversal locomotion, whereas a sustained subtle depolarization of AVA provides continuous stimulation to AVB, promoting forward locomotion between reversal states (Meng et al., 2022).

2.3 Aims of current research

Overall, transient reversal crawling is a part of the avoidance behavior in *C. elegans* which can be triggered by an increase in ambient [O_2] near 21%. In the current study we aimed to investigate the neuronal mechanisms underpinning this sensorimotor transformation.

On the one hand, the underlying neuronal sensorimotor mechanism involved in this reaction can be envisioned as a feedforward flow of information comprising several hierarchically organized components. In this scenario, the first stage involves encoding the stimulus by the primary sensory neurons specialized in detecting increases in [O_2], such as URX, AQR, PQR, and IL2 neurons. Subsequently, a group of interneurons, which receive inputs from these oxygen sensory neurons, is presumed to engage in processing this information. This pool of interneurons likely includes RMG, AUA, and PVP neurons. Finally, premotor interneurons, including AVA, AVE, and AVD, responsible for initiating and sustaining the reversal motor state, are anticipated to integrate input from both sensory and interneurons, ultimately generating a command for the motor response conveyed to the motor neurons in the ventral cord. This perspective aligns with the aforementioned Input-output view of the brain organization and finds support in other studies within the field of *C. elegans*, where identified interneurons and premotor neurons have been described as dedicated encoders of specific sensory inputs or motor outputs, often viewed in context of isolated sensorimotor pathways (Chalasani et al., 2007; Donnelly et al., 2013; Gray et al., 2005; Ha et al., 2010; Ino & Yoshida, 2009; Kimata et al., 2012).

Alternatively, in the light of the Coordination View framework and recent advancements in the realm of *C. elegans* research, we hypothesize that the studied sensorimotor circuit may exhibit a complexity beyond the Input-output View with a feedforward information flow. Numerous recent studies emphasizing the role of motor representation in the brain of *C. elegans* further support this assumption (Gordus et al., 2015; Hendricks, 2012; Kaplan et al., 2020; Li et al., 2014; Luo et al., 2014).

Notably, a study emerging from our laboratory provided substantial empirical support for the Coordination View hypothesis (Kato et al., 2015). This research, leveraging whole-brain Ca^{2+} imaging in *C. elegans*, demonstrated that in the absence of external stimuli, the animal's brain exhibits spontaneous global activity dominated by the motor command signal shared among a large fraction of interneurons and motor neurons. Notably, this global brain state operates within a cyclic dynamic framework, where distinct phases of this cyclic activity align with the sequential order of the animal's behavioral actions, effectively orchestrating the assembly of motor commands into action sequences. Consequently, these findings underscore that the brain's default state is an active dynamic process primarily reflecting behavioral motor commands

Crucially, this study also showed that the low-dimensional organization of global brain dynamics remains robust in the presence of the oxygen sensory stimuli, consistently encoding sequential motor behavioral states. However, sensory input can affect the motor response by consistently adjusting the likelihood of the global brain dynamics being in a specific phase of its cyclical pattern, aligning with the corresponding behavioral state, thereby enabling the animal's reaction.

Overall, these findings contradict the Input-output View with feedforward sensory-motor pathways and instead support the Coordination View. Under this framework, we anticipate that sensory representations must actively interact with the internal state of the system, particularly downstream of sensory neurons. This interaction likely encompasses both feedforward and feedback information flow, incorporating mechanisms such as corollary discharge. Ultimately, this dynamic process influences the behavioral state, defining the animal's response.

The current study aimed to elucidate the neuronal mechanisms underlying the avoidance reaction and the principles governing information transfer in this sensorimotor transformation. Methodologically, we employed whole-brain Ca^{2+} imaging to monitor neuronal activity. Our approach involved inducing reversal avoidance reaction in immobilized worms within a microfluidic chip device, allowing for neuronal recordings. This method enables unbiased observation of brain-wide activity with single-neuron resolution from both head and tail ganglia. Hence, our next methodological objective was to develop a data analysis approach that facilitates the unbiased identification and classification of neurons within the defined sensorimotor transformation chain.

3. Results

3.1 Periodic oxygen stimulation elicits reversal behavior in populations of *C. elegans*

On the first place we wanted to develop an experimental paradigm which would effectively elicit behavioral response to the changes in the environmental oxygen concentration ($[O_2]$), and which could be mimicked at least partially under neuronal imaging conditions.

From the previous research we know that for the *npr-1* animals low environmental $[O_2]$ in the range of 5 – 11% is a preferred concentration which can be found in bacterial lawn borders and social aggregates of *C. elegans* (Cheung et al., 2005; Gray et al., 2004; Rogers et al., 2006). In contrast, the environmental atmosphere 21% $[O_2]$ is a repulsive stimulus which elicits changes in the worm's behavioral state on the first stage characterized by the transient reaction of reversal crawling (Busch et al., 2012; Cheung et al., 2005; Persson et al., 2009; Rogers et al., 2006); then following by the prolonged reaction characterized by the accelerated speed of forward movement (Busch et al., 2012; Laurent et al., 2015). For our project, we focused on the initial transient reaction to gain insights into the instantaneous brain mechanisms underlying the behavioral response to the stimulus. Building on this, we aimed to develop an oxygen stimulation assay in which an increase in the environmental $[O_2]$ would trigger a reversal crawling behavior in the *C. elegans* population.

For our experiments we established a stimulus paradigm with a periodic $[O_2]$ shifts between the levels of 11% lasting 60 seconds and 21% lasting 30 seconds (**fig. 1A**). We set the low boundary of the $[O_2]$ stimulus to 11% since this concentration corresponds to the upper boundary of the preferred concentration limits (Gray et al., 2004). Thus, the increase of the $[O_2]$ from that limit to the repulsive 21% $[O_2]$ was supposed to elicit reversal behavior. 11% $[O_2]$ periods were designed twice as long as 21% $[O_2]$ to increase the chance of acquiring the reversals appearing "spontaneously" and not caused by the 21% $[O_2]$ stimulus. The "spontaneous" reversals were planned to be used in the further analysis of imaging experiments results as a control to stimulus elicited events. Numerous repetitions were made to gain a statistical power for the analysis of the behavioral and further imaging results from each single recorded worm. Overall, the stimulus consisted of 16 periodic repetitions and each repetition was treated in the further analysis as a separate stimulus trial. The block of the periodic $[O_2]$ shifts was preceded by a 450 seconds baseline period with a constant 11 % $[O_2]$. This was made for the purpose of having a period used as an internal control in the data analysis.

In the behavioral assay the population of the adult worms (~100 animals per recording) with a *npr-1* genetical background were freely crawling and feeding on the homogeneous *E. coli* (OP50) bacterial food lawn seeded on the NGM surface. Gas stimulation with a protocol described above was applied

during the video recording procedure. Direct video tracking of each individual worm from the 10 Hz high-resolution recordings during the timespan of the stimulation allowed us for the further quantification of the behavior via the custom designed MATLAB analyses algorithm (see **Methods** for more details).

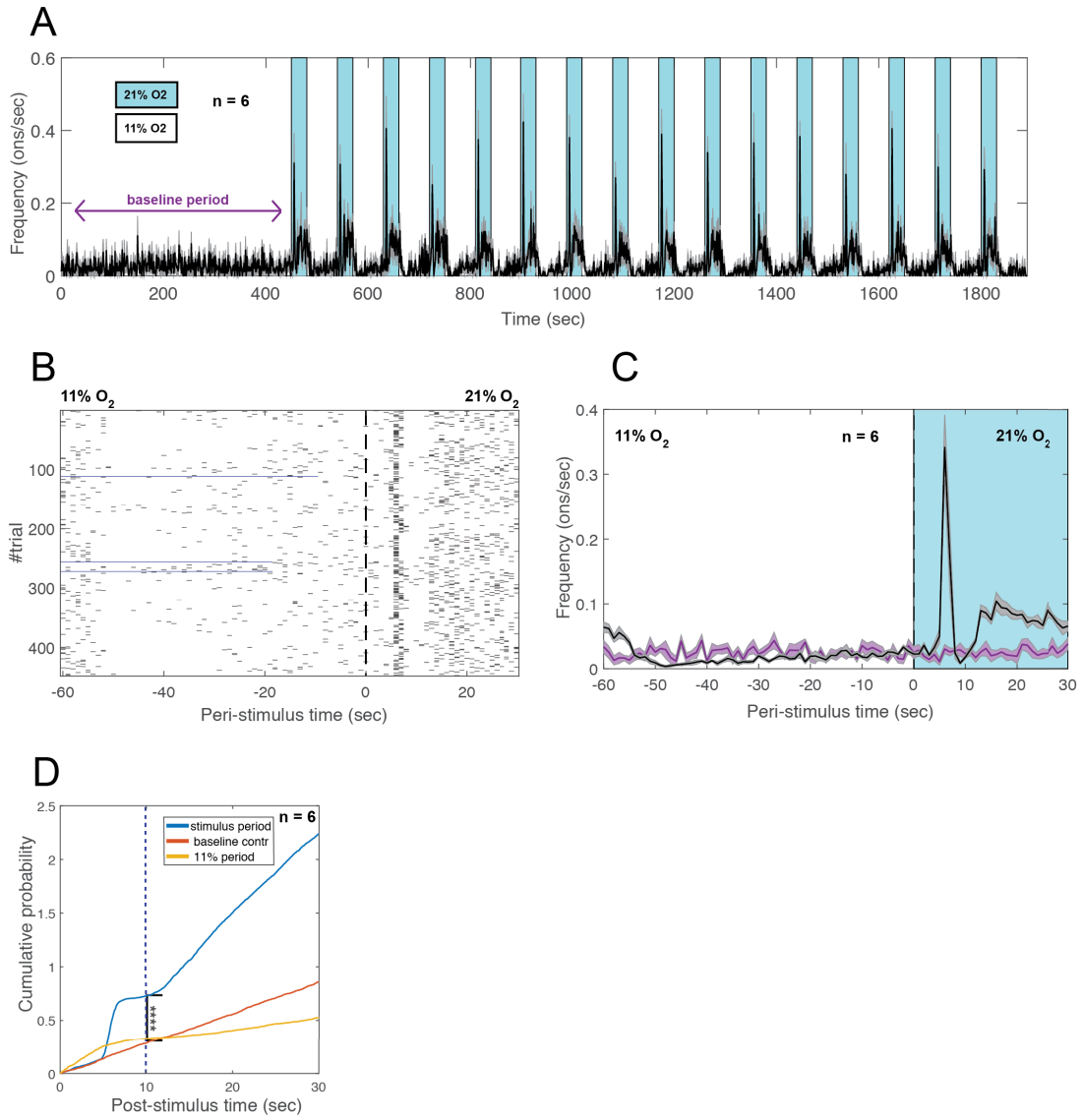

Figure 1. *C. elegans* population response to the periodic oxygen stimulation in the behavioral assay
(**A**) Trace shows the frequency of reversal onsets during the oxygen stimulation assay, which includes repetitive trials (438 traces coming from 6 experimental assays). Shaded area represents ± SEM. Periods of 11% and 21% [O_2] are denoted with white and blue vertical bars. Data is binned into 1-second bins (for A,B,C). (**B**) Raster plot shows reversal onsets across multiple trails from all experiments (only trials with no missing values during 21% [O_2] periods, included n trials = 448). Dashed line at 0 seconds represents the beginning of the 21% beginning of the 21% [O_2] period. Blue color code denotes missing values (NaN). (**C**) Grey line is a stimulus-triggered average of the reversal onsets frequency across 16 trials from 6 experimental datasets (n datasets = 6, n traces = 438). Shaded area represents ± SEM. Magenta line denotes baseline reversal onsets frequency estimated from the initial 450 seconds 11% [O_2] period. (**D**) Reversal onsets cumulative probability calculated from the 21% [O_2] stimulus periods (blue line), 11% [O_2] periods (yellow line) and initial 11% [O_2] baseline period (magenta line). ****, $p < 0.0001$.

In the analysis of the behavioral data, we focused on the reversal behavioral states as we expected that elevated [O_2] would elicit reversals locomotion. In particular, we extracted time points corresponding to the onsets of the reversal states to estimate the time dynamics of the motor command initiation. All the subsequent analyses of the behavioral experiments were based on this measurement.

We found that the population average reversals onset frequency calculated across all the recorded locomotion traces (see **Methods**) was reliably up-modulated during the 21% [O_2] periods throughout all of the stimulation trials relating to the baseline level and then values were decaying to the baseline upon the 11% [O_2] periods (**fig. 1A).** Interestingly, at every stimulation trial we could observe an initial sharp peak of the reversal's onsets frequency following by a secondary low-frequency up-modulation. These findings were also observed on the single-trial level where we could see a reliable appearance of the reversal's onsets following the 21% [O_2] stimulus onsets with approximately 5 seconds latency time (**fig. 1B**). The secondary activation started 10 seconds after the 21% [O_2] stimulus onset and had more variability in the onset timing.

To estimate the dynamics of the reversal onsets in more details we performed stimulus average analysis where reversal onsets were aligned to the 21% [O_2] stimulus onsets and averaged (see **Methods**). Results of this analysis support previous observations and reveal initial peak of the reversal onsets frequency appearing at timing ~7 seconds and decaying towards 10 seconds. The initial peak was reaching maximum value of ~0.3 onsets/second which indicates high trial basis variability of the response. This peak was following by a secondary wave of increased reversal onsets frequency which was lasting throughout the rest of the 21% [O_2] period. However, the secondary wave onsets were more variably in timing on trial-to-trial basis (**fig. 1B,C**), which were reflected in the lower values of the reversal's onsets frequency (~ 0.1 ons/sec; **fig. 1C**). Finally, comparison to the baseline control (**fig. 1C**, magenta line) further supports our finding that the [O_2] stimulus elicited reversals behavior in the population of *C. elegans.*

Next, to reveal the overall response probability robust to variable timing we calculated cumulative probability of the reversal onsets for three conditions: 21% [O_2] period, 11% [O_2] periods and the baseline control (**fig. 1D**). This analysis reveals that the reversal onsets have the same rate at the 21% [O_2] stimulus period with a baseline period during the first 5 seconds. Then it was up-modulated relating to the baseline curve in the time window from 5 to 7 seconds. This up-modulation was followed by the refractory period with a decreased reversals rate. Finally, after the 10 seconds we could observe a second rise of the reversal's frequencies comparing to the baseline control. We performed a statistical randomized resampling test between the stimulus elicited and baseline control results within the 2 seconds time windows centered around the 10 seconds time point as by that time all the reversal's onsets

from the first activation period were accumulated. This statistical test proved the significant difference between the stimulus elicited and baseline control results.

Interestingly, we observed that an elevated level of the reversal's frequencies was still maintained during the ~10 seconds period following the onset of the 11% [O_2] period (**figs. 1B - D**). Following this elevated period we observed the down-regulation of the reversals during the 11% [O_2] period comparing to the baseline (**figs. 1B,D**).

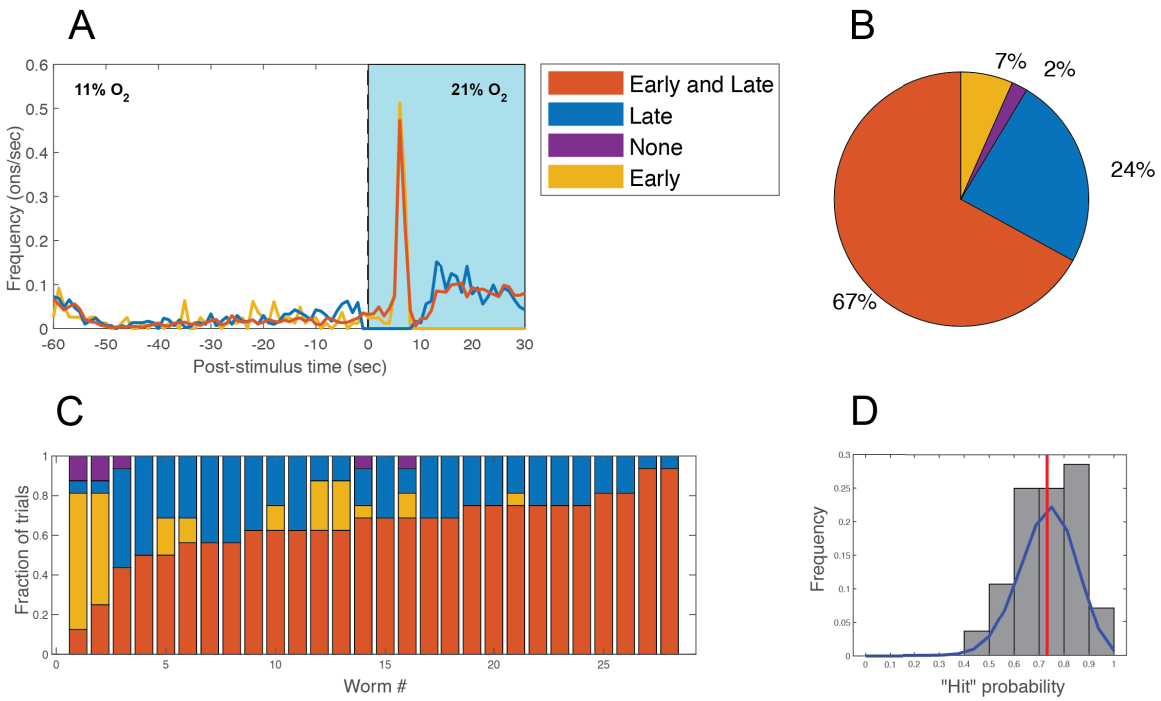

Figure 2. Different temporal types of response in *C. elegans* behavioral assay
(**A**) Each line is a stimulus-triggered average of the reversal onsets frequency across trials coming from three different clusters. Clustering was based on the timing of the reversal onset relating to the 21% [O_2] stimulus onset: "Early" - reversal occur only during first 10 seconds, "Late" - reversal – occur only after first 10 seconds, "Early and Late" – trials with reversal onsets occurring in both time windows. Only trials with no missing values during 21% [O_2] periods were included, n trials = 1245. Data is binned into 1-second bins. Color code is the same for A,B,C. (**B**) Proportion of trials belonging to each of the cluster described in (A) (n trials = 1245). (**C**) Bars show proportion of different type of trials for individual worms (each column corresponds to an individual worm, n = 28). Only data from the worms with no missing values (NaN) during the whole stimulation period is included for C and D. (**D**) Histogram of probabilities of reversal onsets occurring within first 10 seconds after the 21% [O_2] stimulus onsets ("Hit" trials) among individual worms in the population essay. Vertical red line denotes the mean value (0.73, n = 28 worms, same subset of data as in (C)). Blue line is a binomial probability density function with a probability of success for each trial set equal to the mean value (0.73) from the experimental results.

Then, we focused in more details on the time dynamics of the reversal's onsets up-modulations. For that we grouped all the recoded trials into four clusters ("Early", "Late", "Early and Late", "None") based on the reversal onsets timing relating to the 10 seconds threshold starting from the 21% [O_2] period onset (see **Methods**). Using the triggered average analysis (**fig. 2A**), we observed that in most stimulation trials (67%, **fig. 2B**), worms exhibited reversal behavior during both the 'early' and 'late'

time windows. Also, there were observed trials with only "Early" (this is the minority of trials only 7%) and only "Late" reversals (24% of trials). Comparing separately the early and late components of the reversal's onsets-triggered average from the "Early and late" cluster with the corresponding components from the "Early" and "Late" clusters we found that those reversals modulations have a similar pattern across the clusters (**fig. 2A**). This indicate that "early" and "late" responses are two independent type of reactions which could appear separately or on the same trial. Also, there was no observable pre-stimulus history difference for the reversal's dynamics from the different clusters. The "None" trial's cluster where worms did not exhibit any reversal behavior during the 21% [O_2] period was an absolute minority and accounted only 2% of cases.

Further, we analyzed the proportion of each trial types for the individual worms (**fig. 2C**). We found that all the analyzed worms exhibited a mixed types of reactions throughout the stimulation trials. For most worms, the "early and late" reaction type was the prevalent one mixed with the "late" type of reactions. This observation corresponds to the general distribution of the trial types (**fig. 2B**). Interestingly, just 10 worms out of 28 analyzed exhibited "early" trials and only 2 worms had this reaction as a prevalent type, which points out to the suggestion that this type of the reaction is linked to some individual variability.

Finally, we wanted to estimate the overall probability of the worm's response within the first 10 seconds upon the beginning of the 21% [O_2] period across all the stimulus repetitions. For that we pooled together "Early" and "Early and late" clusters and estimated the probability of that pooled response cluster across all the presented trials for each of the individual worm (**. 2D**). We found the mean early response probability ("Hit" probability) across analyzed worms varies in the limits from 0.4 to 1 with a mean value equals 0.73. Thus, indicating that worms in the behavioral experiments had a strong tendency to generate a short latency behavioral response with a certain trial-to-trial variability. Next, we asked if the inter-individual variability in the "Hit" trials probability could be explained by the worms' idiosyncratic characteristics. For that, we calculated the binomial distribution for the trial success rate set equal to mean experimental value above. When compared to the experimental data (**fig. 2D** - blue line vs grey histogram bars) we could see that the experimental "Hit" trials probability results follow the theoretical binomial model. This result suggests that each trial might be independent from each other and that the inter-individual variability of the "Hit" trials probability should not be a result of an idiosyncratic worm's characteristics or the possible current long-lasting worm's behavioral state.

Overall, we found that periodical oxygen stimulus could elicit reversal behavioral response in the population of freely moving *C. elegans*. This response is stable across the whole span of the trials on the populational level; however, it has certain trial-to-trial variability when investigated on a single

worm basis. The reversal onsets resemble a bimodal distribution with an early response appearing within the 10 seconds latency window following the 21% [O_2] stimulus and a late response following it. We have been focusing on the early component of the behavioral response using it as an approximation for the sensorimotor transformation happening in the response to the [O_2] stimulus onset. We found that individual worms have a higher than chance level of reaction to the [O_2] stimulus, although they also revealed a range of the trial-to-trial variability in their responses. This inter-individual range of the responsiveness laid within the limits of the theoretical binomial distribution suggesting the inter-trial independence and thus the absence of the idiosyncratic effect.

3.2 Revealing the profile of oxygen stimuli in behavioral and imaging assays with oxygen dye recordings

For the behavioral and brain imaging assays, the oxygen stimulus was intended as an instantaneous step change for each trial. However, the actual dynamics of [O_2] changes depend on the diffusion rate through the polydimethylsiloxane (PDMS) membrane in the microfluidic chip device and the timing of the gas filling the chamber in the behavioral arena. Therefore, we aimed to empirically estimate the actual dynamics of [O_2] changes on a trial basis for both experimental assays.

For that, we performed imaging recordings of the O_2-sensitive fluorescent ruthenium dye (Klimant & Wolfbeis, 1995) while applying oxygen stimulus paradigm constituted of the calibration parts and parts with a periodic oxygen stimulus which were a modified version of our experimental stimulus paradigm (see **Methods**).

First, we estimated the [O_2] gradient in the microfluidic chip devices. Using the calibration data (**fig. 3A**), we fitted an exponential function (**fig. 3B**) to establish the relationship between dye fluorescence levels and ambient [O_2]. With this calibration function, we then reconstructed the [O_2] trace from the oxygen dye fluorescence trace (**fig. 3C**). On the first place we found that the empirically estimated [O_2] profile was following the preprogrammed parameters changing from 11% to 21% on the trial basis. However, we could also observe trial-to-trial variability in the reconstructed ambient [O_2], appearing most likely due inaccuracy of the dye signal itself. Also, a subtle drift skewing results to the up was observed towards the end of the recording, which could be explained by the bleaching or evaporation of the dye.

To account for these variabilities and focus on the finer time dynamics, we calculated the stimulus-triggered average of the [O_2] trace along with its first derivative over all trials (**fig. 3D,E**). The trail average [O_2] trace and its first derivative traces indicate that the actual [O_2] increase starts shortly after

the theoretical onset time and has an initial steep rise phase following by a shallower shoulder; overall, it takes ~10 seconds for the $[O_2]$ to reach the 21% level. After that $[O_2]$ is plateauing and stays at that

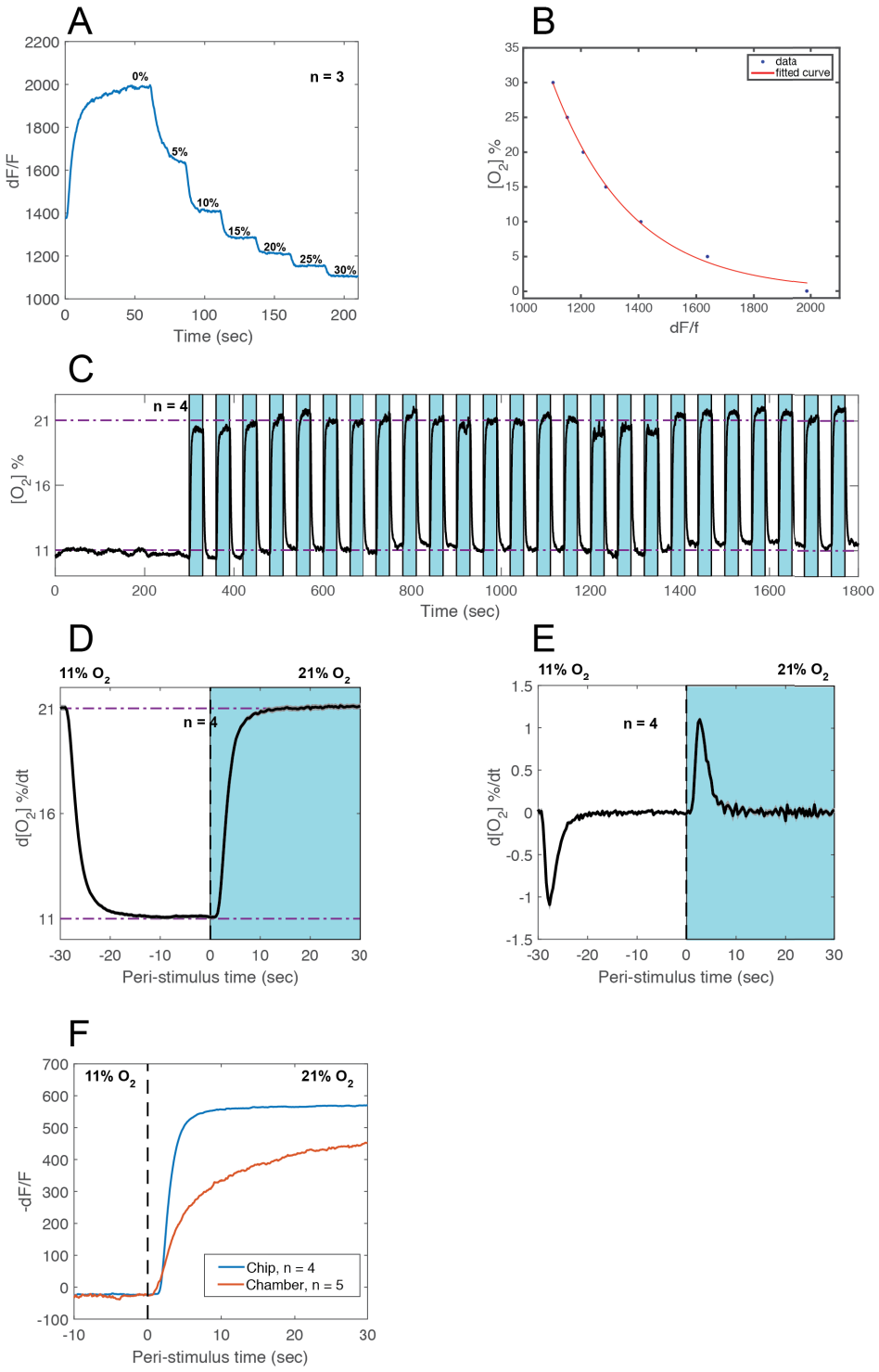

Figure 3. Oxygen stimulus measurements with a ruthenium dye
(**A**) Trace showing oxygen dye fluorescent intensity during the calibration part of the recording. This is an average value from three calibration periods from one example recording. It has seven steps with incremental increase of the $[O_2]$ by 5% at each step from 0% to 30%. (**B**) Red line is an exponential function fitted to the oxygen calibration data from one experimental recording (same as in (A)). Blue dots represent average calibration results for each of the seven steps. (**C**) Grey line is an estimated $[O_2]$ trace averaged across all recordings (n = 4) reconstructed from the dye fluorescence intensity trace (not shown) and fitted model from (B). Violet dotted lines mark 21% and 11% $[O_2]$. Stimulus protocol periods of 11% and 21% $[O_2]$ are denoted with white and blue vertical bars. (**D**) Grey line is a stimulus-triggered average from the

reconstructed [O_2] trace (from panel (C)) over all trials (n = 25). Shaded area represents ± SEM. (**E**) Stimulus-triggered average of the first derivative from the [O_2] trace (D) (n = 25 trials). Shaded area represents ± SEM. (**F**) Triggered average of the dye intensity slope in the chip recording (blue line, n = 4) and behavioral chamber device recordings (red line, n = 5). Period from -10 to 60 seconds around the [O_2] upshift onset is depicted.

level till the end of the 21% [O_2] period. Next, as the set [O_2] drops to the 11% level the empirically acquired [O_2] trace also decreasing and reaching the ~11% level after 10 seconds upon the theoretical onset. The first derivative of the recovered [O_2] trace was reaching maximum value at ~5 seconds upon the theoretical stimulus onset indicating the steepest point of the [O_2] gradient and similar dynamics was observed for the [O_2] gradient downshift.

Next, we compared the [O_2] dynamics in the microfluidic chip devices and the behavioral chamber For that, we recorded separate sets of data and calculated stimulus-triggered averages of the corresponding [O_2] traces (**fig. 3F**). From the trial-averaged dye fluorescence traces, we observed that the [O_2] in the behavioral chamber showed a more gradual gradient increase compared to the microfluidic chip device. The slope of the increase became shallower only after approximately 15 seconds following the theoretical stimulus onset; however, it never reached a plateau within the observed 30-second time window. Additionally, both the behavioral chamber and chip device results indicated a gas delivery delay of ~ 1 second, which is the latency before the experimentally reconstructed [O_2] traces began to rise.

Overall, we found that the empirically measured [O_2] stimulus in the conditions of imaging and behavioral assays did not perfectly match the theoretically programmed step stimulus. In the microfluidic chip device used for imaging, the actual [O_2] took approximately 10 seconds to reach the set concentration, while in the behavioral chamber this process was even slower. Additionally, both recording conditions exhibited a slight delay in gas delivery. These factors should be taken into account when interpreting the results of the whole-brain imaging and behavioral experiments.

3.3 Single-neuron resolution whole-brain imaging allows for the investigation of the brain activity in the oxygen stimulation assay

After having established an experimental paradigm which effectively elicits reversal state in the behavioral experiments, we aimed to transfer it into the whole-brain imaging assay which would allow us to investigate the brain activity underlying the sensorimotor transformation in response to the oxygen stimulus.

For that we used a single-neuron resolution whole-brain Ca^{2+} imaging technique by means of the nuclear localized and pan-neuronally expressed Ca^{2+} indicator GCaMP6f in immobilized *C. elegans* previously established in our laboratory (Kaplan et al., 2020; Kato et al., 2015; Schrödel et al., 2013). In this

approach the worm is immobilized in the custom-made microfluidic chip device which allows for the simultaneous imaging and precise control of the environmental gas concentrations (Zimmer et al., 2009) (**fig. 4A**). The part of the worm channel designated for the imaging had a curved shape allowing to place head and tail ganglions of the worm within the imaging field of the recording microscope: thus, we could record all neurons in the head, retrovesicular and tail ganglia, and an adjacent parts of the ventral cord (**fig. 4B**).

To reproduce conditions previously used in the behavioral assays we imaged adult worms of the same genetic line of the worms with *npr-1* background in the presence of the food (*E. coli* OP50) and applied the same stimulation protocol as was employed for the behavioral assays.

Importantly, current research utilized a novel paralysis technique where worms were paralyzed using histamine through Drosophila histamine-gated chloride (HisCl) channels (Pokala et al., 2014) expressed in the body wall and pharyngeal muscles (see **Methods**). Notably, *C. elegans* neither synthesizes nor utilizes histamine as a neurotransmitter, and exogenous histamine has minimal effect on the behavior of wild-type worms (Chase & Koelle, 2007; Pokala et al., 2014). Therefore, this method is preferred over the tetramisole previously used in our lab, which acts as a nicotinic acetylcholine receptor agonist (Martin et al. 2012) and has the potential to interfere with the function of cholinergic neurons in the worm's brain, such as the URX and IL2 neurons (Pereira et al., 2015).

Using this experimental technique, we acquired a total of n = 14 datasets with a periodic oxygen stimulus presentation suitable for AVA neuron activity analysis. Among these, n = 5 datasets had sufficient recording quality for further pan-neuronal analysis (see **Methods**). Additionally, we recorded two sets of control datasets: n = 10 datasets with a constant 11% [O_2] and n = 10 datasets with a constant 21% [O_2], which were later used in the data analysis.

Position of all neurons were traced throughout the duration of the recording and then their fluorescence traces (dF/F0) were extracted and used for the further analysis as proxy for the neuronal activity. Thus, each recording resulted in a high-dimensional dataset (97-156 neurons per recording) which included sensory, inter- and motor neurons (**fig. 4C**). Next, neuronal cell types were identified based on their stereotypic topographic position and characteristic activity patterns. We could identify from 44 to 61 neurons per recording. Overall, from 5 recorded datasets we could identify 86 neuronal classes which were then used in the further analysis. For the control datasets we were extracting and using only the AVA neuron traces.

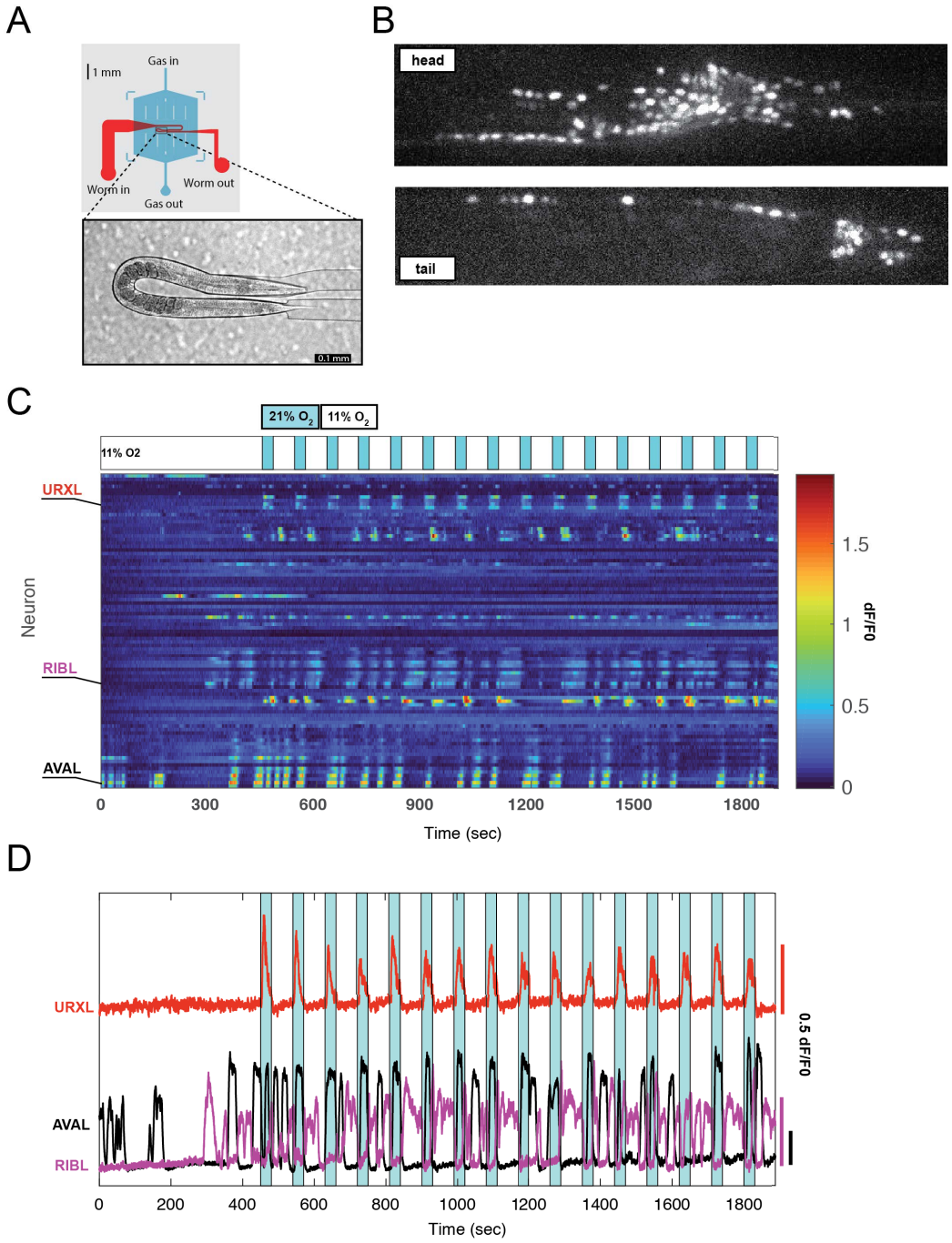

Figure 4. Schematic of the whole-brain calcium imaging experimental approach
(**A**) Microfluidic device used for the whole-brain head and tail GCaMP6f recordings. Top: schematic of the microfluidic device. Bottom: scaled fragment of the microfluidic device depicting a curved fragment of a worm channel with a worm immobilized inside of it. Modified from Kaplan et al. 2020. (**B**) Maximum intensity projection of a representative time frame from an example recording. Top: head ganglion; bottom: tail ganglion and a corresponding part of the ventral nerve cord. (C) and (D) show results acquired from the head part of this recording. (**C**) Example of the whole-brain head and tail GCaMP6f recording. Top: schematic of the oxygen periodic stimulus with periods of 11% and 21% [O_2] denoted with white and blue vertical bars respectively. Bottom: heatmap showing fluorescence (dF/F0) traces of all neurons detected in the recording sorted by correlation (each line corresponds to activity trace of a particular neuron). (**D**) Fluorescence traces of the three neurons of interest. Scale bars on the right represent 0.5 DF/F0; note the amplitude of the AVAL trace was downscaled twice relative to other traces for the matter of representation.

From the heatmap of the example multi-neuron recording we could observe that a large fraction of neurons was active during the duration of the recording (**fig. 4C**). Remarkably, most of the neurons

could be grouped into clusters with a correlated activity. From the previous research we know that the spontaneous brain activity is dominated by the mutually anticorrelated forward and reverse locomotion encoding activity governed by the respective neuronal clusters (Kato et al., 2015a). Here we also can observe that under the periodic oxygen stimulus conditions two major neuronal clusters are represented by the forward and reverse pre-motor interneurons: for the example we marked RIBL and AVAL neurons for each of those cluster correspondingly (**fig. 4C,D**). Individual activity traces of the RIBL and AVAL neurons from the same example recording also demonstrated mutually anticorrelated activity (**fig. 4D**).

Additionally, in our recordings we could observe a neuronal cluster with activity tightly following 21% [O_2] stimuli periods (**fig. 4C**). This cluster includes oxygen sensory neurons as shown with example of the URXL neuron which trace demonstrated tight correlation with oxygen stimulus (**fig. 4D**). This finding indicates that the oxygen stimulus was successfully detected by the worms in the imaging assay.

Overall, we could transfer our stimulation paradigm from the behavioral to the whole-brain imaging experimental assay. Acquired imaging recordings resulted in the multi-neuronal datasets comprising different neuronal classes. A fraction of neurons from each recording was matched to a corresponding neuronal class identity and then results from the same identity classes were combined across recordings and treated together in the further analysis.

3.4 Oxygen sensory neurons reliably encode periodic oxygen stimulus in the whole-brain imaging experiments

After establishing a whole-brain imaging assays and acquiring experimental datasets, we wanted to estimate if the oxygen stimulus is perceived by the worm under the conditions of the whole-brain imaging assay and how this stimulation is encoded on the level of the sensory neurons. For this we focused on the identification the oxygen sensory neurons and analysis of their activity related to the stimulus.

From the previous research we know that *C. elegans* has several classes of sensory neurons governing the worm's avoidance reaction of the increase in the ambient [O_2]. Those neuronal classes are: URX, AQR and PQR neurons (Cheung et al., 2005; Gray et al., 2004; Persson et al., 2009; Rogers et al., 2006; Zimmer et al., 2009); additionally, SDQ, BDU, ALN, and PLN neurons as supposed to contribute to the ambient [O_2] increase perception and related behavioral activity (Chang et al. 2006; Zimmer et al. 2009; Gray et al. 2004). Moreover, previous imaging experiments revealed response of the URX, AQR and PQR neurons to the increase in the [O_2] (Busch et al., 2012; Oda et al., 2017; Persson et al., 2009;

Zimmer et al., 2009) including imaging in freely moving animals for URX and PQR neurons (Busch et al. 2012).

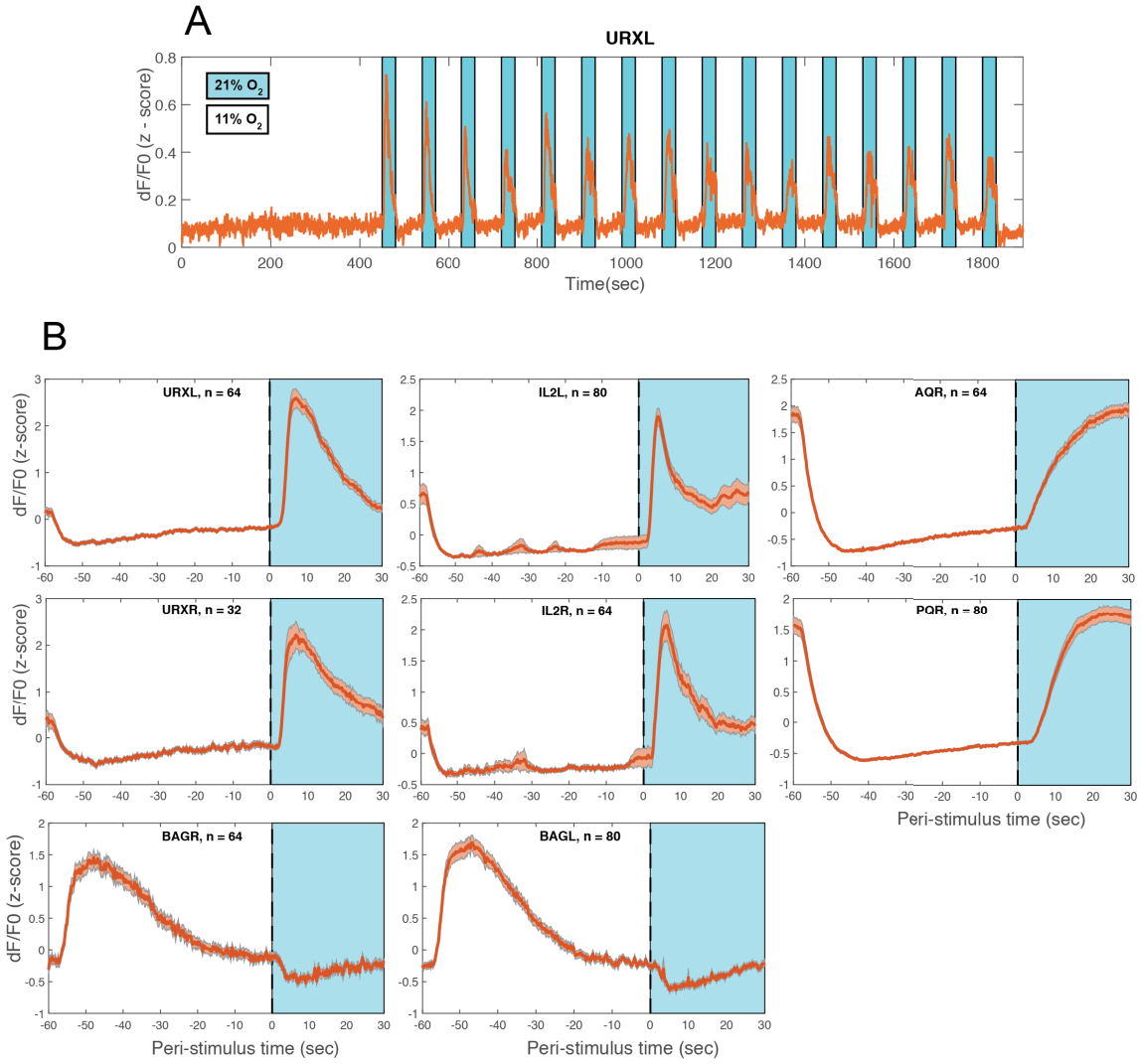

Figure 5. Oxygen sensory neuron's response to the periodic oxygen stimulation.
(**A**) An example fluorescence (dF/F0) trace of the URXL oxygen sensory neuron's activity during the periodic oxygen stimulation. Periods of 11% and 21% [O_2] are denoted with white and blue vertical bars. (**B**) Stimulus-triggered averages of neuronal activity for different oxygen sensory neurons. We could detect multiple neurons reacting to the increase in [O_2] (a pair of URX neurons, a pair of IL2 neurons and single AQR and PQR neurons) and a pair of BAG neurons reacting to the decrease in [O_2]. Shaded area represents ± SEM. N in each box indicates number of trials used for averaging.

We employed an explorative approach by the means of stimulus-triggered average analysis (**fig. S1**) in combination with identifying the characteristic topographic position of the neurons to reveal all potential oxygen sensory neurons in our recorded datasets. With this approach we were able to identify most of the previously described oxygen sensory neurons: pair of the URX neurons, and single AQR neurons in the head ganglion of the worm and a single PQR neuron situated in the tail ganglion. Additionally, we revealed a 21% [O_2] correlated activity in the pair of neurons in the head ganglion

with a topographic position corresponding to the IL2 neurons previously assumed to be potential oxygen sensory neurons (Nichols et al., 2017) (**fig. 5B**).

Once all the oxygen sensory neurons were identified in our recordings, we sought to characterize their activity patterns in response to the oxygen stimulus. As demonstrated with an example of the URXL neuron's activity trace, oxygen sensory neurons demonstrated stereotypic reaction to the [O_2] stimulus throughout presented trials with a certain trial-to-trial amplitude variability (**fig. 5A**). Further, we focused on the stimulus-triggered averages of the fluorescence traces of the identified oxygen sensory neurons.

Exploring the averaged URX activity we revealed that it is characterized by a sharp rise reaching maximum ~7 seconds upon the 21% [O_2] onset and then followed by the gradual activity decline. Notably, its activity was not reaching baseline within the 21% [O_2] period and was decreasing to the baseline during the first ~10 seconds of the following 11% [O_2] period (**fig. 5B**).

AQR and PQR neurons demonstrated a different dynamic in their reaction to 21% [O_2] stimulus: their response was characterized by a gradual increase of the fluorescence reaching plateau towards the end of the 21% [O_2] period. Similarly, to the URX neurons, this plateau activity level was preserved through the rest of the 21% [O_2] period and then falling towards the baseline level during the ~15 seconds of the following 11% [O_2] period (**fig. 5B**).

A pair of IL2 neurons demonstrated a sharp rise of the fluorescent activity similarly to the URX neuronal pair. The fluorescence activity was reaching maximum at ~5-7 seconds upon the 21% [O_2] onset. Following the maximum point the fluorescence activity was decreasing and reaching a plateau phase ~15 seconds upon the 21% [O_2] onset. This plateau phase was stable and lasting throughout the remaining 21% [O_2] period. It was falling to the baseline within ~7 seconds of the following 11% [O_2] period (**fig. 5B**).

Additionally, we were able to identify previously described pair of BAG neurons which is sensitive to the decrease in [O_2] and govern related behavioral responses as was shown in previous behavioral and imaging studies (Kato et al., 2015; Zimmer et al., 2009). BAG neurons in our recordings demonstrated activation during the 11% [O_2] periods: reaching maximum ~15 seconds upon the 11% [O_2] onsets and then falling towards the baseline towards the ~40 sec. Interestingly, we also observed a suppression of the BAG's fluorescence activity following the 21% [O_2] onset, which subsequently returned to baseline levels by the end of this period (**fig. 5B**).

After characterizing the average response properties of oxygen sensory neurons, we aimed to investigate the reliability of their activation in response to the oxygen stimulus across multiple trials. To achieve this, we annotated the rise states of all detected sensory neurons from their fluorescence activity traces and extracted the timings of rise onsets. We specifically focused on the timing of neuronal activity rise onsets on an individual trial basis, using cumulative probabilities calculated across all trials presented. This approach aimed to uncover overall response patterns resilient to variations in timing (see **Methods**). Importantly, due to the inability to identify the left neuron from the URX pair in one of our experimental datasets, we substituted its results with those from the right neuron of the URX pair for our analysis. Subsequently, we treated both neurons together as the URXL\R neuron in our further analyses

Trial-basis observations revealed that URX, AQR and PQR neurons are lacking spontaneous activity during the 11% [O_2] periods and initial 11% [O_2] baseline period of recordings (**figs. 5A, 6A, S2A**) which is also reflected by the flat activity during the 11% [O_2] periods at the triggered averages of corresponding neurons (**fig. 5B**).

URXL\R exhibits activation on most of the trials starting shortly after the 21% [O_2] stimulus onset and the rise onset events were grouped in the 5 seconds time window following the stimulus onset (**fig. 6A**). Alongside with this observation, cumulative probability curve revealed gradual rise within this time window and was reaching value of ~1 within ~5 seconds time window following the stimulus onset (**fig. 6B**). These findings indicate almost deterministic response of the URXL\R neuron to the oxygen stimulus with a subtle response onset variability.

Similar response properties were revealed for the AQR and PQR oxygen sensory neurons. However, it should be noted that on a part of the trials all coming from the same individual dataset AQR and PQR neurons exhibited substantially delayed responses **(fig. S2A)**. This is reflected by the cumulative probability which shows that AQR and PQR response probability reached the only level of ~0.8 value by the 5 seconds from the stimulus onset **(fig. 6B)**. Eventually, the cumulative rise probability values for the AQR and PQR neurons were reaching levels of ~1 and ~0.9 respectively ~17 seconds upon the stimulus onset; thus, demonstrating substantially reliable activation on the trial-to-trial basis along with URXL\R neuron.

Importantly, trial-basis observations revealed that URXL\R, AQR and PQR neurons exhibited not more than one activation per each trial within the 21% [O_2] periods **(figs. 6A, S2A),** which is also reflected by the fact that their rise onsets cumulative probabilities was plateauing at the level not exceeding 1 for the rest of the 21% [O_2] period **(fig. 6B)**.

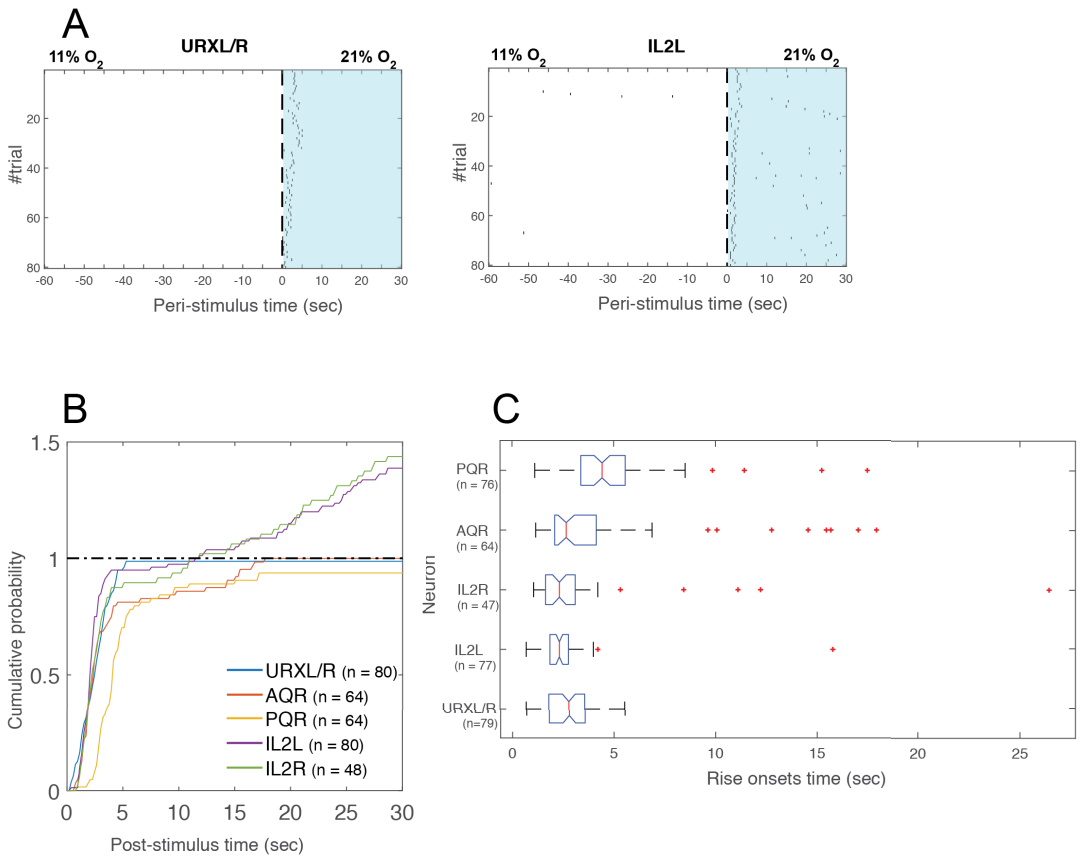

Figure 6. Oxygen sensory neurons exhibit reliable activation in response to the oxygen stimulation.
(**A**) Raster plots showing the onsets of the rises of neuronal activity of the URXL\R (left) and IL2L (right) oxygen sensory neurons. Each horizontal line corresponds to a single stimulation trial. Vertical dashed line at 0 seconds denotes transition from the 11% to 21% [O_2]. (**B**) Each line is a cumulative probability of the neuronal activity rise onsets of different oxygen sensory neurons calculated from the 21% [O_2] stimulus periods. Horizontal dotted line denotes 100% probability level. For the URXL\R and IL2L neurons calculation comes from the same data as represented at (A). N for each neuron indicates the number of trials used for the cumulative probability quantification. (**C**) Box plot showing rise onset times of different oxygen sensory neurons relative to the 21% [O_2] stimulus onset. Red lines represent median values. Only the first activity rise onset was considered for this analysis in case of multiple neuronal activity onsets per trial. N for each neuron identifies the number of the activity rise onsets used for the analysis (this value was not always equal to the number of trials used for the analysis, trials where a neuron did not exhibit activation resulted in missing values (NaN)).

The IL2 pair of neurons exhibited similar response time dynamics in response to the 21% [O_2] stimulus with rise onsets grouped in the 5 seconds time window following the stimulus onset (**figs. 6A, B, S2A**). However, in contrast to the URX, AQR and PQR sensory neurons, IL2 neurons exhibited secondary wave of activation during the 21% [O_2] periods on a large fraction of trials which can be detected on the individual-trial basis observations (**figs. 6A, S2A**) and also is reflected by the rise onsets cumulative probability which reached the value of 1 at ~12 seconds upon the beginning of the 21% [O_2] stimulus period and then continued growing until reaching the level of ~1.4 by the end of the 21% [O_2] stimulus period (**fig. 6B**). Moreover, this secondary wave of the rise onsets should explain previously observed plateau period on the stimulus-triggered average (**fig. 5B**).

Additionally, in contrast to the URX, AQR and PQR sensory neurons we could observe a rare sporadic activity of the IL2 neurons appearing during the 11% [O_2] periods (**figs. 6A, S2A**); which also

contributed to the triggered average pattern where we could observe peaks during the 11% [O_2] period (**fig. 5B**).

Next, we aimed to reveal if there is a consistent sequential structure in the mutual relationship between the activation onsets of different oxygen sensory neurons. To answer this question, the activation onsets latency time were calculated in relation to the 21% [O_2] stimulus onset (**fig. 6C**)**.** The earliest onsets of all sensory neurons were detected within ~1 second upon the oxygen stimulus onset and the median values for all sensory neurons except PQR lied within the same range of ~3-4 seconds. Both IL2 neurons demonstrated a slightly smaller median value of the rise onsets latencies comparing to the rest of the sensory neurons. On the other hand, PQR neuron demonstrated distinguishably higher median value of the onset latencies. Also, the AQR and PQR onset latencies were tailed towards the right with substantial amount of outliers with a long latencies which goes along with a previous individual-trial basis observation that a part of the trials exhibited substantially delayed responses of the AQR and PQR neurons (**fig. S2A**).

Considering previously detected trial-to-trial variability of the rise onsets timing for all sensory neurons in the range of ~5 seconds we sought to investigate their mutual time relationship on the individual trial basis. For that, we compared rise onset timing pairwise for the URXL\R, IL2L and AQR neurons; PQR was not included in this analysis, as it had evidently late response based on the median value (**fig. 6C**).

We found that the scatter plots for each neuronal pair showed variable time relations in their activation onsets (**fig. S2B**), as evidenced by data points dispersed around the identity line. Interestingly, when investigated on the individual dataset level, datasets #1 and #2 consistently showed IL2L activity preceding URXL\R neuron activation. Additionally, dataset #3 uniquely exhibited substantially high latency times for the AQR neuron, corroborating previous analyses. Beyond these observations, our analysis at the individual dataset level did not reveal a clear sequential structure for sensory neuron activation.

Further, we found that URX had low positive correlations of their rise onset latencies with IL2L and AQR neurons when calculated over all recorded datasets (**fig. S2B**). In contrast, AQR and IL2L neurons exhibited a very weak negative correlation. Interestingly, when examining the rise onset correlations of all pairs of oxygen sensory neurons on an individual dataset basis, we observed substantial variability, ranging from weak to strong correlations and shifting from positive to negative for each dataset. This indicates a high degree of inter-dataset variability in the relationships between sensory neuron activation times.

Overall, we found that 21% [O_2] stimulus reliably elicited responses in several oxygen sensory neurons: URX, AQR, PQR, and IL2. These neurons consistently exhibited their responses within a 5-second window following the onset of the oxygen stimulus across presented stimulus trials. However, the timing of mutual activation onsets between these neurons varied significantly across trials and datasets, indicating a lack of a consistent sequential pattern. Further correlation analysis revealed substantial variability between datasets in terms of the relationships between the activation times of these sensory neurons.

3.5 Motor response is significantly entrained by the oxygen stimulus in the whole-brain imaging assay

On the next step we aimed to characterize the motor response to the oxygen stimulus in the whole-brain imaging assay. Similar to our approach in analyzing behavioral data, we focused on the reversal locomotion states, based on our hypothesis that elevated [O_2] levels would trigger this motor response. From the previous research we know that *C. elegans* under the normal conditions freely crawling on a food surface exhibit forward movements spontaneously interrupted by the reversal locomotion (Gray et al., 2005; Pierce-Shimomura et al., 1999) and similar switches of neuronal motor command activity was also observed in the animals restrained in the microfluidic chip device under the whole-brain imaging conditions (Kato et al., 2015). A group of interneurons including AVA, AVE and AVD interneurons are known to be important for driving the reversal locomotion (Chalfie et al., 1985; Zheng et al., 1999). From the connectome map it is known that these interneurons receive inputs from the upstream inter- and sensory neurons; and in turn send outputs directly to the A-type motor neurons in the ventral cord which governs the reverse locomotion (Chalfie et al., 1985; Varshney et al., 2011; White et al., 1986). In particular, the AVA neuron is important for the reversal locomotion as it was shown that AVA activity rises reliably correlates with reversal locomotion periods in freely moving animals' recordings (Kawano et al. 2011; Kato et al. 2015; Ben Arous et al. 2010; Chronis, Zimmer, and Bargmann 2007; Gordus et al. 2015; Faumont et al. 2011; Larsch et al. 2013; Laurent et al. 2015). Moreover, we know that the AVA ablation severely impairs reverse locomotion (Chalfie et al., 1985; Gray et al., 2005; Piggott et al., 2011) evidencing its necessity for the reversal motor command. On the other hand, optogenetic activation of the AVA evokes reversal locomotion (Schmitt et al. 2012; Gordus et al. 2015) supporting the hypothesis of the AVA causal role in the reversal behavior.

Thus, we chose to use the activity of the AVA neuron as a proxy for the reversal locomotion in the conditions of the whole-brain imaging experiments where the worms were paralyzed and immobilized in the channel of the microfluidic device. First, we were analyzing 14 datasets where AVA neuron could be identified; in each datasets the best quality trace from the left-right AVA pair was selected for the

analysis. We applied the same analysis pipeline as was done before for the sensory neurons where we focused on the onsets timing of the long-lasting activation periods (see **Methods**).

Unlike the oxygen sensory neurons which were active almost exclusively during the 21% [O_2] stimulus (**figs. 6A, S2A**) AVA demonstrated intrinsic spontaneous activity which could be observed during the initial 11% [O_2] baseline period of the stimulus assay as well as during the subsequent 11% [O_2] periods of the stimulus (**fig. 7A,B**). This observation goes along with the previously established in the research field concept of a stochastic basis for spontaneous switches to reversal locomotion as a part of normal *C. elegans* behavior (Gray et al., 2005; Pierce-Shimomura et al., 1999; Roberts et al., 2016). In this context it is important to note that for this analysis only the trials with AVA being in the non-active state at the moment of the 21% [O_2] stimulus were selected (see **Methods**),

Next, the raster plot revealed that AVA activity onsets were also scattered in time over the 21% [O_2] period over trials. However, a certain pattern of the AVA activity onsets grouping was observed between 4 and 10 seconds upon the 21% [O_2] stimulus onset (**fig. 7B**). Further quantifications by means of the AVA rise onsets cumulative probabilities also confirmed the AVA activity onsets up-modulation which could be detected by the steep probability rise starting ~4 seconds upon the 21% [O_2] stimulus onset (**fig. 7C**). Additionally, we calculated AVA rise onsets cumulative probability from the first 30 seconds of the 11% [O_2] periods of the periodic stimuli. This result demonstrated a gradual uniform increment in probabilities which indicated the absence of the 11% [O_2] stimulus effect on the AVA activity. When AVA rise onsets dynamic in 21% and 11% [O_2] period were compared to each other we could observe a clear effect of the 21% [O_2] stimulus in the first 10 seconds time window indicated by the steeper slope for the 21% [O_2] period; after this 10 seconds period slopes of the AVA activity onsets cumulative probabilities were getting similar for 21% and 11% periods indicating that from that moment the rate of the AVA activations were equalizing; thus the effect of the 21% [O_2] stimulus was not discernible for the rest of the stimulus period.

Interestingly, AVA activity rise raster plot together with the cumulative probability plot also revealed the AVA silent period during the first ~4 seconds upon the 21% [O_2] stimulus onsets. This finding indicates potential initial suppression of the reversal locomotion activity by the 21% [O_2] stimulus.

Next, we aimed to characterize the AVA response probability on the individual dataset basis. For that we focused on the AVA activity during the initial 10 seconds time window upon the 21% [O_2] stimulus onset; as this in this time window we previously revealed the 21% [O_2] stimulus up-modulation effect (**fig. 7B,C**). For each individual dataset we quantified probability of the occurrence of the trials with AVA activity rise detected within this time window which we defined as “Hit” trials (**fig. 7D**). We could find a range of “Hit” trials probabilities varying from 0 to ~0.9 for each individual dataset with

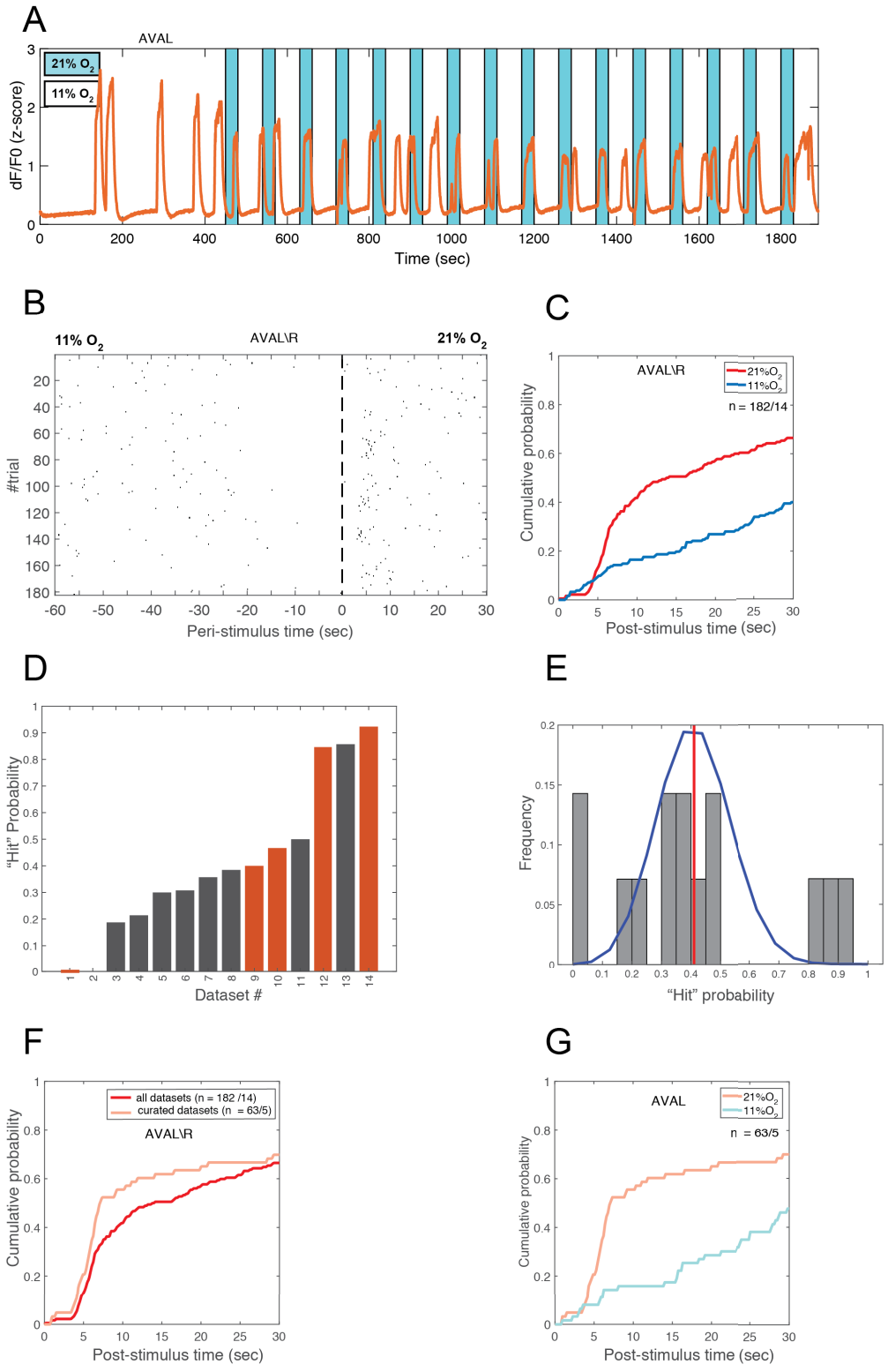

Figure 7. AVA neuronal activity is entrained by the oxygen stimulus in the periodic oxygen stimulation paradigm (**A**) An example fluorescence (dF/F0) trace of the AVAL oxygen sensory neuron activity during the periodic oxygen stimulation. Periods of 11% and 21% [O_2] are denoted with white and blue vertical bars. (**B**) Raster plots denoting the onsets of the long-lasting rises of the AVAL\R neuronal activity. Vertical dashed line at 0 seconds denotes transition from the 11% to 21% [O_2]. Only the trials where AVAL\R neuron was in a "low/fall" activity phase at the moment of the transition from the 11% to 21% [O_2] were considered for the analysis (also for C - G). (**C**) Each line is a cumulative probability of the AVAL\R neuronal activity rise onsets calculated from the 21% [O_2] and the first 30 seconds of the 11% [O_2] stimulus periods for all the recorded datasets (n = 14). Same data as in (B). (**D**) Bars show probabilities of the AVAL\R

activity onsets occurring within first 10 seconds after the 21% [O_2] stimulus onsets ("Hit" trials) across individual worm recordings. Bars highlighted with orange color indicate 5 datasets curated for the pan-neuronal analysis (note the dataset #1 with a "Hit" probability = 0). (**E**) Histogram of probabilities of reversal onsets occurring within first 10 seconds after the 21% [O_2] stimulus onsets ("Hit" trials) across individual worm recordings (the same data as in (D)). Vertical red line denotes the mean value (0.42). Blue line is a binomial probability density function with a probability of success for each trial set equal to the mean value (0.42) from the experimental results. (**F**) Comparison of cumulative probability of the AVAL\R neuronal activity rise onsets for all the recorded datasets (n =14) versus the AVAL in subsample curated for the whole brain analysis (n = 5). (**G**) Each line is a cumulative probability of the AVAL neuronal activity rise onsets calculated from the 21% [O_2] and the first 30 seconds of the 11% [O_2] stimulus periods for the subsample (n = 5) of the datasets curated for the whole brain analysis.

the mean "Hit" trials probability value equal ~0.4 (**fig. 7D,E**). Then, similarly to the behavioral results, we asked if the inter-individual variability in the "Hit" trials probability could be explained by the worms' idiosyncratic characteristics. For that, we calculated the binomial distribution for the trial success rate set equal to mean experimental value above. By comparing the experimental "Hit" trials probability results with the theoretical binomial model we found that the individual worms with "Hit" trials probability in the range from ~0.2 to ~0.5 could be described by the binomial model and thus the variability in this range is not due to the idiosyncratic characteristics. However, the individuals on the left and right sides of the "Hit" trials probability range (with probabilities values equal 0 and 0.8 to 0.9) could not be described by the binomial model; thus, those individuals demonstrated the idiosyncratic response characteristics. Interestingly, these results are at odds with the results from the behavioral experiments where all the individual worms could be described by the theoretical binomial model (**fig. 2D**). This finding indicates certain discrepancy between the worm's reaction to the oxygen stimulus in the freely moving conditions of behavioral experiments versus restrained and paralyzed conditions of the whole-brain imaging experiments.

Importantly the subset of 5 datasets which were used for the further pan-neuronal analysis (**see Methods**) included one dataset with 0 "Hit" probability, two datasets from the mid-range of ~ 0.4 – 0.5 "Hit" probability and two datasets from the high-range or ~0.8 – 0.9 "Hit" probability (**fig. 7D**). Additionally, we compared the AVA rise onsets cumulative probabilities within the 21% [O_2] period for the general set and the pan-neuronal analysis subset and found that they had similar profiles (**fig. 7F**) with the pan-neuronal analysis subset showing slightly stronger response (~20%) by the 10 seconds upon the 21% [O_2] stimulus onset. Thus, we concluded that the datasets subset selected for the pan-neuronal analysis could be used as a representative for the general population.

Finally, we compared probability of the AVA rise onsets in the 21% [O_2] period and the first 30 seconds of the 11% [O_2] periods of the periodic stimuli for the pan-neuronal analysis datasets subset (**fig. 7G**). Similarly, as for the general set of datasets, we found the gradual increment of probabilities for the 11% [O_2] period compared to the steep increment during the first ~10 seconds of the 21% [O_2] period. This finding further evidence for the entrainment of the AVA response by the 21% [O_2] stimulus in the pan-neuronal analysis datasets subset.

3.6 Analysis of control dataset confirms 21% [O_2] entrainment in the periodic oxygen shift experiments

To further confirm the entrainment of the AVA response by the oxygen stimulus we recorded two pools of control datasets: one with stable 11% and the other with stable 21% [O_2] (n = 10 for each pool) presented for the same time duration as a stimulus protocol in the periodic stimulus experimental recordings (see **Methods**). Exploring these datasets we found that under the conditions of a stable ambient [O_2] at both 11% (**fig. 8A,D**) and 21% levels AVA was exhibiting spontaneous activity similarly to what we observed at the baseline periods of the periodic stimulus recordings (**fig. 7A**). This observation confirms that under the experimental conditions of the whole-brain recordings *C. elegans* produces spontaneous forward and reversal motor command dynamics similar to the one normally observed in freely behaving worms (Gray et al., 2005; Pierce-Shimomura et al., 1999).

Next, we sought to compare the characteristics of the AVA activity cycles in the periodic stimulus and both of the control recording groups. To do that we used AVA traces annotated according to the "rise, "high", "fall" and "low" states. To disentangle the active and inactive AVA states we analyzed separately durations of the combined "rise-high-fall" states (**fig. 8B**) and "low" states (**fig. 8C**) correspondingly (see **Methods**).

We found that "rise-high-fall" states (**fig. 8B**) were significantly longer in the 11% [O_2] control datasets compared to both 21% [O_2] controls and periodic stimulus datasets with a median value for the 11% [O_2] control equals ~29 seconds compared to ~24 seconds for the 21% [O_2] controls and periodic 11-21% [O_2] stimulus datasets. On the other hand, the median value for the 21% [O_2] control was in the same range with the periodic stimulus datasets and did not reveal significant difference. Thus, we concluded that under constant 21% [O_2] and periodic 11-21% [O_2] stimulus the duration of the AVA active states was decreased comparing to the 11% [O_2] control protocol.

For the "low" phase durations (**fig. 8C**) we found that they were significantly longer for the 11% and 21% [O_2] controls comparing to the periodic stimulus datasets (median values of ~60, 50 and 40 seconds correspondingly). 11% and 21% [O_2] controls did not show significant difference between each other. Thus, we concluded that periodic oxygen stimulation reduced the duration of inactive AVA states, leading to more frequent AVA activation compared to any stable [O2] conditions.

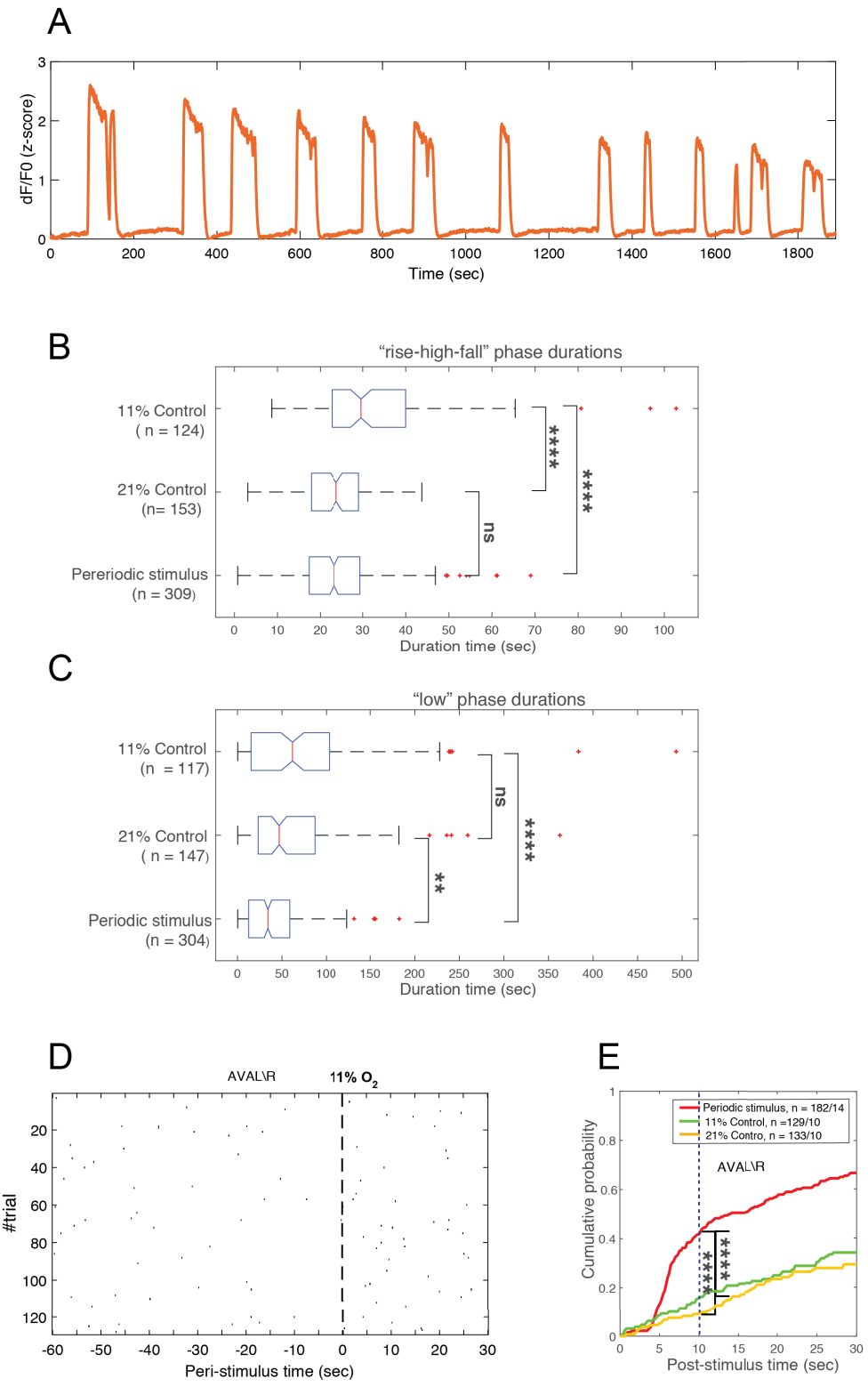

Figure 8. Control recordings with stable [O_2] stimulus verify the entrainment of the AVAL\R neuronal activity in the periodic stimulus datasets

(**A**) An example fluorescence (dF/F0) trace of the AVAL\R oxygen sensory neuron activity during the constant 11% [O_2] stimulus. (**B**) Box plot showing AVAL\R activity "rise-high-fall" phase durations in different stimulation conditions: periodic [O_2] stimulus recordings (n = 14), constant 11% (n = 10) and constant 21% (n =10) [O_2] control recordings. Red lines represent median values. N for each condition identifies the number of the AVA activity cycles used for the analysis. ****, $p < 0.0001$. (**C**) Box plot showing AVAL\R activity "low" phase durations in different stimulation conditions: periodic [O_2] stimulus recordings (n =14), constant 11% (n = 10) and constant 21% (n = 10) [O_2] control recordings. Red lines represent median values. N for each condition identifies the number of the AVAL\R activity cycles used for the

analysis. **, p < 0.01, ****, p < 0.0001. (**D**) Raster plot shows the onsets of the rises of the AVAL\R neuronal activity in the constant 11% [O_2] recordings. Vertical dashed line at 0 seconds denotes transition from the 11% to 21% [O_2] in the periodic [O_2] stimulus protocol. (**E**) Cumulative probabilities of the AVAL\R neuronal activity rise onsets calculated for the 21% [O_2] stimulus periods for the recordings with periodic [O_2] stimulus (n =14) and for the time periods corresponding to the 21%[O_2] periods for the constant 11% (n =10) and constant 21% (n =10) [O_2] control recordings. Vertical dotted line denotes the time point (10 seconds after the 21% [O_2] stimulus onset) used for the statistical comparison. Only the trials where AVAL\R neuron was in a "low/fall" activity phase at the moment of 21% [O_2] stimulus onset for the periodic stimulus datasets and at the time moments corresponding time for the 11% and 21% [O_2] control datasets were considered for the analysis. ****, p < 0.0001.

Overall, we observed that all three introduced oxygen stimulus paradigms were affecting the AVA activity dynamics in a different way. However, the range of the changes was not drastic and allowed to employ the AVA activity traces from the recordings with a stable 11% and 21% [O_2] as a control for the stimulus entrainment in the periodic oxygen stimulus assays. To do this we developed a procedure in which we used theoretical stimulus upshifts time points from the periodic stimulation protocol to align AVA activity traces from the 11% and 21% [O_2] control recordings and calculate corresponding AVA rise onsets cumulative probability control values (see **Methods**, **fig. 8D,E**).

We found that the increased rate of the AVA activity onsets within the 10 seconds time window upon the 21% [O_2] stimulus onset was characteristic only for the recordings with a periodic oxygen stimulus protocol and was not detected in neither of the controls (**fig. 8E**). Thus, we could exclude the potential artefact in the stimulus entrainment which could occur due to the pure alignment of the periodic stimulus with an intrinsic AVA activity. This observation confirms the up-modulation effect of the 11- 21% [O_2] shift on the AVA activity onsets rate.

Next, we observed that the slopes of AVA rise onsets cumulative probabilities for the periodic stimulus and both controls were equalizing after the ~10 seconds upon the stimulus onset (**fig. 8E**). This observation was going in a line with a previous comparison with the internal control of the 11% [O_2] periods (**fig. 7C**). This observation points to the fact that within this time window the oxygen stimulus effect was distinguishable from the baseline controls. Moreover, the permutation statistical test (see **Methods**) revealed significantly higher probability of the AVA rise onsets when measured at the 10 seconds time point.

In conclusion, we found an up-modulatory effect of the 11- 21% periodic [O_2] stimulus on the rate of AVA rises indicating the presence of the fictive reversal locomotion response in the whole-brain imaging assay similarly to our previous findings from the behavioral experiments. Moreover, the intrinsic control from 11% [O_2] periods and from the control datasets with a stable 11 and 21% [O_2] confirmed the statistically significant periodic oxygen stimulus entrainment within the 10 seconds time window upon the 21% [O_2] stimulus onset.

3.7 Reliable sensory encoding and variable motor response reveal the probabilistic nature of the sensorimotor transformation

After confirming the motor response entrainment by the periodic 11-21% [O_2] stimulus, we aimed to estimate the efficiency of the sensorimotor transformation occurring in the experimental conditions of the whole-brain imaging. For that we compared the reliability of the motor response to the reliability of the sensory encoding of the periodic oxygen stimulus over the trials. To do that that we referred to the cumulative probabilities of the AVA and URX neurons correspondingly (**fig. 9A**). We selected the URX neuron as a representative among other oxygen sensory neurons because it exhibited one of the most reliable responses to the periodic 21% [O_2] stimulus, reaching nearly a probability level of 1 within 5 seconds of the oxygen stimulus onset (**figs. 6B, 9A**).

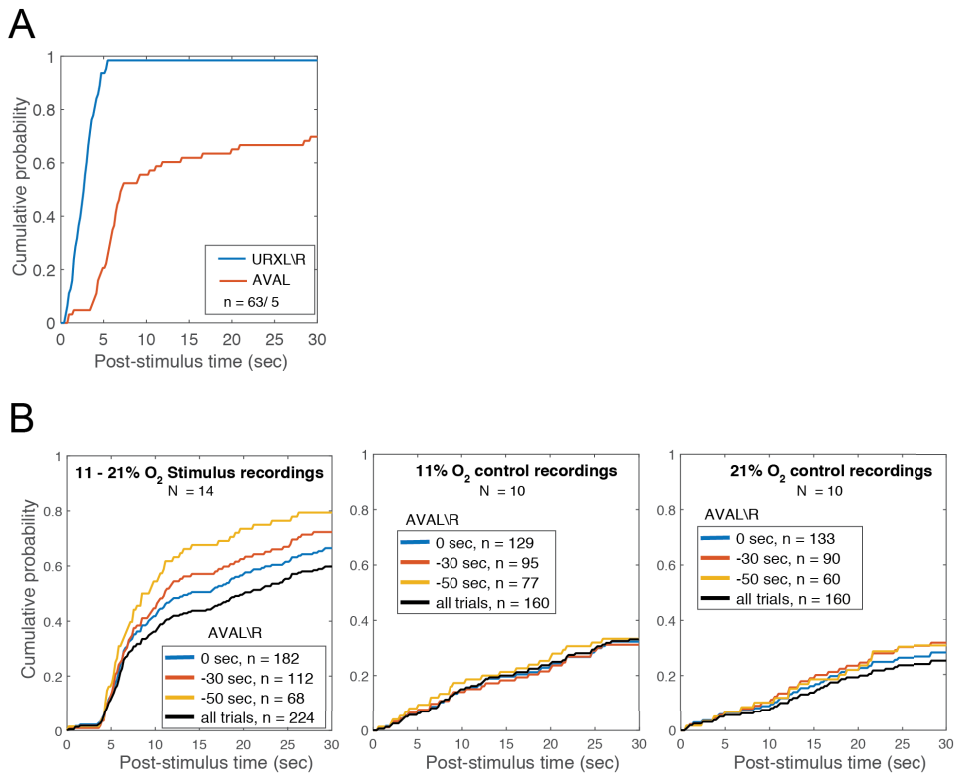

Figure 9. AVA intrinsic state and its past history affects responsiveness of the system
(**A**) Comparison of cumulative probability of the AVAL versus URXL\R neuronal activity rise onsets for the datasets curated for the whole brain analysis (n = 5). Only the trials where the AVA neuron was in a "low/fall" activity phase at the moment of the transition from the 11% to 21% [O_2] were considered for the analysis. (**B**) Cumulative probabilities of the AVAL\R activity onsets for different past history conditions in three different oxygen stimulation conditions: the periodic stimulus essays (n = 14), constant 11% (n =10) and constant 21% (n =10) [O_2] control recordings. Color codes denote four different subsamples of trials used for the cumulative probability quantification. Each condition is defined by the AVA neuronal activity being in a 'low/fall' state for a specified duration before the onset of the 21% [O_2] stimulus (0, 30, or 50 seconds). The '0 sec' condition indicates that the AVA neuron was in a 'low/fall' state precisely at the onset of the 21% [O_2] stimulus. Line with black color code represents all trials.

First, we observed that the onset of AVA responses was delayed by ~4 seconds compared to URX onsets, which began immediately upon the 21% [O_2] stimulus onset (**fig. 9A**). This delay may indicate the time required for sensorimotor transformation. Interestingly, despite this delay, URX and other

oxygen sensory neurons showed comparable slopes in the cumulative probabilities of their response onsets relative to AVA neuron activity (**figs. 9A, 6B**). This similarity suggests that both oxygen sensory neurons and the AVA premotor neuron process oxygen stimuli with similar temporal dynamics and efficiency, implying their involvement in a shared information pathway and coordinated activity.

Importantly, when we considered the 10 seconds time window which was previously established as the period where the AVA response is entrained by the oxygen stimulus, we found that the AVA response probability reached only the level of ~0.6 in contrast to almost 1 probability response of the URX oxygen sensory neuron. This indicates that despite the almost deterministic sensory encoding the motor response had substantial trial-to-trial variability which evidences for the probabilistic nature of the sensorimotor transformation

3.8 Intrinsic AVA state and its history partially explain the probabilistic nature of sensorimotor transformation in response to the oxygen stimulus

After establishing the problem of the probabilistic nature of the sensorimotor transformation we aimed to further investigate the potential neuronal mechanisms underlying it. On the first place, we aimed to investigate the role of the AVA neuron intrinsic state in the response generation. Based on the previous knowledge we hypothesized that the current AVA activity state as well as its past history could influence its responsiveness (Gordus et al., 2015; Kaplan et al., 2018). To test this hypothesis, we sorted all trials based on the past history of the AVA neuron into three clusters: “0 sec”, “30 sec”, “50 sec” - corresponding to the timing for which AVA neuron was in an inactive state prior to the 21% [O_2] stimulus onset and calculated cumulative probability of the AVA neurons activity rise onsets within each of the cluster. Also, similar procedure was applied to the stable 11% and 21% [O_2] control datasets (see **Methods**; **fig. 9B**).

First, we found that in all preselected clusters we could observe the up-modulation of the AVA activity onsets rate in response to the 21% [O_2] stimulus onset. However, already the “0 sec” trial’s cluster with AVA being inactive at the exact moment of the 21% [O_2] stimulus showed the increased response probability compared to “all trials”, indicating the role of the current AVA intrinsic state in the responsiveness. Further this analysis revealed that period of inactivity preceding the onset of the 21% [O_2] stimulus had a positive correlation with AVA response probability such that the longer inactivity history leaded to the higher response probability. Ultimately, the “50 sec” cluster demonstrating ~0.2 increase in the response probability relating to the “all trials” (**fig. 9B** left panel).

Interestingly, when similar analysis was performed on the stable 11% and 21% [O_2] stimulus control datasets, results did not demonstrate such a clear distinguishable trend (**fig. 9B** middle & right panels).

This finding might indicate the stochastic nature of the AVA spontaneous activity where the activation probability does not depend on the duration of the preceding inactive period. At the same time, this highlights the effect of inactive period duration on the response to the 21% [O_2] stimulus.

Overall, we found that the AVA intrinsic state at the moment of the stimulus presentation and its preceding activity history is affecting the responsiveness of the system. The duration of the AVA inactive state preceding the stimulus was correlating with the responsiveness to the 11-21% [O_2] stimulus; even so the spontaneous AVA activity under the conditions of the stable oxygen stimulus demonstrated stochastic character with no dependency on its activity history. However, the intrinsic AVA state and its past history did not explain all of the response variability.

3.8 "Hit-Miss; Evoked-Spontaneous"-triggered average analysis approach for exploring neuronal mechanisms behind the probabilistic nature of sensorimotor transformation

Next, we aimed to further explore the neural basis underlying the motor response variability. A single-neuron resolution whole-brain Ca^{2+} imaging datasets provided us with a unique opportunity to explore potential contribution of the individual neurons to the responsiveness of the system.

To characterize contribution of the individual neurons we developed an analysis pipeline based on the stimulus-triggered average analysis. In this analysis we wanted to analyze the neuronal data from the perspective of the stimulus on one hand and from the perspective of the response on the other hand. For this we used triggering to the 21% [O_2] stimulus time onsets and to the AVA activity onsets representing the locomotion response correspondingly.

Next, we segregated stimulus-triggered trials into "Hit" and "Miss" pools in the same way as it was described in the section above. In short, we focused on the AVA activity during the initial 10 seconds time window upon the 21% [O_2] stimulus onset; as this in this time window we previously revealed the 21% [O_2] stimulus up-modulation effect (**fig. 7B,C**). Trials where AVA activation was detected in this time window were classified as "Hit", whereas the rest of the trials including those with AVA activation occurred later than 10 seconds or did not occur at all were classified as "Miss" trials (**fig. 10A**).

On the other hand, we segregated AVA activity onsets-triggered trials into the "Evoked" and "Spontaneous" clusters. "Evoked" cluster was defined by the presence of the AVA rise onset within first 10 seconds period starting from the 21% [O_2] stimulus onset. Thus, the "Evoked" cluster corresponded to the "Hit" trials cluster from the stimulus-triggered average classification. On the other hand, the "Spontaneous" cluster was defined on a residual basis; thus, it included AVA rises occurred

within the 21% [O_2] periods but later than 10 seconds from the stimulus onset and AVA rises which occurred within the 11% [O_2] periods (**fig. 10A**).

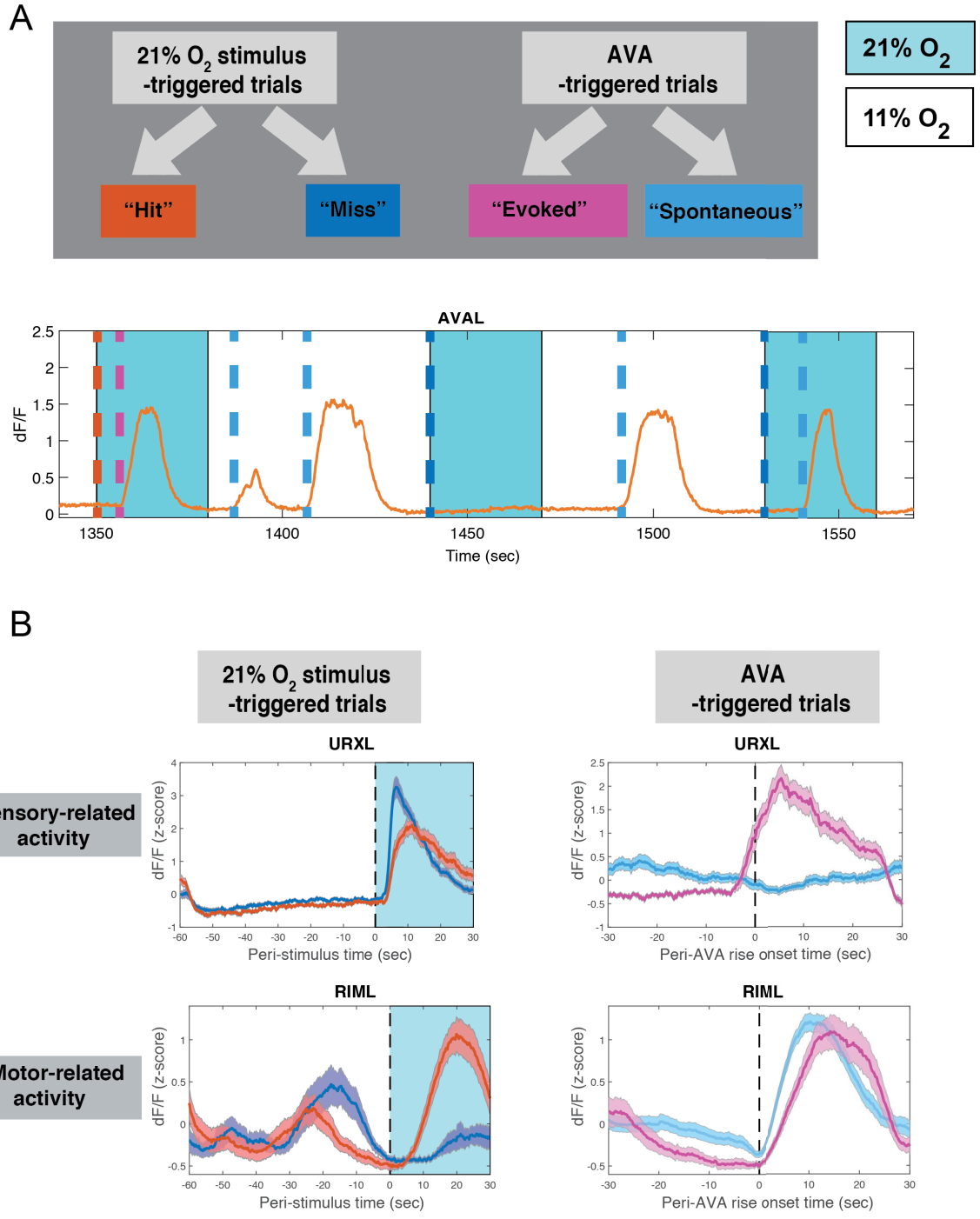

Figure 10. Schematics of the "Hit-Miss; Evoked-Spontaneous"-triggered average analysis.
(**A**) Top: Diagram demonstrating the logic of the "Hit-Miss; Evoked-Spontaneous"-triggered average analysis. Trials triggered to the 21% [O_2] stimulus times were divided into "Hit" and "Miss" clusters. Trials triggered to the AVA activity rise onsets were divided into "Evoked" and "Spontaneous" clusters. Note that the "Evoked" AVA-triggered trials correspond to the "Hit" stimulus-triggered trials. Bottom: An example AVAL trace fragment illustrating instances of the "Hit-Miss" stimulus triggering time points and "Evoked-Spontaneous" AVA-activity triggering time points (vertical dashed lines) corresponding to the description above. Color code for the boxes at the diagram on top corresponds to the color code of the dashed lines denoting triggering time points on the bottom figure. (**B**) Example illustrating how "Hit-Miss; Evoked-

Spontaneous" triggered average analysis can distinguish between sensory-related neuronal activity and motor-output-related neuronal activity. Top row: sensory-related activity of the URXL oxygen sensory neuron. Bottom row: motor-output-related activity of the RIML interneuron. Left column: stimulus "Hit-Miss"-triggered averages. Right column: AVAL rise onset "Evoked-Spontaneous"-triggered averages. Shaded area represents ± SEM.Vertical dashed line denotes transition from the 11% to 21% [O_2] in the stimulus-triggered averages (left column) and transition from the pre-AVA rise onset to the post-AVA rise onset time epochs in the AVA-triggered averages. Color code is the same for (A) and (B).

Finally, we applied triggered average analysis for each of the four trial's clusters and compared resulted averaged neuronal activity patterns for the stimulus-triggered "Hit" versus "Miss" clusters; and for the AVA-triggered "Evoked" versus "Spontaneous" clusters separately (**fig. 10B**). This analysis was applied systematically to all identified neurons and neurons which demonstrated significant difference in the activity amplitude in either pre- or post-triggering time point windows were automatically detected (**fig. S3,4, Tables S1,2**, see **Methods**).

Additionally, this two-sided approach to the data allowed us to disentangle neurons with sensory-related and motor-related activity profiles. We previously established that sensory response was highly reliable across trials (**fig. 6B**) and therefore occurring at both "Hit" and "Miss" trials. Consequently, neurons with sensory-related activity were expected reveal activation on both "Hit" and "Miss" stimulus-triggered averages and additionally at the "Evoked" AVA-triggered averages corresponding to the "Hit" stim trig (**fig. 10B**). On the opposite, we expected that neurons with the motor-related activity would exhibit activation pattern at the "Hit" but not "Miss" stimulus-triggered averages and at both "Evoked" and "Spontaneous" clusters of the AVA-triggered averages, as those neurons activity is linked to the response independently of the fact if it was occurring in response to the stimulus or "spontaneously" (**fig. 10B**).

Overall, multiple neurons revealed significantly distinct activity patterns at the "Hit" versus "Miss" trials of the stimulus-triggered averages (**fig. S3, Table S1**). This indicates that the successful sensorimotor transformation of the oxygen stimulus in our experimental paradigm was accompanied by the characteristic neuronal activity detectable with the Ca^{2+} imaging technique. Further, we review these findings in detail with a focus on the sensory neurons, the primary interneurons, and premotor interneurons.

3.9 Role of the oxygen sensory neurons in sensorimotor transformation

3.9.1 Oxygen sensory neurons detecting the increase in the environmental oxygen concentration reveale distinct activity for the "Hit" and "Miss" trials

First, we aimed to focus on the oxygen sensory neurons as they represent the first information processing relay from the oxygen stimulus. As we expected, all of the oxygen sensory neurons: URX, AQR, PQR, IL2 and BAG demonstrated activity up-modulation at both "Hit" and "Miss" trials of the stimulus-triggered average; whereas at the AVA-triggered averages a distinct activity up-modulation

was revealed only at the "Evoked" trials which correspond to the "Hit" trials (**figs. 11, 12, S3, S4**). This means that on average the activation of the oxygen sensory neurons was linked to the oxygen stimulus and not to the motor response.

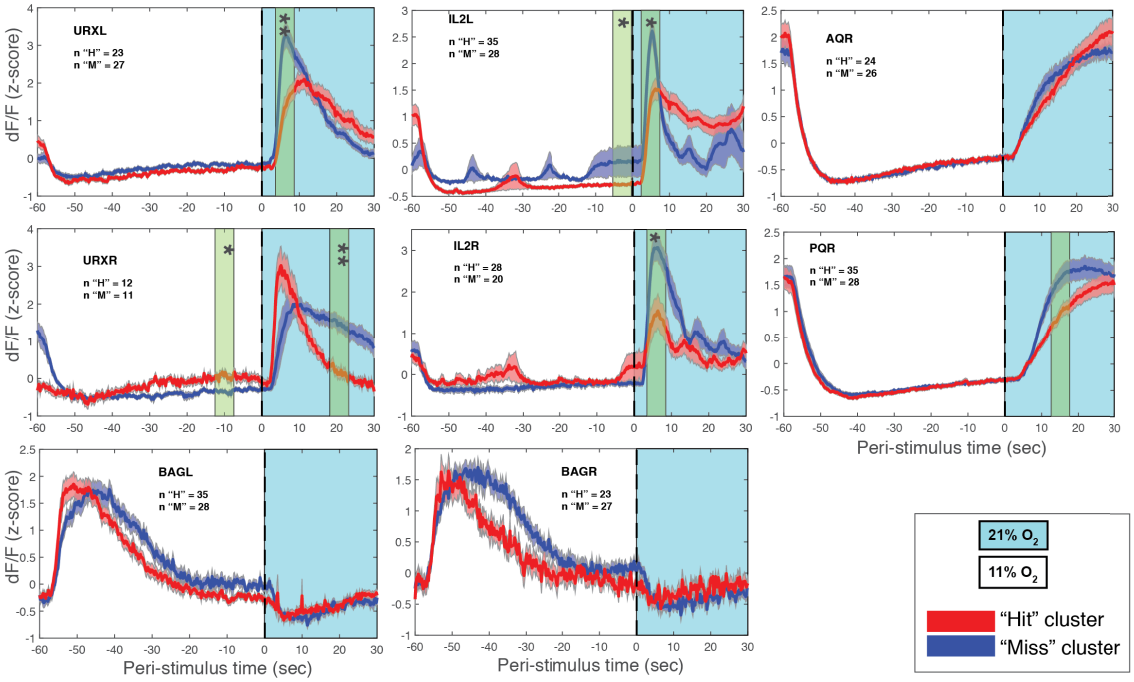

Figure 11. "Hit-Miss" stimulus-triggered averages of neuronal activity of the oxygen sensory neurons
Each box corresponds to a different oxygen sensory neuron. Within each box trials averages of neuronal activity for "Hit" and "Miss" clusters are depicted with different color-code. Shaded areas represent ± SEM. Vertical dashed line at 0 seconds represents transition between 11% and 21% [O_2] periods. N "H" and n "M" in each box indicates number of trials used for averaging for the "Hit" and "Miss" clusters respectively. Green bars represent the 15 seconds time windows where statistical tests were performed. *, $p < 0.05$; **, $p < 0.01$.

Previously we found that the oxygen sensory neurons had a highly reliable activation response over presented stimulus trials (**fig. 6B**). However, the amplitude of their response was varying over trials as could be seen with an example of the URX neuron (**fig. 5A**). Thus, we aimed to explore the relationship between oxygen sensory neurons response amplitude and the motor response. Surprisingly, we found that URXL, PQR and both IL2 neurons showed significantly higher response amplitude values at "Miss" trials compared to the "Hit" trials (**fig. 11**). For the URXL and a pair of Il2 neurons the maximum amplitude delta values were detected within ~5 seconds upon the 21% [O_2] stimulus onset, whereas for the PQR neuron it was detected with ~15 seconds latency. This observation is consistent with a previous finding that the PQR neuron had longer onset latency time comparing to the URX and IL2 neurons (**fig. 6C**) and a slower activation dynamic (**fig. 5B**). AQR neuron demonstrated trend similar to the PQR neuron with activity amplitude on the "Miss" trials tending exceed those on the "Hit" trials during the first ~20 seconds upon the 21% [O_2] stimulus onset. Interestingly, following the ~20 seconds timing the response on the "Hit" trials kept rising in the contrast to "Miss" trials response which reached the plateau phase till the end of the 21% [O_2] period. Thus, during the last 10 seconds of the 21% [O_2] period the

"Hit-Miss" activity amplitude ratio reversed and the "Hit" trials activity amplitude exceeded the "Miss" trials amplitude. However, for the AQR neuron described response amplitude discrepancies were subtle and did not reach statistically significant level.

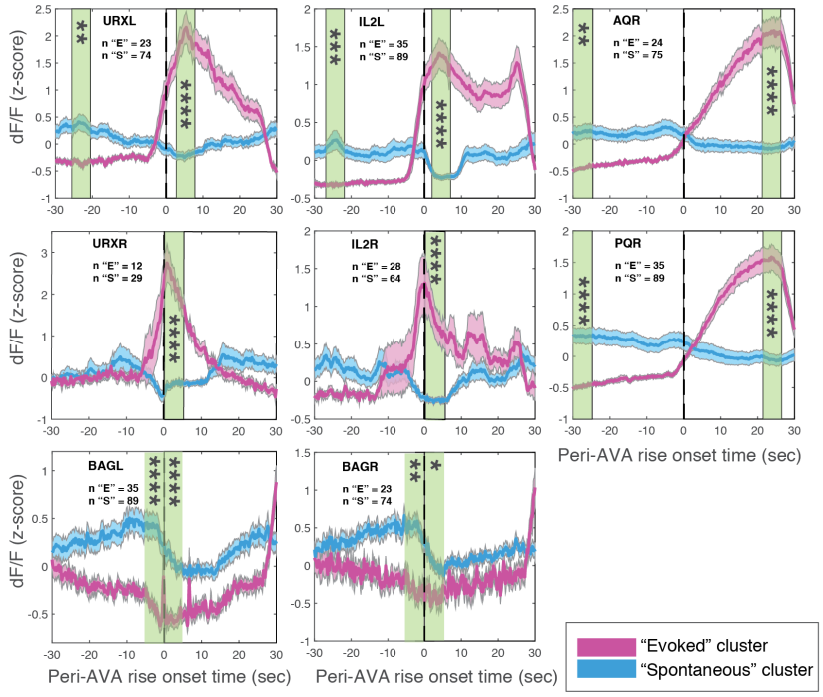

Figure 12. "Evoked-Spontaneous" AVA-triggered averages of neuronal activity of the oxygen sensory neurons. Each box corresponds to a different oxygen sensory neuron. Within each box trials averages of neuronal activity for "Evoked" and "Spontaneous" clusters are depicted with different color-code. Shaded areas represent ± SEM. Vertical dashed line at 0 seconds represents the transition between pre- and post- AVA rise onset time periods. N "E" and n "S" in each box indicates number of trials used for averaging for the "Evoked" and "Spontaneous" clusters respectively. Green bars represent the 15 seconds time windows where statistical tests were performed. *, $p < 0.05$; **, $p < 0.01$; ***, $p < 0.001$; ****, $p < 0.0001$.

Moreover, we found that for the URX neurons the timing of the peak amplitude values were shifted at "Hit" versus "Miss" trials (**fig. 11**). For the URXL neuron peak amplitude value was shifted for the longer value at "Hit" trials: ~11 seconds versus ~ 6.5 seconds at "Miss" trials. The opposite pattern was observed for URXR right neuron where the peak amplitude was detected earlier at "Hit" trials ~5 seconds versus ~10 seconds for the "Miss" trials.

"Evoked" trials of the AVA-triggered averages revealed that for all sensory neurons their activation onsets were preceding AVA activity (**fig. 12**). URX and IL2 neurons activation slopes were preceding AVA activity onset for the major fraction of time. In particular, the URXR and IL2R neuron's activation onsets were at ~8 and ~14 seconds prior to the AVA onset correspondingly and their activity peak coincided with the AVA activity rise onset time. Whereas URXL and IL2L had activity onsets ~5 seconds prior to the AVA onset and demonstrated activation peak ~5 seconds following the AVA activity onset. On the opposite, AQR and PQR neurons had activation onsets just ~2 seconds prior to

the AVA onset and the major fraction of their activity rise slope was following the AVA activity; the activity peak was detected at ~25 seconds following the AVA activity rise onset. Thus, potentially URX and IL2 neuron's activity (in particular their right counterparts) and less likely AQR and PQR activity might have a causative role for the AVA response.

Interestingly, URXR neuron showed the opposite trend with the "Hit" trail activity amplitude exceeding the "Miss" trials, however this difference was not reaching statistically significant level (**fig. 11**). Significant difference for the URXR neuron was detected later ~20 seconds upon the 21% [O_2] stimulus onset with a "Miss" trials showing higher amplitude values due to the more gradual decay dynamic.

Importantly, URXL, AQR, PQR and IL2R neurons demonstrated no difference at their baseline activity during the 11% [O_2] periods preceding the 21% [O_2] stimulus onset at "Hit" versus "Miss" trials (**fig. 11**). This indicates that their activity prior to the stimulus could not serve as a predictor for the further responsiveness of the system. On the contrast, two oxygen sensory neurons URXR and IL2L demonstrate a difference in the "Hit" versus "Miss" trials baseline activity level during the 11% [O_2] periods. URXR neuron showed slightly increased level of the baseline activity prior to the 21% [O_2] stimulus onset at the "Hit" trials. Opposite pattern regarding the 11% [O_2] activity baseline was found for the IL2L neuron with the baseline activity prior to the "Miss" trials being at the slightly higher level comparing to the "Hit" trials.

Interestingly, we observed that all oxygen sensory neurons showed suppression of neuronal activity during "Spontaneous" AVA-triggered trials (**fig. 12**). However, the precise timing of this suppression varied among the different sensory neurons. For the URX, AQR, and IL2R neurons, the onset of suppression slightly preceded the rise in AVA activity. This suggests that spontaneous down-modulation in the activity of these oxygen sensory neurons might facilitate the initiation of AVA activation. Notably, the URXR and IL2R neurons reached their minimum suppression points precisely at the onset of AVA activity, reinforcing this idea. Conversely, it could indicate the presence of an alternative neuronal source that initiates the decision of reverse locomotion and suppresses sensory neurons beforehand.

The IL2L and PQR neurons exhibited a different trend, with the onset of their suppression coinciding with the rise in AVA activity. This timing suggests that AVA activation may play a causal role in the suppression of IL2L and PQR neurons.

Furthermore, the suppression of the URXR and a pair of IL2 neurons was steep, followed by a down-plateau lasting ~5 seconds, after which activity quickly returned to baseline. In contrast, the suppression of the AQR and PQR neurons was less pronounced but lasted longer, ~30 seconds following the onset

of AVA activity. This observation suggests that the mechanisms and physiological roles of suppression may differ between the URX and IL2 neurons and the AQR and PQR neurons.

In conclusion, we found that the URXL, PQR, and IL2 oxygen sensory neurons exhibited significantly different average activation amplitudes during “Hit” versus “Miss” trials. Notably, the activation amplitude was higher during “Miss” trials compared to “Hit” trials. This finding suggests two potential physiological mechanisms: one possibility is that a weaker response from the oxygen sensory neurons might facilitate the initiation of reversal motor behavior via AVA neuron activation; alternatively, the lower activation amplitude during “Hit” trials might indicate a suppressive feedback mechanism that down-regulates oxygen sensory neurons following the initiation of reversal motor behavior. Additionally, we observed that all oxygen sensory neurons showed suppression of their baseline activity during “Spontaneous” trials prior to the onset of AVA activity. Thus, the activity of the oxygen sensory neurons is also linked to reversal motor events that occur independently of an oxygen stimulus.

3.9.2 Inhibition of BAG neurons by elevated environmental oxygen concentration precedes AVA activation

We investigated the activity of BAG neurons, which are known to detect decreases in environmental [O_2]. BAG neurons did not exhibit a statistically significant difference in activity during the 11% [O_2] periods preceding "Hit" versus "Miss" trials. However, we observed a trend indicating that "Hit" trials were characterized by a steeper activation and decay compared to the slower rise and decay dynamics observed in "Miss" trials (**fig. 11**). This activity pattern suggests that BAG neurons may have a stronger response to [O_2] downshifts prior to "Hit" trials.

As previously described, BAG neurons showed a suppression from baseline activity that began immediately upon the onset of the 21% [O_2] stimulus (**fig. 5B**). This suppression exhibited an abrupt pattern, after which BAG activity gradually recovered to baseline levels by the end of the 30-second 21% [O_2] period. Notably, using "Hit-Miss"-triggered average analysis, we found that this suppression occurred in both "Hit" and "Miss" trials (**fig. 11**). The suppression observed in "Hit" trials was also evident in the AVA-triggered "Evoked" trials (**fig. 12**), where it was clearly indicated that BAG suppression begins prior to AVA activity onset. These observations align with previous research (Zimmer et al., 2009), which demonstrated that BAG neurons exhibit subtle responses to [O_2] upshifts as part of their receptive properties.

Next, as previously noted, we also observed BAG suppression in the AVA-triggered "Spontaneous" trials alongside other oxygen sensory neurons (**fig. 12**), which begins shortly before the onset of AVA activity. This suggests a potential suppressive feedback mechanism that regulates BAG neurons, consistent with one of the theories described earlier.

Further, detailed observation of the data revealed additional insights. In "Evoked" trials, BAG suppression preceded AVA activity by ~5 seconds, whereas in "Spontaneous" trials, it preceded by ~2 seconds. During "Evoked" trials, BAG suppression reached its minimum level coinciding with the onset of AVA activity rise, followed by immediate recovery. This pattern was prominently displayed in BAGL neuron. Conversely, during "Spontaneous" trials, BAG activity continued to decrease after AVA activity began rising. After reaching its minimum, BAGL neuron activity remained suppressed for approximately 5 seconds before gradually recovering to baseline. In contrast, BAGR neuron activity started recovering slowly immediately after reaching its minimum value. These findings underscore the suggestion of distinct physiological mechanisms and roles for BAG suppression in response to oxygen stimuli compared to cases involving spontaneous AVA activation.

Overall, we found a trend indicating that "Hit" trials might exhibit steeper activation and decay dynamics compared to "Miss" trials in BAG neurons, suggesting a potentially stronger response to [O_2] downshifts. However, this trend was not statistically significant. Furthermore, we consistently observed suppression of BAG baseline activity in response to oxygen stimuli and spontaneous reversal events, revealing distinct temporal dynamics that suggest diverse underlying neuronal mechanisms for this suppression.

3.9.3 Activation timing and response variability of the oxygen sensory neurons do not account for the motor response variability

Additionally, we sought to explore if the latency time of the oxygen sensory neurons activity onsets correlated with the motor response variability. Initial observations of the stimulus-triggered “Hit-Miss” averages did not reveal any substantial discrepancies as all the sensory neurons seem to demonstrate activity onsets starting approximately at the same time at “Hit” and “Miss” trials (**fig. 11**). However, such an analysis could mask possible subtle shifts in the activation onsets timing due to the averaging. Thus, we developed an analysis procedure where we modified previously described analysis of the sensory neuron’s onsets latency times (**fig. 6**) to estimate it separately for the “Hit” and “Miss” trial’s pools (see **Methods**).

Neuronal activity onsets histograms for the oxygen sensory neurons revealed (**fig. 13A**) no statistically significant onsets latency differences for the “Hit” versus “Miss” trials estimated by the delta between median values. Moreover, IL2L, URX and AQR neuron’s demonstrated aligned activity onset’s latencies median values: ~2.4, ~2.8 and 2.8 seconds correspondingly; these values closely corresponded to the results revealed before where all trials were analyzed together: ~2.3, ~2.8 and ~2.8 seconds in the same order (**fig. 6C**). It should be mentioned, that the IL2R and PQR neurons revealed a trend with “Miss” trials showing slightly shorter activity onsets median value comparing to the “Hit” trials pool

(~2.0 and ~4.4 seconds correspondingly for the "Miss" trials versus ~2.9 and ~4.9 seconds for the "Hit" trials). However, the median delta values were not statistically significant.

Moreover, this analysis revealed that the outlier activity onsets with long latencies which were previously described for the AQR and PQR neurons (**fig. 6C**) were substituted by the events coming from both "Hit" and "Miss" trials (**fig. 13A**). Overall, we concluded that the oxygen sensory neurons activity onsets times on the "Hit" and "Miss" trials come from the same distribution.

Next, we aimed to extend the analysis of the sensory neuron's response probability over stimulus trials. Previously we have established that oxygen sensory neurons had a reliable response over stimulus trials (**fig. 6**). However, it should be highlighted that AQR and PQR neurons reached only ~0.8 response probability value by the 10 seconds upon the 21% [O_2] stimulus onset (**fig. 6B**), time where we measured significant AVA entrainment; hence, AQR and PQR neurons demonstrated a probabilistic character of the response over presented trials. Moreover, the activity onset's timing analysis revealed that the oxygen sensory neurons had variable latencies of the response over presented trials (**fig. 6C**).

Thus, we aimed to explore if the detected sensory response variability and their response latency variability were correlated with the motor response variability. To do this we modified previously described activity onset cumulative probability analysis and performed the same quantification separately for the "Hit" and "Miss" trials (see **Methods**).

Firstly, URX and IL2L showed no discrepancies for their activity onsets cumulative probabilities on the "Hit" versus "Miss" trials, in both cases reaching the value ~1 by the 10 seconds upon the 21% [O_2] stimulus onset (**fig. 13B**). This result was expected, since URX and IL2L neurons demonstrated ~1 response probability values when calculated for the "Hit" and "Miss" trials mixed together (**fig. 6B**). Importantly, we found that AQR and PQR neurons also had identical profiles of their activity onsets cumulative probabilities on the "Hit" versus "Miss" trials, in both cases reaching the value ~0.8 by the 10 seconds upon the 21% [O_2] stimulus onset (**fig. 13B**). This finding indicates that their response variability was not correlated with the motor response variability.

Importantly, the identical response probabilities of oxygen sensory neurons in "Hit" and "Miss" trials support the hypothesis that the amplitude difference observed in the stimulus-triggered averages (**fig. 11**) reflects genuine variations in response strength, rather than an artefact caused by absent activity in either trial group.

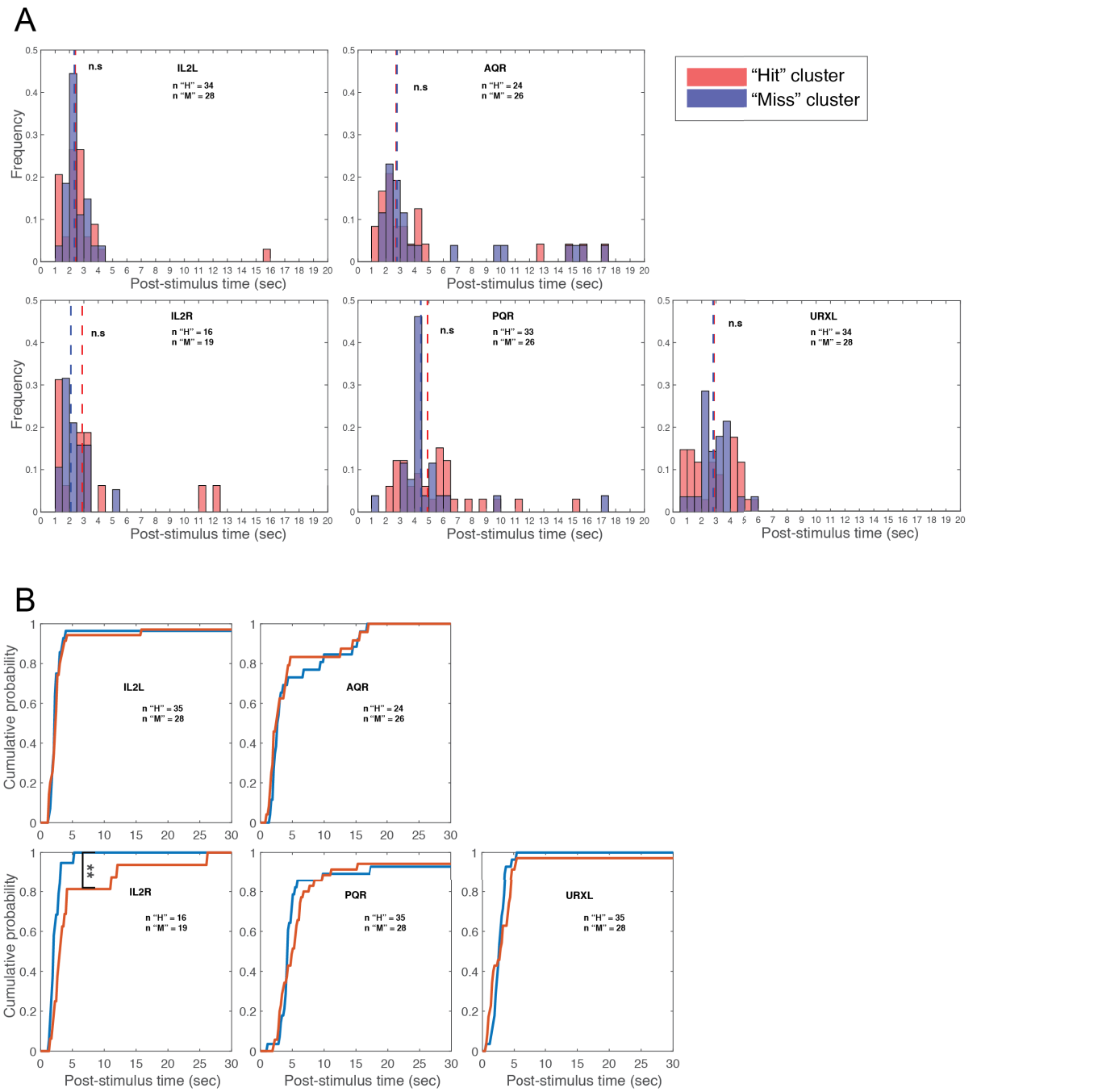

Figure 13. Oxygen sensory neurons demonstrate robust activity onsets patterns on the "Hit" versus "Miss" trials
(**A**) Each panel corresponds to a different oxygen sensory neuron. Within each panel histograms showing timing of the neuronal activity rise onsets for the "Hit" and "Miss" trials are overlaid. Vertical dashed lines denote the median values for the "Hit" and "Miss" clusters. N "H" and n "M" indicates the number of the onsets used for the analysis from "Hit" and "Miss" clusters respectively. Statistical test compares median values. n.s, $p > 0.05$. (**B**) Each panel corresponds to a different oxygen sensory neuron. Each line is a cumulative probability of the neuronal activity rise onsets calculated from the 21% [O_2] period for the "Hit" and "Miss" trials clusters separately. N "H" and n "M" indicates the number of trials used for the analysis from "Hit" and "Miss" clusters respectively. **, $p < 0.01$.

Additionally, identical slopes of the activity rise cumulative probability at the "Hit" and "Miss" trials for the URX, IL2L and AQR neurons further confirms that there was no difference between distributions of the activation onset latencies for the "Hit" and "Miss" trials as was detected before with the activity onset's time histograms (**fig. 13A**). PQR and IL2R neurons demonstrated a slightly steeper

cumulative probability curve at “Miss” trials which is complementary to the previously described finding that those neurons demonstrated a trend of having slightly shorter activity onsets median value at “Miss” trials comparing to “Hit” trials (**fig. 13A**).

Interestingly, we found differences in “Hit” versus “Miss” trials cumulative probability profiles for the IL2R neuron (**fig. 13B**). Specifically, the initial slope of the cumulative probability (from 0 to ~5 seconds) was slightly steeper during 'Miss' trials. Subsequently, the slope of the cumulative probability after ~5 seconds following the 21% [O_2] stimulus was significantly shallower during 'Hit' trials compared to 'Miss' trials. Consequently, the absolute response probability between 5 to 7 seconds was significantly lower in “Hit” trials tcompared “Miss” trials. However, the cumulative probability of activity onset during “Hit” trials eventually reached the value of 1 by the end of the 30-second period following the 21% [O_2] stimulus onset. This indicates a reduced rate of IL2R activity between 5 and 30 seconds after the 21% [O_2] stimulus onset, potentially reflecting a suppressive feedback mechanism from the reversal pre-motor neurons.

In summary, we found that neither the response latency nor the trial-to-trial response variability of oxygen sensory neurons correlated with motor response variability. The only oxygen sensory neuron that showed a significant difference in the cumulative probability of activity onset between 'Hit' and 'Miss' trials was the IL2R neuron. This neuron exhibited a transient suppression period during 'Hit' trials, potentially indicating a suppressive feedback mechanism from pre-motor interneurons.

3.10 Role of the primary interneurons in sensorimotor processing of the environmental oxygen stimulus

After inspecting the oxygen sensory neurons response with the “Hit-Miss; Evoked-Spontaneous”-triggered average analysis approach, we aimed to focus on the interneurons which could be potentially involved in the processing of the information from the oxygen sensory neurons.

Connectome organization suppose three pairs of the candidate interneurons which might serve this function: RMG, AUA and PVP neurons. In particular, RMG neurons are recurrently connected with URX sensory neurons via chemical synapses and gap junctions; and with IL2 neurons via gap junctions. Similarly, AUA neurons receive major chemical synapses inputs from the URX neurons. PVP neuron has gap junctions with AQR and PQR sensory neurons. On the other hand, AUA, RMG and PVP interneurons each send chemical synapses to one or more of the reverse premotor interneurons AVA, AVD and AVE. Overall, this connectome arrangement puts AUA, RMG and PVP interneurons in the position where they could potentially be involved in the information transfer between the layer of the oxygen sensory neurons and premotor interneurons (Macosko et al., 2009; White et al., 1986)

This assumption was further supported by the Ca^{2+} imaging studies which revealed that the AUA and RMG neurons demonstrate activation in response to the elevated environmental [O_2] correlated with the URX response. (Busch et al., 2012; Laurent et al., 2015; Nichols et al., 2017; Oda et al., 2017). Moreover, it was shown that the URX ablation (Laurent et al., 2015) or GCY-35 guanylate cyclase mutation which disrupts oxygen sensation in the oxygen sensory neurons (Busch et al., 2012), lead to the disruption of the response in the RMG and AUA neurons. These findings testify to the hypothesis that the Ca^{2+} response in the RMG and AUA neurons is driven by the oxygen sensory neurons input. Thus**,** it was experimentally proven that the oxygen sensory neurons transmit the information about the rise in the environmental [O_2] to the AUA and RMG interneurons.

On the other hand, ablation studies demonstrated that RMG and AUA contribute to the change of the behavioral state in response to the changes in the environmental [O_2]. Importantly, in the same study it was shown that ablating RMG interneurons also reduced the transient reversals and turns elicited during the rise in [O_2] (Busch et al., 2012). Additionally, optogenetic stimulation studies demonstrated that RMG activity is sufficient for inducing up-modulation of the forward locomotion (Laurent et al., 2015). Additionally, it was shown that the RMG neuron serves as a hub center in the distributed neuronal circuit which regulates oxygen related aggregation behavior (Macosko et al., 2009);

Overall, the connectome organization, Ca^{2+} functional imaging, optogenetic and ablation studies convergently point towards the importance of the RMG, AUA and PVP neuron's functional role in the processing of the information from the oxygen sensory neurons and forming the corresponding behavioral response.

3.10.1 Stimulus-triggered average analysis identifies primary interneurons in the whole-brain imaging recordings

We applied an explorative approach by the means of stimulus-triggered average analysis **(fig. S1)** in combination with identifying the characteristic topographic position of the neurons as we described previously for the oxygen sensory neurons. With this approach we could detect all the above-mentioned interneurons: RMG, AUA neurons in the head ganglion and PVP neuron in the tail ganglion (**fig. 14**). They demonstrated activity profiles similar to the up-shift sensing oxygen sensory neurons: URX, IL2, AQR and PQR (**fig. 5**) with activity up-modulation upon the 21% [O_2] stimulus.

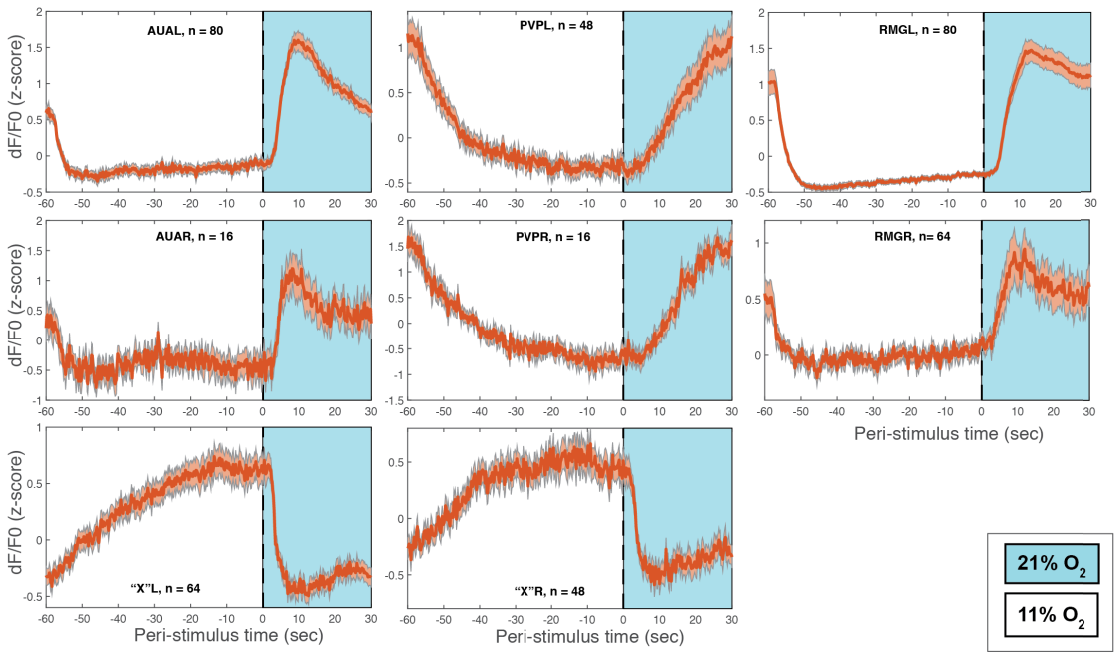

Figure 14. Stimulus-triggered averages of neuronal activity in primary interneurons
Each box corresponds to a different primary interneuron. Orange line within each box is a stimulus-triggered average of the neuronal activity. We could detect three pairs of the interneurons reacting to the increase in [O_2] similarly to the oxygen sensory neurons (AUA, PVP and RMG) and a pair of neurons ("X" neuron) ramping its activity during the 11% [O_2] period. Shaded area represents ± SEM. Vertical dashed line at 0 seconds represents the transition between 11% and 21% [O_2] periods. N in each box indicates number of trials used for averaging.

AUA and RMG neurons demonstrated relatively steep activation slope reminding those of the URX and IL2 neurons (**fig. 14**). The maximum level of activity was reached ~10 seconds upon the 21% [O_2] onset and then followed by the gradual decrease. AUAR neuron's activity was stabilized at the elevated plateau level starting from ~15 seconds upon the 21% [O_2] onset. RMG neurons were reaching the maximum level of activity ~12 seconds upon the 21% [O_2] onset which was followed by the very gentle activity decrease plateauing at the elevated level till the end of the 21% [O_2] period. Further, upon the onset of the 11% [O_2] activity of AUA and RMG neurons was steeply decreasing and reaching the baseline during the ~10 sec.

PVP neurons had a gradual linear activation slope similar to the one of the AQR and PQR sensory neurons (**fig. 14**) reaching maximum towards the end of the 21% [O_2] period. Further, PVP's activity was decreasing and reaching baseline during the first ~20 seconds of the following 11% [O_2] period. Thus, both activation and suppression slopes of the PVP neurons was slower comparing to the AUA and RMG neurons.

Next, by screening the results of the stimulus-triggered average analysis we identified new neuronal pair with activity linked to the oxygen stimulus (**figs. 14, S1**). We gave it a putative name "X" neuron. This neuron was characterized by the activity which started to rise immediately upon the 11% [O_2]

onset and was gradually ramping up reaching the maximum level towards the end of the 11% [O_2] period and then dropping down to the baseline within the first 5 seconds upon the 21% [O_2] onset. Thus, this neuron was activated during the 11% [O_2] stimulus period similar to BAG oxygen sensory neurons (**fig. 5**), however it had different activity dynamic pattern, as BAG neuron's activity was reaching maximum shortly upon the 11% [O_2] onsets and then falling towards the baseline within the ~40 sec.

Overall, in our recordings we could identify all the previously described major interneurons related to the oxygen stimulus processing in the head and tail ganglions, which were AUA, RMG and PVP neurons. All these neurons demonstrated activation aligned with the 21% [O_2] stimulus and relaxation of the activity during the 11% [O_2] periods. AUA and RMG neurons had steeper activation dynamics similar to the URX and IL2 oxygen sensory neurons, whereas PVP neurons had more gradual linear activation slope similar to the one of the AQR and PQR sensory neurons. These results align with the *C. elegans* connectome data from which we know that AUA and RMG neurons has recurrent connections with the URX neurons and PVP neurons are interconnect with AQR and PQR oxygen sensory neurons by the gap junctions. Furthermore, we identified an interneuron which was not previously described in the literature whose activity was gradually ramping during the 11% [O_2] periods reaching the maximum in the end of it and then relaxing to the baseline in the subsequent 21% [O_2] periods; this neuron is identified by the putative name "X" neuron in the current work.

3.10.2 The "Hit-Miss; Evoked-Spontaneous"-triggered average analysis shows that primary interneurons exhibit activity indicative of the reversal motor response decision-making process

Having established that the AUA, RMG, PVP, and "X" primary interneurons exhibit an activity profile in response to 21% [O_2] stimulus, we aimed to test the hypothesis that these interneurons might play a role in the decision-making mechanism underlying the previously observed trial-to-trial response variability. (**figs. 7 - 9**). To test this hypothesis, we scrutinized the results of the "Hit-Miss; Evoked-Spontaneous"-triggered average analysis (**figs. 15, 16, S3, S4, Table S1**) for these neurons.

First, we found that AUA, RMG, PVP and "X" primary interneurons demonstrated activity up-modulation at both "Hit" and "Miss" trials of the stimulus-triggered average, whereas at the AVA-triggered averages a distinct activity up-modulation was revealed only at the "Evoked" trials which correspond to the "Hit" trials from the stimulus-triggered average (**figs. 15, 16**). This is the activity pattern that was predicted to be observed for the neurons with a sensory-related activity (**fig. 10**) and which was previously found for the oxygen sensory neurons in our recordings (compare **fig. 11** and **fig. 12**). Thus, we concluded that the activity of the primary interneurons was on average linked to the oxygen stimulus and not to the motor response.

Further we aimed to reveal if those interneurons were demonstrating activity discrepancies correlating with “Hit” versus “Miss” trials. Interestingly, AUA and PVP neurons demonstrated identical activity at “Hit” and “Miss” trials. Thus, their activity did not reflect information related to the motor response decision (**fig. 15**). This result was particularly surprising because our previous findings revealed that URX and PQR oxygen sensory neurons, which are expected to relay information about environmental [O_2] to the AUA and PVP interneurons, exhibited significantly different average activity amplitudes during “Hit” versus “Miss” trials (**fig. 11**). Therefore, we identified a difference in the information carried by the oxygen sensory neurons and primary interneurons.

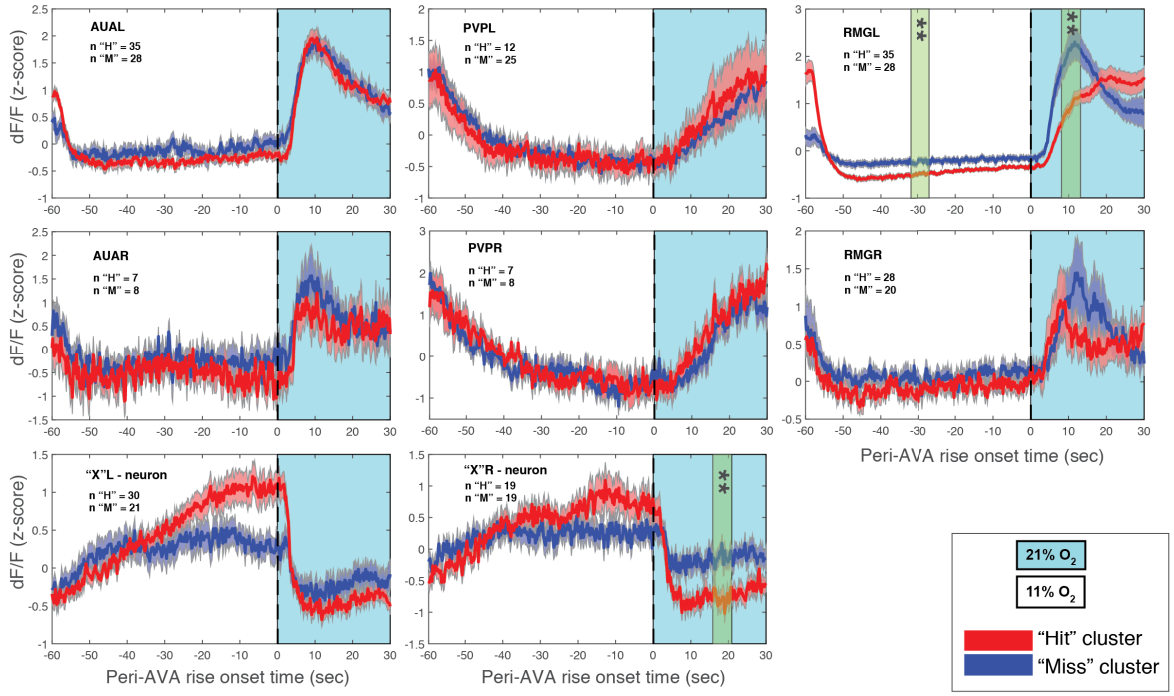

Figure 15. “Hit-Miss” stimulus-triggered averages of neuronal activity for different primary interneurons
Each box corresponds to a different primary interneuron. Within each box trials averages of neuronal activity for “Hit” and “Miss” clusters are depicted with different color-code. Shaded areas represent ± SEM. Vertical dashed line at 0 seconds represents the transition between 11% and 21% [O_2] periods. N “H” and n “M” in each box indicates number of trials used for averaging for the “Hit” and “Miss” clusters respectively. Green bars represent the 15 seconds time windows where statistical tests were performed. **, $p < 0.01$.

In contrast, the RMG neurons revealed a difference of their activity patterns at “Hit” versus “Miss” trials (**fig. 15**). In particular, the RMGL neuron demonstrated different activity profiles at “Hit” versus “Miss” trials: “Miss” trials demonstrated a steep activity rise reaching a peak ~10 seconds upon the 21% [O_2] stimulus onset followed by a steep activity decline. On the other hand, at “Hit” trials activity had a gradual rise slope and was reaching a high plateau after ~20 seconds upon the 21% [O_2] stimulus onset; further the activity was staying at this plateau level till the end of the 21% [O_2] period. Importantly, we found significantly higher amplitude values at “Miss” trials compared to the “Hit” trials ~10 seconds upon the 21% [O_2] stimulus onset. Furthermore, we observed that the baseline activity

during the 11% [O_2] periods preceding "Miss" trials was slightly higher compared to the activity preceding "Hit" trials, with a significant difference particularly evident around -30 seconds, suggesting it may be an integral part of the decision-making mechanism. RMGR neuron also revealed a trend with activity at “Miss” trials reaching higher amplitude value comparing to the “Hit” trials. However, the “Hit-Miss” amplitude delta value in this case was not statistically significant. Overall, RMG neurons exhibited activity patterns similar to those observed in the URXL oxygen sensory neuron, showing higher activity amplitudes during "Miss" trials compared to "Hit" trials.

A particularly interesting activity pattern trend was observed for the newly detected “X” neuron. Previously we mentioned that the stimulus-triggered average revealed gradual ramping up of the “X” neuron’s activity during the 11% [O_2] periods (**fig. 14**). “Hit-Miss; Evoked-Spontaneous”-triggered average analysis revealed that this activity ramp had a different pattern at the 11% [O_2] periods of the “Hit” versus “Miss” trials: at “Hit” trials the activity was steadily increasing till the end of the 11% [O_2] period, whereas at “Miss” trials it stopped rising after the initial ~20 seconds staying at the plateau level till the end of the 11% [O_2] period (**fig. 15**). Thus, starting from ~40 prior to the 21% [O_2] stimulus we observed an amplitude difference for the “Hit” versus “Miss” trials with the “X” neuron activity eventually reaching higher values at the “Hit” trials prior to the 21% [O_2] stimulus onset. This trend was more prominent for the left neuron in the “X” neurons pair. It is important to mention that despite the clear trend, the “Hit”–“Miss” trials maximum amplitude delta was not reaching statistically significant level. Upon the onset of the 21% [O_2] stimulus, the activity of the "X" neurons dropped to baseline. Interestingly, for the "XR" neuron, activity during "Hit" trials reached lower values compared to "Miss" trials, suggesting the effect of feedback modulation.

3.10.2 Primary interneurons demonstrate activation preceding the AVA activity onset

“Evoked” AVA-triggered averages revealed that the AUA and RMG neurons had their activity onsets prior to the AVA onsets, whereas PVP neurons onsets were aligned with the AVA onset’s time (**fig. 16**). AUA neuron’s activation onsets were ~5s prior to the AVA onset; similarly, to the URX neurons (**fig. 12**). AUAR neuron’s activity peak coincided with the AVA activity rise onset time, whereas AUAL activity peak was ~5 seconds following the AVA activity onset.

RMGL neuron’s activation onsets were ~5 seconds prior to the AVA activity onset and the activation reached the maximum plateau ~15 seconds upon the AVA activity onset, then then activity started to decline ~27 seconds upon the AVA activity onset. RMGR neuron activity rise started ~8 seconds prior to the AVA activity onset and then reached maximum shortly after the AVA rise onset time; after that activity dropped to an intermediate level plateau; then activity started to decline ~27 seconds upon the AVA activity onset similarly as for the RMGL neuron. Thus, both oxygen stimulus-triggered averages

(**fig. 15**) and AVA-triggered averages (**fig. 16**) revealed left-right functional asymmetry for RMG neurons.

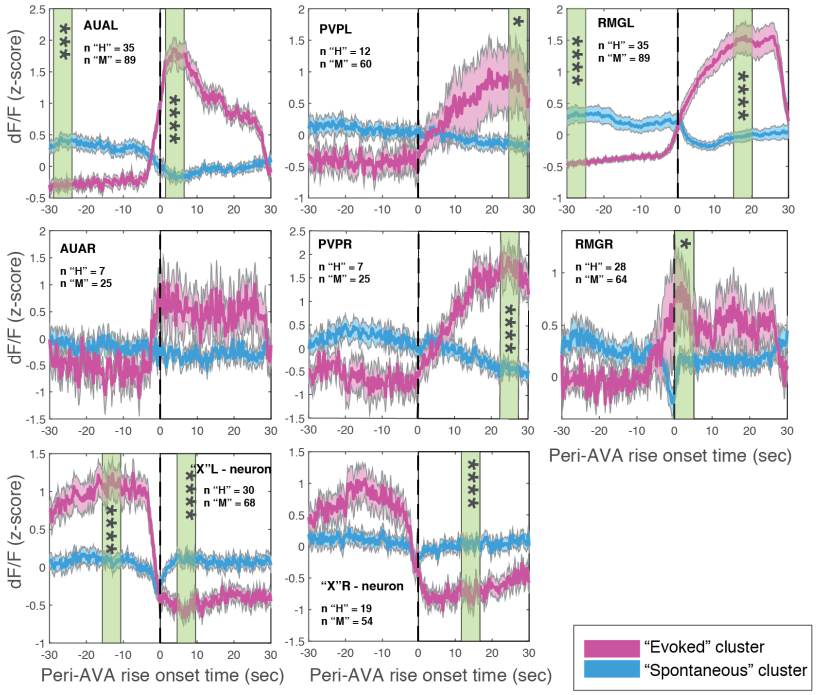

Figure 16. "Evoked-Spontaneous" AVA-triggered averages of neuronal activity for different primary interneurons Each box corresponds to a different primary interneuron. Within each box trials averages of neuronal activity for "Evoked" and "Spontaneous" clusters are depicted with different color-code. Shaded areas represent ± SEM. Vertical dashed line at 0 seconds represents the transition between pre- and post- AVA rise onset time periods. N "E" and n "S" in each box indicates number of trials used for averaging for the "Evoked" and "Spontaneous" clusters respectively. Green bars represent the 15 seconds time windows where statistical tests were performed. *, $p < 0.05$; ***, $p < 0.001$; ****, $p < 0.0001$.

Interestingly, "Evoked" trials of the AVA-triggered averages revealed that "X"L neuron activity started to decline ~4 seconds prior to the AVA activity onset and was reaching the baseline level at the time aligned with the AVA rise onset (**fig. 16**). "X"R neuron demonstrated different pattern with the activity reaching the baseline only ~3 seconds upon the AVA rise onset.

3.10.3 Primary interneurons show activity suppression at "Spontaneous" AVA-triggered trials

When investigating the activity of the AUA, RMG, PVP and "X" primary interneurons at the "Spontaneous" AVA-triggered trials (**figs. 16, S4**), we observed a suppression pattern resembling that previously described for the oxygen sensory neurons (**fig. 12**). This suppression pattern varied among the different interneurons.

In particular, for the AUAL neuron the activity suppression initiated ~5 seconds prior to the AVA activity onset and then the activity gradually declined until reaching the minimum at ~5 seconds upon the AVA activity onset; following that the AUAL activity stayed at the suppressed level till the end of

the 30 seconds observation window. On the contrary, the AUAR neuron did not demonstrate a detectable suppression at the AVA-triggered averages.

PVP neurons revealed a gradual and subtle activity suppression which started following the AVA activity onset and lasted till the end of the 30 seconds observation window.

The suppression patterns of RMG neurons differed between the left and right neurons in the pair. For the RMGL neuron, the onset of suppression coincided with the onset of AVA activity, and the activity remained suppressed for the entire 30-second observation window. In contrast, the RMGR neuron exhibited an abrupt suppression starting ~5 seconds before the AVA activity onset. The lowest point of suppression coincided with the onset of AVA activity, after which the RMGR neuron's activity rapidly returned to baseline within ~3 seconds. Additionally, both "X" neurons demonstrated a suppression pattern identical to that of the RMGR neuron

In conclusion, we found that AUA, RMG, PVP and "X" primary interneurons activity was linked to the oxygen stimulus and not to the motor response. Thus, their activity was similar to the one of the oxygen sensory neurons. Surprisingly, AUA and PVP activity demonstrated similar activity patterns at the "Hit" versus "Miss" trials. Hence, for these interneurons we did not reveal an involvement in the motor response decision making process. On the contrary, RMG interneurons demonstrated difference of their activity patterns at the "Hit" versus "Miss" trials with the stronger average activity amplitude at the "Miss" trials. This pattern is similar to the one previously found for the URX, PQR and IL2 oxygen sensory neurons (**fig. 11**). Moreover, the newly identified "X" neuron revealed a trend of its activity to reach higher amplitude values at the end of 11% [O_2] periods preceding "Hit" trials compared to "Miss" trials. However, this "Hit-Miss" trials amplitude delta was not statistically significant in the currently explored datasets. Further, the AVA-triggered averages revealed that the described interneuron's activity had variable relation to the to the AVA activity onset timing on the "Evoked" trials which suggests their diverse roles in the information sensorimotor information processing. Finally, we found that AUA, RMG, PVP and "X" primary interneurons demonstrated a suppression of their baseline activity around the time of the spontaneous AVA activation at the "Spontaneous" trials. This finding points towards the idea that activity of these interneurons is interrelated with reversal motor command generating also in the absence of the oxygen sensory stimulus.

3.10.4 RMG interneurons demonstrated trial-to-trial response variability interrelated with the reversal motor command

Our previous results showed that the RMG interneuron demonstrated significant discrepancies of the activity patterns at "Hit" versus "Miss" trials at the stimulus-triggered averages. Considering this experimental finding and previously described role of the RMG interneuron in sensory processing and behavioral responses related to the oxygen sensory system (Busch et al., 2012; Laurent et al., 2015; Macosko et al., 2009; Oda et al., 2017), we aimed to further elaborate the analysis of the RMG interneuron's activity. In particular, we sought to focus on the variability of the RMG interneuron's response over trials and its activity onsets latencies with regards to the motor response.

Firstly, the observation of the activity onsets raster plots (**fig. 17A**) showed that RMGL neuron exhibited activation on most of the trials starting shortly after the 21% [O_2] stimulus onset and the rise onset events were grouped in the 5 seconds time window following the stimulus onset. Additionally, we observed that RMGL neuron had long-latency and secondary activity onsets on a fraction of trials. In contrast, RMGR neuron demonstrated notably sparse responses and the activity onsets were scattered in time. It should be noted that RMGR neuron was not possible to identify in one of the datasets hence, the raster plot reveals missing values. Additionally, in one of the datasets RMRG neuron was completely silent and did not exhibit any activity over the whole-time span of the recording.

Next, we aimed to quantify the responsiveness of the RMG neurons over trials; for that we used the activity onsets cumulative probability analysis, similarly as was described before for the oxygen sensory neurons and the AVA neuron (**fig. 17B**, see **Methods**). We found that during the first ~4 seconds upon the 21% [O_2] stimulus onset the RMGL neuron had the same steepness of the cumulative probability curve as the URX oxygen sensory neuron. This indicates that for this period RMGL and URX neurons had the same response probability and the same variability of the response onsets latencies over trials. Further, starting from ~4 second and till the end of the 30 seconds 21% [O_2] period RMGL cumulative probability demonstrated slow gradual rise and by the 10 seconds reached the value of ~0.8 in contrast to ~1 probability of the URX neuron. This means that for this period RMGL neuron response probability was lower compared to the URX response, and it had higher variability of the onset's latencies over trials. We also found that RMGL response probability was exceeding AVAL response probability by ~30 precents at the 10 seconds time point, thus revealing substantially more reliable response over the stimulus trials. On the contrary, RMGR neuron demonstrated notably low response probability reaching only the value of ~0.2 by the 10 seconds time window, which reflects the sparseness of its activity previously revealed by the raster plot (**fig. 17A**). Thus, in the further analysis we focused only on the RMGL neuronal activity.

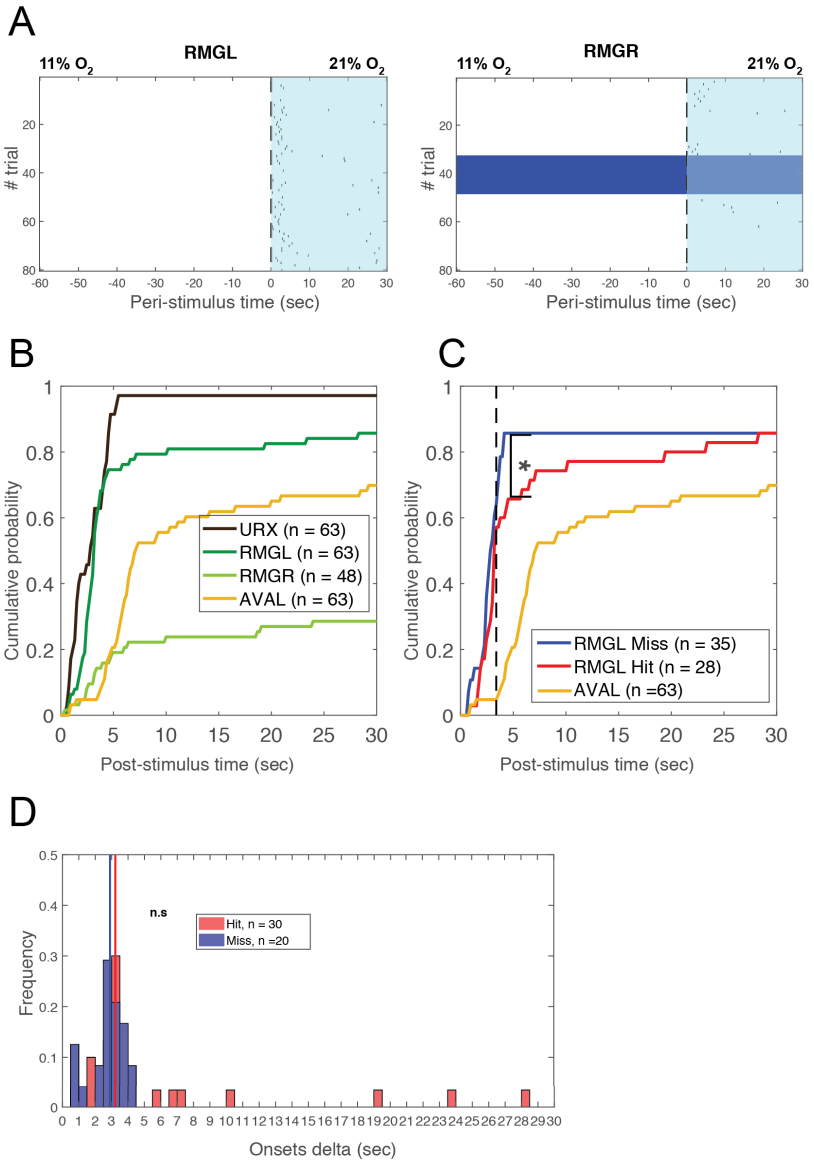

Figure 17. Characterization of the RMG interneurons activity onsets on the "Hit" versus "Miss" trials
(**A**) Raster plots showing the onsets of the rises of neuronal activity of the RMGL (left) and RMGR (right) interneurons. Each horizontal line corresponds to a single stimulation trial. Vertical dashed line at 0 seconds denotes transition from the 11% to 21% [O_2]. Note that in one of the recording datasets we could not identify RMGR neuron, thus corresponding trials are the missing values (NaN) denoted with a dark-blue color code. (**B**) Each line is a cumulative probability of the neuronal activity rise onsets of different neurons calculated from the 21% [O_2] stimulus periods. Horizontal dotted line denotes 100% probability level. N for each neuron indicates the number of trials used for the cumulative probability quantification. Only trials where the AVAL neuron was in a "low/fall" activity phase at the moment of the transition from the 11% to 21% [O_2] were considered for the analysis (the same applied for the (C) and (D)). Only the first activity rise onset was considered for this analysis in the case of multiple neuronal activity onsets per trial (the same applied for the (C)). (**C**) Each line is a cumulative probability of the neuronal activity rise onsets of RMGL and AVAL neurons calculated from the 21% [O_2] stimulus periods. For the RMGL neuron cumulative probability was calculated separately for the "Hit" and "Miss" trials clusters. N for each neuron or condition indicates the number of the trials used for the analysis. *, $p < 0.05$. (**D**) Histogram showing the timing of the RMGL activity rises onsets for the "Hit" and "Miss" trials separately within the 21% [O_2] stimulation period. Vertical dashed lines denote the median values for the "Hit" and "Miss" clusters. N for each condition indicates the number of the onsets used for the analysis. Statistical test compares median values. ****, $p > 0.05$.

As the RMGL neuron demonstrated trial-to-trial response variability with activation during the 10 seconds time window being present at ~0.8 trials, we aimed to explore if this response variability was correlated with the motor response variability. To do this we applied analysis procedure where

cumulative probabilities of the RMGL activity onsets were calculated separately for the "Hit" and "Miss" trials, as was previously described for the oxygen sensory neurons (**fig. 17C**, see **Methods**). We found that the activity onsets cumulative probabilities were identical on "Hit" and "Miss" trials during the first ~4 seconds upon the 21% [O_2] stimulus onset. However, starting from the ~4 seconds the cumulative probability rate diverged between "Hit" and "Miss" trials. Cumulative probability for the "Miss" trials maintained the same slope until reached the maximum plateau of ~0.83 value level by ~5 seconds. In contrast, cumulative probability slope for the "Hit" trials became progressively more gradual from ~4 seconds timing till the end of the 21% [O_2] period, indicating lower rate of the activity onsets. The difference in probability values between "Hit" and "Miss" trials was statistically significant at the peak divergence observed at 5 seconds. Importantly, the beginning of the "Hit"- "Miss" RMGL activity cumulative probabilities divergence (~4 sec) coincided with the onset of the AVA cumulative probability slope rise. It is important to note that by the end of the 21% [O_2] period the cumulative probability of the RMGL activity at "Hit" trials reached the same ~0.8 value as at "Miss" trials. Thus, overall probability of the RMGL response at "Hit" and "Miss" trials was equal, but at the "Hit" trials it was achieved by means of the long-latency activations. Overall, we observed a suppression of the RMGL activity at "Hit" trials compared to "Miss" trials and the onset of this suppression coincided with the onset of the AVA activation period. This might indicate a presence of a potential feedback mechanism which down-regulates RMGL activity upon the initiation of the reversal behavior.

Additionally, we observed that the cumulative probability slope of the RMGL activity at "Miss" trials slightly preceded the one at "Hit" trials which indicates potential shift in the activity onset's timing. To investigate this finding in more details we applied the "Hit-Miss" separated analysis of the activity onset's timing as it was described before for the oxygen sensory neurons (**fig. 17D**, see **Methods**). This analysis revealed that the activity onsets latencies had slightly smaller median value at "Hit" trials compared to "Miss" trials; however, the delta between median values was not statistically significant. Further, the neuronal activity onsets histogram clearly demonstrated that for the "Miss" trials the activity onsets latencies were within 0 to 5 seconds boundaries, whereas "Hit" trials contained a fraction of the long-latency events. This finding corresponds to the previous finding from the activity onsets cumulative probability analysis where we found that the probability at "Miss" trials reached maximum within the 5 seconds time window, whereas "Hit" trials contained a fraction of the long-latency events.

In conclusion, we found that the RMG neurons had certain trial-to-trial variability of their responsiveness. RMGR neuron demonstrated particularly low response probability: ~0.2 within the 10 seconds time window. In contrast, RMGL neuron reacted at ~80% of trials within the 10 seconds time window. Further analysis of the RMGL neuron's responsiveness revealed that its activation was suppressed at "Hit" trials compared to "Miss" trials. Importantly, the beginning of the RMGL suppression period coincided in time with the beginning of the time window where the AVA activity

onsets were observed. Thus, we assume that RMGL's activity might be suppressed upon the initiation of the reversal behavior by the potential feedback mechanism. Finally, analysis of the RMGL activity onset's latencies showed that this parameter is not correlated with the reversal motor response. It is important to mention that the lower probability of the RMGL neuron activation at "Hit" trials compared to "Miss" trials upon the ~4seconds from the 21% [O_2] stimulus onset might to some extend explain lower average activity amplitude values at "Miss" trials compared to the "Hit" trials detected previously (**fig. 15**).

3.11 The intrinsic state of AVA preceding the 21% [O_2] stimulus exerts minimal impact on the response of oxygen sensory neurons and primary interneurons to the stimulus

Previously, we observed that the AVA intrinsic state influences its responsiveness to the oxygen stimulus, such that a longer AVA inactive state before the onset of the 21% [O_2] stimulus led to a higher response probability (**fig. 9B**). In the "Hit-Miss; Evoked-Spontaneous"-triggered average analysis, "Hit" trials were defined by AVA responding within 10 seconds of the 21% [O_2] stimulus (see **Methods**), while all other trials were considered "Miss" trials. Consequently, "Hit" trials were more likely to have a longer AVA inactive state preceding them compared to "Miss" trials.

Thus, the reversal motor response defined by AVA activation was intertwined with the history of AVA inactivity prior to the stimulus. Hence, we aimed to test the theory that the differences in "Hit-Miss" responses observed in oxygen sensory neurons and primary interneurons (**figs. 11, 15**) could reflect the history of AVA intrinsic state preceding the onset of the 21% [O_2] stimulus rather than AVA responsiveness to the oxygen stimulus.

To achieve this, we implemented an analysis procedure where we categorized all trials into three clusters based on the past history of the AVA neuron: "0 sec", "30 sec", and "50 sec", corresponding to the duration during which the AVA neuron was inactive before the onset of the 21% [O_2] stimulus. We then calculated stimulus-triggered averages for the neurons of interest within each cluster (see **Methods**). Subsequently, we compared the average responses across these time clusters (**fig. 18**).

We found that sensory neurons and primary interneurons showed only subtle effects of the preceding AVA inactive history on their activity before the 21% [O_2] stimulus. For instance, oxygen sensory neurons including URX, AQR, and IL2 demonstrated subtle modulations in response amplitude to the 21% [O_2] stimulus. Primary interneurons including AUA, PVP, and RMG showed baseline activity modulations during the 11% [O_2] period. An interesting observation was noted for "X" neurons, which exhibited progressively higher activity amplitudes during the 11% [O_2] period in trial clusters with longer AVA inactive periods.

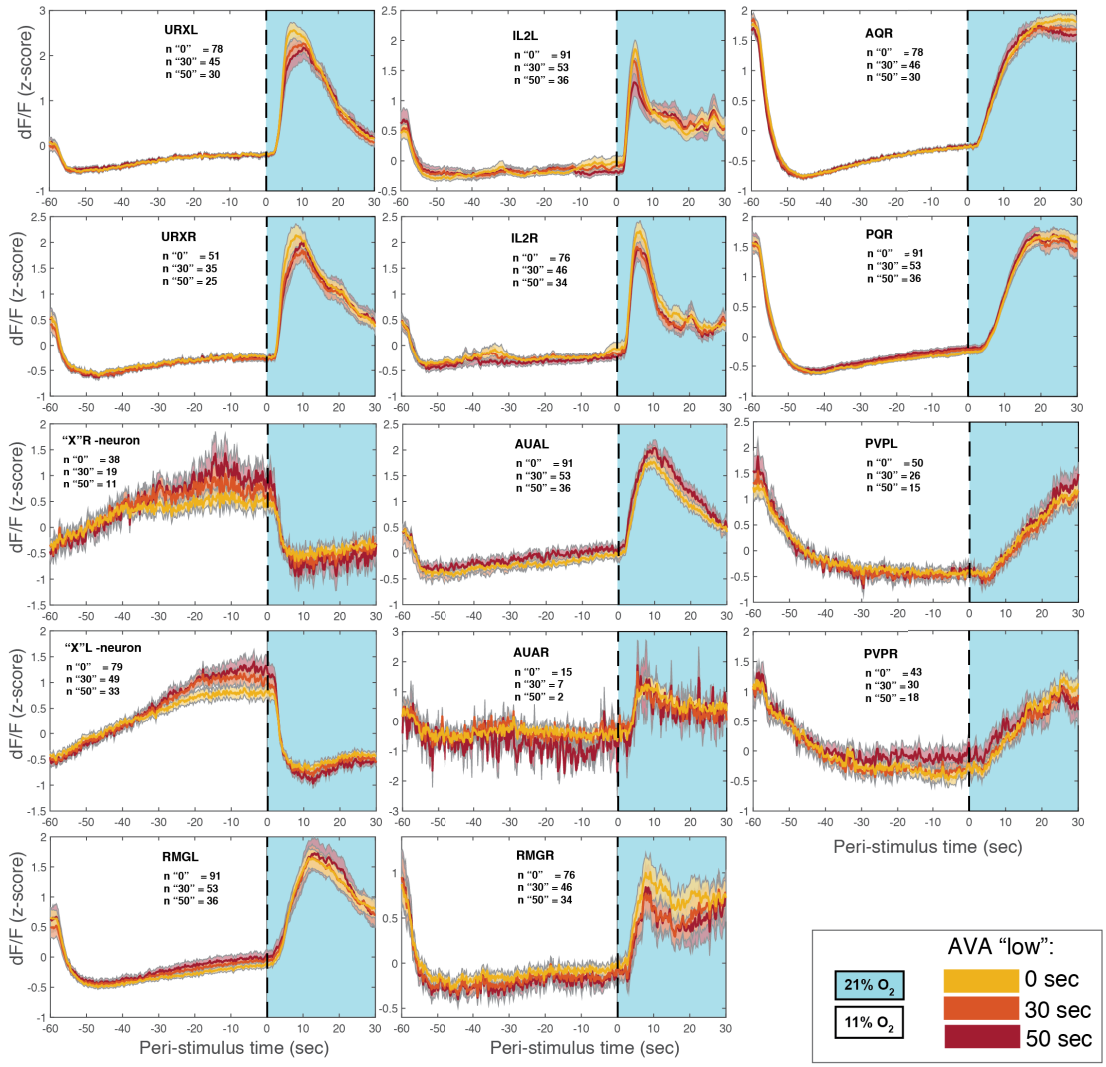

Figure 18. Stimulus-triggered averages of neuronal activities sorted by different AVA past history conditions
Each box corresponds to a different neuron: oxygen sensory neurons and primary interneurons are demonstrated on the figure. Color codes denote three different subsamples of trials used for the stimulus-triggered averages quantification. Each condition is defined by the AVA neuronal activity being in a "low/fall" state for a specified duration before the onset of the 21% [O2] stimulus (0, 30, or 50 seconds). The "0 sec" condition indicates that the AVA neuron was in a 'low/fall' state precisely at the onset of the 21% [O2] stimulus. N "0", n "30" and n "50" in each box indicates number of trials used for averaging for each of the AVA "low/fall" conditions. Vertical dashed line at 0 seconds represents the transition between 11% and 21% [O_2] periods.

We concluded that the AVA intrinsic state history preceding the onset of the 21% [O_2] stimulus had only a minimal impact on the activity patterns of the investigated neurons. Therefore, it is unlikely to influence the results of the "Hit-Miss; Evoked-Spontaneous"-triggered average analysis, which aims to reflect the decision-related activity in sensorimotor transformation.

3.12 Head motor neurons demonstrated activity with opposite modalities on "Hit" and "Miss" trials

Exploration of the acquired whole-brain imaging datasets revealed three pairs of neurons situated in the ventral ganglion in the proximity of the SMDD neurons with a regular periodic activity which were not

described in the literature before. We assigned to these neurons putative names Head Motor Neuron 1,2 and 3 (HMN1, HMN2, HMN3). HMN1, HMN2 neurons was characterized by the activity partially overlapping with the head bending related activity of the SMDD and SMDV neurons respectively (Kaplan et al. 2020; Hendricks 2012; Shen et al. 2016; Ouellette et al. 2018). HMN3 neuron was characterized by the activity partially overlapping with the RIB neuron activity which is known be to correlated with forward locomotion related activity.

Next, stimulus-triggered average analysis (**figs. 19, S1**) revealed that HMN1 and HMN2 neurons had an activity slowly ramping upon the 21% [O_2] stimulus onset and reaching maximum by the end of 21% [O_2] period. Then, the activity was slowly decaying to the baseline during the 11% [O_2] periods and reached the baseline at ~ -20 seconds. For the HMN3 neuron the activity rose during the 21% [O_2] period and reached maximum peak at ~15 seconds upon the stimulus onset, then it decayed to the baseline by the end of the 21% [O_2] period. During the 11% [O_2] HMN3 neuron activity initially rose with a peak ~ -50 seconds and then slowly decayed to the baseline by the ~ -10 seconds.

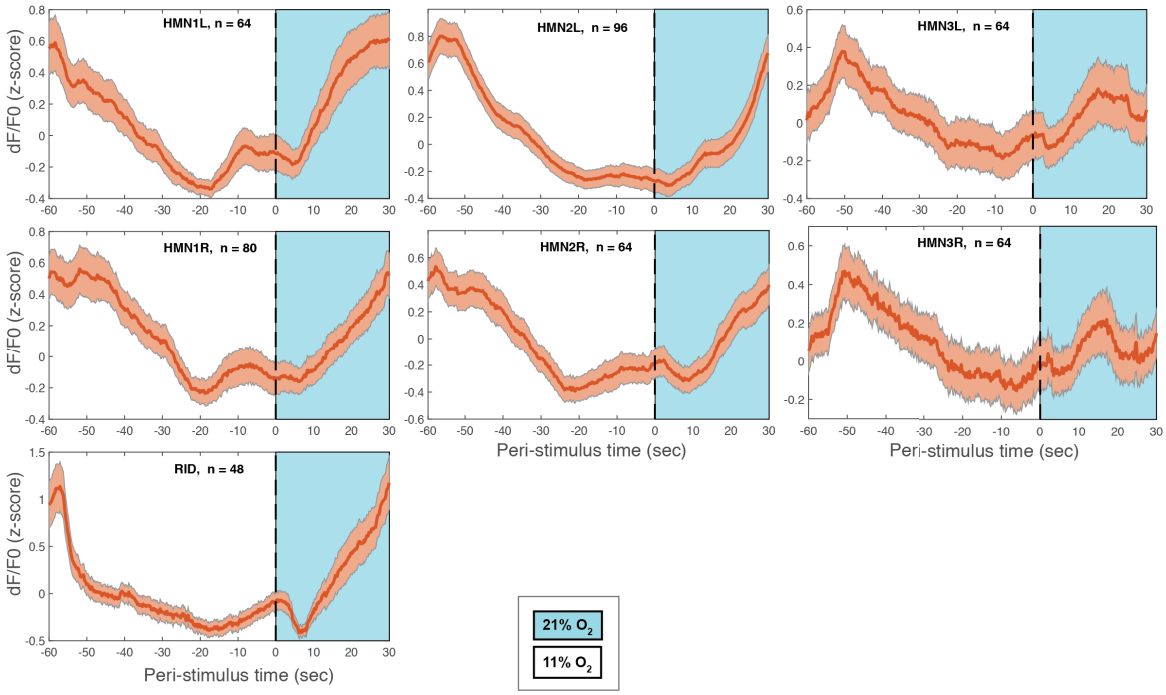

Figure 19. Stimulus-triggered averages of neuronal activity in head motor neurons
Each box corresponds to a different oxygen sensory neuron. Orange line within each box is a stimulus-triggered average of the neuronal activity. Shaded area represents ± SEM. Vertical dashed line at 0 seconds represents the transition between 11% and 21% [O_2] periods. N in each box indicates number of trials used for averaging.

Further, with the stimulus-triggered averages analysis exploration we detected another neuron with an activity profile similar to HMN neurons which was identified as an RID neuron (**figs. 19, S1**). RID neuron is a neuropeptide releasing single neuron which is known to promote forward locomotion in *C.*

elegans as a part of a locomotion arousal state (Chew et al., 2018; Lim et al., 2016; Mori et al., 2019). RID neuron receives major synaptic input from the PVC neuron (White et al., 1986) which is responsible for the forward locomotion in response to the tail touch (W. Li et al., 2011) and is connected by gap junctions with a forward command AVB neuron (White et al., 1986).

3.12.1 "Hit-Miss"-triggered average analysis of the HMN and RID neurons

We aimed to inspect a potential role of these newly identified neurons in the sensorimotor transformation of the oxygen stimulus. Thus, we scrutinized results of the "Hit-Miss"-triggered average analysis for these neurons. Interestingly, all these neurons demonstrated similar pattern of the activity difference between "Hit" and "Miss" trials (**figs. 20, S3**). Upon the onset of the 21% [O_2] stimulus the activity was rising on "Miss" trials with a maximum peak between 10 and 20 seconds. In contrast, on "Hit" trials the activity was down-modulated and reached minimum level in the same time period between 10 and 20 seconds. Thus, the average activity amplitude was significantly different at "Hit" versus "Miss" trials between 10 and 20 seconds of the 21% [O_2] period. Next, For the HMN1 and HMN2 neurons activity was slowly rising after the through, whereas for the HMN3 it stayed at the suppressed level till the end of the 21% [O_2] period. Additionally, for the HMN1 and HMN2 neuron we observed a trend with the activity starting to rise on "Miss" trials ~10 seconds prior to the 21% [O_2] stimulus, in contrast to "Hit" trials where it started to get down-modulated at the same time of ~10 seconds prior to the 21% [O_2] stimulus.

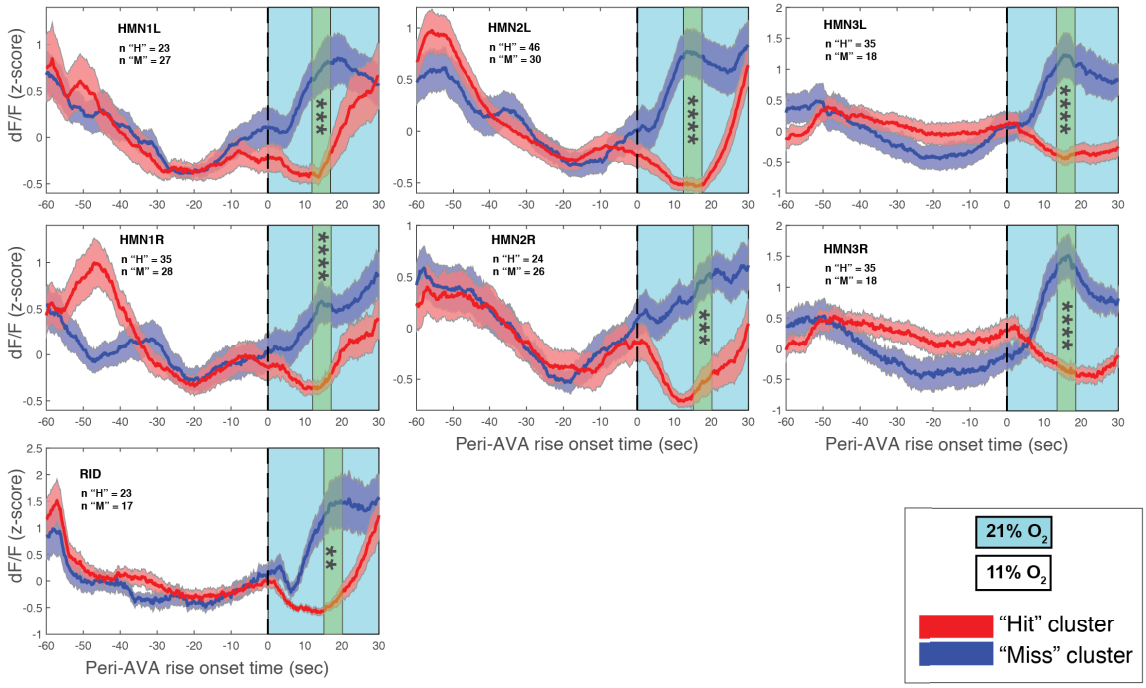

Figure 20. Head motor neurons demonstrate opposite activity patterns at "Hit" versus "Miss" trials
We could detect three pairs of head motor neurons (HMNs) in the ventral ganglion region, they have been labeled HMN1, HMN2 and HMN3 (see Methods). Together with the RID neuron they demonstrate opposite patterns of activity at "Hit" versus "Miss" trials. Each box corresponds to a different head motor neuron. Within each box trials averages of neuronal activity for "Hit" and "Miss" clusters are depicted with different color-code. Shaded areas represent ± SEM. Vertical

dashed line at 0 seconds represents the transition between 11% and 21% [O_2] periods. N "H" and n "M" in each box indicates number of trials used for averaging for the "Hit" and "Miss" clusters respectively. Green bars represent the 15-second time windows where statistical tests were performed. **, $p < 0.01$.

During the 11% [O_2] period both HMN2 neurons had similar activity patterns on "Hit" versus "Miss" trials. In contrast, HMN1 neurons showed left -right functional asymmetry, as HMN2L had similar activity profile on "Hit" versus "Miss" trials the same as HMN2 neurons, whereas HMN1R neuron demonstrated activity rise upon the 11% [O_2] stimulus onset with a peak at ~ -45 seconds which then decayed and reached the baseline at ~ - 35 seconds.

HMN3 neurons had opposite activity patterns during the 11% [O_2] period on "Hit" versus "Miss" trials. On "Hit" trials the activity slightly rose during the first 10 seconds upon the 11% [O_2] stimulus onset and stayed at the elevated level till the end of the 11% [O_2] period. In contrast, on "Miss" trials activity gently decayed starting from 10 seconds upon the 11% [O_2] stimulus onset and reached the baseline at ~ -20 seconds timing. As a result, HMN3 activity was slightly stronger during most of the 11% [O_2] period on "Hit" trials compared to "Miss" trials.

Finally, the RID neuron revealed a "Hit-Miss" trials activity difference similar to the one described for the HMN neurons. RID activity rose during the 21% [O_2] period on "Hit" trials and in contrast it was down-modulated on "Miss" trials. Thus, its average activity amplitude was significantly different at "Hit" versus "Miss" trials similar to HMN neurons. Importantly, RID neuron demonstrated a transient suppression preceding the activation at "Miss" trials. This activity down-modulation started shortly after the 21% [O_2] stimulus onset and reached a through at ~7 seconds upon the oxygen stimulus onset. During the 11% [O_2] period RID neuron had similar activity profile at "Hit" versus "Miss" trials similar to the HMN1L and HMN2 neurons.

3.12.2 "Evoked-Spontaneous" AVA-triggered average analysis of the HMN and RID neurons

AVA-triggered average analysis showed that all HMN neurons and RID neuron exhibited activity down-modulation on both "Evoked" and "Spontaneous" trial's clusters (**figs. 21, S4**). This testifies to the assumption that their activity is linked to the motor response. Next, we found that the down-modulation of the HMN and RID neurons started prior to the AVA activity rise onset on "Evoked" and "Spontaneous" trials. Further, HMNL3 neuron had stronger level of activity down-modulation on "Spontaneous" trials compared to "Evoked" trials with significant difference for HMN3R counterpart.

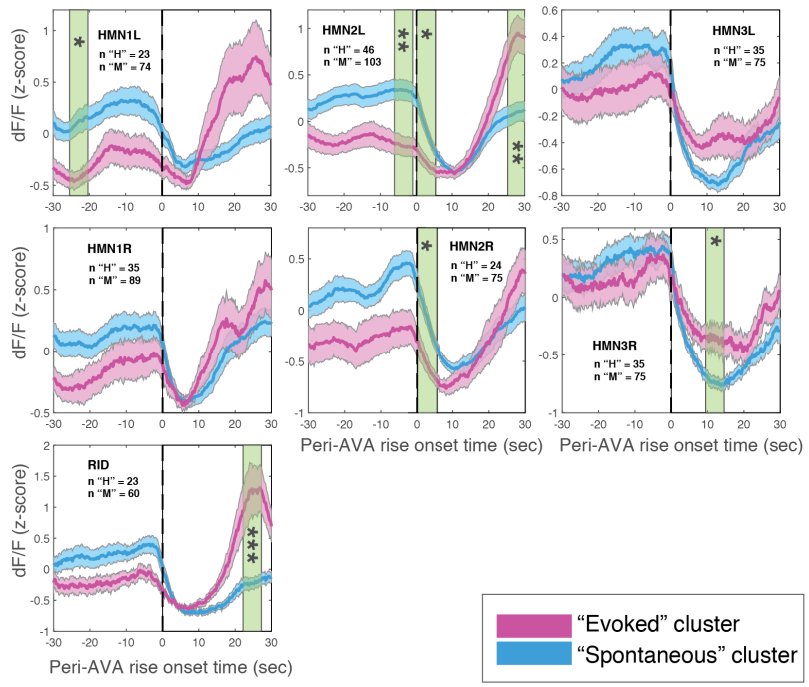

Figure 21. "Evoked-Spontaneous" AVA-triggered averages of neuronal activity for different head motor neurons
Each box corresponds to a different head motor. Within each box trials averages of neuronal activity for "Evoked" and "Spontaneous" clusters are depicted with different color-code. Shaded areas represent ± SEM. Vertical dashed line at 0 seconds represents the transition between pre- and post- AVA rise onset time periods. N "E" and n "S" in each box indicates number of trials used for averaging for the "Evoked" and "Spontaneous" clusters respectively. Green bars represent the 15-second time windows where statistical tests were performed. *, $p < 0.05$; ***, $p < 0.001$; ****, $p < 0.0001$.

Next, the initial down-modulation upon the AVA activity onset was followed by an up-modulation. This activity up-modulation had a steeper slope and reached higher average amplitude values on "Evoked" trials compared to "Spontaneous" trials with a significant difference detected for HMN2L and RID neurons

Also, we found that HMN1, HMN2 and RID had higher activity level prior to the AVA activity onset on "Spontaneous" trials compared to "Evoked" trials. In particular, the activity difference was statistically significant for HMN1L and HMN2L neurons.

In conclusion, we detected three pairs of neurons in the ventral ganglion which had similar activity profile correlating with the head bending related activity of SMD neurons and forward locomotion related activity of RIB neuron. These neurons have not been described in the literature before and we assigned them with putative names Head Motor Neuron 1,2 and 3 (HMN1,2,3). The average activity profile of HMN neurons showed modulation related to the oxygen stimulus. Additionally, we found that RID neuron had a similar stimulus-triggered average activity profile. Thus, we further investigated results of the "Hit-Miss; Evoked-Spontaneous"-triggered average analysis for the HMN neurons and RID neuron together. We found that HMN and RID neurons had activity modulation on both "Hit" and "Miss" trial's clusters of the stimulus-triggered average analysis and on "Evoked" and "Spontaneous"

trial's clusters of the AVA-triggered average analysis. Therefore, we concluded that HMN and RID neurons activity reflected sensory input as well as motor command state. Further, we found that HMN and RID neurons had opposite activity modalities on the "Hit" versus "Miss" trials such that their activity was down-modulated upon the 21% [O_2] stimulus on "Hit" and in contrast it was up-modulated on the "Miss" trials. Thus, we hypothesized that HMN and RID neurons might function as a gating mechanism with their activity up-modulation preventing reversal motor response, whereas their activity suppression might be allowing for the reversal motor response.

3.13 Neurons encoding forward locomotion exhibit activity that may be predictive for sensorimotor transformation

In this section we aimed to focus on the neurons governing the forward locomotion of *C. elegans* and their reaction to the oxygen stimulus in our experimental paradigm. In particular, we sought to investigate if their activity could be linked to the responsiveness of the reversal command AVA neuron over trials.

As was described before, freely crawling *C. elegans* under the normal conditions exhibit intermittent forward and reverse locomotion behaviors (Gray et al., 2005; Pierce-Shimomura et al., 1999) and corresponding intermittent neuronal motor command activity was found in the restrained animals under the whole-brain imaging conditions (Kato et al., 2015).

The major command interneuron governing forward locomotion is the AVB neuron as was shown by the Ca 2+ imaging studies where its activity correlated with forward locomotion and was reciprocal to the activity of the AVA reversal command interneuron (Faumont et al., 2011; Kato et al., 2015). This role of the AVB neuron is also supported by the ablation studies (Chalfie et al., 1985; Zheng et al., 1999). Next, the RIB a second-layer interneuron (Gray et al., 2005) which receives major inputs from the AUA interneuron and BAG oxygen sensory neuron (White et al., 1986) is known to be involved in the forward locomotion. This is supported by a Ca 2+ imaging studies which revealed correlation if the RIB activity with forward locomotion and ablation and optogenetic stimulation experiments (Gray et al., 2005; Kato et al., 2015; Z. Li et al., 2014; Tsalik & Hobert, 2003; Wang et al., 2020).

Additionally, it was shown that the activity of the AVB and RIB neurons correlated with the speed of forward locomotion and their activity down-modulation preceded switch from forward to reverse locomotion (Kato et al., 2015). Therefore, we assumed that the AVB and RIB activity might be predictive for the AVA trial-to-trial response variability in relation to the 21% [O_2] stimulus.

3.13.1 RIB interneurons show activity down-modulation to oxygen stimulus in both 'Hit' and 'Miss' trials

As was expected AVB and RIB interneurons demonstrated activity down-modulation on the stimulus-triggered averages upon the 21% [O_2] stimuli onsets (**fig. S1**). This was coherent with the facts that the reversal command AVA neuron was on average up-modulated by the 21% [O_2] stimulus (**fig. S1**) and that the forward and reversal driving neurons are known to have an anticorrelated activity. Surprisingly, we also found a down-modulation of the AVB and RIB activities upon the 11% [O_2] stimuli onsets.

Next, we inspected the results of the "Hit-Miss; Evoked-Spontaneous"-triggered average analysis for AVB and RIB neurons. To our surprise, the analysis revealed that RIB and AVB neurons had an average activity down-modulation on both "Hit" and "Miss" trials (**figs. 22A, S3**) upon the 21% [O_2] stimulus onsets. Importantly, the activity down-modulation on "Hit" trials was significantly stronger comparing to the "Miss" trials.

The RIB activity down-modulation had a transient character on "Miss" trials: it reached minimum through at ~5 seconds upon the 21% [O_2] stimulus and then abruptly recovered to the baseline by ~15 seconds. In contrast, the down-modulation on "Hit" trials was sustained over time: activity reached minimum through at ~5 seconds similarly to "Miss" trials, however afterwards it recovered slowly and reached the baseline by the end of the 30 seconds 21% [O_2] period.

For the AVB neuron activity down-modulation on "Hit" trials had similar pattern to the one described for the RIB neuron. However, activity on the "Miss" had different pattern: upon the down-modulation from the elevated level, it reached the plateau which lasted for the rest of the 21% [O_2] period.

Importantly, we found for both RIB and AVB neurons that their activity patterns on "Hit" versus "Miss" trials started to deviate relating to each other already prior to the 21% [O_2] stimulus onsets. In particular, the activity on average rose prior to the 21% [O_2] stimulus on the "Miss" trials. In contrast, on the "Hit" it showed a gentle decay prior to the 21% [O_2] stimulus for the RIB neuron and was flat prior to the 21% [O_2] stimulus for the AVB neuron.

Additionally, we found that RIB activity down-modulation detected upon the 11% [O_2] stimulus had a trend to be stronger on "Hit" trials comparing to the "Miss" trials. However, this effect was not evident in the AVB neuron.

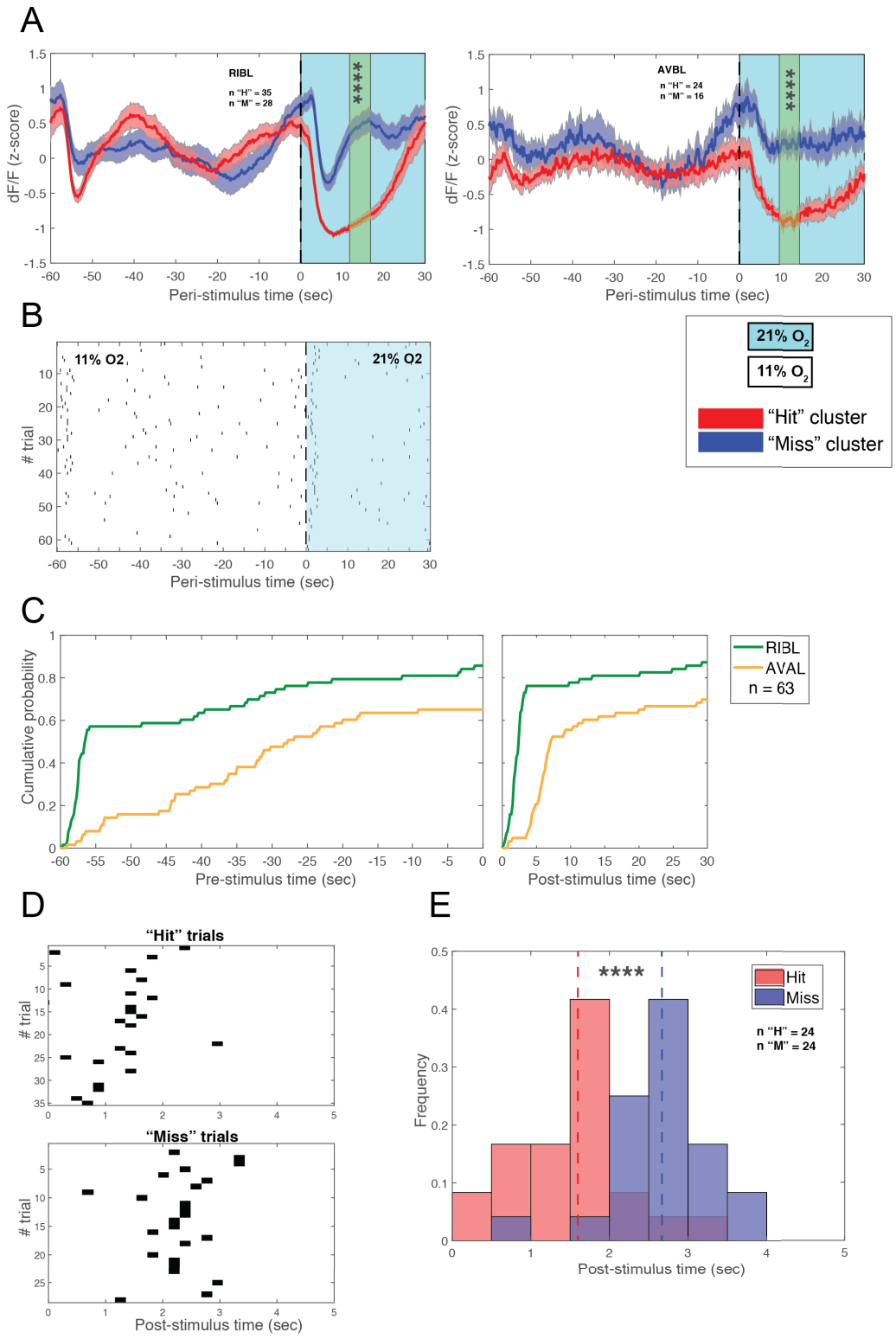

Figure 22. RIB neuron modulates its activity on the "Hit" versus "Miss" trials
(**A**) "Hit-Miss" stimulus-triggered averages of the forward command interneurons activity: RIBL (left panel) and AVBL (right panel). Trials averages of neuronal activity for "Hit" and "Miss" trials clusters are depicted with different color-code. Shaded areas represent ± SEM. Vertical dashed line at 0 seconds represents the transition between 11% and 21% [O_2] periods. N "H" and n "M" in each box indicates number of trials used for averaging for the "Hit" and "Miss" clusters respectively. Green bars represent the 15-second time windows where statistical tests were performed. ****, $p < 0.0001$. Only the trials where AVA neuron was in a "low/fall" activity phase at the moment of the transition from the 11% to 21% [O_2] were considered for the analysis (also for B - E). (**B**) Raster plot denoting the RIBL activity falls onsets. Vertical dashed line at 0 seconds denotes transition from the 11% to 21% [O_2]. (**C**) Comparison of cumulative probability of the RIBL activity falls onsets versus the AVAL activity rise onsets. Left panel shows quantification for the 11% [O_2] period

with -60 seconds time point corresponding to the [O_2] downshift. Right panel shows quantification for the 21% [O_2] period with 0 seconds time point corresponding to the [O_2] upshift. Only the first activity onset at each trial was used for the quantification for both RIBL and AVAL neurons. N denotes the number of trials used for the analysis. (**D**) Raster plots show the RIBL activity falls onsets separately for the "Hit" (top panel) and "Miss" trials clusters (bottom panel). Figure depicts 5-second period following the 21% [O_2] onset. (**E**) Histogram showing the timing of the RIBL activity falls onsets for the "Hit" and "Miss" trials clusters separately within the 5-second period following the 21% [O_2] onset (quantification related to (D)). Vertical dashed lines denote the median values for the "Hit" and "Miss" clusters. N "H" and n "M" indicates the number of the onsets used for the analysis from "Hit" and "Miss" clusters respectively. Statistical test compares median values. ****, $p < 0.0001$.

3.13.2 RIB down-modulation events exhibit higher trial reliability compared to AVA and show timing variations with sensorimotor transformation outcomes

Furthermore, we aimed to provide a detailed analysis of the RIBL neuron activity, specifically focusing on the timing of the activity down-modulations' onset. This analysis was conducted in a similar manner to our previous examination of the activity rise onset timing in other neurons. To do that, fall states of the RIBL neuron were annotated from its fluorescence activity traces and the timings of fall onsets were extracted (see **Methods**).

Firstly, the activity falls onsets raster plot (**fig. 22B**) revealed that RIBL neuron exhibited activity down-modulations on most of the trials starting shortly after the 21% [O_2] and 11% [O_2] stimuli onsets. Initial activity fall onset events were grouped in the ~4 seconds time window following the 21% [O_2] and 11% [O_2] stimuli. The initial fall events were followed by ~5 seconds long refractory period with no detectable activity falls. After this refractory period, we could detect fall onsets scattered in time over the rest of the 21% and 11% [O_2] periods which reflect spontaneous RIBL activity down-modulations.

Next, we sought to quantify the reliability of the RIBL neuron down-modulations in the response to the oxygen stimulus over trials; for that we used the activity onsets cumulative probability analysis, similarly as was described before for other neurons (see **Methods**). In the current modification of this analysis, we performed cumulative probability quantification separately with a relation to the 21% and 11% [O_2] stimuli onsets (**fig. 22C**).

The RIBL activity fall onsets cumulative probability curve for the 21% [O_2] period had a steep rise during the first ~4 seconds upon the oxygen stimulus onset and reached the value of ~0.78 by the end of this period. After ~7 seconds plateau phase we observed a gentle rise of the cumulative probability curve till the end of the 21% [O_2] period where it reached the value of ~0.82. This gentle rise period could reflect a long latency down-modulation events which might happened at a fraction of the "Miss" trials. Importantly, we found that RIB activity down-modulation in response to the 21% [O_2] stimulus was more reliable over trials compared to the AVAL activity rise events. This finding corresponded to the observation that RIBL neuron exhibit average activity down-modulation on both "Hit" and "Miss" trials (**fig. 22A**), whereas AVA neuron was active only at "Hit" trials following the definition.

Additionally, comparison of the cumulative probability curves for the RIBL and AVAL neurons showed that on average the RIBL down-modulation preceded the AVA activity rise.

The RIBL activity fall onsets cumulative probability curve for the 11% [O_2] period had a steep rise during the first ~4 seconds upon the oxygen stimulus onset and reached the value of ~0.6 by the end of this period. After ~7 seconds plateau phase we observed a gentle rise of the cumulative probability curve till the end of the 11% [O_2] period where it reached the value of ~0.82. Thus, on the ~60% of trials 11% [O_2] stimulus elicited immediate RIBL down-modulation. On the contrary, AVAL neuron showed gentle even increment of the activity rises during the 11% [O_2] reflecting the spontaneous activity without the effect of the 11% [O_2] stimulus.

Further, we aimed to investigate if the latency time of the RIB activity down-modulation in response to the 21% [O_2] stimulus onsets correlated with the motor response variability. To do that we applied a "Hit-Miss" separated analysis of the down-modulation onset's timing similarly as it was described before for the oxygen sensory neurons. Initial observation of the separated "Hit" and "Miss" trials raster plots (**fig. 22D**) revealed that RIB fall onsets on the "Hit" trials had shorter latencies in relation to the 21% [O_2] stimulus onset compared to the "Miss" trials. Further quantification of the RIB activity fall onsets latencies proved this observation (**fig. 22E**) revealing that the median latency time for the "Hit" trials cohort (~ 1.6 seconds) preceded the one for the "Miss" trials (~2.7 seconds) by ~1 second. Importantly, detected difference between the distributions of the fall onsets latencies for the "Hit" versus "Miss" trials was significantly different.

In summary, we found that RIB and AVB forward locomotion neurons exhibited activity down-modulation upon the 21% and 11% [O_2] stimulus. Importantly, we revealed that this response to the 21% [O_2] stimulus was present at "Hit" and "Miss" trials. Thus, the RIB response to the oxygen stimulus over trials was shown to be more reliable compared to the reversal locomotion response estimated by the AVA activity. Finally, we found that the RIB activity down-modulation in response to the 21% [O_2] stimulus had significantly shorter latency time on "Hit" trials compared to "Miss" trials.

3.13.3 AVA-triggered average analysis reveals different RIB activity pattern at "Evoked" versus "Spontaneous" trials

AVA-triggered average analysis showed that RIB and AVB neurons exhibited activity down-modulation on both "Evoked" and "Spontaneous" trial's clusters (**figs. 23A, S4**). This testifies to the assumption that their activity is linked to the motor response.

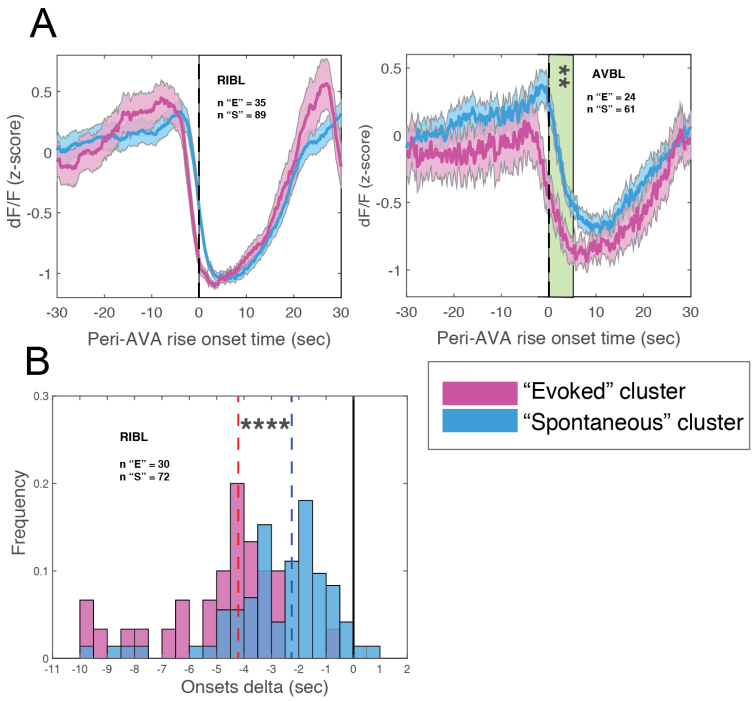

Figure 23. RIB neuron modulates its activity on the "Evoked" versus "Spontaneous" trials
(**A**) "Evoked-Spontaneous" AVA-triggered averages of the forward command interneurons: RIBL (left panel) and AVBL (right panel). Trials averages of neuronal activity for "Evoked" and "Spontaneous" clusters are depicted with different color-code. Shaded areas represent ± SEM. Vertical dashed line at 0 seconds represents the transition between pre- and post- AVA rise onset time periods. N "E" and n "S" in each box indicates number of trials used for averaging for the "Evoked" and "Spontaneous" clusters respectively. Green bars represent the 15-second time windows where statistical tests were performed. **, $p < 0.01$. (**B**) Histogram showing the timing of the RIBL activity falls onsets for the "Evoked" and "Spontaneous" trials separately. Quantification was made for the time window of ± 10 seconds centered around the AVA rise onset time. Vertical dashed lines denote the median values for the "Hit" and "Miss" clusters. N "E" and n "S" indicates the number of the onsets used for the analysis for the "Evoked" and "Spontaneous" clusters respectively. Statistical test compares median values. ****, $p < 0.0001$

Next, we found that the down-modulation of the AVB and RIB neurons starts prior to the AVA activity rise onset on "Evoked" and "Spontaneous" trials. Interestingly, "Evoked" and "Spontaneous" trials showed a difference in the activity patterns such that the down-modulation onset on "Evoked" trials on average preceded the one "Spontaneous" trials. In addition, the AVB neuron revealed significantly stronger activity down-modulation on the "Evoked" trials compared to the "Spontaneous" trials.

To investigate in more details "Spontaneous" versus "Evoked" trials activity difference we quantified RIB neuron fall onsets latencies in relation to the AVA activity rise onset (see **Methods**). We found that RIB fall onsets occurred significantly earlier (with ~1.9 seconds delta time) at the "Evoked" trials (median latency ~4.3 seconds prior to the AVA activity rise onset) compared to the "Spontaneous" trials (median latency ~2.4 seconds prior to the AVA activity rise onset) (**fig. 23B**).

In conclusion, we found that AVB and RIB neurons had an activity linked to both sensory stimulus and motor response as indicated by the fact that their activity modulation was detected on "Hit" and "Miss" trials of the stimulus-triggered average analysis (**fig. 22A**) and on "Evoked" and "Spontaneous" trials

of the AVA-triggered average analysis (**fig. 23A**). Moreover, we revealed that the RIB activity down-modulation occurred significantly earlier in relation to the AVA activity onset on the "Evoked" trials compared to the "Spontaneous" trials. This indicates that RIB and AVB neurons might play a different functional role in the neuronal dynamics generating reversal behavior in response to the oxygen stimulus and spontaneously. Specifically, oxygen stimulus evoked reversal motor command is associated with earlier recruitment of the RIB activity down-modulation with regards to the AVA activity rise onset timing.

3.13.4 Variations in relative timing of oxygen sensory and RIB neuron activity with sensorimotor transformation outcome

Previously we found that the RIB neuron significantly shifted its activity down-modulation onset timing towards shorter latencies on the "Hit" trials comparing to the "Miss" trials (**fig. 22D, E**). In contrast, all the identified oxygen sensory neurons (URX, IL2, AQR and PQR neurons) had their activity rise onset latencies in response to the 21% [O_2] stimulus being robust with regards to the "Hit-Miss" trials separation (**fig. 13A**). Thus, we sought to investigate the relative activity timing of the oxygen sensory neurons and RIB neuron on a single trial basis for the "Hit" versus "Miss" trial's clusters. For this we focused on the URX and IL2 oxygen sensory neurons as they had the most reliable activation over stimulus trials (**fig. 6B**). We subtracted RIB activity down-modulation onsets time from the oxygen sensory neurons activity rise onset time on a trial basis separately for "Hit" and "Miss" trials (see **Methods**) and plotted resulted delta times as a histogram (**fig. 24A**). Hence, positive delta values corresponded to the case when RIB down-modulation preceded oxygen sensory neuron activation and negative delta values corresponded to cases when RIB down-modulation followed oxygen sensory neuron activation.

We found that the distribution of delta values varied from negative to positive values on both "Hit" and "Miss" trials for all tested oxygen sensory neurons. This indicates the presence of relative timing patterns with RIB down-modulation preceding and following oxygen sensory neuron activation onset on different trials. As we expected, we observed a significant shift of delta values distributions between "Hit" and "Miss" trials such that the median delta value shifted to the right for the "Hit" compared to "Miss" trials. This means that the single trial based relative activity timing between the RIB and oxygen sensory neurons changed with respect to the success of the sensorimotor transformation.

Importantly, we found that medians of delta time distributions for all tested oxygen sensory neurons had positive values for the "Hit" trials indicating that RIB neurons down-modulation tended to precede oxygen sensory neurons activation. In contrast, on the "Miss" trials the delta time distribution's median was close to 0 value for URX and IL2L neurons indicating that relative timing patterns with RIB down-modulation preceding and following activation onset of these oxygen sensory neuron were equally

possible. However, for the IL2R counterpart neuron the “Miss” trials delta time distribution’s median had negative value indicating a that RIB down-modulation tended to follow its activity onset.

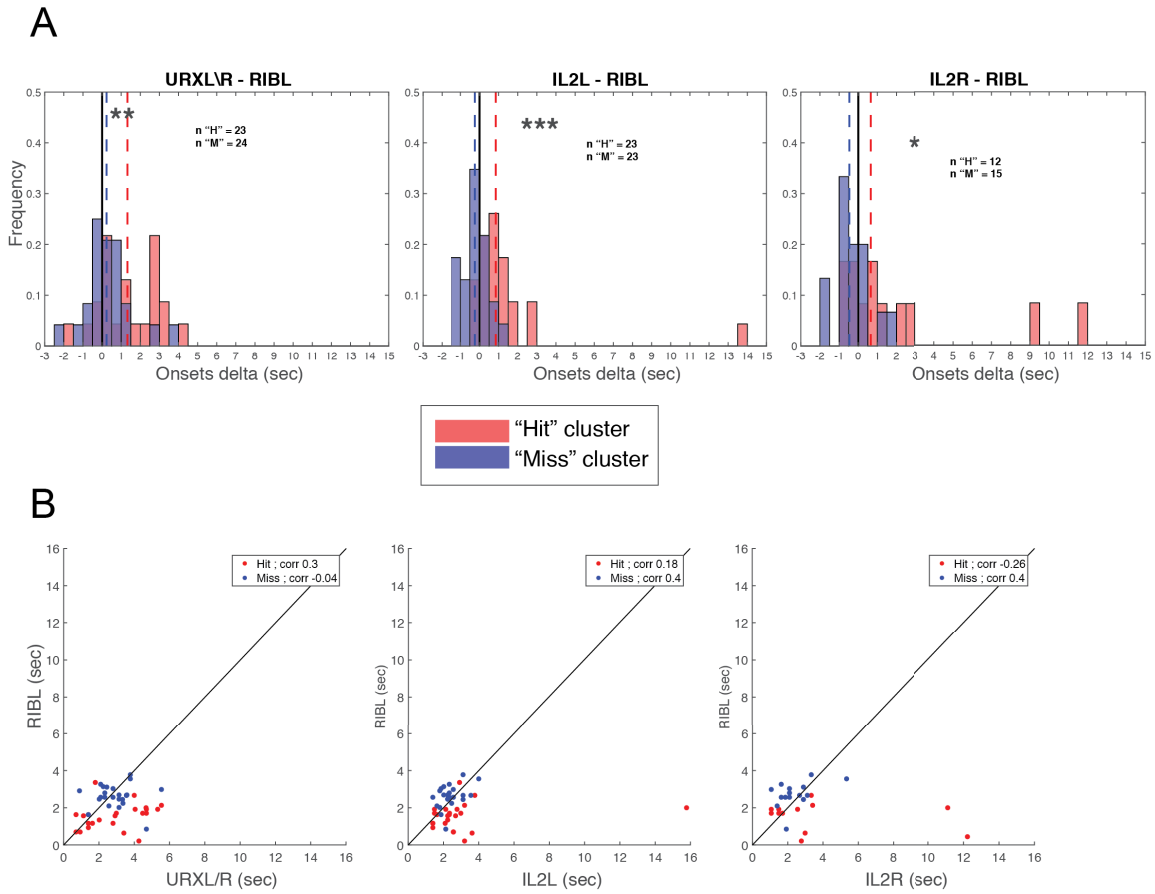

Figure 24. RIB neuron modulates its activity on the “Hit” and “Miss” trials relative to the stable activity of the oxygen sensory neurons
(**A**) Each panel shows a histogram of trial-by-trial differences between the timing of the RIB fall onset and corresponding sensory neuron rise onset. Histograms for the “Hit” and “Miss” trials are depicted overlaid. Vertical dashed lines denote the median values for the “Hit” and “Miss” clusters. N “H” and n “M” at each panel indicates the number of the onsets used for the analysis for the “Hit” and “Miss” clusters respectively. Statistical test compares median values. Solid vertical black line denotes 0 value. (**B**) Scatter plot with every dot representing timing of the RIBL fall onset (y-axis) and corresponding oxygen sensory neuron rise onset (x-axis) separately for the “Hit” and “Miss” trials.

These findings are further supported by observations from the scatter plot (**fig. 24B**), illustrating that on a trial-by-trial basis, the relative timing of RIB and URX activity onset was evenly distributed around the identity line during "Miss" trials, whereas "Hit" trials showed a tendency towards shorter RIB onset timings.

Overall, we found that the timing of RIB neuron activity down-modulation is significantly shifted relative to the activation timing of oxygen sensory neurons on 'Hit' versus 'Miss' trials. Additionally, the correlation pattern between these events changes on “Hit” versus “Miss” trials. Moreover, we found that the onsets of RIB down-modulation tend to precede the activity onset of the oxygen sensory neurons

on 'Hit' trials, whereas on 'Miss' trials they exhibit a more evenly distributed pattern in relation to the activity onset of oxygen sensory neurons.

4. Discussion

4.1 The principal objectives of the research project

The objective of this research project was to explore the sensorimotor transformation mechanisms in the nematode worm *C. elegans*. The term "sensorimotor transformation" traditionally pertains to the complex neural processes that convert sensory input into motor commands. A more comprehensive perspective on this process involves the complex interaction between sensory representation and the intrinsic activity of the nervous system, ultimately leading to the coordination of motor responses. These processes are crucial for biological organisms to interact with and adapt to their ever-changing environments by effectively directing and coordinating actions and movements in response to external stimuli.

In this study, we focused on the oxygen sensory system that enables the worms to orient in their environment, locate food, avoid surfacing, and maintain internal oxygen homeostasis (Cheung et al., 2005; Gray et al., 2004). *C. elegans* prefer environmental [O_2] in range of 5-11% (Gray et al., 2004) and exhibit a reverse crawling avoidance reaction to elevated environmental [O_2] (Busch et al., 2012; Cheung et al., 2005; Persson et al., 2009; Rogers et al., 2006). Thus, we aimed to reproduce this avoidance reaction under experimental conditions and study the underlying sensorimotor transformation processes.

Simplified scheme of the underlying neuronal mechanism presumably involves several steps. First, primary oxygen sensory neurons (URX, AQR, PQR, IL2) should detect stimulus and pass information to the connected interneurons (RMG, AUA, PVP) which might perform additional computations. Ultimately, inputs from sensory neurons and interneurons are integrated by premotor interneurons (AVA, AVE, AVD) which initiate and sustain the reversal motor state and then relay commands to ventral cord motor neurons. Furthermore, based on numerous previous findings (Kaplan et al. 2020; Li et al. 2014; Luo et al. 2014; Gordus et al. 2015; Hendricks 2012; Kato et al. 2015) we propose that the sensorimotor transformation in *C. elegans* may exhibit complexity beyond the Input-output View. This complexity involves intricate interactions between sensory inputs and the internal state of the nervous system, thereby endorsing the Coordination View (Pantin, C.F.A., 1956; Passano and Hutchinson 1963; Keijzer, van Duijn, and Lyon 2013).

Overall, our goal was to investigate sensorimotor transformation by identifying related neuronal circuits and characterizing their activity patterns. To achieve this, we developed a data analysis approach using whole-brain recordings to identify sensory and interneurons involved in the oxygen avoidance reaction and clarify their functional roles. Additionally, we aimed to explore how external stimuli interact with

the internal state, a critical aspect aligned with the principles proposed in the Coordination View hypothesis.

4.2 Reversal motor response to the oxygen stimulus in freely moving worms

The initial aim of my project was to create an experimental approach for exploring sensorimotor transformation in *C. elegans*, focusing on the avoidance reaction of reversal crawling in response to elevated ambient [O_2]. Overall, we successfully mimicked this reaction in the population behavioral conditions where we found that worms elicit reversal crawling in response to the elevated [O_2] from 11% to 21% (**fig. 1**) which is consistent with numerous results from other studies (Cheung et al., 2005; Gray et al., 2004; Rogers et al., 2006). It is crucial to underscore that, in contrast to previous studies which employed a single stimulus, our study uniquely used multiple stimulus repetitions. Further, under the conditions of multiple stimulus repetitions we observed no significant habituation of the response, affirming that this paradigm could be utilized further in our imaging experiments (**fig. 1A**).

It is crucial to mention that we also observed a reversal response latency time of roughly 5 seconds (**fig. 1B - D**). However, our experimental estimation for the gas delivery delay time was only ~1 second (**fig. 3D**). Consequently, there is still a roughly 4-second delay in the behavioral response that requires further explanation.

A detailed view on our results showed that reversals were initiated into two bouts during the 30 seconds period of elevated [O_2]: an initial sharp peak of the reversal's onsets frequency following by a secondary low-frequency up-modulation with a refractory period in-between (**fig. 1**). At the same time our oxygen measurements in the behavioral chamber showed constant rise of the [O_2] level during the whole 30-second stimulus period (**fig. 3F**). This observation contrasts with previous studies which showed that population of worms exhibits reversal state as long the [O_2] level is rising (Busch et al., 2012; Rogers et al., 2006). The observed discrepancy could potentially be attributed to the methods used in other studies, which often analyze continuous reversal periods across a population of worms. This approach could obscure the bimodal distribution of reversal onsets. However, in our study, the analysis of discrete time points of reversal onsets allowed us to uncover finer details of the response timing.

Further, more detailed observations revealed that bimodal response ("Early and Later" cluster) constituted the majority of stimulus trials however there were also trials characterized by only "Early" and only "Late" response types (**fig. 2A,B**). Importantly we found that different types of trials did not come from different individual worms but rather each individual worm demonstrated mixed types of reactions across trials (**fig. 2C**). In this project, our foremost interest was in the initial stage of the response to the stimulus, which we used as a representation for the sensorimotor transformation

triggered by the onset of the oxygen stimulus. Consequently, we classified "Early" and "Early and Late" response clusters together to create a "Hit" response cluster in contrast to the "Late" response cluster, where the initial response component was absent. Notably, we observed a relatively high probability of a "Hit" across stimulus trials for each individual worm, suggesting a consistent early reversal response across all subjects. Moreover, comparing our experimental data to the binomial distribution model (**fig. 2D**) suggested that each trial could be independent, and the variability between individuals regarding the probability of "Hit" trials should not be influenced by unique worm characteristics or the potential long-lasting behavioral state of the worm. This was a significant finding because it let us presume a uniformity across the worm population concerning the studied sensorimotor transformation brain mechanism. This was especially relevant for the subsequent analysis of the neuronal imaging data.

In summary, we created an oxygen stimulus paradigm that replicated conditions relevant to the natural behavior of *C. elegans*, triggering a specific avoidance response. This facilitated the progression to imaging experiments, enabling us to examine the neural foundations of sensorimotor transformation.

4.3 Multiple classes of sensory neurons encode oxygen stimulus

4.3.1 Different classes of sensory neurons are involved in the oxygen perception

Our primary objective was to investigate whether *C. elegans* is capable of perceiving an oxygen stimulus under the conditions present during a whole-brain imaging assay. Additionally, we aimed to understand how this stimulation is interpreted at the level of sensory neurons. Prior research had established that *C. elegans* possesses multiple classes of oxygen sensory neurons detecting increases in oxygen concentration (Busch et al., 2012; Cheung et al., 2005; Gray et al., 2004; Oda et al., 2017; Persson et al., 2009; Rogers et al., 2006; Zimmer et al., 2009). In line with these previous findings, our study confirmed the presence of several classes of sensory neurons that respond to an increase in ambient [O_2] (**fig. 5B**).

Specifically, we observed a pair of URX and IL2 neurons and a single AQR neuron in the head ganglia, as well as PQR neuron in the tail ganglia, that exhibited responses to the increase in [O_2]. These findings align with previous studies and further support the notion that distinct classes of oxygen sensory neurons are responsible for detecting changes in environmental [O_2]. By identifying and characterizing these specific neuronal classes, we contribute to the understanding of how *C. elegans* perceives and responds to oxygen stimuli.

It should be highlighted that current research made a particularly significant discovery by detecting the response of IL2 neurons. To our knowledge only one prior study from our laboratory had mentioned the IL2 response to oxygen stimulation in brain imaging experiments (Nichols et al., 2017). Therefore,

our findings provide further evidence for the assumption of the functional role of IL2 neurons in oxygen sensing. On the other hand, we were unable to identify SDQ, BDU, and PLN neurons, which have been previously implicated in enhanced oxygen perception and associated behavioral response (Chang et al. 2006; Zimmer et al. 2009; Gray et al. 2004). It is probable that these neurons did not exhibit any activity in response to the stimulus pattern utilized in our experiments. Further, while we did successfully identify ALN neurons based on their distinctive topographical position, they did not demonstrate any stimulus-related activity (**fig. S1**).

Overall, the findings of our current study, in conjunction with previous research, highlight the utilization of multiple classes of sensory neurons by *C. elegans* for detecting an increase in ambient [O_2]. This suggests that ambient [O_2] serves as a crucial and ethologically significant stimulus for the worms. Furthermore, these findings align with the previously described ethological behavior of *C. elegans*, wherein they actively avoid environments with high [O_2] (Busch et al., 2012; Cheung et al., 2005; Persson et al., 2009; Rogers et al., 2006).

4.3.2 Potential role of multiple neuronal classes in sensory processing

One hypothesis explaining the existence of multiple classes of oxygen sensory neurons in *C. elegans* is that each class is specialized in detecting distinct stimulus characteristics, thereby fulfilling specific roles in sensory processing. This fundamental mechanism exists in the brains of all animals and is present across various sensory systems, allowing for consistent processing of information. To name just one prominent example: human's retina contains two types of photoreceptors known as cones and rods where cones serves for the acute and color vision whereas rods are responsible for the peripheral and dim-light vision. Moreover, cone receptors are further into three classes (S, M and L) detecting different light wavelengths which constitutes a color vision (Kandel, 2013). This phenomenon exemplifies the capacity of a sensory system within a particular sensory modality to exhibit sensitivity towards diverse features within the stimulus landscape.

To explore the possibility of this hypothesis we characterized sensory neurons activity in further details. Corroborating the findings of previous studies (Busch et al., 2012; Nichols et al., 2017; Persson et al., 2009; Zimmer et al., 2009) our observation showed that URX, IL2, AQR and PQR sensory neurons have a bi-phasic response profile with an initial rapid rise in activity followed by a period of sustained activity (**fig. 5B**). These two components approximately correspond to the phasic and tonic components previously described in the literature (Busch et al., 2012). Notably, the initial activation component was distinctly sharper in URX and IL2 neurons, peaking around 7 seconds after the stimulus, while AQR and PQR neurons displayed a more gradual rise in activity, reaching a plateau near the end of the 21%

[O_2] exposure period (**fig. 5B**). Even though earlier studies did not explicitly remark on these distinct traits, our results are congruent with the data previously reported in the literature.
Interestingly, when examining the profile of the oxygen stimulus, we found that the phasic response component of the URX and IL2 neurons mirrored the first derivative of the stimulus (compare **fig. 3E** and **fig. 5B**). Conversely, the response pattern of the AQR and PQR neurons was reflective of the actual oxygen stimulus profile (compare **fig. 3D** and **fig. 5B**), demonstrating a distinct difference in the response characteristics of these neuron classes. This finding suggests that the URX and IL2 neurons, as opposed to the AQR and PQR neurons, are attuned to different stimulus features. Specifically, we assume that there might be a division of functions between these sets of neurons in terms of differentiation versus integration of the stimulus in temporal domain. This functional division might equip the worm with the capacity to recognize the beginning and end of rapid oxygen shifts, while simultaneously allowing it to monitor the duration of the stimulus exposure. Importantly, these results support the theory that the multiple classes of oxygen sensory neurons in *C. elegans* may each serve a unique functional role in sensory perception.

Further, when comparing the results of behavioral experiments with neuronal activity imaging, we observed that the timing of the first reversal onset's frequency peak corresponds with the peak in phasic activity of the URX and IL2 oxygen sensory neurons (compare **fig. 1C** and **fig. 5B**). Subsequently, the secondary upregulation of reversal behavior aligns with the tonic activity of the oxygen sensory neurons. This temporal relationship suggests that the early phase of the behavioral response may be driven by the phasic activity component of URX and IL2 neurons, while the later phase could be modulated by the tonic activity component of oxygen sensory neurons, including AQR and PQR neurons. A similar concept was introduced by researchers, who proposed that the phasic component of the URX response drives a reversal response immediately following a rapid [O_2] switch (Busch et al., 2012). However, these findings should be interpreted with care, as slight discrepancies in [O_2] dynamics were observed between the behavioral chamber and the imaging chip devices (**fig. 3F**). Consequently, we cannot definitively conclude that the oxygen sensory response observed in the behavioral experimental conditions was identical to that observed in the imaging experiments. Therefore, further studies involved oxygen sensory neurons imaging in freely moving worms would be necessary to establish a direct correlation between the tonic and phasic components of the sensory response and the early and late components of the behavioral reversal response. Further, selective ablation or optogenetic inhibition with a focus on individual sensory neurons, can aid in distinguishing the impacts of input from various sensory neurons (URX, IL2 vs AQR, PQR). By conducting such experiments, we could gain a clearer understanding of how these various factors interact and contribute to the observed behavioral response.

Further, is important to emphasize that several oxygen sensory neurons, such as URX, IL2, and AQR, are located in the head ganglion of the worm and extend their processes to the tip of the nose. In contrast, a single PQR neuron is situated in the tail ganglion and projects to the tail. Notably, due to the slow diffusion of O_2 in water, even a separation of 1 mm between the sensory endings of URX in the head and PQR in the tail of an adult organism can generate sharp gradients (Rogers et al., 2006). Taking these factors into account, it is reasonable to propose that the head and the tail oxygen sensory neurons may function in detecting an increase in ambient [O_2] in front of and behind the animal, respectively. Consequently, these neurons could play a role in driving the animal's behavior in response to the elevated [O_2] in their respective regions. Moreover, this hypothesis goes along with the findings that optogenetic activation of the URX neuron as well as an air puff directed to the nose of the animal elicits reversal locomotion; whereas optogenetic activation of the PQR neuron as well as an air puff directed to the tail of the animal elicits acceleration of the forward locomotion without reversals (Busch et al., 2012).

The second hypothesis is that the presence of multiple classes of sensory neurons within a given sensory modality contributes to the resilience and robustness of the system in instances of developmental defects. This is also a common brain mechanism which is closely interrelated with the mechanism described in the first hypothesis. Returning to the example of mammalian vision, when one of the cone types is defective, it results in impaired color vision, leading to color blindness. However, other aspects of vision remain unaffected due to the normal functioning of the remaining classes of cones (Gordon, 1998). In the context of the oxygen sensory system in *C. elegans*, it has been observed that disabling the synaptic transmission exclusively from the URX neuron does not have an impact on the reversal response. This finding highlights the redundancy of the URX neuron, despite its crucial role in driving the response (Busch et al., 2012). Controversial results were provided by another study where it was shown that URX is redundant for the [O_2] decrease evoked reversal but is necessary for the [O_2] increase evoked reversal (Zimmer et al., 2009). However, this discrepancy can be attributed to variations in experimental paradigms, encompassing factors such as the genetic background of the worms and diverse experimental conditions. Specifically, Busch et al. (2012) employed the *npr-1* strain of worms in the presence of food, whereas Zimmer et al. (2009) utilized N2 worms in the absence of food.

4.3.3 Constraints and future outlooks in exploring the functional role of various oxygen sensory neuron classes in *C. elegans*

In the light of these findings, it is crucial to acknowledge limitations in our experimental approach, which relate to the used imaging chip device. In our experiments, the [O_2] changed uniformly along the length of the worm's body. Consequently, the presented step increase in [O_2] simultaneously activated oxygen sensory neurons in both the head and the tail of the worm simultaneously. Similar considerations should be taken into account when interpreting the results of the behavioral assays, as the oxygen

stimulus applied in those experiments tends to be homogeneous across the surface. This could be potentially confusing type of stimulus for the animal's nervous system and is unlikely to occur in its natural environment where *C. elegans* encounters more heterogeneous oxygen conditions, with variations in [O_2] across different regions. Therefore, future research should focus on developing an imaging chip device that allows for independent control of [O_2] in the head and tail regions of the worm. This would enable the presentation of rising oxygen stimuli separately to the head and tail, mimicking natural conditions where the worm encounters regions of high [O_2] that repel either the head or tail first. Such conditions would likely elicit opposite avoidance reactions, including reversed locomotion and accelerated forward locomotion, respectively.

Overall, according to our results multiple oxygen sensory neurons are involved in the detection of the rising ambient [O_2] including URX, IL2 AQR in the head of the worm and PQR neuron in the tail. Such a variety of oxygen sensory neuron classes evidence for the idea that [O_2] must be an ethologically important stimulus for *C. elegans*. Diversity of the oxygen sensory neuron classes might serve for detecting different features within the stimulus landscape and thus be implicated in executing different behavioral reactions. Thus, future research should aim to reveal more about the role of different classes of the oxygen sensory neurons in the sensorimotor processing.

An essential experiment within the scope of my project would involve implementing laser ablation techniques to disable URX, IL2, AQR, and PQR neurons. This experiment would provide valuable insights into the distribution of functions among these neurons and shed light on their respective roles in mediating the organism's response to oxygen stimuli. By systematically disabling different combinations of neurons, we can discern their individual and collective contributions to the observed behavioral changes. This approach would help unravel the intricate network of interactions between these sensory neurons and provide a more detailed understanding of their involvement in generating specific sensorimotor responses.

4.4 Reversal motor response in the whole-brain imaging experiments

4.4.1 Premotor interneuron AVA entrains the oxygen stimulus in the whole-brain imaging experiments

Next, we planned to describe the motor response triggered by the oxygen stimulus, utilizing the whole-brain imaging assay. Similarly, to the analysis of behavioral data, our focus was on the onsets of reversal locomotion states, as they were hypothesized to represent the reaction to increased [O_2]. We recognized that animals being paralyzed and immobilized in the chip device might not display the same response as was previously identified under behavioral experimental cconditions. Due to the immobilization of animals within the chip device channel and paralysis achieved via the histamine paralysis technology,

we were unable to obtain direct motor behavior readouts, unlike in the behavioral experiments. To circumvent this constraint, we turned our attention to the activity of premotor interneurons. A set of interneurons, encompassing the AVA, AVE, and AVD interneurons, has been previously identified as playing significant role in orchestrating reversal locomotion (Chalfie et al., 1985; Zheng et al., 1999). Specifically, in numerous previous studies the AVA interneuron has been noted to be particularly pivotal for reversal locomotion. There is a reliable correlation between the AVA activity rises and periods of reversal locomotion, as demonstrated in recordings from freely moving animals (Kato et al. 2015; Laurent et al. 2015; Gordus et al. 2015; Larsch et al. 2013; Kawano et al. 2011; Ben Arous et al. 2010; Chronis, Zimmer, and Bargmann 2007). Furthermore, a substantial body of evidence from both ablation (Chalfie et al., 1985; Gray et al., 2005; Piggott et al., 2011) and optogenetic activation studies (Schmitt et al. 2012; Gordus et al. 2015) underscore its indispensable and causative role in reversal locomotion. Therefore, in imaging experiments, AVA neuron can provide an apt representation of the reversal locomotion state.

While scrutinizing the time series of AVA neuronal activity, we echoed our methodology from the behavioral data analysis by focusing on the initiation of reversal locomotion states, which were hypothesized to indicate the reaction to enhanced [O_2] levels. To achieve that we employed a semi-automatic approach to annotate traces of neuronal activity, identifying the "rise," "high," "fall," and "low" phases in a manner akin to previous methodologies (Kato et al., 2015). The "rise" and "fall" phases were defined as the time points at which their time derivatives exceeded a small positive threshold or dipped below a negative threshold, respectively. The periods between the corresponding "rise" and "fall" phases were designated as the "high" and "fall" phases. Finally, the time points of “rise” onsets were identified, and these time series were subsequently used for further analysis (see **Methods** for more details). Further, we used quantification of the cumulative probability of the “rise” onsets over stimulus trials as this measure provided us with the overall response probability robust to variable on the individual trial basis timing. This analysis procedure was the same for the sensory neurons and AVA neuron.

A critical discovery arising from this analysis is that AVA activity entrains the 21% [O_2] stimulus between 4 to 10 seconds from the onset of the stimulus. This phenomenon was initially uncovered through a comparative investigation of AVA activity dynamics in response to both the [O_2] upshift and downshift conditions (**fig. 7C,G**). A crucial aspect of my project involved validating the entrainment of the oxygen stimulus through the utilization of control datasets featuring a constant [O_2] level throughout the recording. As the internal control derived from the periodic stimulus, the AVA activity could have potentially been affected in two ways: firstly, it might have been influenced by the historical context and previous [O_2] shifts, and secondly, it could have been influenced by the [O_2] downshift stimulus, which served as the control condition. Hence, it was essential to discern the influence of the [O_2] upshift

on AVA activity dynamics in contrast to the spontaneous activity dynamics observed under the conditions of a constant [O_2] level. Importantly, we showed that each of the three oxygen stimulus paradigms influenced the AVA activity dynamics distinctly (**fig. 8B,C**). Nevertheless, the magnitude of these changes was modest. This made it possible to use the AVA activity traces from recordings with stable 11% and 21% [O_2] stimulus as a control for stimulus entrainment in the periodic [O_2] stimulus tests. Crucially, when comparing the AVA activity in the periodic stimulus paradigm to controls, we verified the enhancing effect of the periodic shift from 11% to 21% [O_2] on the frequency of AVA rises within the 10 seconds upon the stimulus onset (**fig. 8E**). Overall, these findings prove that worms respond to the [O_2] upshifts with a fictive reversal locomotion response in the whole-brain imaging assay, reproducing our previous observations from behavioral experiments. Notably, these results align with previous observation from our laboratory, wherein it was demonstrated that the identical oxygen stimulation during imaging experiments enhances the likelihood of the global neural state associated with reversal motor behavior (Kato et al. 2015).

4.4.2 Characterization of the reversal response for the individual animals reveals inter-individual variability

In our subsequent analysis, we sought to determine the responsiveness of the worms at the individual level within the imaging experimental assay. Our findings demonstrated a median "Hit" probability of approximately 0.4. Notably, this is less than the corresponding metric observed in behavioral experiments, which displayed a "Hit" probability of roughly 0.72. This suggests a diminished response likelihood in the imaging experiments when compared with behavioral experiments (compare **fig. 7E** and **fig. 2D**). Following the behavioral findings, we also examined if individual worm traits influenced the variability in “Hit” trial probability. Using a theoretical binomial model based on our experimental mean, we compared it with the observed "Hit" probabilities. Worms with “Hit” probabilities between ~0.2 and ~0.5 matched the binomial model, implying no influence from unique traits. However, outliers (values at 0 and 0.8-0.9) suggested idiosyncratic responses. This contrasts with behavioral data, where all responses fit the binomial model, underscoring potential differences in worm reactions between freely moving and constrained imaging conditions (compare **fig. 7E** and **fig. 2D**).

In this context, it is important to mention that for subsequent pan-neuronal analysis, we chose five datasets based on their recording quality. This selection ensured that we could identify the maximum number of individual neurons and extract their activity time series efficiently. Importantly, this selected subpopulation of animals (**fig. 7D**, bars highlighted in orange versus all bars) included individuals representing all ranges of the responsiveness spectrum described above and was comparable by means of the AVA response entrainment (**fig. 7F**). Thus, we assumed that the datasets subset selected for the pan-neuronal analysis could be used as a representative for the general population. However, in future

research, it would be prudent to select individuals whose response rate falls within the range predicted by the binomial model. This approach would mitigate the incorporation of worms exhibiting potential unique traits of brain anatomy or physiology, ensuring a more uniform data set used for the pan-neuronal analysis.

4.4.3 Discrepancy between behavioral and imaging reversal response might be explained by the difference in the stimulus profile and restrained animal's conditions

Importantly, in the imaging experiments, AVA entrained to the stimulus only within the 10-second post-stimulus time window (**fig. 8E**). This contrasts with our behavioral experiments results, where we observed a bimodal reversal response pattern: an initial strong reversal response followed by a secondary low-frequency reversal up-modulation starting 10 seconds after stimulus onset and continuing throughout the stimulus trial. Thus, the imaging experiments reveal only the response component corresponding to the first component of the behavioral reaction (compare **fig. 1B - D** with **fig. 7B,C** and **fig. 8E**). Another disparity between the imaging and behavioral results is that the imaging experiment revealed inter-individual variability in the reversal response rate, which contrasts with the results obtained from freely moving animals in behavioral assays (compare **fig. 7E** and **fig. 2D**).

The above-mentioned discrepancies between the reversal response patterns in the behavioral and imaging essays could be explained by a combination of factors that distinguish conditions of behavioral and imaging experiments.

First, the actual oxygen stimulus profile differs between the behavioral chamber and the imaging chip device (**fig. 3F**). In the imaging chip device, the $[O_2]$ increases rapidly over the initial 10 seconds, then stabilizes and maintains a high plateau for the remainder of the 21% $[O_2]$ duration. Thus, in the imaging experiments, the worms transiently react to the rising $[O_2]$ levels following the first derivative of the stimulus profile (**fig. 3E**). In contrast, in the behavioral chamber, the $[O_2]$ gradually increases throughout the entire period (**fig. 3F**). Interestingly, our behavioral results remind results of previous studies, which showed that the worm population exhibited enhanced reversal behavior as long as the $[O_2]$ level was rising and remained elevated (Busch et al., 2012; Rogers et al., 2006).

Also, the higher response probability in the behavioral experiments in this context might mean that steadily increasing $[O_2]$ is more likely to evoke reversal response in comparison to the sharp step increase observed in the imaging chip device. This hypothesis can be validated through subsequent experiments by modulating the rate of change (dC/dT) of the $[O_2]$ stimulus during the imaging sessions. Such experimentation should afford an estimation of the optimal stimulus that evokes the reversal response and provide insights into the processing of stimulus features.

Second, the physical confinement within the canal of the imaging chip device has been recognized to influence AVA activity, leading to extended states of high plateaus, which could in turn modify the response to the oxygen stimulus (Kato et al. 2015). This environment may have ethological significance, mirroring scenarios where *C. elegans* becomes ensnared within the constraining rings of the predatory fungi, *Drechslerella doedycoides* – a natural predator of *C. elegans* (Maguire et al., 2011). Our hypothesis posits that such a state could signify the worm's continuous efforts to initiate reversal locomotion in the absence of proprioceptive feedback confirming successful movement. This specific scenario could consequently alter the worm's sensitivity to the oxygen stimulus.

In conclusion, in this study we succeeded to establish a whole-brain imaging experimental paradigm where *C. elegans* worms reacted to the presentation of the elevated oxygen stimulus with a fictive reversal locomotion detected by the means of the AVA activity. Although, the observed response characteristics diverged somewhat from those previously established in the behavioral essay, this innovative approach provided us with a possibility to investigate the neural mechanisms underpinning sensorimotor transformations in *C. elegans* using the acquired whole-brain Ca^{2+} imaging datasets.

4.5 The comparison of sensory and motor responses reveals the phenomenon of response variability

A pivotal finding in my research concerns the observed difference in the over-trial response probability between the oxygen sensory neuron, which reflects sensory processing, and the AVA neuron, indicative of the motor command output in the sensorimotor transformation pathway. Crucially, every identified oxygen sensory neuron demonstrated a robust response to the 21% [O_2] stimulus throughout the stimulation trials (**fig. 6B**). The URX neuron, in particular, exhibited the most consistent response characteristics compared to other oxygen sensory neurons. Its response probability approached an approximate value of 1 within a timeframe of $\sim$ 5 seconds after stimulus initiation. This suggests that, under the experimental conditions utilized for imaging, worms can consistently detect the oxygen stimulus. Repeated stimulus presentations further highlight an almost deterministic reaction of the URX neuron to the oxygen stimulus, with only minor variations in the timing of response initiation (**fig. 6A - C**). Conversely, the motor response, as inferred from the AVA neuron activity, achieved only a probability of approximately 0.6 within the predefined 10-second timeframe (**figs. 7F, 9A**), which was identified as the period when the AVA response is entrained by the oxygen stimulus (**fig. 8E**). This suggests that, despite the near-deterministic sensory encoding, the motor output exhibited significant variability across trials. This underscores the inherent probabilistic aspect of the sensorimotor transformation process.

This observed divergence between the consistent sensory response and the probabilistic motor response (**fig. 9A**) aligns with the prevailing perspective in the field that the nervous system does not simply operate as a linear input-output apparatus. This underscores the significance of endogenous activity in contributing to response variability. It is widely recognized that variability in an organism's response to repeated presentations of a specific stimulus can be detected, even under stringent laboratory conditions. This variability manifests across various scales, ranging from individual synapses to comprehensive behavioral patterns of the entire organism (Maye et al. 2007; Bell 2014).

This phenomenon can be interpreted from two perspectives: one posits that it arises as a byproduct of the intrinsic chaotic nature of neural network behavior (Sabarathinam et al., 2013), resulting in response inaccuracies. Conversely, the alternative hypothesis proposes that this variability fulfills an ethological role, serving as an adaptive trait that enhances an animal's ability to cope with environmental conditions by introducing innovative elements into its behavioral strategies (Brembs, 2011b). Numerous examples across various species demonstrate how behavioral variability facilitates the ethological function of the animal in such instances as escape behavior (Domenici et al., 2008; Domenici & Blake, 1993; Driver & Humphries, 1988; Eaton et al., 1981), exploration behavior (Brembs, 2011b; Charnov, 1976; Humphries et al., 2010) and learning (Chaisanguanthum et al., 2014; Ölveczky et al., 2005; Tumer & Brainard, 2007). Further, besides the question of the functional role of the response variability the question of the neuronal sources of this variability is of a great interest in neuroscience as it represents one of the basic properties of the brain physiology and thus can shed a light on the basic principles of brain functioning. Several hypotheses have been advanced regarding the neuronal origins of response variability within the nervous system. These theories posit that such variability can emerge at different levels. At the sensory system level, for instance, stochastic noise might enhance the detection of low-amplitude signals, albeit at the expense of accuracy. Additionally, this variability can be introduced during synaptic transmission or at subsequent neuronal stages within the sensorimotor processing pathway (Barlow, 1972; Barlow et al., 1971; Benzi et al., 1981; Bialek, 2003; Lillywhite & Laughlin, 1979; Longtin et al., 1991)

Importantly, there is abundant evidence suggesting that the current internal state of a biological system at the time of stimulus presentation can decisively influence the system's response (Barlow, 1972; Barlow et al., 1971; Benzi et al., 1981; Bialek, 2003; Lillywhite & Laughlin, 1979; Longtin et al., 1991). This phenomenon has been documented across diverse species, including examples such as flies, where the spontaneous activity of the ellipsoid body underlies the variability in walking behavior (Martin, Faure, and Ernst 2001; Sorribes et al. 2011), and humans, where fluctuations in the activity of the default network (Martin, Faure, and Ernst 2001; Sorribes et al. 2011) are predictive of response variability.

With its relatively simple nervous system and defined connectome, *C. elegans* can serve as an exemplary model organism for exploring the neuronal underpinnings of this phenomena at the scale of single neurons. A notable example is the study by Gordus et al. (2015), which shares significant parallels with our current work (Gordus et al. 2015). This study established that *C. elegans* demonstrates a significant level of variability in motor responses to attractive odors, despite the reliable detection by the AWC sensory neuron. Importantly, through an examination of the preselected subcircuit engaged in odor perception, which comprises three interneurons (AIB, RIM, and AVA) chosen based on existing connectome knowledge, scientists succeeded in identifying the origin of this response variability. They traced it back to a specific RIM interneuron, thus highlighting the critical role of these neuron in the observed variability. The authors hypothesized that the presence of this variability in response could prevent the reversal circuit from becoming overly deterministic, which could potentially be maladaptive. This hypothesis aligns with previously discussed perspectives on the ethological implications of response variability.

Therefore, our research goal was to elucidate the neuronal underpinnings of the observed response variability within the oxygen sensation sensorimotor circuit. Importantly, our investigation was not confined to a subset of preselected neurons. Instead, we had an advantage to have access to comprehensive whole-brain imaging datasets, which provided us the opportunity to devise an unbiased methodology for identifying the sources of response variability.

4.6 AVA intrinsic state history as a factor affecting the response variability

Another pivotal concept, along with its associated analytical method aligned with the notion of response dependency on the brain's internal state, was articulated in the manuscript emerging from our laboratory (Kaplan et al., 2018). The hypothesis posited that the intrinsic state of premotor interneurons, which are tasked with generating motor command responses like AVA neuron, may influence the reaction to a given stimulus. This was exemplified in the study's exploration of sensorimotor transformation in response to an attractive odorant stimulus, where organisms are anticipated to display a reversal response upon the removal of the odorant. Specifically, findings indicated that when AVA neuron is in a "high" activity state during the stimulus presentation, it fails to generate a response. This could be attributed to AVA's bi-stability: if the neuron is already in a high activity state, it cannot further increase its activity. Conversely, a low, inactive state predisposes AVA neuron for response generation. Consistent with this notion, the paper also introduced an analytical technique that stratifies trials based on the AVA's intrinsic state at the time of stimulus presentation. By clustering trials in this manner, it allows for a more homogeneous grouping of neuronal data within each cluster. This stratified analysis can yield a more nuanced understanding of the brain's information processing principles. For example,

for the purpose of further analysis in these studies, only the trials wherein the AVA was in its inactive state during stimulus presentation were considered.

Importantly, the above-mentioned study by Gordus et al. (2015) also made similar observations in the context of their experiments (Gordus et al. 2015). While they employed a comparable analytical approach, their research primarily centered on the suppression of reversal interneuron activity. Consequently, they selected trials wherein these neurons exhibited a "high" activity state during stimulus presentation. This was imperative for them to observe any off-reactions, given that neurons in the "low" activity state cannot undergo further suppression.

In the present study, we not only replicated but also expanded upon this method by examining the impact of activity history preceding the stimulus. Our findings underscored that the intrinsic activity state of the AVA at the time of stimulus presentation plays a crucial role in the system responsiveness (**fig. 9B** left panel). Notably, we also observed that the activity history preceding the stimulus influences the system responsiveness to the introduced oxygen stimulus. Specifically, the the inactive "low" state duration was found to be positively correlated with the likelihood of response to the presented oxygen stimulus.

Further results from this analysis when applied to control datasets with stable [O_2], indicate that spontaneous reversal commands are generated stochastically, without a discernible dependence on past history (**fig. 9B** middle and right panels). This aligns with numerous experimental and theoretical studies emphasizing the significance of stochastic processes in the brain (Braun, 2021; Deco et al., 2009; Rolls & Deco, 2010). In particular, firing sequences of neurons in mammalian brain can be characterized by Poisson distributions which means that despite a neuron exhibiting a consistent firing rate, the precise moments of its spikes appear to be random and independent (Jackson, 2004) This inherent randomness introduced in the neuronal network might enhance the efficiency of the decision-making mechanisms (Churchland et al., 2008). On the other hand, this observation provides a control for the results from the periodic stimulus datasets making it evident that prestimulus history of the AVA intrinsic activity influence only the responsiveness to the stimulus but does not increase the likelihood of spontaneous AVA activation.

It is crucial to emphasize that all premotor interneurons are categorized into either a forward or reversal command state ensemble (Chalfie et al., 1985; Varshney et al., 2011; White et al., 1986). Furthermore, as previously discussed, the global brain state continually transitions through states corresponding to various motor commands (Kato et al. 2015). AVA specifically represents the pool of reversal premotor interneurons (Chalfie et al., 1985; Zheng et al., 1999), and its activity is known to closely correlate with the reversal behavior in the freely moving worms (Kato et al. 2015; Laurent et al. 2015; Gordus et al.

2015; Larsch et al. 2013; Kawano et al. 2011; Ben Arous et al. 2010; Chronis, Zimmer, and Bargmann 2007). Therefore, it is essential to consider an alternative framework to understand the above described findings. Specifically, if we view AVA activity as just one means of reading the instantaneous brain-wide motor command state, then it is plausible to propose that it is the global brain state and its prior history that could determine the system's responsiveness. Therefore, future research efforts should aim to untangle the contributions of individual interneurons versus their collective dynamics in shaping responses to sensory stimuli.

In conclusion, although the motor command state plays a role in the observed response variability, it explains only part of it (**fig. 9B**, left panel). This indicates the presence of other factors influencing this variability. Therefore, we extended our study by conducting a pan-neuronal analysis to identify these additional sources, with the aim of providing a more comprehensive understanding of neural response dynamics.

4.7 A "Hit-Miss; Evoked-Spontaneous"-triggered average analysis pipeline allows for a thorough exploration of the whole-brain imaging datasets

In our further analysis of the pan-neuronal datasets, we aimed to achieve two primary objectives. Firstly, our interest lay in identifying neurons potentially integral to the decision-making process. We aimed to elucidate the underlying neuronal activity patterns linked to this mechanism and assess their potential influence on the inherent response variability observed in our established sensorimotor paradigm. Secondly, we sought to distinguish between neurons whose activities primarily reflect sensory-related information and those associated with motor-related information. This differentiation is pivotal in understanding each neuron's functional role within the designated sensorimotor circuit.

To realize these objectives, we developed an automated analysis pipeline designed for the outlined purposes. Our approach capitalized on a key experimental design attributes and properties of the oxygen sensorimotor transformation chain previously discovered in this project. Firstly, the open-loop experimental design ensured that outcomes did not influence the presented stimulus. Secondly, the observed intrinsic response variability together with presence of the spontaneous AVA activity (**fig. 6**), were an advantage to our analysis. Collectively, these characteristics ensured that the motor response was not entirely synchronized with the stimulus, which aided in differentiating sensory from motor-related neuronal information.

To develop this analysis approach, a critical step involved differentiating between the trials where the animal exhibited successful sensorimotor transformation against those where no response was evident which we called "Hit" and "Miss" trials respectively (**fig. 10A**). Similar conceptual approach is widely

used in neuroscience among different species and different recording techniques to reveal decision making mechanism correlates (Crochet et al., 2019; Fotowat et al., 2011; Goodale et al., 2021). Our primary criterion for this categorization revolved around the observation that the AVA was entrained by the stimulus within a 10 seconds timeframe post stimulus onset (**fig. 8E**). Hence, trials where AVA activation occurring within this time window were assumed to be significantly influenced by the stimulus, in contrast to activations post this threshold, which bore similarities to the spontaneous activation rate derived from control datasets. Consequently, we labeled trials exhibiting AVA activation within this 10-second period as “Hit” trials, while others were categorized as “Miss” trials. It is important to note that some AVA activations occurring beyond this threshold might still be stimulus-driven, possibly reflecting the late response component observed in our behavioral experiments (**fig. 1**). However, due to our inability to statistically validate this late response, our investigation primarily centered on the early component, representative of rapid sensorimotor transformation. This part of the analysis has been completed by applying event-triggered average separately for the “Hit” and “Miss” trials and developing a further stimulus-triggered average analysis which automatically reveals statistically significant differences in the neuronal response at these two clusters (**fig. S3**, **Table S1**).

A further extension of our analytical approach aimed to elucidate the functional role of neurons within the designated sensorimotor pathway, tracing from sensory reception to motor execution. This analytical step was accomplished by employing triggered average analysis, utilizing stimulus time points and motor response time points as key reference events used in further triggered average analysis (**fig. 10A**). Additionally to aforementioned separation of stimulus-triggered trials into “Hit” and “Miss” categories, motor response events were divided into "Evoked" and "Spontaneous" categories, contingent on their occurrence within the aforementioned critical 10-second window (see **Methods**). This methodology was predicated on the notion that it would enable the determination of whether a neuron predominantly conveys sensory-related, motor-related, or a hybrid of both types of information. A comparable methodology has been successfully applied in zebrafish whole-brain imaging studies. Researchers in this field employed regressors based on both stimulus and behavioral parameters to unravel the functional organization of neuronal circuits (Ahrens et al., 2012; Feierstein et al., 2015; Portugues et al., 2014). This approach allowed them to create detailed functional brain maps, clearly distinguishing regions linked to sensory input from those associated with specific behavioral responses.

In summary, we created an automated “Hit-Miss; Evoked-Spontaneous”-triggered average analysis pipeline, facilitating a thorough investigation of pan-neuronal datasets to unveil the neuronal foundations of sensorimotor transformation and the distinctive signatures of decision-making mechanisms. All the subsequent results in this project (**figs. 11 - 24**, **S3, S4, Tables S1,2**) were derived from this analysis algorithm. Crucially, the analytical algorithm formulated in this study exhibits significant versatility. It is structured in a manner that permits ready adaptability for subsequent

investigations involving varied stimulus paradigms, as well as diverse analytical techniques beyond just event-triggered averages. As a testament to its adaptability, within the current project, we have already leveraged this framework to evaluate the onset timing of neuronal activity, contextualized within the "Hit" versus "Miss" trial distinctions (**figs. 13, 17D, 22E, 23B, 24**).

4.8 Overview of the results of the “Hit-Miss; Evoked-Spontaneous”-triggered average analysis

4.8.1 The activity profiles of sensory neurons and primary interneurons are predominantly associated with the stimulus

Firstly, we focused on the oxygen sensory neurons and primary interneurons. The "Hit-Miss; Evoked-Spontaneous"-triggered average analysis revealed that the oxygen sensory neurons exhibited activity primarily related to the stimulus and not to the motor state (compare **fig. 11** and **fig. 12**). Emphasizing the nontrivial aspect of this finding is important, given the substantial body of research across a variety of animal species that underscores substantial modulation of neuronal activity in the primary sensory regions of the brain caused by motor activity (Aimon et al., 2019; Chiappe et al., 2010; Fujiwara et al., 2017; Musall et al., 2019; Niell & Stryker, 2010; Salkoff et al., 2020; Steinmetz et al., 2019; Stringer et al., 2019).

Remarkably, all identified primary interneurons, comprising AUA, PVP, and RMG neurons, also exhibited a sensory-related activity pattern primary associated with a stimulus (compare **fig. 15** and **fig. 16**). Moreover, average activation profiles of primary interneurons resembled those of the sensory neurons. In particular, AUA and RMG neurons exhibited relatively steep activation slopes, similar to those observed in URX and IL2 neurons. Conversely, PVP neurons have a gradual linear activation slope, much like the AQR and PQR sensory neurons (compare **fig. 5B** and **fig. 14**). This correspondence aligns with the connectome pattern, where AUA and RMG neurons receive inputs from URX sensory neurons through both chemical synapses and gap junctions, while PVP neurons form gap junctions with AQR and PQR sensory neurons (Macosko et al., 2009; White et al., 1986).

The results are particularly intriguing given the expectation that primary interneurons would display activity patterns associated with higher-order computations during stimulus processing. One possible explanation might be that the stimulus used in this study did not fully engage the circuit’s functional repertoire. Therefore, further experiments employing a more elaborated stimulus landscape, such as varying [O_2] gradients and non-periodic stimulus timing, are essential to comprehensively explore the roles played by these primary interneurons.

An alternate explanation might involve limitations of nuclear Ca^{2+} imaging, which may not fully capture neuronal activity, particularly when it is confined to neurites and involves localized subcellular processes. This type of compartmentalized activity has been observed in specific *C. elegans* neurons, where signaling occurs within neurite segments independently of the soma, enabling nonlinear integration and postsynaptic transmission without altering somatic activity (Clark et al. 2006; Chalasani et al. 2007; Hendricks 2012; Li et al. 2014; Ruach et al. 2023).

4.8.2 Sensory neurons and primary interneurons activity suppression suggests several alternative neuronal mechanisms

However, it is crucial to note that we observed a motor-related suppression of the baseline activity at "Spontaneous" AVA-triggered trials which was consistent across sensory and primary interneurons (**figs. 12**, **16**). Interestingly, the precise pattern and time course of this suppression varied across neuronal classes. Nevertheless, we propose three alternative hypotheses which might provide generalized explanation for this phenomenon.

First, this activity suppression might reflect a potential feedback mechanism such as corollary discharge (Cullen 2004; Poulet and Hedwig 2007; Fukutomi and Carlson 2020; Busse et al. 2017; Crapse and Sommer 2008; Busse 2020) which precludes potential sensory and related interneuron activity at the time of the reversal locomotion. In the current research activity patterns of Il2L, PQR, PVP and RMGL neurons align with this hypothesis as their suppression initiated simultaneously with the onset of the reversal motor command (**figs. 12**, **16**).

The second hypothesis proposes that we observe a spontaneous down-modulation in the activity of oxygen sensory neurons reflected in the primary interneurons, which could potentially facilitate the initiation of AVA activation. This hypothesis is consistent with the activity patterns observed in sensory neurons URXR, IL2R, AQR and interneurons RMGR, AUAL, where a reduction in activity was noted just before the initiation of the reversal motor command. Notably, for URXR, IL2R, and RMGR neurons, this reduction reached its lowest point precisely at the moment coinciding with the onset of the reversal motor command.

Our third hypothesis combines the corollary discharge mechanism with the observation that sensory neurons URXR, IL2R, AQR and interneurons RMGR, AUAL are getting suppressed before the AVA reversal commands initiation. This hypothesis proposes the existence of an alternative neuronal source that initiates the decision to reverse locomotion prior to activating the reversal command interneurons. This proposition is supported by our finding that reversal interneurons share the same activation onset times (compare AVA and AVE neurons activity patterns at **figs. S3, S4**), indicating the necessity to

investigate sources outside the pool of reversal interneurons. Such an alternative source may have the potential to activate reversal command interneurons while priorly suppressing sensory and interneurons.

Importantly, we also observed down-modulation of BAG neuron activity during "Spontaneous" trials (**fig. 12**). This is consistent with previous research demonstrating that RIM neurons suppress BAG neuron activity during reversal motor states, inhibiting the perception of self-generated CO_2 traces (Riedl et al., 2022). However, our current results show that RIM activation onset aligns with AVA premotor neuron activation onsets at "Spontaneous" trials (**fig. S4**), and thus cannot initiate the BAG suppression that starts prior to AVA activity onset (**fig. 12**). Therefore, alternative neuronal mechanisms should be investigated further. Given the potential limitations in the temporal resolution of the Ca^{2+} imaging technique, these results should be interpreted with caution and subject to further investigation.

4.8.3 Sensory neurons and primary interneurons activity modulation reflects the sensorimotor transformation

An important goal in conducting this analysis was to uncover a neuronal mechanism underlying the motor responses variability. On the first place we asked if the variability in the response amplitudes of oxygen sensory neurons and primary interneurons (**fig. 5A**) could determine it. Initially, we hypothesized that stronger sensory neuron or interneuron activation might lead to a higher probability of a motor response, which would result in greater average response amplitudes during "Hit" trials compared to "Miss" trials. Contrary to our hypothesis, we discovered that several oxygen sensory neurons, including URXL, Il2, and PQR neurons, exhibited lower activation in “Hit” trials compared to “Miss” trials (**fig. 11**) and the same pattern was observed for the RMGL primary interneuron (**fig. 15**).

We have formulated two alternative explanations to account for this unexpected observation. The first hypothesis revolves around the idea that the amplitude difference between "Hit" and "Miss" trials could play a causal role in motor responses. In this scenario, it is plausible that stronger activation of oxygen sensory neurons and primary interneurons might be suppressive for the motor response. This hypothesis is particularly relevant to the IL2R neuron since its activation started significantly earlier than the onset of AVA activity and peaked simultaneously with the onset of AVA activity (**fig. 12**). Furthermore, this hypothesis echoes a previously formulated idea suggesting that a spontaneous reduction in the activity of oxygen sensory and primary interneurons could potentially facilitate the initiation of AVA activation.

Our second hypothesis pertains to the URXL, IL2L, PQR, and RMGL neurons, which exhibited activity beginning shortly before and peaking after the onset of AVA activity (**figs. 12, 16**). This temporal pattern suggests that the observed amplitude differences between 'Hit' and 'Miss' trials (**figs. 11, 15**) may reflect a feedback mechanism originating from motor-command interneurons or other elements of

the sensorimotor circuit. Furthermore, for IL2L, PQR, and RMGL neurons, this interpretation aligns with the previously proposed suggestion that the down-modulation of sensory and associated interneuron activity during 'Spontaneous' trials reflects a feedback signal such as a corollary discharge.

Further, we found that AUA, PVP, and RMGR neurons showed no significant amplitude difference between 'Hit' and 'Miss' trials (**fig. 15**), contrary to expectations. This is notable because their average activity mirrored that of the sensory neurons (**fig. 14**), which is consistent with the established connectome (White et al., 1986) and previous findings indicating that sensory neurons drive activity in primary interneurons (Busch et al., 2012; Laurent et al., 2015; Nichols et al., 2017; Oda et al., 2017).

One possible explanation relates to the potential limitations of nuclear Ca^{2+} imaging in scenarios involving compartmentalized neurite activity, as previously discussed. Alternatively, these interneurons might perform active computations similar to normalizing or binarizing the sensory input, potentially filtering out some amplitude-related information. Such a mechanism would allow downstream circuits to operate on a simplified, thresholded representation of the sensory landscape, potentially supporting robust behavioral responses despite variability in input strength.

4.8.4 The onset timing analysis highlights the motor response resilience to fine-scale sensory modulations and further supports the suppressive corollary discharge hypothesis

The onset timing analysis of oxygen sensory neurons and RMG neurons (which emerged as the most intriguing candidates among the primary interneurons) received particular attention. Notably, we discovered that the variation in activation onset latencies across different trials did not influence the motor response (**figs. 13A, 17D**). This underscores the system's robustness in effectively managing minor fluctuations in sensory input.

Furthermore, a noteworthy discovery was made regarding the over-trials response variability in all detected oxygen sensory neurons, except for IL2L neuron (**fig. 13B**). This variability was found to have no correlation with the system's responsiveness. This implies that the motor response variability does not depend on the slight variations observed in the oxygen sensory neurons or primary interneurons. Furthermore, this finding reinforces the results obtained from the average amplitude analysis, as it suggests that amplitude differences should not be attributed to the neurons missing more trials in “Hit” or “Miss” trials.

Importantly we observed lower probability of the IL2L and RMGL activations at “Hit” trials compared to “Miss” trials (**figs. 13B, 17C**). Firstly, this indicate that the average response amplitude difference discussed above might be at least partially explained by the neuron being inactive at the “Hit” trials. Secondly, the onset of this suppression as estimated by the cumulative response probability coincided

with the onset of the AVA activation period. This finding comes along and further contribute to the above developed concept that the IL2L and RMGL neurons could potentially receive inhibitory corollary discharge signals from motor command interneurons or other potential elements within the sensorimotor pathway. Importantly, the similarity in activity patterns between RMG and IL2L could potentially be explained by their interconnectedness through gap junctions (White et al., 1986).

Moreover, it is crucial to emphasize that all the “Hit” versus “Miss” trials disparities observed in activity patterns must be solely attributed to the response decision and may not be connected to the history of the intrinsic activity state of AVA neurons, which, in turn, is associated with their responsiveness. This assertion is supported by the control analysis, which demonstrated that the impact of the AVA neurons' prior inactivity, preceding the 21% [O_2] stimulus, on their response was minimal (**fig. 18**).

4.8.5 Neuronal activity prior to the 21% [O_2] stimulus may contribute to the reversal response decision-making mechanism

In the course of this project, we made a remarkable discovery involving the identification of an interneuron pair located in the posterior section of the lateral ganglion. This interneuron displayed a unique activity pattern, characterized by a gradual increase in its activity levels during periods of 11% [O_2] (**fig. 14**). It is noteworthy that no neuron with a similar activity pattern has been documented in the existing literature on *C. elegans*. Interestingly, the location of this interneuron which was in the proximity to RIM neuron posterior to it suggests that it could potentially correspond to the AIZ interneuron. However, it is important to note that the AIZ neuron has not been previously described as having oxygen-related activity, although one study indicates its involvement in the CO_2 - related response (Guillermin et al., 2017). Until further clarification this neuron has been temporarily designated with the putative name "X" neuron.

Notably, the activity of the "X" neurons displayed stronger activation during the 11% [O_2] periods that preceded the "Hit" trials when compared to the "Miss" trials (**fig. 15**). Intriguingly, another noteworthy observation related to the BAG sensory neuron complements this finding. The BAG neuron is recognized for its role in sensing decrease in [O_2] and regulating corresponding behavioral reactions. Interestingly, we observed a pattern of sharper BAG activation during the "Hit" trials as opposed to the "Miss" trials (**fig. 11**). Considering that both the "X" neuron and BAG neuron showed increased activity preceding the "Hit" trials, it leads us to hypothesize that the internal state of the circuit prior to the 21% [O_2] stimulus might play a defining role in the system's response or alternatively response strength to the preceding [O_2] downshift might influence the subsequent response to the [O_2] upshift. However, it is crucial to emphasize that the observed amplitude difference was not statistically significant. Additionally, this trend could potentially reflect the history of the intrinsic activity AVA activity (**fig. 18**).

4.8.6 Head motor neurons might function as a gating mechanism in the sensorimotor transformation chain

Through “Hit-Miss; Evoked-Spontaneous”-triggered average analysis, we made another notable discovery regarding the newly identified head motor neurons (HMN1,2 and 3), located near the SMDD neurons in the ventral ganglion. These neurons displayed periodic activity that partially overlapped with the head bending-related activities of SMDD and SMDV neurons, as well as the forward locomotion-related activity of RIB neurons.

When considering HMN1, 2, 3 neurons alongside with RID neuron, which is known to be involved in the forward locomotion circuit (Chew et al., 2018; Lim et al., 2016; Mori et al., 2019), their activity appears to integrate both sensory and motor information (**figs. 20**, **21**). This suggested their potential role in coordinating motor responses to stimuli and contributing to decision-making mechanisms. Importantly, the down-modulation of HMN and RID neurons started before the onset of AVA activity rise in both "Spontaneous" and "Evoked" trials, with "Evoked" trials corresponding to "Hit" trials from the stimulus-triggered average analysis. This further suggests that the activity of HMN and RID neurons may play a causative role in the response of pre-motor neurons.

Next, HMN1, 2, 3 together with RID neurons exhibited opposite activity patterns during "Hit" versus "Miss" trials. Their activity decreased below the baseline in "Hit" trials and increased above the baseline in "Miss" trials.

Based on this finding, we formulated a hypothesis that HMN and RID neurons may serve as a gating mechanism. In short, we assumed that their activity up-modulation could prevent a reversal motor response, while their activity suppression might enable it. Notably, research on *C. elegans* provides examples where a single neuron can exert opposing effects within the same neural circuit. For instance, the RIM interneuron demonstrates the ability to both enhance and suppress the activity of AVA and AVE reversal interneurons through different synaptic and extrasynaptic mechanisms, depending on the RIM neuron's activity state (Li et al. 2023).

4.9 Forward locomotion signal potentially provides a phasic framework gating the system response

A further noteworthy discovery emerged with a focus on the RIB and AVB interneurons, both described in the literature for their involvement in the forward locomotion circuit (Chalfie et al. 1985; Zheng et al. 1999; Tsalik and Hobert 2003; Gray, Hill, and Bargmann 2005; Li et al. 2014; Kato et al. 2015; Wang et al. 2020). As anticipated, it was observed that both RIB and AVB neurons exhibited a decrease in activity in response to the onset of a 21% [O_2] stimulus (**fig. S1**). This aligns with their established

inverse relationship with the AVA neuron (Faumont et al. 2011; Kato et al. 2015), which showed an increased average activity when exposed to the 21% [O_2] stimulus (**fig. S1**).

Further, two significant and unexpected observations were made via the “Hit-Miss; Evoked Spontaneous”-triggered average analysis. Firstly, it revealed that this down-modulation occurred in both “Hit” and “Miss” trials. Notably, this phenomenon was most pronounced in the RIB neuron (**fig. 22A**). This result is surprising considering the conventional perspective that RIB's involvement in forward locomotion suggests it should only be found in “Hit” trials. It is important to mention that the down-modulation observed in “Miss” trials is transient and exhibits a lower amplitude compared to the prolonged and more pronounced down-modulation seen in “Hit” trials. Secondly, closer examination of the average RIB activity, detected “low-amplitude” baseline activity modulations, and their down-modulations preceded “Hit” trials, while up-modulations preceded “Miss” trials (**fig. 22A**).

Following these findings, we have developed a concept in which the RIB neuron might play a crucial role in providing a reference framework for the oxygen sensorimotor circuit's response during reverse locomotion response to the 21% [O_2] stimulus. This concept is primarily founded on several key facts.

First, RIB is a second-layer interneuron (Gray et al., 2005) which receives a majority of inputs from the AUA interneuron and send major part of outputs to the AVE pre-motor interneuron (White et al., 1986). The AUA interneuron, as documented in the literature (Busch et al., 2012; Laurent et al., 2015; Nichols et al., 2017) and in the current research, is recognized as a component of the oxygen sensorimotor circuit and conveys stimulus-related signal (**figs. 14, 15**). On the other hand, the AVE neuron plays a crucial role in the reversal locomotion circuit (Chalfie et al., 1985; Zheng et al., 1999) and directly synapses onto motor neurons in the ventral cord (Chalfie et al., 1985; Varshney et al., 2011; White et al., 1986). Thus, from a connectome standpoint, the RIB neuron is strategically situated to be able to mediate interactions between oxygen sensory neurons and the reversal motor circuit. Furthermore, the empirical findings derived from the "Hit-Miss, Evoked Spontaneous" analysis showed that the RIB neuron combines sensory and motor-related information within its activity (compare **figs. 22A and 23A, S3 and S4**). These facts suggest the involvement of the RIB neuron in the oxygen sensorimotor transformation circuit.

Second, earlier studies from our laboratory revealed that the onset of reversals is consistently preceded by a deceleration of forward locomotion being proposed as a preparatory event (Kato et al. 2015). Aligning with this, RIB down-modulation is known to precede forward to reverse locomotion transition, reflecting a strong correlation between its activity level and the speed of forward locomotion (Kato et al. 2015; Li et al. 2014). Our current study also demonstrated consistent results with the down-modulation of RIB activity preceding AVA activity rise (**figs. 22C, 23, S4**). Therefore, it is theoretically

plausible that RIB may play a defining role in regulating AVA activity. In particular, we posit that the deceleration preparatory events, as delineated by RIB activity, might offer a gating time window for the system to react with a reversal locomotion command to the oxygen stimulus.

Lastly, our results demonstrated that the down-modulation of RIB activity in response to the 21% [O_2] stimulus had a significantly shorter latency in "Hit" trials compared to "Miss" trials (**fig. 22E**). In contrast, sensory neurons maintained stable activity onset latencies (**fig. 13A**). This caused an alteration in the relative onset timing between RIB and sensory neurons, with the RIB down-modulation preceding sensory neuron responses in "Hit" trials (**fig. 24**). This is a significant discovery, suggesting that RIB activity down-modulation may not solely arise from oxygen sensory neuron inputs but could also provide a framework for it. Coupled with above mentioned observation that the "low-amplitude" down-modulation component precedes "Hit" trials, whereas up-modulation precedes "Miss" trials (**fig. 22A**), these results strongly suggest a phase relationship between RIB activity and sensory activation. This relationship may play a crucial role in regulating the initiation of the reversal motor response.

In summary, we propose that the phase of "low-amplitude" spontaneous RIB modulations defines a gating time window for the system to respond with a reversal locomotion command to the oxygen stimulus. Specifically, the down-modulation phase aids in facilitating this response, whereas the up-modulation phase acts as an inhibitory mechanism. Additionally, the 21% [O_2] stimulus can induce a transient down-modulation of RIB activity independently of the "low-amplitude" modulation phase. This suggests that sensory neurons in "Miss" trials may still transmit information triggering a deceleration event, although insufficient to initiate a reversal response. Furthermore, when the 21% [O_2] stimulus aligns with the RIB "low-amplitude" down-modulation phase, it results in stronger RIB activity down-modulation, which triggers the reversal motor response. Lastly, activation of the reversal premotor interneurons further interacts with RIB activity, leading to prolonged and more pronounced down-modulation, thereby further facilitating reversal locomotion.

The concept of neuronal activity phase-locking is well established in the existing literature. Notably, a recent study conducted in our laboratory introduced a new concept, supported by experimental evidence, suggesting that the functional organization of the *C. elegans* nervous system operates within a hierarchical neuronal dynamics framework (Kaplan et al. 2020). According to it, each subsequent level of activity in this hierarchy is intricately synchronized with the preceding one in terms of phase relationships. Consequently, it is reasonable to assume that the organism's response to external stimuli also might depend on its phase relationship to the ongoing behavior and corresponding brain activity. In line with this assumption, it has been found that the head motor neurons of *C. elegans* which drives phasic head movements set a framework which gates olfactory perception via the RIA interneuron (Ouellette et al., 2018). This mechanism enables the worm to adapt its motor response appropriately to spatially

asymmetric input. Importantly, similar mechanisms related to phasic behaviors have been observed in other species as well. For instance, in mice, the act of respiration during sniffing acts as a gate for olfactory perception, and a similar gating mechanism is evident during whisking (Eggermann et al., 2014; Rothermel et al., 2014).

It is important to emphasise that this mechanism exhibits a probabilistic nature, functioning as a facilitator rather than a strict determinant. Our results provide evidence that, in fraction of instances, early RIB down-modulations can be associated with "Miss" trials. Conversely, in some instances reversal motor response can be induced even outside the preferred RIB phase. This suggests the existence of additional mechanisms that can either hinder or facilitate the reversal reaction, potentially encompassing factors previously mentioned in this manuscript, such as the AVA state and sensory neuron activation amplitude, among others.

Further studies are necessary to delve deeper into the role of RIB neurons in the oxygen sensorimotor circuit. First, it is important to consider that the difference in the latency timing of the RIB down-modulation onset in "Hit" versus "Miss" trials may be attributed to the presence of the "low-amplitude" component in "Hit" trials. Therefore, further analysis is required to separate "low-amplitude" and "high-amplitude" modulation components and independently estimate the timing of their dynamics. Next, further experiments should include optogenetic manipulations. It would be crucial to investigate whether inhibiting RIB neurons shortly before the 21% [O_2] stimulus facilitates the reversal motor response and, conversely, if activating RIB neurons impedes it.

4.10 Conclusion and further perspectives

This project sought to investigate the sensorimotor transformation involved in the avoidance response of *C. elegans* to elevated ambient [O_2]. The primary goals were twofold: firstly, to identify and thoroughly describe the specific neuronal circuits implicated in this process, and secondly, to reveal the neural activity patterns responsible for sensorimotor transformation and understand their functional role.

Throughout the project, we designed an effective experimental paradigm to investigate sensorimotor transformation in *C. elegans*, leveraging the advantages of whole-brain Ca^{2+} imaging. We subsequently developed a complementary analysis algorithm that enables unbiased identification of neurons involved in information processing and distinguishes between sensory- and motor-related neural activity.

The approach employed in this study yielded intriguing results elucidating the neurological processes involved in the sensorimotor transformation in *C. elegans*. Firstly, we successfully identified sensory

and interneurons participating in the studied sensorimotor circuit. Our findings revealed that various classes of sensory neurons exhibit distinct response profiles, potentially contributing to reactions to different stimulus features. Surprisingly, upon estimating information content, we discovered that interneurons primarily contain sensory-related information and may not introduce significant novel elements. We hypothesize that they might become engaged with more complex stimuli, a hypothesis to be tested in future experiments.

Conceptually, with reference to the theoretical perspectives contrasting the Input-Output and Coordination views, our findings provide support for the latter. Specifically, we identified several signatures suggestive of feedback mechanisms that may modulate the responsiveness of sensory and interneurons depending on the current behavioral state of the circuit. This observation aligns with the concepts of feedback regulation and corollary discharge, providing evidence in favor of the Coordination View. Moreover, our findings demonstrated an interaction between stimulus responsiveness and the internal state of the system, particularly in relation to AVA activity, further supporting this perspective.

The revelation of response variability immediately prompted inquiries into its neural sources. Significantly, we identified several potential candidate neurons, including sensory and interneurons, that could potentially influence responses. Notably, we made a particularly intriguing discovery concerning the second-layer interneuron RIB, known for its involvement in governing forward locomotion. Our observations suggest that the phase of the low-amplitude spontaneous RIB modulations defines the gating time window for the system to respond with a reversal locomotion command to the oxygen stimulus. This concept of phase relation is well-documented in existing literature and, notably, has been introduced in a recent study conducted in our laboratory, which proposes that the functional organization of the nervous system in *C. elegans* adheres to a hierarchical neuronal dynamics framework (Kaplan et al. 2020). These discoveries necessitate comprehensive testing in future experiments, with a particular emphasis on incorporating optogenetic manipulation of the RIB neuron. This approach is crucial for examining the causal role of its activity phases in influencing the responsiveness of the circuit.

Several notable constraints were present in this study. Firstly, the employed setup, with worms immobilized in the channel of the microfluidic chip device, is acknowledged to influence the worm's brain activity. Our current study also presented experimental evidence of distinct reaction patterns in worms constrained within the chip device compared to freely moving worms. Therefore, future investigations should include imaging experiments on specific candidate neurons under conditions where worms are freely moving, enabling the study of the sensorimotor processes under circumstances similar to the natural environment for the animal. Another significant limitation was the use of a

repetitive stimulus with a simple pattern. In future experiments, it would be beneficial to alter the stimulus, introducing a more intricate and non-repetitive landscape. Such modifications could enhance engagement for neurons within the sensorimotor circuit and potentially provide deeper insights into its functional organization.

Additionally, when interpreting the gathered results, it is essential to proceed with caution, considering that our approach relied exclusively on a readout based on nuclear activity. Given the recent revelation of neural activity compartmentalization in *C. elegans* (Clark et al. 2006; Chalasani et al. 2007; Hendricks 2012; Li et al. 2014; Ruach et al. 2023), it is important to note that employed methodology did not allow for the detection of potential computations occurring within the neurites. While this constraint is challenging to avoid in whole-brain imaging experiments, future studies might explore focusing on specific candidate neurons to delve into a more detailed level of neurite computations.

5. Methods

5.1 Worm culture and strain

Worms were maintained under standard conditions at 20°C on nematode growth medium (NGM) plates seeded with *E. coli* (OP50 strain) as a food source (Brenner, 1974). All behavioral and imaging experiments were performed on young adult (1 day post L4 stage, one row of eggs) hermaphrodites of *C. elegans*, utilizing the same transgenic strain.

Name	**Genotype**	**Construct (plasmid no.) and injection concentrations**
ZIM2107	*mzmEx496; mzmIs38; mzmIs52; lite-1 (ce314); npr-1 (ad609);*	P*myo-2*::HisCl::SL2::mCherry – 10 ng/uL; P*myo-3*::HisCl - 20ng/ul; P*Flp-17*::mCherry - 1.5ng/uL; P*unc-31*::NLSGCaMP6f (pTS100, codon-optimized and with introns) - 2.5ng/uL

The ZIM2107 transgenic line carried the *lite-1* mutation (ce314), which decreases sensitivity to blue light and UV radiation (Edwards et al. 2008; J. Liu et al. 2010; Gong et al. 2016). Additionally, the genetic backgrounds of mzmEx496; [P*myo*-2::HisCl::SL2::mCherry] and mzmIs38; [myo-3::HisCl; pFlp-17::mCherry] facilitated histamine-induced paralysis of the pharyngeal and body wall muscles, respectively.

5.2 Behavioral experiments

Behavioral experiments (**figs. 1,2**) were performed as described previously (Kato et al., 2015). 20-25 young adult hermaphrodite worms were picked onto an NGM assay plate that had been seeded with *E. coli* OP50 food the day prior to the experiment. The 25 mm x 25 mm assay arena was bordered with Whatman paper soaked with 20 mM CuCl2 to repel and keep worms from escaping the arena. Next, worms on the assay plate were habituated to the experimental room conditions for 1 hour before recording. Further, worms were preincubated at 11% [O_2] for 5 min before recordings were started to accustom them to the gas flow. Recording started with 450 seconds of 11% [O_2] gas flow which was followed by periodic steps of [O_2] between 21% (30-second periods) and 11% (60-second periods) repeating 16 times and resulting in 1890 seconds long recording. Throughout the experiment constant gas flow (50mL/min) was delivered using a custom plexiglass device of 39mm x 39mm x 0.7mm, which was positioned on top of the arena (Hums et al., 2016). Gas mixtures were balanced using N_2 to maintain

constant gas flow. Gas flow was controlled using a static gas mixer connected to mass flow controllers (Vögtling Instruments) using Micro-Manager software. Behavior arenas were illuminated with red LEDs and recorded at time resolution of 10fps with 5 megapixel CMOS cameras (Teledyne DALSA), resulting in pixel resolution of 0.0129 mm/pixel. Movie analysis and behavior detection was performed using MATLAB-based (Mathworks) custom image processing and tracking software as described previously (Hums et al., 2016; Kaplan et al., 2020; Ramot et al., 2008; Zimmer et al., 2009)Using this methodology, we obtained six experimental recording datasets. They contained 438 traces of worm behavior overall. Considering that each trace was spending across 16 stimulus trials it resulted in 7008 trials. For all calculations except the cumulative probability (**fig. 1D**) time series of reversal onsets were binned by averaging into 10 frames, which equals to 1 second time interval.

Whole experiment reversal frequency and stimulus-triggered average frequency (**fig. 1A,C**). For these analyses we were estimating experiment-to-experiment variability. Sample sizes were the number of experiments.

For the **whole experiment reversal frequency** (**fig. 1A**) we calculated frequency of the reversal onsets across all worm traces detected within each experiment per each 1 second time bin. For this all missing values (NaN values corresponding to time frames where an animal was not tracked) were excluded from this analysis. Then, the mean between experiments and SEM was calculated and used for plots.

For the **stimulus-triggered average onsets frequency** (**fig. 1C**) theoretical stimulus upshifts time points from the stimulation protocol were used. Reversal onsets time series were aligned to these events and averaged among all trials from all traces within each experiment resulting in the reversal onset probability for each dataset. Then, the mean of the reversal onset probability between experiments and SEM was calculated and used for plots.

For estimation of the **baseline reversal rate** we used initial 450 seconds 11% [O_2] stimulation baseline. Simulated triggering time points with periodicity corresponding to the real periodic stimulus were fitted to that period (5 trials 90 seconds duration each) (**fig. 1C** magenta line) and used for the further triggered average calculations which was done by the same algorithm as calculations of the stimulus period data. For the reversal onsets cumulative probability analysis (**fig. 1D** magenta line) stimulus grid was modified into 60 seconds periods (with equal 30 seconds simulated 11% and 21% [O_2] periods) in order to increase control data sample (7 trials 60 seconds duration each).

For the next analyzes traces from all 6 recording datasets were pooled together and treated regardless of the dataset.

Cumulative probability of the reversal onsets (**fig. 1D).** This analysis has been done on the unbinned reversal onsets time series in order to capture potential fine time scale fluctuations. We aligned all traces from all experimental datasets to the stimulus event times as described in the **stimulus-triggered average frequency** section. Then we calculated reversal onsets cumulative probability for the 30 seconds time window corresponding to the 21% [O_2] period starting from the [O_2] upshift onset. To compare reversal dynamic upon [O_2] upshifts and downshifts, the same calculation has been done for the first 30 seconds of 11% [O_2] periods starting from the [O_2] downshift onset. Additionally, the same procedure was applied to the 450 seconds 11% [O_2] baseline period as described above.

Statistical test for the cumulative probability analysis (**fig. 1D**). We tested whether the delta value i.e., difference, between the cumulative probability values for the 21% [O_2] periods and the 450 seconds 11% [O_2] baseline period was significantly different from random. Cumulative probability value for the 21% [O_2] periods and the 11% [O_2] baseline period were averaged within the 2 seconds time windows centered around the time point =10 sec. Then resulted value were subtracted from each other ("21% [O_2] periods" – "11% [O_2] baseline period"). Obtained delta value was stored for the further statistical analysis to test whether "21% [O_2] periods" and "11% [O_2] baseline period" values represent different distributions generating significant i.e., non-random delta values. Next, we resampled the data from the original "21% [O_2] periods" and "11% [O_2] baseline period" clusters. For that we combined "21% [O_2] periods" and "11% [O_2] baseline period" clusters together into one matrix and then selected randomly ("randperm" MATLAB function) n trials (with n = n original "21% [O_2] periods" trials) and the remaining n' trials (with n' = n "11% [O_2] baseline period" trials) forming two control clusters. Then, the **cumulative probability of the reversal onsets** procedure for the 30 seconds time window corresponding to the 21% [O_2] period was applied to the data in control clusters and delta values were calculated according to the procedure described above. This procedure was repeated 10^6 times to obtain an average random distribution of delta values. The p value was defined as the fraction of delta values from the random resampled distribution that are at least as large in absolute value as the experimental delta value. Significance level based on the adjusted p values is depicted with stars: ***, $p < 0.001$.

For the **separation analysis (fig. 2)** we used only trials with no missing values (NaN) during the whole 21% [O_2] period (n trials = 1245). We divided the whole 21% [O_2] stimulus time window into two periods: 0 to 10 seconds starting from the 21% [O_2] stimulus onset and from 10 seconds to the 60 seconds (end of the trial). This division was based on the distribution of the reversal onsets peaks. Based on the reversal onsets timing relating to the 10 seconds threshold we predefined four clusters. "Early" - onsets occurring only during first 10 seconds, "Late" onsets – occurring after first 10 seconds, "Early and Late" – trials with reversal onsets occurring in both time windows and "None" – trials with no

reversals. Then, all trials were sorted according to these criteria and stimulus-triggered average was done for each cluster independently (**fig. 2A**). For this all trials from the corresponding cluster were aligned to the 21% [O_2] stimulus onsets and averaged.

For the **"Hit" probability analysis** (**fig. 2D**) we selected only traces with no missing values (NaN) at any of the 21% [O_2] period (from all 16 trials) – which resulted in n = 28 traces (448 trials) each corresponding to an individual worm. "Hit" trials were defined by the presence of the reversal onset within first 10 seconds period starting from the 21% [O_2] stimulus onset. Thus, "Hit" trials include two clusters from the previous classification: "Early" and "Early and Late". Then, we calculate frequency of those trials per worm trace (n of "Hit"/ 16 (N of trials)). Resulting frequencies from 28 traces are presented as a histogram (**fig. 2D**). To estimate **the individual worms' proportions** from the same subset of data we also quantified proportion of each type of trials for each individual worm (**fig. 2C**).

5.3 Oxygen dye recordings

Tris-(4,7-diphenyl-1,10-phenanthrolin)-ruthenium(II)-dichlorid-Komplex water solution (1:30) was used for the experimental measurements of the [O_2] profile in the behavioral chamber and imaging chip devices. Imaging was performed with an inverted compound microscope (Zeiss Axio Observer.Z1) using EMCCD cameras (iXon3,Andor) with mCherry setting.

Stimulus for calibration measurements was composed of three calibration periods and two periodic stimulus periods in-between. During the calibration period [O_2] rose from 0% to 35% in 7 steps increasing by 5% on each step. Each step lasted for 25 seconds, except of the first step where [O_2] changed from the 11% baseline to 0% which was set to 60 seconds. Periodic stimulus consisted of up- and downshifts of [O_2] between 11% and 21% (30 seconds duration of each step) repeating 25 times.

We acquired n = 4 recordings in the behavioral chamber. All three calibration periods within each recording were averaged resulting in a trial average (**fig. 3A**). Then, the intensity value within the last 6 frames (2 seconds) time window at each concentration step were averaged. This average values then were used for fitting an exponential function to estimate the [O_2] function over the dye intensities (MATLAB "fit" function with a setting "exp1" was used for this procedure) (**fig. 3B**). Two periods of the periodic 11-21% [O_2] fluctuation were also averaged for each recording resulting in a recording average. Then, the [O_2] trace was reconstructed by applying an obtained model on the recording average dye intensity trace from the [O_2] fluctuation period. Next, resulting reconstructed traces among all recordings (n = 4) were averaged resulting in the average reconstructed estimate of the [O_2] stimulus (**fig. 3C**).

For the **stimulus-triggered average [O_2] trace** stimulus upshifts initiation time points from the stimulation protocol were used. Reconstructed average [O_2] trace was aligned to these events and averaged among all trials (n = 25). Then, the trials mean value and SEM was calculated and used for plots (**fig. 3D**). First derivative of the [O_2] average trace was calculated for each trial separately using Maltab function "diff". Then, the mean value over trials and SEM were used for the plot (**fig. 3E**)

For the **comparison of the oxygen flow in the behavioral chamber device and chip (fig. 3F)** we used separate recordings with a different stimulus paradigm. We acquired 4 recordings in the behavioral chamber device and 5 recordings in the chip devices (3 chip devices). Stimulus consists of two repetitions of [O_2] shifts from 11 to 21 % with each step lasting for 360 seconds. Values of the dye fluorescence intensity were averaged across all chamber- and all chip- recordings respectively, then stimulus-triggered average [O_2] trace was calculated similarly to the approach described above. For the depiction we used fragment from -10 to +30 seconds around the upshift time point (**fig. 3F**)

5.4 Whole-brain Ca^{2+} imaging

Whole-brain Ca^{2+} imaging experiments (**figs. 4 - 24, S1 - S4**) were performed as described previously (Kato et al. 2015). The same genetic strain (ZIM2107) of C. elegans and age group (young adult hermaphrodites) as used in the behavioral assays were employed for the experiments. Importantly, this strain expresses the pan-neuronal genetically encoded Ca^{2+} indicator GCaMP6f (Chen et al., 2013) and contains a mutation in the *lite-1* gene (ce314 allele) that diminishes responsiveness to UV and blue light (Gong et al. 2016; Liu et al. 2010; Edwards et al. 2008).

Notably, current research utilized a novel **paralysis technique** where worms were paralyzed using histamine via the Drosophila histamine-gated chloride (HisCl) channels (Pokala et al., 2014) expressed in the body wall and pharyngeal muscles (*myo-2*::, *myo3*::hisCl). In contrast to tetramisole, which paralyzes worms by causing the contraction of the body wall muscles, HisCl method paralyzed worms by relaxing their muscles. Importantly, previous research in our laboratory has shown that worms paralyzed using the HisCl method maintain cyclic global brain activity (Salazar Thula, 2024). Notably, *C. elegans* neither synthesizes nor uses histamine as a neurotransmitter, and exogenous histamine has minimal impact on the behavior of wild-type worms (Chase & Koelle, 2007; Pokala et al., 2014). Therefore, this approach is preferable compared to the previously used tetramisole in our lab, which acts as a nicotinic acetylcholine receptor agonist (Martin et al. 2012) and may potentially disrupt the function of cholinergic neurons in the worm's brain, such as the URX and IL2 neurons (Pereira et al., 2015).

Animals were imaged using custom microfluidic two-layer PDMS device (**fig. 4A**) to regulate the [O_2] environment (Zimmer et al., 2009). The device's curved worm channels ensured immobilization and lateral alignment of the animals (Kato et al. 2015; Schrödel et al. 2013; Cáceres et al. 2012). This curved design minimized the necessary imaging area by aligning the animal's head and tail, allowing for simultaneous imaging of all neurons in the head and tail ganglia, the retro vesicular ganglion, and multiple motor neurons along the ventral cord (**fig. 4B**).

The microfluidic device assembly and worm loading procedure were conducted as described in previous studies (Hums et al., 2016; Zimmer et al., 2009). Briefly, the worm channel of the microfluidic device was connected to a syringe containing nematode growth medium (NGM) buffer mixed with 20 mM histamine to maintain paralysis throughout the experiment and *E. coli* OP50 suspension to simulate the 'on-food' conditions of previously tested behavioral experiments (his-NGM-OP50 buffer). The OP50 concentration in the buffer was determined by measuring the optical density at 600 nm (OD600) with a biophotometer device. The absorbance was set to value 1.6, with an allowed margin error of 10%.

All components were connected using Tygon tubing (0.02 in ID, 0.06 in OD; Norton) and 23G Luer-stub adapters (Intramedic). Constant gas flow of an O_2 and N_2 mixture (50 ml/min) was supplied via a gas mixer connected to mass flow controllers (Vögtling Instruments), controlled by LabView software. The baseline [O_2] was set to 11%, to which the worms were exposed for approximately 5 minutes during the setup of the microfluidic device on the microscope stage and the initiation of recording, thereby replicating 5 min 11% [O_2] gas flow habituation used in behavioral assays. The oxygen stimulus protocol was identical to that used in the behavioral experiments. Recording began with 450 seconds of 11% [O_2] gas flow, followed by periodic steps of [O_2] alternating between 21% (30-second periods) and 11% (60-second periods), repeated 16 times, resulting in a total recording duration of 1890 sec.

Worms were transferred to the experimental room approximately 1h before the beginning of experiments to allow habituation to the conditions of the room. Worms were picked onto NGM agar mixed with 20 mM histamine plates seeded with *E. coli* OP50 and allowed to feed for 30-45 minutes, the time required to induce paralysis, which was monitored visually. Next, paralyzed individual worm were picked on a food-free NGM agar plate and placed into a drop of his-NGM-OP50 buffer. Then, worm was loaded into Tygon tubing filled with his-NGM-OP50 buffer by manually applying a vacuum with a syringe to draw individual worms into the tubing. This tubing was subsequently reconnected to the worm inlet of the microfluidic PDMS device, where the worm was pushed into the microfluidic device and positioned in the curved channel under visual control using a microscope.

After this, the microfluidic chip device was placed and adjusted in the imaging microscope setup. Recording began approximately 10 minutes after loading the worm. We used an inverted confocal

microscope, Zeiss Axio Observer.Z1, equipped with a Yokogawa CSU-X1 spinning disk, an EMCCD camera (Photometrics Evolve 512), and a 40x/1.2 LD LCI Plan-Apochromat water-immersion objective (Zeiss), all controlled by VisiView software (Visitron Systems GmbH). The exposure time was set to 10 ms, with 2 µm steps between Z-planes controlled by a Piezo stage (P-736 PInano, Physik Instrumente GmbH). These settings allowed for an imaging rate of 4.26–4.54 volumes per second with 14–15 Z-planes, resulting in high-resolution data of neuronal activity in the head and tail ganglia.

Neuronal time series extraction was performed as previously described (Kato et al. 2015) by tracking the intensity maxima in each volume over time and calculating the fluorescence intensities (F) for individual cells (**fig. 4C**). The background intensity (F0) was determined as the average fluorescence intensity throughout the recording. Following background subtraction, ΔF/F0 was computed for each neuron, followed by bleach correction using linear detrending and exponential fitting. Further, an additional bleach correction stage was introduced in our analysis, using a cumulative sum-based adjustment of the trace intensity values.

In each recording, we detected 97-156 neurons (mean: 121.8, std: 21.1); the remaining neurons were likely inactive during recording, resulting in very low fluorescence levels. Additionally, some neurons might have been excluded due to artifacts or difficulties in distinguishing the activities of neighboring neurons. It is also possible that the transgene is not expressed in a small subset of neurons.

Further, we performed **neuronal identification** according to the previously described methodic (Kato et al. 2015), which involved evaluating their anatomical positions, topographical relationships with neighboring neurons (http://www.wormatlas.org), characteristic activity patterns, and our prior knowledge from red fluorophore expression in specific marker lines as detailed in earlier studies (Skora, Mende, and Zimmer 2018; Nichols et al. 2017; Kato et al. 2015; Kaplan et al. 2020). This classification was further refined with recent advancements using (Uzel et al., 2022). We successfully identified between 44 and 61 neurons per recording (mean: 54.8, std: 6.7). Across the five recorded datasets, we identified a total of 86 neuronal classes, which were subsequently used for further analysis.

Importantly, [O_2] stimulation protocol in the current experiments facilitated identification of the primary oxygen sensory (URX,AR,PQR and IL2) and primary interneurons (RMG, AUA, PVP) which were exhibiting prominent and reliable response to the [O_2] stimulus. Additionally, by screening the results of the stimulus-triggered average analysis we identified new neuronal pair with activity linked to the oxygen stimulus it activated during the 11% [O_2] periods similar to BAG neurons (**figs. 14, S1**). We gave it a putative name “X” neuron. This neuron was identified in all 5 five datasets used for the pan-neuronal analysis, although in two of these datasets, only a single “X” neuron from the pair was

detected. “X” neuron was located posterior to the RIM neuron in the posterior section of the lateral ganglion, though its exact position and distance from RIM varied across datasets. Based on its location, we suggest that it may correspond to the AIZ interneuron. Interestingly, although the AIZ interneuron hasn’t been linked to oxygen-related activity before, one study has suggested its role in response to CO_2 (Guillermin et al., 2017).

We acquired a total of 14 whole-brain imaging datasets, of which 5 were of sufficient quality for further pan-neuronal analysis. These datasets were selected based on the reliable tracking and detection of most neurons, allowing for further neuronal identification and comprehensive analysis. However, all 14 datasets exhibited well-detectable traces of AVA neuronal activity, making them suitable for focused AVA neuron activity analysis. Additionally, we acquired a cohort of control recordings consisting of 10 datasets at stable 11% [O_2] and 10 datasets at stable 21% [O_2], each with a recording duration of 1890 seconds to match the length of the periodic stimulus recordings. These datasets were used for AVA-focused analysis. For each dataset, we identified the highest-quality AVA neuron from the left-right pair (AVAL\AVAR) and used that neuron for further analysis.

To calculate **stimulus-triggered averages of neuronal activity (figs. 5B, 14, 19, S1)** theoretical stimulus upshifts time points from the stimulation protocol were used. Z-scored fluorescence (dF/F0) time series for the neuron of interest were aligned to these events. This was done for all recording datasets (n datasets = 5) where the neuron of interest was identified. Then, the aligned time series from all the trials of all recordings involved were concatenated together. Then, the mean of the z-scored fluorescence time series and SEM was calculated and used for plots. This procedure was performed systematically for all identified neurons (**fig. S1**).

Neuronal activity rise onsets analysis traces of neuronal activity were semi-automatically annotated to detect “rise”, “high”, “fall” and “low” phases similarly as described previously (Kato et al., 2015). “Rise” and “fall” phases were defined as time points when their time derivative was greater than a small positive threshold or smaller than a negative threshold, respectively. “High” and “fall” phases were defined as periods between corresponding “rise” and “fall” phases. Next, traces were inspected and annotation errors were corrected manually. Then, the time points of the rise onsets were detected and time series of neuronal rise onsets were used for the further analysis (**fig. 6**).

Treating the URX neurons pair. In one of the recording datasets from 5 used for the pan-neuronal analysis we could not identify URXL neuron, but the URXR neuron which is a contralateral neuron from the pair was identified. Thus, we used time series of the URXR neuron from this dataset and

combined them with results for URXL neuron from the rest of the datasets. Hence, for the analyses where the combined data were used, we denoted it as a URXL\R neuron.

Cumulative probability of the oxygen sensory neurons activity rise onsets (**fig. 6B**). This procedure was implemented in the similar way as for the **cumulative probability of the reversal onsets** described above. Time series of neuronal rise onsets were used for this analysis. We calculated rise onsets cumulative probability for the 30 seconds time window corresponding to the 21% [O_2] period starting from the [O_2] upshift onset. It is important to note that some neurons had multiple rise onsets during the same stimulation trial, thus resulting cumulative probability might reach values above 1.

For the **sensory neurons rise onsets timing analysis (fig. 6C)** we considered only the first neuronal activity rise onset for each trial in case more than one was present. We quantified timing of the rise onsets counting from the onset of the 21% [O_2] stimulus at each trial. Median value and 25th and 75th percentile values were depicted as a box plot.

5.5 AVA neuron activity analysis

For the analysis in this section we used 14 whole-brain imaging recordings, including 5 recordings which were also used for the pan-neuronal analysis. For each dataset we identified the best quality AVA neuron in the left-right pair (AVAL\R) and were using it for the further analysis. Next, we selected only "AVA low/fall 0 sec" trials for the further analysis, this condition means that the AVAL\R neuron was in a "low" or "fall" activity state at the moment of the 21% [O_2] stimulus onset.

Cumulative probability of the AVA neurons activity rises onsets. This procedure was implemented in the similar way as for the **cumulative probability of the oxygen sensory neurons activity rise onsets.** For this analysis we selected only the first activity rise following the stimulus onsets (for both 11% to 21 % and 21% to 11% [O_2] transition). Thus, the cumulative probability could only reach the maximum value of 1. First, we calculated rise onsets cumulative probability for the 30 seconds time window corresponding to the 21% [O_2] period starting from the [O_2] upshift onset. To compare reversal dynamic upon [O_2] upshifts and downshifts, the same calculation has been done for the first 30 seconds of 11% [O_2] periods starting from the [O_2] downshift onset. Then, the cumulative probability values for two time epochs were plotted on top of each other. This was done separately for all the 14 datasets (**fig. 7C**) and for 5 datasets (**fig. 7G**) out selected for the pan-neuronal analysis. For the **fig.7F** we compared rise onsets cumulative probabilities from the 21% [O_2] periods for the full set of 14 datasets versus 5 datasets out selected for the pan-neuronal analysis.

To **control the entrainment of the stimulus (fig. 8)** in the periodic stimulus datasets we developed a procedure in which we used theoretical stimulus upshifts time points from the periodic stimulation protocol to align AVAL\R activity traces from the 11% and 21% [O_2] control recordings (**fig. 8D** shows the example of aligned rise onsets traces for the stable 11% [O_2] datasets). Then the **cumulative probability of the AVA neurons activity rise onsets** procedure was applied for the 30 seconds time window starting from the fictitious [O_2] upshift onset and corresponding to the fictitious 21% [O2] period. Finally, cumulative probability values for both type of controls (11% and 21% stable [O_2]) were plotted and compared to the one from the periodic stimulus datasets (**fig. 8E**).

Statistical test for the cumulative probability analysis (**fig. 8E**)**.** We tested whether the delta value i.e., difference, between the cumulative probability values for the periodic stimulus datasets ("Periodic stimulus") and each of the control (11% and 21% stable [O_2] datasets, "Control") was significantly different from random. Cumulative probability value for the periodic stimulus datasets and the control were averaged within the 2 seconds time windows centered around the time point =10 sec. This time was chosen based on the observation that the difference between cumulative probabilities for the "Periodic stimulus" and both of the "Control" conditions was peaking around the 10 seconds from the 21% [O_2] stimulus onset (**fig. 8E**). Then resulted value were subtracted from each other ("Periodic stimulus" – "Control"). Obtained delta values were stored for the further statistical analysis to test whether "Periodic stimulus" and "Control" values represent different distributions generating significant i.e., non-random delta values. Next, we resampled the data from the original "Periodic stimulus" and "Control" clusters. For that we combined "Periodic stimulus" and "Control" trials clusters together into one matrix and then selected randomly ("randperm" MATLAB function) n trials (with n = n original "Periodic stimulus" trials) and the remaining n' trials (with n' = n "Control" trials) forming two control clusters. Then, the **cumulative probability of the AVA neurons activity rise onsets** procedure for the 30 seconds time window corresponding to the 21% [O_2] period was applied to the data in control clusters and delta values were calculated according to the procedure described above. This procedure was repeated 10^6 times to obtain an average random distribution of delta values. The p value was defined as the fraction of delta values from the random resampled distribution that are at least as large in absolute value as the experimental delta value. This control procedure was done separately for the "Periodic stimulus" vs 11% [O_2] "Control" and "Periodic stimulus" vs 21% [O_2] "Control". To correct for multiple comparisons, statistical significance was determined by the Benjamini-Hochberg-Yekutieli procedure (Benjamini & Yekutieli, 2001). Significance level based on the adjusted p values is depicted with stars: ****, $p < 0.0001$ (**fig. 8E**).

For the **AVAL\R phase duration quantification (fig. 8B,C)** AVAL\R traces were annotated as described above in the **neuronal activity rise onsets analysis.** Then, "rise, "high" and "fall" phases

were combined together into the “rise-high-fall” state. Then, the onsets and offsets of this state were detected. Next, durations of the “rise-high-fall” states were quantified as “offset time” – “onset time”; only complete activity cycles were considered for the analysis. “Low” phases were quantified as “onset time” – “offset time”. This procedure was performed for the “Periodic stimulus” and each of the “Control” (11% and 21% [O_2]) datasets. Resulting durations were presented as box plots: the central mark indicates the median, and the bottom and top edges of the box indicate the 25th and 75th percentiles, respectively. The whiskers extend to the most extreme data points not considered outliers, and the outliers are plotted individually using the '+' marker symbol.

Statistical test for the AVAL\R phase duration quantification (fig. 8B,C). For all three conditions (“Periodic stimulus”, 11% and 21% [O_2] “Control”) we tested whether the delta value i.e., difference, between their median values was significantly different from random. This procedure was done systematically between all conditions. First, median values for the two tested conditions were subtracted from each other and obtained delta values were stored for the further p-values quantification. Next, we resampled the data from the original clusters. For that we combined data in two clusters together and then selected randomly (“randperm” MATLAB function) n trials (with n = n original events for Condition#1) and the remaining n' trials (with n' = n events for Condition#2) forming two control clusters. Then, the delta value between median values for that clusters were quantified. This procedure was repeated 10^6 times to obtain an average random distribution of delta values. The p value was defined as the fraction of delta values from the random resampled distribution that are at least as large in absolute value as the experimental delta value. To correct for multiple comparisons, statistical significance was determined by the Benjamini-Hochberg-Yekutieli procedure (Benjamini & Yekutieli, 2001). Significance level based on the adjusted p values is depicted with stars: **, $p < 0.01$; ****, $p < 0.0001$.

For each of the “Periodic stimulus” datasets (n =14) we quantified the **“Hit” trials probability.** “Hit” trials were defined by the presence of the AVAL rise onset within the 10 seconds period starting from the 21% [O_2] stimulus onset (Similarly to the **“Hit probability” analysis** in the behavioral experiments). This time threshold was chosen based on the observation that the difference between cumulative probabilities for the “Periodic stimulus” and both of the “Control” conditions was peaking around the 10 seconds from the 21% [O_2] stimulus onset (**fig. 8E**). Then, we calculate the probability of the “Hit” trials per each recording (n of “Hit”/ 16 (N of trials)). Resulting probabilities from 28 traces are presented as a bar plot (**fig. 7D**) and a histogram (**fig. 7E**). Also, we calculated a binomial probability density function with a probability of success for each trial set equal to the mean value (0.42) from the experimental results (**fig. 7E**).

Cumulative probabilities of the AVA activity onsets for different past history conditions (**fig. 9B**). For this analysis we sorted all trials based on the past history of the AVAL neuron. Three clusters were predefined for sorting: “0 sec”, “30 sec”, “50 sec” - corresponding to the timing for which AVAL neuron was in a “low” or “fall” state prior to the 21% [O_2] stimulus onset. “0 sec” condition means that AVAL neuron was in a “low’ or “fall” state at the moment of the 21% [O_2] stimulus onset. Then the **cumulative probability of the AVA neurons activity rise onsets** procedure was applied to each cluster separately. In particular, we calculated rise onsets cumulative probability for the 30 seconds time window corresponding to the 21% [O_2] period starting from the [O_2] upshift onset. The same procedure was applied to the AVAL\R activity from the 11% and 21% [O_2] “Control” datasets. For this we used theoretical stimulus upshifts time points from the periodic stimulation protocol as a fictitious stimulus times. The rest of the procedure was done the same as described above for the periodic stimulus datasets. Then, cumulative probability values for all conditions were plotted on top of each other separately for the periodic stimulus datasets and two control set of datasets (**fig. 9B**).

Stimulus-triggered averages of neuronal activities sorted by different AVAL past history conditions. For this analysis we sorted all trials for each neuron of interest based on the past history of the AVAL neuron at the corresponding trial. Three clusters were predefined for sorting: “0 sec”, “30 sec” and “50 sec” - corresponding to the timing for which AVAL neuron was in a “low” or “fall” state prior to the 21% [O_2] stimulus onset. “0 sec” condition means that AVAL neuron was in a “low’ or “fall” state at the moment of the 21% [O_2] stimulus onset. Then the **stimulus-triggered averages of neuronal activity** procedure was applied to each cluster separately. Finally, averaged times series from all clusters were plotted on top of each other (**fig. 18**).

5.6 “Hit-Miss; Evoked-Spontaneous”-triggered average analysis

“Hit-Miss; Evoked-Spontaneous”-triggered average analysis (figs. 10-12, 15, 16, 20, 21, 22A, 23A, S3, S4) is a variation on the triggered average analysis. This analysis was done for all recording datasets (n datasets = 5) where the neuron of interest was identified This analysis consisted of two parts.

First part is a modified **stimulus-triggered averages of neuronal activity** (see **Methods** above). For this theoretical stimulus upshifts time points from the stimulation protocol were used. First, we selected only “AVA low 0 sec” trials for the further analysis, this condition means that the AVAL neuron was in a “low” or “fall” activity state at the moment of the 21% [O_2] stimulus onset. Then, all the trials were split into the “Hit” and “Miss” clusters. “Hit” trials were defined by the presence of the AVAL rise onset within the 10 seconds period starting from the 21% [O_2] stimulus onset (Similarly to the **“Hit probability” analysis** in the behavioral experiments). On a residual basis, “Miss” trials included trials with AVAL rise onset appearing after the 10 seconds period starting from the 21% [O_2] stimulus onset

and trials with no AVAL rises during the whole 21% [O_2] period. Then, the **stimulus-triggered averages of neuronal activity** was applied in the way described above separately for the "Hit" and "Miss" trial clusters resulting in the "Hit" and "Miss"-triggered averages. Finally, averaged fluorescent time series and SEM for "Hit" and "Miss" clusters were plotted on top of each other for all analysed neurons separately (**figs. 11, 15, 20, 22A, S3**).

Second part is a triggered averaging of neuronal activity with AVAL rise onsets used as a triggering time points. AVAL neuron activity was chosen as a readout of the system's response based on the previous research (Kato et al. 2015) showing that AVA activity tightly correlates with the reversal motor behavior in freely moving *C. elegans*. For this analysis time series of the AVAL rise onsets obtained in **neuronal activity rise onsets analysis** were used. All the AVAL rises were split into the "Evoked" and "Spontaneous" clusters. "Evoked" AVA rises were defined by the presence of the AVAL rise onset within first 10 seconds period starting from the 21% [O_2] stimulus onset. Thus, the "Evoked" cluster corresponded to the "Hit" trials from the stimulus-triggered average classification. On the other hand, the "Spontaneous" cluster was defined on a residual basis, and included AVAL rises occurring within 21% [O_2] periods after 10 seconds epoch and all the AVAL rises occurring within the 11% [O_2] periods except of the initial 450 seconds 11% [O_2] baseline period. Importantly, "AVA low 0 sec" were preselected for the AVA "Evoked" trials, AVA "Spontaneous" trials were selected out of all trials. Then, the **stimulus-triggered averages of neuronal activity** was applied in the way described above using the AVAL rise onsets time points separately for "Evoked" and "Spontaneous" clusters resulting in the "Evoked" and "Spontaneous"-triggered averages. For this modification of the **stimulus-triggered averages of neuronal activity** we used time window of $\pm$30 seconds centred around each triggering time point. Finally, averaged fluorescent time series and SEM for "Spontaneous" and "Evoked" clusters were plotted on top of each other for all analysed neurons separately (**figs. 12, 16, 21, 23A, S4**).

Statistical test for the "Hit-Miss; Evoked-Spontaneous"-triggered average analysis (Tables 1, 2). For all identified neurons in the analysis, we tested whether the delta between the average amplitude of neuronal activity at "Hit" and "Miss" clusters was significantly different from random. First, we split the whole trial time window into the pre- and post- triggering time point epochs (corresponding to the pre- and post- stimulus time for the stimulus-triggered averages and pre- and post- AVA rise onset time for the AVA rise onsets-triggered averages). Further procedures were performed separately for each of those time epochs within the 30 seconds time window. Next, the average "Miss" and "Hit" cluster's Z-scored fluorescence (dF/F0) time series were smoothed to avoid the influence of local activity fluctuations ("smooth" MATLAB function, smoothing parameter = 15 frames). Smoothed "Miss" average time series were subtracted from the smoothed "Hit" average. Then, we detected time points corresponding to the maximum and minimum values of the resulted difference. Original average time series for "Hit" and "Miss" clusters were averaged within the 15 seconds time windows centered around

these time points and resulted value were subtracted from each other ("Hit" – "Miss"). Obtained delta values were stored for the further p-values quantification. Next, we resampled the data from the original "Hit" and "Miss" clusters. For that we combined "Hit" and "Miss" trials clusters together into one matrix and then selected randomly ("randperm" MATLAB function) n trials (with n = n original "Hit" trials) and the remaining n' trials (with n' = n "Miss" trials) forming two control clusters. Then, the **stimulus-triggered averages of neuronal activity** procedure was applied to the data in control clusters and delta values between the average control time series was calculated according to the procedure described above for the previously defined maximum and minimum time points. This procedure was repeated 10^5 times to obtain an average random distribution of delta values. The p value was defined as the fraction of delta values from the random resampled distribution that are at least as large in absolute value as the actual delta value. To correct for multiple comparisons, statistical significance was determined by the Benjamini-Hochberg-Yekutieli procedure (Benjamni and Yekutieli, 2001). This procedure was applied to the p values within four categories ("pre-triggering min", "pre-triggering max", "post-triggering min' "post-triggering max") separately. Significance level based on the adjusted p values is depicted with stars: *, $p < 0.05$; **, $p < 0.01$; ***, $p < 0.001$, ****, $p < 0.0001$**(figs. 10-12, 15, 16, 20, 21, 22A, 23A)**. The same procedure was performed for the AVA rise onsets-triggered "Evoked" versus "Spontaneous"-triggered averages.

5.7 "Hit-Miss" neuron's activity onsets timing analysis for the oxygen sensory neurons and RMG neuron analysis

This analysis was performed in the same way for all oxygen sensory neurons and RMG neurons. For the **stimulus related activity rise onsets timing on "Hit-Miss" trials** analysis the time series of the neuronal activity onsets were aligned in the respect to the 21% [O_2] stimulus onsets as described in the **"Hit-Miss" analysis** section. Then, we quantified time latencies between the 21% [O_2] stimulus onsets and the first following activity rise onsets at each trial for each neuron. This procedure was done separately for the "Hit" and "Miss" trials clusters. Finally, the results were depicted as a histogram with data quantified in the 0.5 seconds time bins (**figs. 13A, 17D**).

Cumulative probability of the neurons activity rise onsets for "Hit-Miss" trials were quantified in a similar way as was described above for the **cumulative probability of the AVA neurons activity rise onsets.** In the current modification this procedure was done separately for the "Hit" and "Miss" trials clusters. The cumulative probability values for the "Hit" and "Miss" trials were plotted on top of each other separately for each neuron of the interest (**figs. 13B, 17C**).

Statistical test for the cumulative probability analysis (**figs. 13B**, **17C**). We tested whether the delta value i.e., difference, between the cumulative probability values for the "Hit" and "Miss" trial's pools

was significantly different from random. Cumulative probability value for the periodic stimulus datasets and the control were averaged within the 2 seconds time windows centered around the time point = 7 seconds for the IL2R neuron and 6 seconds for the RMGL neuron. These time points were chosen since the difference between cumulative probabilities for the "Hit" and "Miss" trial's pools was reaching maximum there. Next, the computations were performed in the same way as was described above in the **statistical test for the cumulative probability analysis** of the section **AVA neuron activity analysis.** Significance level based on the adjusted p values is depicted with stars: *, $p < 0.05$; **, $p < 0.01$.

5.8 RIB neuron analysis methods

For the analysis of the forward command neurons activity, we focused on the RIBL neuron. First, activity states of the RIBL neuron were annotated as was described above in the **neuronal activity rise onsets analysis** section. Here we detected time points of the fall onsets, then time series of neuronal fall onsets were used for further analysis. Importantly, similarly as in the **AVA neuron activity analysis** section we selected only "AVA low/fall 0 sec" trials for all the further procedures.

Cumulative probability of the RIBL neurons activity fall onsets (**fig. 22C**) were quantified in a similar way as was described above for the **cumulative probability of the AVA neurons activity rise onsets.** This procedure was done for the 30 seconds of the 21% [O_2] period and for the whole 60 seconds of the 11% [O_2] period. The cumulative probability values for the RIBL fall onsets and AVAL rise onsets (calculated before) were plotted on top of each other.

For the **stimulus related RIBL fall onsets timing analysis** (**fig. 22E**) time series of the RIBL activity fall onsets were aligned in the respect to the 21% [O_2] stimulus onsets as described in the **"Hit-Miss" analysis** section. Then, we quantified time latencies between the 21% [O_2] stimulus onsets and the first following RIBL fall onsets at each trial. For this we considered only the RIBL fall onsets occurring within the 5 seconds time window following the 21% [O_2] stimulus onset. This procedure was done separately for the "Hit" and "Miss" trials clusters. Finally, the results are depicted as a histogram with data quantified in the 0.5 seconds time bins. In the same way we quantified timing of the activity rise onsets for the oxygen sensory neurons (**fig. 24A**).

For the **AVAL rise onset related RIBL fall onsets timing** (**fig. 23B**) the time series of the RIBL activity fall onsets were aligned in the respect to the AVAL rise onsets as described in the **"Evoked-Spontaneous"-triggered average analysis** section. Then, we quantified time latencies between the AVAL rise onset and the nearest RIBL fall onset at each trial in the $\pm$ 10 seconds time window centered around the AVAL rise onset. This procedure was done separately for the "Evoked" and "Spontaneous"

trials clusters. Finally, the results were depicted as a histogram with data quantified in the 0.5 seconds time bins.

We quantified **trial-by-trial differences between the timing of the RIB fall onsets and corresponding sensory neuron rise onsets** (**fig. 24B**). For this procedure we used previously quantified time latencies of the RIBL and oxygen sensory neurons with relation to the 21% [O_2] stimulus onset. Then the values of the RIBL fall onsets latencies were subtracted from the values of the latencies for the oxygen sensory neurons at the corresponding trial. This procedure was done separately for the “Hit” and “Miss” trials clusters. Finally, the results were depicted as a histogram with data quantified in the 0.5 seconds time bins.

Statistical test for the onsets timing quantifications (figs. 22E, 23B, 24A) described in this section were performed in the next way: in each case we tested whether the difference between the median values for the “Hit” and “Miss” (or “Evoked” versus “Spontaneous”) trial clusters values was significantly different from random. First, median values for the two tested conditions were subtracted from each other and obtained delta values were stored for the further p-values quantification. Next, we resampled the data from the original clusters. For that we combined data in two clusters together and then selected randomly (“randperm” MATLAB function) n trials (with n = n original events for Condition#1) and the remaining n' trials (with n' = n events for Condition#2) forming two control clusters. Then, the delta value between median values for that clusters were quantified. This procedure was repeated 10^6 times to obtain an average random distribution of delta values. The p value was defined as the fraction of delta values from the random resampled distribution that are at least as large in absolute value as the experimental delta value. Significance level based on the adjusted p values is depicted with stars: n.s, $p > 0.05$; *, $p < 0.05$; **, $p < 0.01$; ***, $p < 0.001$, ****, $p < 0.0001$.

6. Supplementary Materials

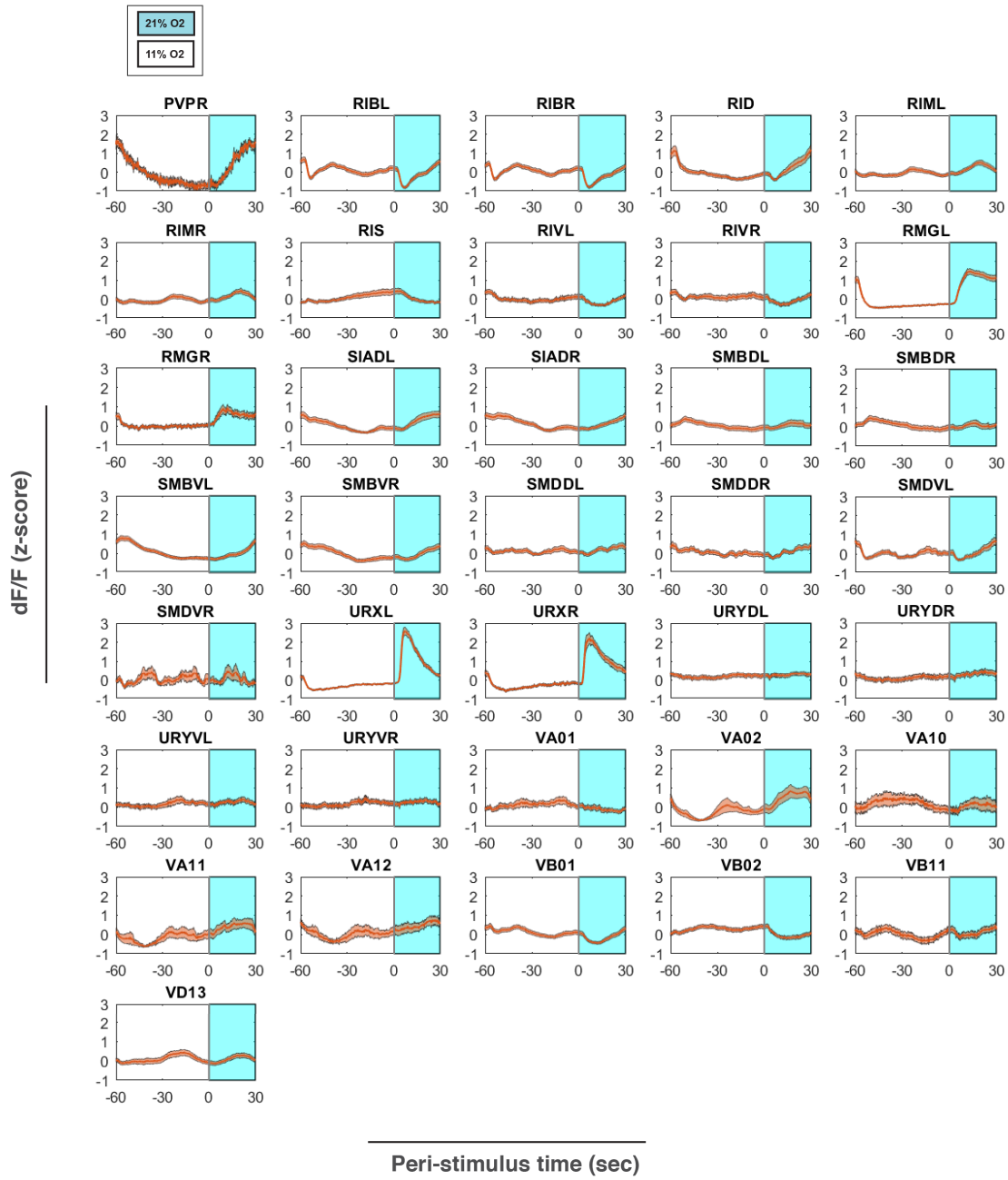

Figure S1. Stimulus-triggered averages of neuronal activity of all identified neurons
Each panel corresponds to a particular neuron. Within each panel trials averages of neuronal activity are depicted. Shaded areas represent ± SEM. Vertical line at 0 seconds represents the transition between 11% and 21% [O_2] periods.

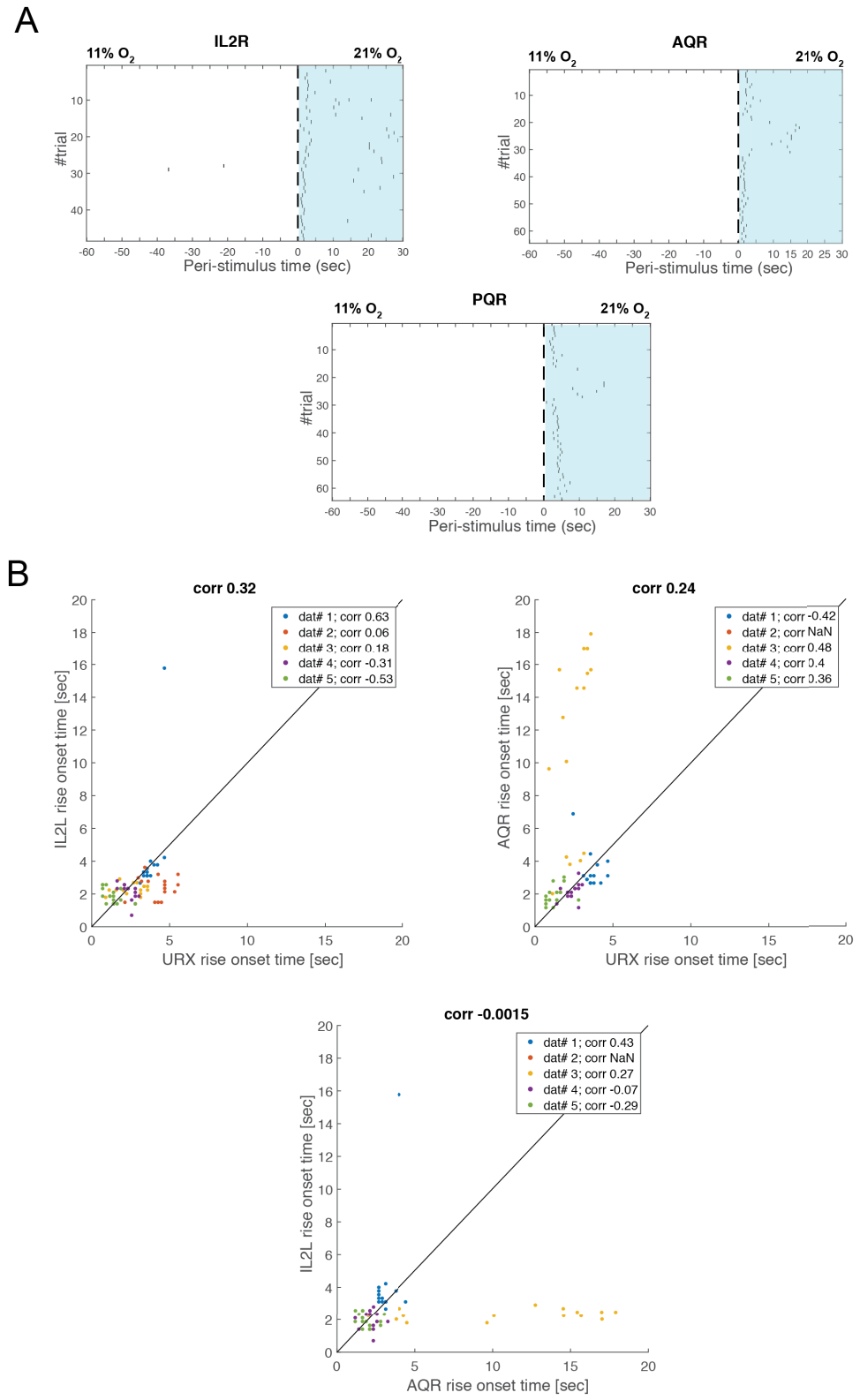

Figure S2. Characterization of the oxygen sensory neurons activation onset timing
(**A**) Raster plots showing the onsets of the rises of neuronal activity of the AQR, PQR and IL2R oxygen sensory neurons. Each horizontal line corresponds to a single stimulation trial. Vertical dashed line at 0 seconds denotes transition from the 11% to 21% [O_2]. (**B**) Scatter plots showing the rise onset times for different pairs of oxygen sensory neurons. Color code indicate data coming from the individual datasets. Insets within each scatter plot show the color code corresponding to individual datasets and the correlation coefficient calculated between the rise onset times of the indicated neuron pairs for each dataset. Number on top of each scatter plot is a correlation coefficient calculated between the rise onset times of an indicated pair of neurons across all datasets.

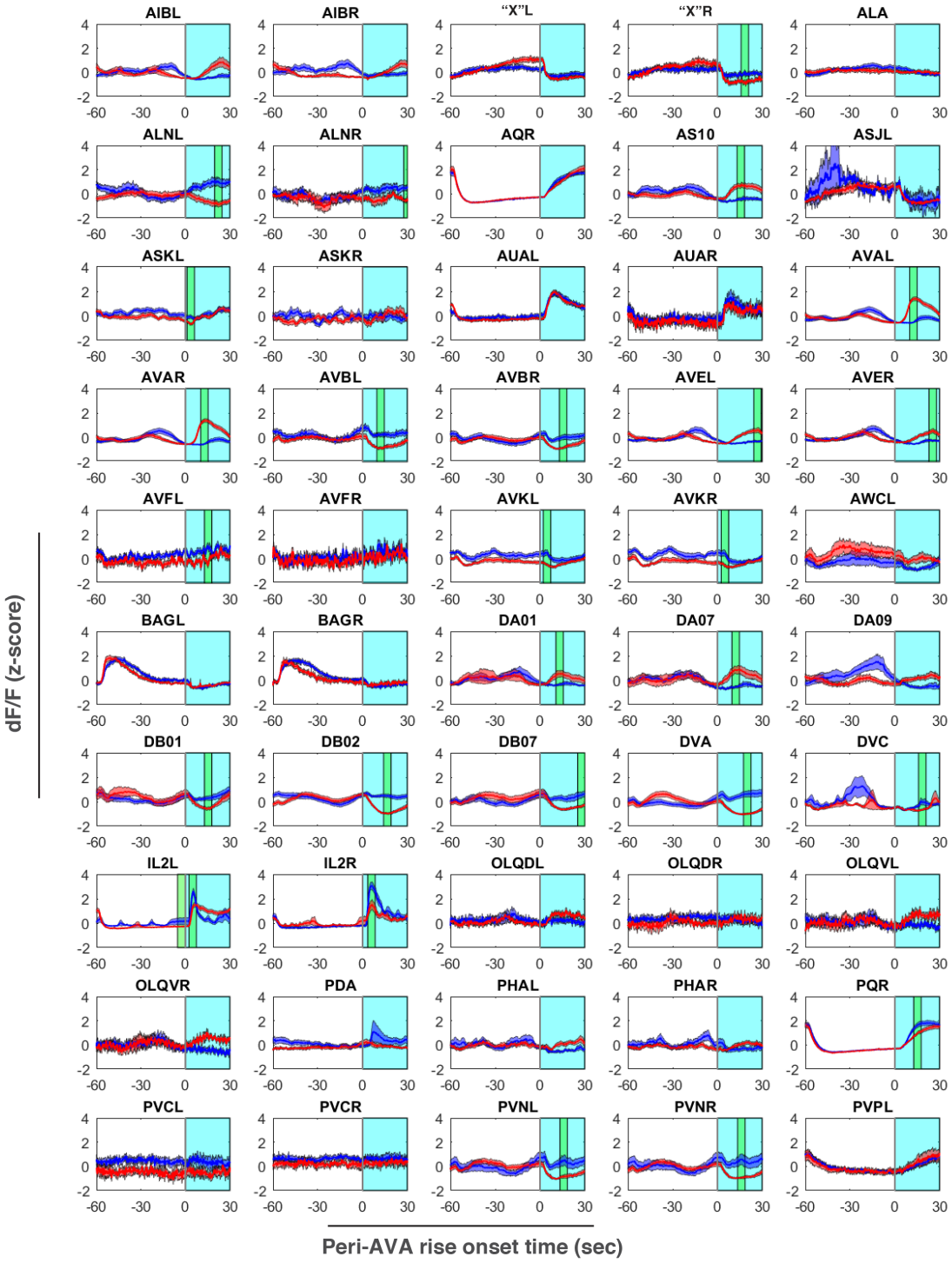
AIBL
AIBR
"X"L
"X"R
ALA
ALNL
ALNR
AQR
AS10
ASJL
ASKL
ASKR
AUAL
AUAR
AVAL
AVAR
AVBL
AVBR
AVEL
AVER
AVFL
AVFR
AVKL
AVKR
AWCL
BAGL
BAGR
DA01
DA07
DA09
DB01
DB02
DB07
DVA
DVC
IL2L
IL2R
OLQDL
OLQDR
OLQVL
OLQVR
PDA
PHAL
PHAR
PQR
PVCL
PVCR
PVNL
PVNR
PVPL
dF/F (z-score)
Peri-AVA rise onset time (sec)

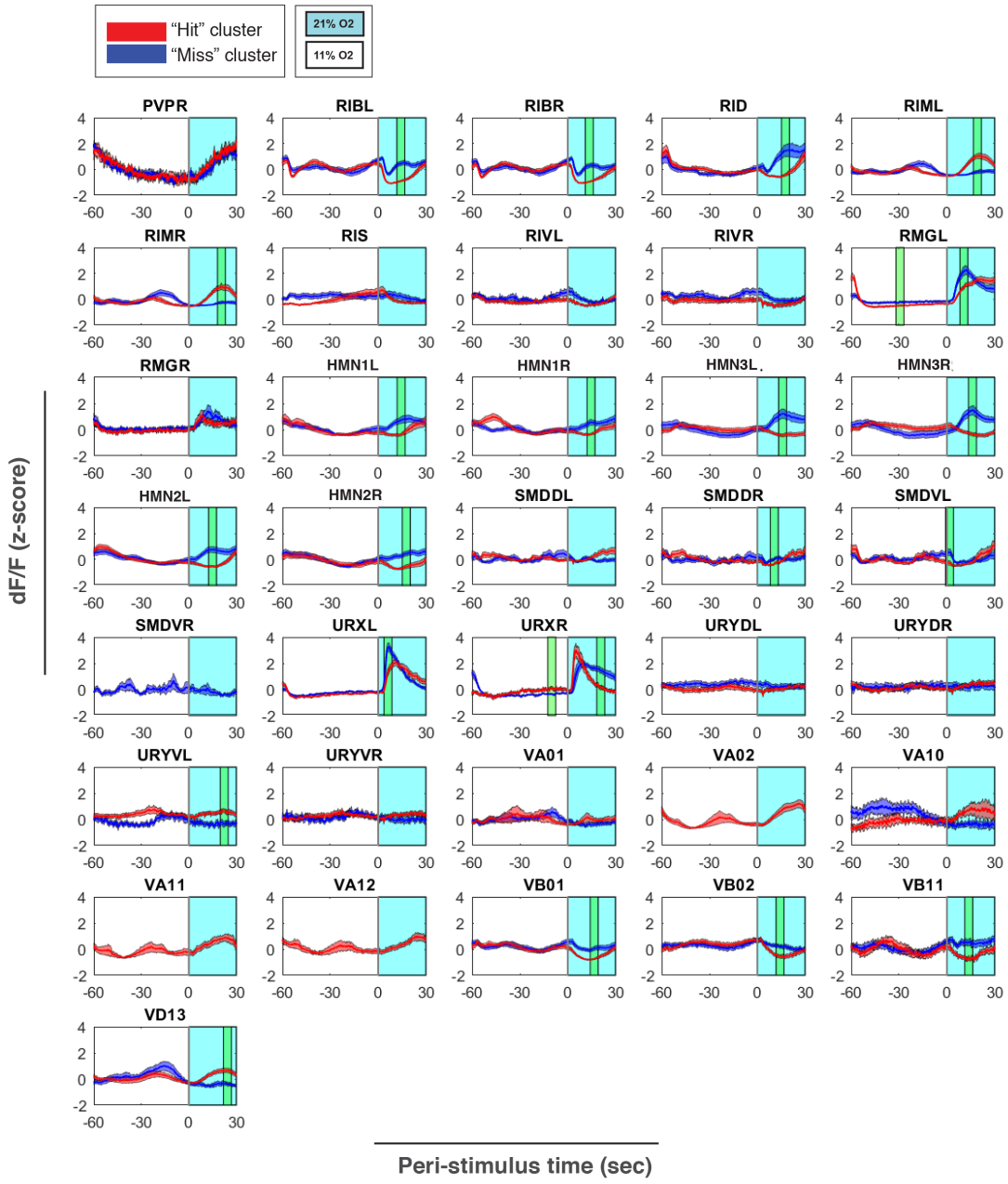

Figure S3. "Hit-Miss" stimulus-triggered averages of neuronal activity of all identified neurons
Each panel corresponds to a particular neuron. Within each panel trials averages of neuronal activity for "Hit" and "Miss" clusters are depicted with different color-code. Shaded areas represent ± SEM. Vertical line at 0 seconds represents the transition between 11% and 21% [O_2] periods. Green bars represent the 15 seconds time windows where statistical tests were performed.

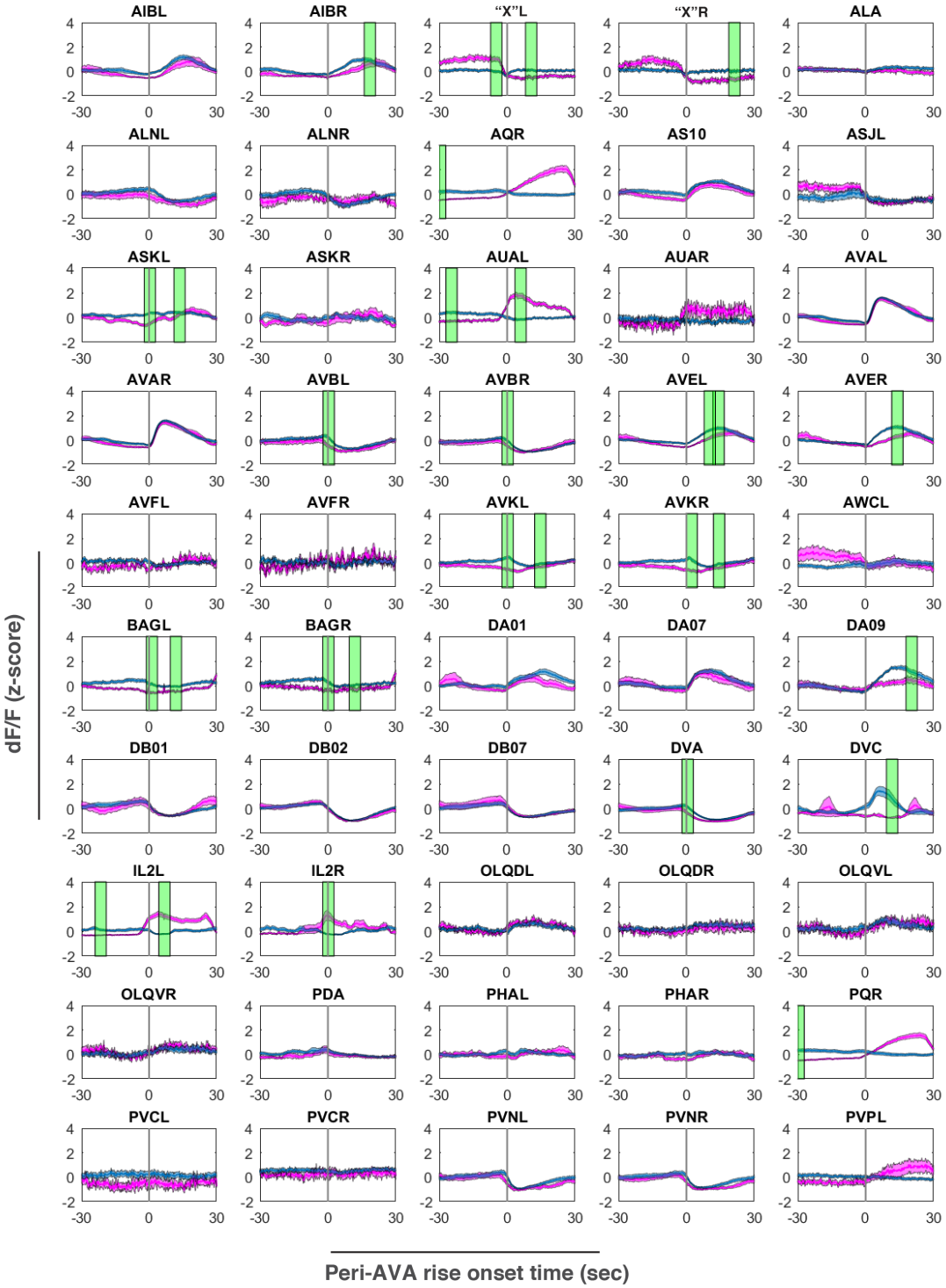
AIBL
AIBR
"X"L
"X"R
ALA
ALNL
ALNR
AQR
AS10
ASJL
ASKL
ASKR
AUAL
AUAR
AVAL
AVAR
AVBL
AVBR
AVEL
AVER
AVFL
AVFR
AVKL
AVKR
AWCL
BAGL
BAGR
DA01
DA07
DA09
DB01
DB02
DB07
DVA
DVC
IL2L
IL2R
OLQDL
OLQDR
OLQVL
OLQVR
PDA
PHAL
PHAR
PQR
PVCL
PVCR
PVNL
PVNR
PVPL
dF/F (z-score)
Peri-AVA rise onset time (sec)

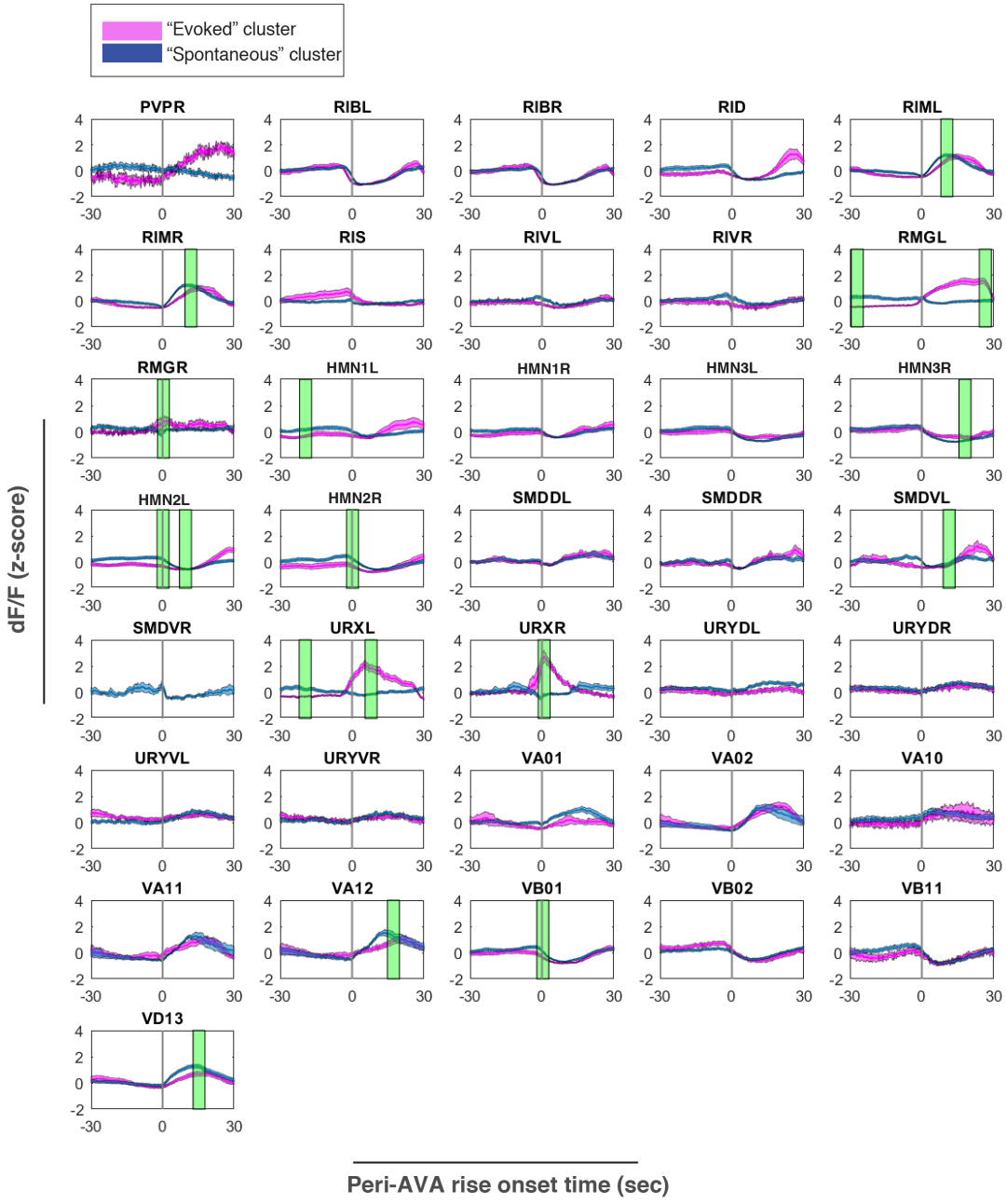

Figure S4. "Evoked-Spontaneous" AVA-triggered averages of neuronal activity of all identified neurons
Each panel corresponds to a particular neuron. Within each panel trials averages of neuronal activity for "Evoked" and "Spontaneous" clusters are depicted with different color-code. Shaded areas represent ± SEM. Vertical line at 0 seconds represents the transition between pre- and post- AVA rise onset time periods. Green bars represent the 15 seconds time windows where statistical tests were performed.

NeuronID	N Hit	N Miss	Pre Max	Pre Min	Post Max	Post Min
AIBL	16	19	n.s	n.s	n.s	n.s
AIBR	17	18		n.s	n.s	n.s
"X"L	30	21	n.s		n.s	n.s
"X"R	19	19	n.s		n.s	7,08E-03
ALA	23	27		n.s	n.s	n.s
ALNL	17	8	n.s	n.s	n.s	2,21E-03
ALNR	5	7	n.s	n.s		3,55E-02
AQR	24	26	n.s	n.s	n.s	n.s
AS10	23	17	n.s	n.s	5,25E-04	
ASJL	11	2	n.s	n.s	n.s	n.s
ASKL	35	28		n.s	n.s	3,33E-02
ASKR	12	11	n.s	n.s	n.s	n.s
AUAL	35	28		n.s	n.s	n.s
AUAR	7	8	n.s	n.s	n.s	n.s
AVAL	35	28		n.s	<1E-06	n.s
AVAR	35	28	n.s	n.s	<1E-06	n.s
AVBL	24	16	n.s	n.s		<1E-06
AVBR	24	16	n.s	n.s		6,62E-04
AVEL	35	28	n.s	n.s	2,10E-03	n.s
AVER	35	28	n.s	n.s	1,58E-03	n.s
AVFL	12	15		n.s		1,32E-02
AVFR	7	8	n.s	n.s	n.s	n.s
AVKL	17	18		n.s		7,47E-03
AVKR	17	18		n.s		8,40E-03
AWCL	7	8	n.s		n.s	n.s
BAGL	35	28		n.s	n.s	n.s
BAGR	23	27		n.s	n.s	n.s
DA01	12	15	n.s	n.s	2,58E-02	n.s
DA07	12	15	n.s	n.s	1,35E-03	
DA09	17	8		n.s	n.s	n.s
DB01	12	15	n.s		n.s	7,47E-03
DB02	35	28	n.s		n.s	<1E-06
DB07	23	17	n.s		n.s	4,51E-03
DVA	24	16	n.s	n.s		<1E-06
DVC	5	7		n.s	n.s	1,47E-02
IL2L	35	28		1,07E-02	n.s	1,04E-02
IL2R	28	20	n.s		n.s	3,42E-02
OLQDL	18	10	n.s	n.s	n.s	n.s
OLQDR	7	8	n.s	n.s	n.s	n.s
OLQVL	7	8	n.s	n.s	n.s	n.s
OLQVR	7	8	n.s	n.s	n.s	
PDA	35	18	n.s	n.s	n.s	n.s
PHAL	24	16	n.s	n.s	n.s	n.s
PHAR	24	16		n.s	n.s	n.s
PQR	35	28	n.s	n.s	n.s	1,65E-02
PVCL	5	7		n.s		n.s
PVCR	5	7		n.s		n.s
PVNL	19	9	n.s	n.s		1,36E-02
PVNR	19	9	n.s	n.s		3,58E-03
PVPL	12	25	n.s	n.s	n.s	n.s
PVPR	7	8	n.s	n.s	n.s	n.s

NeuronID	N Hit	N Miss	Pre Max	Pre Min	Post Max	Post Min
RIBL	35	28	n.s	n.s		<1E-06
RIBR	35	28	n.s	n.s		<1E-06
RID	23	17	n.s	n.s		1,40E-03
RIML	35	28	n.s	n.s	<1E-06	n.s
RIMR	35	28	n.s	n.s	<1E-06	n.s
RIS	30	21	n.s	n.s	n.s	n.s
RIVL	35	28	n.s	n.s	n.s	n.s
RIVR	17	18		n.s	n.s	n.s
RMGL	35	28		1,42E-02	n.s	4,16E-03
RMGR	28	20	n.s	n.s	n.s	n.s
HMN1L	23	27	n.s	n.s	n.s	9,17E-04
HMN1R	35	28	n.s	n.s		<1E-06
HMN3L	35	18	n.s		n.s	<1E-06
HMN3R	35	18	n.s		n.s	<1E-06
HMN2L	46	30	n.s	n.s		<1E-06
HMN2R	24	26	n.s	n.s		3,61E-04
SMDDL	35	28	n.s	n.s	n.s	n.s
SMDDR	35	28	n.s	n.s	n.s	1,99E-02
SMDVL	23	27	n.s	n.s	n.s	1,78E-02
SMDVR						
URXL	23	27		n.s	n.s	2,30E-03
URXR	12	11	3,64E-02		n.s	1,06E-03
URYDL	28	20		n.s	n.s	n.s
URYDR	23	13	n.s	n.s	n.s	n.s
URYVL	23	13	n.s		1,23E-02	
URYVR	23	13	n.s	n.s	n.s	n.s
VA01	12	25	n.s	n.s	n.s	n.s
VA02	12	1	n.s	n.s	n.s	n.s
VA10	7	8	n.s	n.s	n.s	
VA11	12	1	n.s	n.s	n.s	n.s
VA12	12	1	n.s	n.s	n.s	n.s
VB01	35	28	n.s	n.s		<1E-06
VB02	35	28	n.s		n.s	1,40E-03
VB11	12	15	n.s	n.s		1,06E-03
VD13	35	18		n.s	<1E-06	n.s

Table S1. Results of statistical tests for the "Hit-Miss" stimulus-triggered averages analysis (related to fig. S3)
Second and third columns: Number of "Hit" and "Miss" trials (correspondingly) used for the statistical test and for the triggered average analysis (**fig. S3**). Fourth to seventh columns: p-values for resampling statistical test of deltas between the average amplitude of neuronal activity at "Hit" and "Miss" trials. Fourth column: statistical test performed at the pre-stimulus time window for instances where the average amplitude value for "Hit" trials exceeded those for "Miss" trials. Fifth column: statistical test performed at the pre-stimulus time window for instances where the average amplitude value for "Miss" trials exceeded those for "Hit" trials. Sixth column: statistical test performed at the post-stimulus time window for instances where the average amplitude value for "Hit" trials exceeded those for "Miss" trials. Seventh column: statistical test performed at the post-stimulus time window for instances where the average amplitude value for "Miss" trials exceeded those for "Hit" trials. Empty cells indicate cases where statistical was not performed since such instance didn't exist. P values were corrected for multiple comparisons (Methods).

NeuronID	N Evoked	N Spontaneous	Pre Max	Pre Min	Post Max	Post Min
AIBL	16	49	n.s	n.s	n.s	n.s
AIBR	17	50	n.s	n.s	n.s	2,58E-02
"X"L	30	68	n.s	n.s		<1E-06
"X"R	19	54	n.s	n.s		<1E-06
ALA	23	74	n.s	n.s		n.s
ALNL	17	36	n.s	n.s		n.s
ALNR	5	21	n.s	n.s	n.s	n.s
AQR	24	75	n.s	3,97E-03	<1E-06	n.s
AS10	23	60	n.s	n.s		n.s
ASJL	11	14	n.s		n.s	n.s
ASKL	35	89	n.s	<1E-06	n.s	8,54E-04
ASKR	12	29	n.s	n.s	n.s	n.s
AUAL	35	89	n.s	6,62E-04	<1E-06	n.s
AUAR	7	25	n.s	n.s	n.s	n.s
AVAL	35	89	n.s	n.s	n.s	n.s
AVAR	35	89	n.s	n.s	n.s	n.s
AVBL	24	61	n.s	n.s	n.s	5,26E-03
AVBR	24	61	n.s	n.s	n.s	2,58E-02
AVEL	35	89	n.s	4,97E-03	n.s	4,75E-04
AVER	35	89	n.s	n.s		<1E-06
AVFL	12	46	n.s	n.s	n.s	n.s
AVFR	7	25	n.s	n.s	n.s	n.s
AVKL	17	50		4,97E-03		<1E-06
AVKR	17	50		7,94E-03		<1E-06
AWCL	7	25	n.s		n.s	n.s
BAGL	35	89		<1E-06	n.s	<1E-06
BAGR	23	74		1,70E-03	n.s	1,44E-02
DA01	12	46	n.s	n.s		n.s
DA07	12	46	n.s	n.s		n.s
DA09	17	36	n.s	n.s	n.s	<1E-06
DB01	12	46	n.s	n.s	n.s	n.s
DB02	35	89	n.s	n.s		n.s
DB07	23	60	n.s		n.s	n.s
DVA	24	61	n.s	n.s		2,41E-02
DVC	5	21	n.s	n.s	n.s	2,85E-03
IL2L	35	89	n.s	6,62E-04	<1E-06	n.s
IL2R	28	64	n.s	n.s	<1E-06	n.s
OLQDL	18	39	n.s	n.s	n.s	n.s
OLQDR	7	25	n.s	n.s		n.s
OLQVL	7	25	n.s	n.s	n.s	n.s
OLQVR	7	25	n.s	n.s	n.s	n.s
PDA	35	75	n.s	n.s	n.s	n.s
PHAL	24	61	n.s	n.s	n.s	n.s
PHAR	24	61	n.s	n.s	n.s	n.s
PQR	35	89		<1E-06	<1E-06	n.s
PVCL	5	21		n.s		n.s
PVCR	5	21		n.s	n.s	n.s
PVNL	19	40	n.s	n.s		n.s
PVNR	19	40	n.s	n.s		n.s
PVPL	12	60		n.s	3,53E-02	n.s
PVPR	7	25		n.s	<1E-06	n.s

NeuronID	N Evoked	N Spontaneous	Pre Max	Pre Min	Post Max	Post Min
RIBL	35	89	n.s	n.s	n.s	n.s
RIBR	35	89	n.s	n.s	n.s	n.s
RID	23	60		n.s	3,15E-04	n.s
RIML	35	89	n.s	n.s	n.s	1,17E-03
RIMR	35	89	n.s	n.s	n.s	4,75E-04
RIS	30	68	n.s	n.s	n.s	n.s
RIVL	35	89		n.s	n.s	n.s
RIVR	17	50		n.s	n.s	n.s
RMGL	35	89		<1E-06	<1E-06	n.s
RMGR	28	64	n.s	n.s	3,53E-02	n.s
HMN1L	23	74		1,83E-02	n.s	n.s
HMN1R	35	89		n.s	n.s	n.s
HMN3L	35	75		n.s	n.s	n.s
HMN3L	35	75		n.s	1,89E-02	n.s
HMN2L	46	103		4,97E-03	4,58E-03	1,88E-02
HMN2L	24	75		n.s	n.s	2,56E-02
SMDDL	35	89	n.s	n.s	n.s	n.s
SMDDR	35	89		n.s	n.s	n.s
SMDVL	23	74	n.s	7,94E-03	1,89E-02	n.s
SMDVR						
URXL	23	74	n.s	4,97E-03	<1E-06	n.s
URXR	12	29	n.s	n.s	<1E-06	n.s
URYDL	28	64		n.s		n.s
URYDR	23	43	n.s	n.s	n.s	n.s
URYVL	23	43	n.s	n.s	n.s	n.s
URYVR	23	43	n.s	n.s	n.s	n.s
VA01	12	60	n.s	n.s		n.s
VA02	12	15	n.s	n.s	n.s	n.s
VA10	7	25		n.s	n.s	n.s
VA11	12	15	n.s		n.s	n.s
VA12	12	15	n.s	n.s	n.s	6,10E-03
VB01	35	89		n.s	n.s	2,11E-02
VB02	35	89	n.s		n.s	n.s
VB11	12	46	n.s	n.s	n.s	n.s
VD13	35	75	n.s	n.s		1,14E-02

Table S2. Results of statistical tests for the "Evoked-Spontaneous" AVA-triggered averages analysis (related to fig. S4)

Second and third columns: Number of "Evoked" and "Spontaneous" trials (correspondingly) used for the statistical test and for the triggered average analysis (**fig. S4**). Fourth to seventh columns: p-values for resampling statistical test of deltas between the average amplitude of neuronal activity at "Evoked" and "Spontaneous" trials. Fourth column: statistical test performed at the pre-stimulus time window for instances where the average amplitude value for "Evoked" trials exceeded those for "Spontaneous" trials. Fifth column: statistical test performed at the pre-stimulus time window for instances where the average amplitude value for "Spontaneous" trials exceeded those for "Evoked" trials. Sixth column: statistical test performed at the post-stimulus time window for instances where the average amplitude value for "Evoked" trials exceeded those for "Spontaneous" trials. Seventh column: statistical test performed at the post-stimulus time window for instances where the average amplitude value for "Spontaneous" trials exceeded those for "Evoked" trials. Empty cells indicate cases where statistical was not performed since such instance didn't exist. P values were corrected for multiple comparisons (Methods).

7. References

Ahrens, M. B., Li, J. M., Orger, M. B., Robson, D. N., Schier, A. F., Engert, F., & Portugues, R. (2012). Brain-wide neuronal dynamics during motor adaptation in zebrafish. *Nature*, *485*(7399), 471. https://doi.org/10.1038/NATURE11057

Aimon, S., Cheng, K. Y., Gjorgjieva, J., & Kadow, I. C. G. (2023). Global change in brain state during spontaneous and forced walk in drosophila is composed of combined activity patterns of different neuron classes. In *eLife* (Vol. 12). https://doi.org/10.7554/eLife.85202

Aimon, S., Katsuki, T., Jia, T., Grosenick, L., Broxton, M., Deisseroth, K., Sejnowski, T. J., & Greenspan, R. J. (2019). Fast near-whole-brain imaging in adult drosophila during responses to stimuli and behavior. In *PLoS Biology* (Vol. 17, Issue 2). https://doi.org/10.1371/journal.pbio.2006732

Altun, Z. F., & Hall, D. H. (2011). Nervous system, general description. In *WormAtlas*. https://doi.org/10.3908/wormatlas.1.18

Akerboom, J., Chen, T. W., Wardill, T. J., Tian, L., Marvin, J. S., Mutlu, S., Calderón, N. C., Esposti, F., Borghuis, B. G., Sun, X. R., Gordus, A., Orger, M. B., Portugues, R., Engert, F., Macklin, J. J., Filosa, A., Aggarwal, A., Kerr, R. A., Takagi, R., … Looger, L. L. (2012). Optimization of a GCaMP calcium indicator for neural activity imaging. *Journal of Neuroscience*, *32*(40), 13819–13840. https://doi.org/10.1523/JNEUROSCI.2601-12.2012

Allen, E. N., Ren, J., Zhang, Y., & Alcedo, J. (2015). Sensory systems: Their impact on C. elegans survival. *Neuroscience*, *296*, 15–25. https://doi.org/10.1016/j.neuroscience.2014.06.054

Bamgartl, H., Kritzler, K., Zimelka, W., & Zinkler, D. (1994). Local PO2 measurements in the environment of submerged soil microarthropods. *Acta Oecologica (Montrouge)*, *15*(6), 781–789.

Bargmann, C. I. (1998). Neurobiology of the Caenorhabditis elegans genome. *Science*, *282*(5396), 2028–2033. https://doi.org/10.1126/SCIENCE.282.5396.2028/SUPPL_FILE/986006.XHTML

Bargmann, C. I. (2006). Chemosensation in C. elegans. *WormBook : The Online Review of C. Elegans Biology*, 1–29. https://doi.org/10.1895/WORMBOOK.1.123.1

Barlow, H. B. (1972). Single units and sensation: A neuron doctrine for perceptual psychology? *Perception*, *1*(4), 371–394. https://doi.org/10.1068/p010371

Barlow, H. B. (2013). Possible Principles Underlying the Transformations of Sensory Messages. *Sensory Communication*, 216–234. https://doi.org/10.7551/mitpress/9780262518420.003.0013

Barlow, H. B., Levick, W. R., & Yoon, M. (1971). Responses to single quanta of light in retinal ganglion cells of the cat. *Vision Research*, *11*(SUPPL. 3), 87–101. https://doi.org/10.1016/0042-6989(71)90033-2

Barrett, L. (2011). Beyond the brain: How body and environment shape animal and human minds. Princeton University Press.

Barsalou, L. W. (1999). Perceptual symbol systems. *Behavioral and Brain Sciences*, *22*(4), 577–609. https://doi.org/10.1017/S0140525X99002149

Beck, J. M., Ma, W. J., Pitkow, X., Latham, P. E., & Pouget, A. (2012). Not Noisy, Just Wrong: The Role of Suboptimal Inference in Behavioral Variability. *Neuron*, *74*(1), 30–39. https://doi.org/10.1016/j.neuron.2012.03.016

Bell, C. C. (1989). Sensory coding and corollary discharge effects in mormyrid electric fish. *Journal of Experimental Biology*, *146*(1), 229–253. https://doi.org/10.1242/JEB.146.1.229

Bell, C. C. (1995). The Generation of Expectations in Cerebellum-Like Structures. *The Neurobiology of Computation*, 373–378. https://doi.org/10.1007/978-1-4615-2235-5_61

Bell, C. C., & Grant, K. (1989). Corollary discharge inhibition and preservation of temporal information in a sensory nucleus of mormyrid electric fish. *The Journal of Neuroscience : The Official Journal of the Society for Neuroscience*, *9*(3), 1029–1044. https://doi.org/10.1523/JNEUROSCI.09-03-01029.1989

Bell, H. C. (2014). Behavioral Variability in the Service of Constancy. *International Journal of Comparative Psychology*, *27*(2). https://doi.org/10.46867/ijcp.2014.27.02.02

Ben Arous, J., Tanizawa, Y., Rabinowitch, I., Chatenay, D., & Schafer, W. R. (2010). Automated imaging of neuronal activity in freely behaving Caenorhabditis elegans. *Journal of Neuroscience Methods*, *187*(2), 229–234. https://doi.org/10.1016/j.jneumeth.2010.01.011

Benjamini, Y., & Yekutieli, D. (2001). The control of the false discovery rate in multiple testing under dependency. *Https://Doi.Org/10.1214/Aos/1013699998*, *29*(4), 1165–1188. https://doi.org/10.1214/AOS/1013699998

Bennett, M. R. (1999). The early history of the synapse: From plato to sherrington. *Brain Research Bulletin*, *50*(2), 95–118. https://doi.org/10.1016/S0361-9230(99)00094-5

Benzi, R., Sutera, A., & Vulpiani, A. (1981). The mechanism of stochastic resonance. *Journal of Physics A: Mathematical and General*, *14*(11), L453. https://doi.org/10.1088/0305-4470/14/11/006

Bialek, W. (1987). Physical limits to sensation and perception. *Annual Review of Biophysics and Biophysical Chemistry*, *16*, 455–478. https://doi.org/10.1146/ANNUREV.BB.16.060187.002323

Braitenberg, V. (1984). *Vehicles: Experiments in synthetic psychology*. MIT Press.

Braun, H. A. (2021). Stochasticity Versus Determinacy in Neurobiology: From Ion Channels to the Question of the "Free Will." *Frontiers in Systems Neuroscience*, *15*(May), 1–13. https://doi.org/10.3389/fnsys.2021.629436

Brembs, B. (2011a). Spontaneous decisions and operant conditioning in fruit flies. *Behavioural Processes*, *87*(1), 157–164. https://doi.org/10.1016/j.beproc.2011.02.005

Brembs, B. (2011b). Towards a scientific concept of free will as a biological trait: Spontaneous actions and decision-making in invertebrates. *Proceedings of the Royal Society B: Biological Sciences*, *278*(1707), 930–939. https://doi.org/10.1098/rspb.2010.2325

Brenner, S. (1974). The Genetics of Caenorhabditis elegans. *Genetics*, *77*(1), 71. https://doi.org/10.1093/GENETICS/77.1.71

Brezovec, B. E., Berger, A. B., Hao, Y. A., Chen, F., Druckmann, S., & Clandinin, T. R. (2024). Mapping the neural dynamics of locomotion across the Drosophila brain. *Current Biology*, *34*(4), 710-726.e4. https://doi.org/10.1016/J.CUB.2023.12.063

Brooks, R. A. (1999). Cambrian Intelligence: The Early History of the New AI. *Cambrian Intelligence*. https://doi.org/10.7551/MITPRESS/1716.001.0001

Buhrmann, T., Di Paolo, E. A., & Barandiaran, X. (2013). A Dynamical Systems Account of Sensorimotor Contingencies. *Frontiers in Psychology*, *4*(MAY). https://doi.org/10.3389/FPSYG.2013.00285

Bullock, T. H. (1993). Neuron Doctrine and Electrophysiology. *How Do Brains Work?*, 91–96. https://doi.org/10.1007/978-1-4684-9427-3_10

Bullock, T. H. (1997). Signals and signs in the nervous system: The dynamic anatomy of electrical activity is probably information-rich. *Proceedings of the National Academy of Sciences of the United States of America*, *94*(1), 1–6. https://doi.org/10.1073/pnas.94.1.1

Bullock, T. H., Bennett, M. V. L., Johnston, D., Josephson, R., Marder, E., & Fields, R. D. (2005). The neuron doctrine, redux. *Science*, *310*(5749), 791–793. https://doi.org/10.1126/science.1114394

Burock, M. (2008). Information and the function of neurons. *https://philsci-archive.pitt.edu/8734/1/information_and_the_function_of_neurons.pdf*

Busch, K. E., Laurent, P., Soltesz, Z., Murphy, R. J., Faivre, O., Hedwig, B., Thomas, M., Smith, H. L., & Bono, M. De. (2012). Tonic signaling from O 2 sensors sets neural circuit activity and behavioral state. *Nature Publishing Group*, *15*(4), 581–591. https://doi.org/10.1038/nn.3061

Buschman, T. J., & Miller, E. K. (2007). Top-down versus bottom-up control of attention in the prefrontal and posterior parietal cortices. *Science*, *315*(5820), 1860–1864. https://doi.org/10.1126/science.1138071

Busse, L. (2020). The influence of locomotion on sensory processing and its underlying neuronal circuits. *Neuroforum*, *24*(1), A41–A51. https://doi.org/10.1515/nf-2017-A046

Busse, L., Cardin, J. A., Chiappe, M. E., Halassa, M. M., McGinley, M. J., Yamashita, T., & Saleem, A. B. (2017). Sensation during active behaviors. *Journal of Neuroscience*, *37*(45), 10826–10834. https://doi.org/10.1523/JNEUROSCI.1828-17.2017

Cáceres, I. de C., Valmas, N., Hilliard, M. A., & Lu, H. (2012). Laterally Orienting C. elegans Using Geometry at Microscale for High-Throughput Visual Screens in Neurodegeneration and Neuronal Development Studies. *PLoS ONE*, *7*(4), 35037. https://doi.org/10.1371/JOURNAL.PONE.0035037

Carrillo, M. A., Guillermin, M. L., Rengarajan, S., Okubo, R. P., & Hallem, E. A. (2013). O2-sensing neurons control CO2 response in C. elegans. *Journal of Neuroscience*, *33*(23), 9675–9683. https://doi.org/10.1523/JNEUROSCI.4541-12.2013

Chaisanguanthum, K. S., Shen, H. H., & Sabes, P. N. (2014). Motor Variability Arises from a Slow Random Walk in Neural State. *Journal of Neuroscience*, *34*(36), 12071–12080. https://doi.org/10.1523/JNEUROSCI.3001-13.2014

Chalasani, S. H., Chronis, N., Tsunozaki, M., Gray, J. M., Ramot, D., Goodman, M. B., & Bargmann, C. I. (2007). Dissecting a circuit for olfactory behaviour in Caenorhabditis elegans. *Nature*, *450*(7166), 63–70. https://doi.org/10.1038/nature06292

Chalfie, M., Sulston, J. E., White, J. G., Southgate, E., Nichol Thomson, J., & Brenner, S. (1985). The neural circuit for touch sensitivity in Caenorhabditis elegans. *Journal of Neuroscience*, *5*(4), 956–964. https://doi.org/10.1523/jneurosci.05-04-00956.1985

Chang, A. J., Chronis, N., Karow, D. S., Marletta, M. A., & Bargmann, C. I. (2006b). A Distributed Chemosensory Circuit for Oxygen Preference in C. elegans. *PLoS Biology*, *4*(9), e274. https://doi.org/10.1371/journal.pbio.0040274

Chang, S., Johnston, R. J., Frøkjær-Jensen, C., Lockery, S., & Hobert, O. (2004). MicroRNAs act sequentially and asymmetrically to control chemosensory laterality in the nematode. *Nature 2004 430:7001*, *430*(7001), 785–789. https://doi.org/10.1038/nature02752

Charnov, E. L. (1976). Optimal foraging, the marginal value theorem. *Theoretical Population Biology*, *9*(2), 129–136. https://doi.org/10.1016/0040-5809(76)90040-X

Chase, D. L., & Koelle, M. R. (2007). Biogenic amine neurotransmitters in C. elegans. *WormBook : The Online Review of C. Elegans Biology*, 1–15. https://doi.org/10.1895/wormbook.1.132.1

Chemero, A. (2009). Radical embodied cognitive science. MIT Press.

Chen, T. W., Wardill, T. J., Sun, Y., Pulver, S. R., Renninger, S. L., Baohan, A., Schreiter, E. R., Kerr, R. A., Orger, M. B., Jayaraman, V., Looger, L. L., Svoboda, K., & Kim, D. S. (2013). Ultra-sensitive fluorescent proteins for imaging neuronal activity. *Nature*, *499*(7458), 295. https://doi.org/10.1038/NATURE12354

Cheung, B. H. H., Cohen, M., Rogers, C., Albayram, O., & De Bono, M. (2005). Experience-dependent modulation of C. elegans behavior by ambient oxygen. *Current Biology*, *15*(10), 905–917. https://doi.org/10.1016/j.cub.2005.04.017

Chew, Y. L., Tanizawa, Y., Cho, Y., Zhao, B., Yu, A. J., Ardiel, E. L., Rabinowitch, I., Bai, J., Rankin, C. H., Lu, H., Beets, I., & Schafer, W. R. (2018). An Afferent Neuropeptide System Transmits Mechanosensory Signals Triggering Sensitization and Arousal in C. elegans. *Neuron*, *99*(6), 1233-1246.e6. https://doi.org/10.1016/j.neuron.2018.08.003

Chiappe, M. E., Seelig, J. D., Reiser, M. B., & Jayaraman, V. (2010). Walking modulates speed sensitivity in drosophila motion vision. *Current Biology*, *20*(16), 1470–1475. https://doi.org/10.1016/j.cub.2010.06.072

Chronis, N., Zimmer, M., & Bargmann, C. I. (2007). Microfluidics for in vivo imaging of neuronal and behavioral activity in Caenorhabditis elegans. *Nature Methods*, *4*(9), 727–731. https://doi.org/10.1038/nmeth1075

Churchland, A. K., Kiani, R., & Shadlen, M. N. (2008). Decision-making with multiple alternatives. *Nature Neuroscience*, *11*(6), 693–702. https://doi.org/10.1038/nn.2123

Clark, A. (2013). Whatever next? Predictive brains, situated agents, and the future of cognitive science. *Behavioral and Brain Sciences*, *36*(3), 181–204. https://doi.org/10.1017/S0140525X12000477

Clark, A., & Grush, R. (1999). Towards a cognitive robotics. *Adaptive Behavior*, *7*(1), 5–16. https://doi.org/10.1177/105971239900700101

Clark, D. A., Biron, D., Sengupta, P., & Samuel, A. D. T. (2006). The AFD sensory neurons encode multiple functions underlying thermotactic behavior in Caenorhabditis elegans. *Journal of Neuroscience*, *26*(28), 7444–7451. https://doi.org/10.1523/jneurosci.1137-06.2006

Clark, A. (2008). Supersizing the mind: Embodiment, action, and cognitive extension. Oxford University Press.

Clemens, J., & Murthy, M. (2017). The use of computational modeling to link sensory processing with behavior in drosophila. *Decoding Neural Circuit Structure and Function: Cellular Dissection Using Genetic Model Organisms*, 241–260. https://doi.org/10.1007/978-3-319-57363-2_9/COVER

Coates, J. C., & De Bono, M. (2002). Antagonistic pathways in neurons exposed to body fluid regulate social feeding in Caenorhabditis elegans. *Nature*, *419*(6910), 925–929. https://doi.org/10.1038/nature01170

Cochella, L., & Hobert, O. (2012). Embryonic priming of a miRNA locus predetermines postmitotic neuronal left/right asymmetry in C. elegans. *Cell*, *151*(6), 1229–1242. https://doi.org/10.1016/j.cell.2012.10.049

Collett, T. S., & Land, M. F. (1975). Visual control of flight behaviour in the hoverfly Syritta pipiens L. *Journal of Comparative Physiology ■ A*, *99*(1), 1–66. https://doi.org/10.1007/BF01464710

Cook, S. J., Jarrell, T. A., Brittin, C. A., Wang, Y., Bloniarz, A. E., Yakovlev, M. A., Nguyen, K. C. Q., Tang, L. T. H., Bayer, E. A., Duerr, J. S., Bülow, H. E., Hobert, O., Hall, D. H., & Emmons, S. W. (2019). Whole-animal connectomes of both Caenorhabditis elegans sexes. *Nature*, *571*(7763), 63–71. https://doi.org/10.1038/s41586-019-1352-7

Crapse, T. B., & Sommer, M. A. (2008). Corollary discharge across the animal kingdom. *Nature Reviews Neuroscience*, *9*(8), 587–600. https://doi.org/10.1038/nrn2457

Crochet, S., Lee, S. H., & Petersen, C. C. H. (2019). Neural Circuits for Goal-Directed Sensorimotor Transformations. *Trends in Neurosciences*, *42*(1), 66–77. https://doi.org/10.1016/j.tins.2018.08.011

Croll, N. A. (1975). Components and patterns in the behaviour of the nematode Caenorhabditis elegans. *Journal of Zoology*, *176*(2), 159–176. https://doi.org/10.1111/j.1469-7998.1975.tb03191.x

Cruse, H. (2003). The evolution of cognition - A hypothesis. *Cognitive Science*, *27*(1), 135–155. https://doi.org/10.1016/S0364-0213(02)00110-6

Cullen, K. E. (2004). Sensory signals during active versus passive movement. *Current Opinion in Neurobiology*, *14*(6), 698–706. https://doi.org/10.1016/j.conb.2004.10.002

De Bivort, B. L., & Van Swinderen, B. (2016). Evidence for selective attention in the insect brain. *Current Opinion in Insect Science*, *15*, 9–15. https://doi.org/10.1016/j.cois.2016.02.007

De Bono, M., & Bargmann, C. I. (1998). Natural variation in a neuropeptide Y receptor homolog modifies social behavior and food response in C. elegans. *Cell*, *94*(5), 679–689. https://doi.org/10.1016/S0092-8674(00)81609-8

De Bono, M., & Maricq, A. V. (2005). Neuronal substrates of complex behaviors in C. elegans. *Annual Review of Neuroscience*, *28*, 451–501. https://doi.org/10.1146/annurev.neuro.27.070203.144259

De Robertis, E. D., & Bennett, H. S. (1955). Some features of the submicroscopic morphology of synapses in frog and earthworm. *The Journal of Biophysical and Biochemical Cytology*, *1*(1), 47–58. https://doi.org/10.1083/jcb.1.1.47

Deco, G., Rolls, E. T., & Romo, R. (2009). Stochastic dynamics as a principle of brain function. *Progress in Neurobiology*, *88*(1), 1–16. https://doi.org/10.1016/j.pneurobio.2009.01.006

DeFelipe, J. (2009). Cajal's Place in the History of Neuroscience. *Encyclopedia of Neuroscience*, 497–507. https://doi.org/10.1016/B978-008045046-9.00989-X

Denninger, J. W., & Marletta, M. A. (1999). Guanylate cyclase and the .NO/cGMP signaling pathway. *Biochimica et Biophysica Acta - Bioenergetics*, *1411*(2–3), 334–350. https://doi.org/10.1016/S0005-2728(99)00024-9

Denny, M. (1993). *Air and water: the biology and physics of life's media*. https://books.google.com/books?hl=en&lr=&id=XjNS6v7q130C&oi=fnd&pg=PR17&ots=sKnBQFPAid&sig=-mxe0L0eG9n7-aYe82i9jZTfKik

Domenici, P., & Blake, R. W. (1993). Escape Trajectories in Angelfish (Pterophyllum Eimekei) . *Journal of Experimental Biology*, *177*(1), 253–272. https://doi.org/10.1242/jeb.177.1.253

Domenici, P., Booth, D., Blagburn, J. M., & Bacon, J. P. (2008). Cockroaches Keep Predators Guessing by Using Preferred Escape Trajectories. *Current Biology*, *18*(22), 1792–1796. https://doi.org/10.1016/J.CUB.2008.09.062

Donnelly, J. L., Clark, C. M., Leifer, A. M., Pirri, J. K., Haburcak, M., Francis, M. M., Samuel, A. D. T., & Alkema, M. J. (2013). Monoaminergic Orchestration of Motor Programs in a Complex C. elegans Behavior. *PLoS Biology*, *11*(4). https://doi.org/10.1371/journal.pbio.1001529

Doroquez, D. B., Berciu, C., Anderson, J. R., Sengupta, P., & Nicastro, D. (2014). A high-resolution morphological and ultrastructural map of anterior sensory cilia and glia in Caenorhabditis elegans. *ELife*, *2014*(3), 1–35. https://doi.org/10.7554/eLife.01948

Drew, M. (1992). Soil aeration and plant root metabolism. *Soil Science*, *154(4)*, 259–268.

Driver, P. M., & Humphries, D. A. (1988). *Protean behaviour: The biology of unpredictability*. Clarendon Press; Oxford University Press.

Dunn, T. W., Gebhardt, C., Naumann, E. A., Riegler, C., Ahrens, M. B., Engert, F., & Del Bene, F. (2016). Neural Circuits Underlying Visually Evoked Escapes in Larval Zebrafish. *Neuron*, *89*(3), 613–628. https://doi.org/10.1016/J.NEURON.2015.12.021

Eaton, R. C., Lavender, W. A., & Wieland, C. M. (1981). Identification of Mauthner-initiated response patterns in goldfish: Evidence from simultaneous cinematography and electrophysiology. *Journal of Comparative Physiology □ A*, *144*(4), 521–531. https://doi.org/10.1007/BF01326837

Edwards, S. L., Charlie, N. K., Milfort, M. C., Brown, B. S., Gravlin, C. N., Knecht, J. E., & Miller, K. G. (2008). A novel molecular solution for ultraviolet light detection in Caenorhabditis elegans. *PLoS Biology*, *6*(8), 1715–1729. https://doi.org/10.1371/journal.pbio.0060198

Eggermann, E., Kremer, Y., Crochet, S., & Petersen, C. C. H. (2014). Cholinergic Signals in Mouse Barrel Cortex during Active Whisker Sensing. *Cell Reports*, *9*(5), 1654–1660. https://doi.org/10.1016/j.celrep.2014.11.005

Engel, T. A., Steinmetz, N. A., Gieselmann, M. A., Thiele, A., Moore, T., & Boahen, K. (2016). Selective Modulation of Cortical State During Spatial Attention. *Science Research Reports*, *354*(6316), 1140–1144.

Faumont, S., Rondeau, G., Thiele, T. R., Lawton, K. J., McCormick, K. E., Sottile, M., Griesbeck, O., Heckscher, E. S., Roberts, W. M., Doe, C. Q., & Lockery, S. R. (2011). An Image-Free Opto-Mechanical system for creating virtual environments and imaging neuronal activity in freely moving caenorhabditis elegans. *PLoS ONE*, *6*(9). https://doi.org/10.1371/journal.pone.0024666

Feierstein, C. E., Portugues, R., & Orger, M. B. (2015). Seeing the whole picture: A comprehensive imaging approach to functional mapping of circuits in behaving zebrafish. *Neuroscience*, *296*, 26–38. https://doi.org/10.1016/j.neuroscience.2014.11.046

Finn, J. T., Grunwald, M. E., & Yau, K. W. (1996). Cyclic nucleotide-gated ion channels: An extended family with diverse functions. *Annual Review of Physiology*, *58*, 395–426. https://doi.org/10.1146/annurev.ph.58.030196.002143

Flanders, M. (2011). What is the biological basis of sensorimotor integration? *Biological Cybernetics*, *104*(1–2), 1–8. https://doi.org/10.1007/s00422-011-0419-9

Fotowat, H., Harrison, R. R., & Gabbiani, F. (2011). Multiplexing of Motor Information in the Discharge of a Collision Detecting Neuron during Escape Behaviors. *Neuron*, *69*(1), 147–158. https://doi.org/10.1016/j.neuron.2010.12.007

Fox, M. D., Snyder, A. Z., Vincent, J. L., & Raichle, M. E. (2007). Intrinsic Fluctuations within Cortical Systems Account for Intertrial Variability in Human Behavior. *Neuron*, *56*(1), 171–184. https://doi.org/10.1016/j.neuron.2007.08.023

Frézal, L., & Félix, M. A. (2015). C. elegans outside the Petri dish. *ELife*, *4*, 1–14. https://doi.org/10.7554/eLife.05849

Friston, K. (2005). A theory of cortical responses. *Philosophical Transactions of the Royal Society B: Biological Sciences*, *360*(1456), 815–836. https://doi.org/10.1098/RSTB.2005.1622

Fujiwara, T., Brotas, M., & Chiappe, M. E. (2022). Walking strides direct rapid and flexible recruitment of visual circuits for course control in Drosophila. *Neuron*, *110*(13), 2124-2138.e8. https://doi.org/10.1016/j.neuron.2022.04.008

Fujiwara, T., Cruz, T. L., Bohnslav, J. P., & Chiappe, M. E. (2017). A faithful internal representation of walking movements in the Drosophila visual system. *Nature Neuroscience*, *20*(1), 72–81. https://doi.org/10.1038/nn.4435

Fukutomi, M., & Carlson, B. A. (2020). A History of Corollary Discharge: Contributions of Mormyrid Weakly Electric Fish. *Frontiers in Integrative Neuroscience*, *14*(July). https://doi.org/10.3389/fnint.2020.00042

Gao, S., Guan, S. A., Fouad, A. D., Meng, J., Kawano, T., Huang, Y. C., Li, Y., Alcaire, S., Hung, W., Lu, Y., Qi, Y. B., Jin, Y., Alkema, M., Fang-Yen, C., & Zhen, M. (2018). Excitatory motor neurons are local oscillators for backward locomotion. *ELife*, *7*, 1–32. https://doi.org/10.7554/eLife.29915

Gelder, T. Van. (1995). *What Might Cognition Be, If Not Computation?* (pp. 345–381). J Philos 92(7). https://philpapers.org/rec/GELWMC

Goldberg, M. E., & Wurtz, R. H. (1972). Activity of superior colliculus in behaving monkey. I. Visual receptive fields of single neurons. *Journal of Neurophysiology*, *35*(4), 542–559. https://doi.org/10.1152/jn.1972.35.4.542

Gong, J., Yuan, Y., Ward, A., Kang, L., Zhang, B., Wu, Z., Peng, J., Feng, Z., Liu, J., & Xu, X. Z. S. (2016). The C. elegans taste receptor homolog LITE-1 is a photoreceptor. *Cell*, *167*(5), 1252. https://doi.org/10.1016/J.CELL.2016.10.053

Goodale, S. E., Ahmed, N., Zhao, C., de Zwart, J. A., Özbay, P. S., Picchioni, D., Duyn, J., Englot, D. J., Morgan, V. L., & Chang, C. (2021). Fmri-based detection of alertness predicts behavioral response variability. *ELife*, *10*, 1–20. https://doi.org/10.7554/eLife.62376

Goodman, M. B., Hall, D. H., Avery, L., & Lockery, S. R. (1998). Active currents regulate sensitivity and dynamic range in C. elegans Neurons. *Neuron*, *20*(4), 763–772. https://doi.org/10.1016/S0896-6273(00)81014-4

Gordon, N. (1998). Colour blindness. *Public Health*, *112*(2), 81–84. https://doi.org/10.1038/SJ.PH.1900446

Gordus, A., Pokala, N., Levy, S., Flavell, S. W., & Bargmann, C. I. (2015). Feedback from network states generates variability in a probabilistic olfactory circuit. *Cell*, *161*(2), 215–227. https://doi.org/10.1016/j.cell.2015.02.018

Gray, J. M., Hill, J. J., & Bargmann, C. I. (2005). A circuit for navigation in Caenorhabditis elegans. *Proceedings of the National Academy of Sciences of the United States of America*, *102*(9), 3184–3191. https://doi.org/10.1073/pnas.0409009101

Gray, J. M., Karow, D. S., Lu, H., Chang, A. J., Chang, J. S., Ellis, R. E., Marietta, M. A., & Bargmann, C. I. (2004). Oxygen sensation and social feeding mediated by a C. elegans guanylate cyclase homologue. *Nature*, *430*(6997), 317–322. https://doi.org/10.1038/nature02714

Guillermin, M. L., Carrillo, M. A., & Hallem, E. A. (2017). A Single Set of Interneurons Drives Opposite Behaviors in C. elegans. *Current Biology*, *27*(17), 2630-2639.e6. https://doi.org/10.1016/j.cub.2017.07.023

Guillery, R. W. (2007). Relating the neuron doctrine to the cell theory. Should contemporary knowledge change our view of the neuron doctrine? *Brain Research Reviews*, *55*(2), 411–421. https://doi.org/10.1016/J.BRAINRESREV.2007.01.005

Ha, H. ick, Hendricks, M., Shen, Y., Gabel, C. V., Fang-Yen, C., Qin, Y., Colón-Ramos, D., Shen, K., Samuel, A. D. T., & Zhang, Y. (2010). Functional Organization of a Neural Network for Aversive Olfactory Learning in Caenorhabditis elegans. *Neuron*, *68*(6), 1173–1186. https://doi.org/10.1016/j.neuron.2010.11.025

Hendricks, M. (2012). Compartmentalized calcium dynamics in a C. elegans interneuron encode head movement. *Nature*, *487*(7405), 99–103. https://doi.org/10.1038/nature11081

Hobert, O., Johnston, R. J., & Chang, S. (2002). Left–right asymmetry in the nervous system: the Caenorhabditis elegans model. *Nature Reviews Neuroscience 2002 3:8*, *3*(8), 629–640. https://doi.org/10.1038/nrn897

Horridge, G. A. (1968). The origins of the nervous system. In G. H. Bourne (Ed.), *The structure and function of nervous tissue* (Vol. 1, pp. 1–31). Academic Press.

Hubel, D. H., & Wiesel, T. N. (1959). Receptive fields of single neurones in the cat's striate cortex. *The Journal of Physiology*, *148*(3), 574–591. https://doi.org/10.1113/JPHYSIOL.1959.SP006308

Hubel, D. H., & Wiesel, T. N. (1998). Early exploration of the visual cortex. *Neuron*, *20*(3), 401–412. https://doi.org/10.1016/S0896-6273(00)80984-8

Humphries, N. E., Queiroz, N., Dyer, J. R. M., Pade, N. G., Musyl, M. K., Schaefer, K. M., Fuller, D. W., Brunnschweiler, J. M., Doyle, T. K., Houghton, J. D. R., Hays, G. C., Jones, C. S., Noble, L. R., Wearmouth, V. J., Southall, E. J., & Sims, D. W. (2010). Environmental context explains Lévy and Brownian movement patterns of marine predators. *Nature 2010 465:7301*, *465*(7301), 1066–1069. https://doi.org/10.1038/nature09116

Hums, I., Riedl, J., Mende, F., Kato, S., Kaplan, H. S., Latham, R., Sonntag, M., Traunmüller, L., & Zimmer, M. (2016). Regulation of two motor patterns enables the gradual adjustment of locomotion strategy in caenorhabditis elegans. *ELife*, *5*(MAY2016). https://doi.org/10.7554/ELIFE.14116

Hurley, S. (2001). Perception and action: Alternative views. *Synthese*, *129*(1), 3–40. https://doi.org/10.1023/A:1012643006930

Huston, S. J., & Jayaraman, V. (2011). Studying sensorimotor integration in insects. *Current Opinion in Neurobiology*, *21*(4), 527–534. https://doi.org/10.1016/j.conb.2011.05.030

Iemi, L., Busch, N. A., Laudini, A., Haegens, S., Samaha, J., Villringer, A., & Nikulin, V. V. (2019). Multiple mechanisms link prestimulus neural oscillations to sensory responses. *ELife*, *8*, 1–34. https://doi.org/10.7554/eLife.43620.001

Ino, Y., & Yoshida, K. (2009). Parallel use of two behavioral mechanisms for chemotaxis in Caenorhabditis elegans. *Journal of Neuroscience*, *29*(17), 5370–5380. https://doi.org/10.1523/JNEUROSCI.3633-08.2009

Ito, M. (1970). Neurophysiological aspects of the cerebellar motor control system. *International Journal of Neurology*, *7*(2), 162–176. https://europepmc.org/article/med/5499516

Jackson, B. S. (2004). Including long-range dependence in integrate-and-fire models of the high interspike-interval variability of cortical neurons. *Neural Computation*, *16*(10), 2125–2195. https://doi.org/10.1162/0899766041732413

Kandel, E. R. (2013). *Principles of Neural Science, Fifth Edition*. McGraw-Hill Education. https://books.google.at/books?id=s64z-LdAIsEC

Kaplan, H. S., Nichols, A. L. A., & Zimmer, M. (2018). Sensorimotor integration in Caenorhabditis elegans: A reappraisal towards dynamic and distributed computations. *Philosophical Transactions of the Royal Society B: Biological Sciences*, *373*(1758). https://doi.org/10.1098/rstb.2017.0371

Kaplan, H. S., Salazar Thula, O., Khoss, N., & Zimmer, M. (2020). Nested Neuronal Dynamics Orchestrate a Behavioral Hierarchy across Timescales. *Neuron*, *105*(3), 562-576.e9. https://doi.org/10.1016/j.neuron.2019.10.037

Kato, S., Kaplan, H. S., Schrödel, T., Skora, S., Lindsay, T. H., Yemini, E., Lockery, S., & Zimmer, M. (2015). Global Brain Dynamics Embed the Motor Command Sequence of Caenorhabditis elegans. *Cell*, *163*(3), 656–669. https://doi.org/10.1016/j.cell.2015.09.034

Kawano, T., Po, M. D., Gao, S., Leung, G., Ryu, W. S., & Zhen, M. (2011). An imbalancing act: Gap junctions reduce the backward motor circuit activity to bias C. elegans for forward locomotion. *Neuron*, *72*(4), 572–586. https://doi.org/10.1016/j.neuron.2011.09.005

Kawato, M. (1999). Internal models for motor control and trajectory planning. *Current Opinion in Neurobiology*, *9*(6), 718–727. https://doi.org/10.1016/S0959-4388(99)00028-8

Kazatskaya, A., Yuan, L., Amin-Wetzel, N., Philbrook, A., Bono, M. de, & Sengupta, P. (2020). The URX oxygen-sensing neurons in C. elegans are ciliated. *MicroPublication Biology*, *2020*. /pmc/articles/PMC7520127/%0Ahttps://www.ncbi.nlm.nih.gov/pmc/articles/PMC7520127/

Keijzer, F. (2001). Representation and Behavior. *Representation and Behavior*. https://doi.org/10.7551/MITPRESS/5889.001.0001

Keijzer, F. (2014). Searching for the roots of experience: Early nervous systems and the origins of the animal sensorimotor organization. *AISB 2014 - 50th Annual Convention of the AISB*, 1–2.

Keijzer, F. (2015). Moving and sensing without input and output: early nervous systems and the origins of the animal sensorimotor organization. *Biology and Philosophy*, *30*(3), 311–331. https://doi.org/10.1007/s10539-015-9483-1

Keijzer, F., & Arnellos, A. (2017). The animal sensorimotor organization: a challenge for the environmental complexity thesis. *Biology and Philosophy*, *32*(3), 421–441. https://doi.org/10.1007/s10539-017-9565-3

Keijzer, F., van Duijn, M., & Lyon, P. (2013). What nervous systems do: Early evolution, input-output, and the skin brain thesis. *Adaptive Behavior*, *21*(2), 67–85. https://doi.org/10.1177/1059712312465330

Keller, G. B., & Mrsic-Flogel, T. D. (2018). Predictive Processing: A Canonical Cortical Computation. *Neuron*, *100*(2), 424–435. https://doi.org/10.1016/j.neuron.2018.10.003

Kim, A. J., Fenk, L. M., Lyu, C., & Maimon, G. (2017). Quantitative Predictions Orchestrate Visual Signaling in Drosophila. *Cell*, *168*(1–2), 280-294.e12. https://doi.org/10.1016/j.cell.2016.12.005

Kim, A. J., Fitzgerald, J. K., & Maimon, G. (2015). Cellular evidence for efference copy in Drosophila visuomotor processing. *Nature Neuroscience*, *18*(9), 1247–1255. https://doi.org/10.1038/nn.4083

Kimata, T., Sasakura, H., Ohnishi, N., Nishio, N., & Mori, I. (2012). Thermotaxis of C. elegans as a model for temperature perception, neural information processing and neural plasticity. *Worm*, *1*(1), 31–41. https://doi.org/10.4161/worm.19504

Klimant, I., & Wolfbeis, O. S. (1995). Oxygen-Sensitive Luminescent Materials Based on Silicone-Soluble Ruthenium Diimine Complexes. *Analytical Chemistry*, *67*(18), 3160–3166. https://doi.org/10.1021/ac00114a010

Körding, K. P., & Wolpert, D. M. (2004). Bayesian integration in sensorimotor learning. *Nature*, *427*(6971), 244–247. https://doi.org/10.1038/nature02169

Lalazar, H., & Vaadia, E. (2008). Neural basis of sensorimotor learning: modifying internal models. *Current Opinion in Neurobiology*, *18*(6), 573–581. https://doi.org/10.1016/j.conb.2008.11.003

Larsch, J., Ventimiglia, D., Bargmann, C. I., & Albrecht, D. R. (2013). High-throughput imaging of neuronal activity in Caenorhabditis elegans. *Proceedings of the National Academy of Sciences of the United States of America*, *110*(45). https://doi.org/10.1073/pnas.1318325110

Laurent, P., Soltesz, Z., Nelson, G. M., Chen, C., Arellano-carbajal, F., Levy, E., & Bono, M. De. (2015). *Decoding a neural circuit controlling global animal state in C . elegans*. 1–32. https://doi.org/10.7554/eLife.04241

Lee, D. L. (1965). The physiology of nematodes. *The Physiology of Nematodes.*, *3*.

Lee, H., Choi, M. K., Lee, D., Kim, H. S., Hwang, H., Kim, H., Park, S., Paik, Y. K., & Lee, J. (2012). Nictation, a dispersal behavior of the nematode Caenorhabditis elegans, is regulated by IL2 neurons. *Nature Neuroscience*, *15*(1), 107–112. https://doi.org/10.1038/NN.2975

Li, W., Kang, L., Piggott, B. J., Feng, Z., & Xu, X. Z. S. (2011). The neural circuits and sensory channels mediating harsh touch sensation in Caenorhabditis elegans. *Nature Communications*, *2*(1). https://doi.org/10.1038/ncomms1308

Li, Z., Liu, J., Zheng, M., & Xu, X. Z. S. (2014). Encoding of both analog- and digital-like behavioral outputs by one C. Elegans interneuron. *Cell*, *159*(4), 751–765. https://doi.org/10.1016/j.cell.2014.09.056

Li, Z., Zhou, J., Wani, K. A., Yu, T., Ronan, E. A., Piggott, B. J., Liu, J., & Xu, X. Z. S. (2023). A C. elegans neuron both promotes and suppresses motor behavior to fine tune motor output. *Frontiers in Molecular Neuroscience*, *16*, 1228980. https://doi.org/10.3389/FNMOL.2023.1228980/BIBTEX

Lichtneckert, R., & Reichert, H. (2007). Origin and evolution of the first nervous system. *Evolution of Nervous Systems*, *1*, 289–315. https://doi.org/10.1016/B0-12-370878-8/00157-9

Lillywhite, P. G., & Laughlin, S. B. (1979). Transducer noise in a photoreceptor. *Nature 1979 277:5697*, *277*(5697), 569–572. https://doi.org/10.1038/277569a0

Lim, M. A., Chitturi, J., Laskova, V., Meng, J., Findeis, D., Wiekenberg, A., Mulcahy, B., Luo, L., Li, Y., Lu, Y., Hung, W., Qu, Y., Ho, C. Y., Holmyard, D., Ji, N., McWhirter, R., Samuel, A. D. T., Miller, D. M., Schnabel, R., … Zhen, M. (2016). Neuroendocrine modulation sustains the C. elegans forward motor state. *ELife*, *5*(NOVEMBER2016), 1–33. https://doi.org/10.7554/eLife.19887

Lindsay, T. H., Thiele, T. R., & Lockery, S. R. (2011). Optogenetic analysis of synaptic transmission in the central nervous system of the nematode Caenorhabditis elegans. *Nature Communications*, *2*(1). https://doi.org/10.1038/ncomms1304

Liu, J., Ward, A., Gao, J., Dong, Y., Nishio, N., Inada, H., Kang, L., Yu, Y., Ma, D., Xu, T., Mori, I., Xie, Z., & Xu, X. Z. S. (2010). C. elegans phototransduction requires a G protein-dependent cGMP pathway and a taste receptor homolog. *Nature Neuroscience*, *13*(6), 715. https://doi.org/10.1038/NN.2540

Liu, Q., Hollopeter, G., & Jorgensen, E. M. (2009). Graded synaptic transmission at the Caenorhabditis elegans neuromuscular junction. *Proceedings of the National Academy of Sciences of the United States of America*, *106*(26), 10823–10828. https://doi.org/10.1073/pnas.0903570106

Liu, Q., Kidd, P. B., Dobosiewicz, M., & Bargmann, C. I. (2018). C. elegans AWA Olfactory Neurons Fire Calcium-Mediated All-or-None Action Potentials. *Cell*, *175*(1), 57-70.e17. https://doi.org/10.1016/j.cell.2018.08.018

Lockery, S. R., & Goodman, M. B. (2009). The Quest for Action Potentials in C. elegans Neurons Hits a Plateau. *Nature Neuroscience*, *12*(4), 377. https://doi.org/10.1038/NN0409-377

Longtin, A., Bulsara, A., & Moss, F. (1991). Time-interval sequences in bistable systems and the noise-induced transmission of information by sensory neurons. *Physical Review Letters*, *67*(5), 656–659. https://doi.org/10.1103/PhysRevLett.67.656

López-Muñoz, F., Boya, J., & Alamo, C. (2006). Neuron theory, the cornerstone of neuroscience, on the centenary of the Nobel Prize award to Santiago Ramón y Cajal. *Brain Research Bulletin*, *70*(4–6), 391–405. https://doi.org/10.1016/J.BRAINRESBULL.2006.07.010

Luo, L., Wen, Q., Ren, J., Hendricks, M., Gershow, M., Qin, Y., Greenwood, J., Soucy, E. R., Klein, M., Smith-Parker, H. K., Calvo, A. C., Colón-Ramos, D. A., Samuel, A. D.

T., & Zhang, Y. (2014). Dynamic encoding of perception, memory, and movement in a C. elegans chemotaxis circuit. *Neuron*, *82*(5), 1115–1128. https://doi.org/10.1016/j.neuron.2014.05.010

MacOsko, E. Z., Pokala, N., Feinberg, E. H., Chalasani, S. H., Butcher, R. A., Clardy, J., & Bargmann, C. I. (2009). A hub-and-spoke circuit drives pheromone attraction and social behaviour in C. elegans. *Nature*, *458*(7242), 1171–1175. https://doi.org/10.1038/nature07886

Maguire, S. M., Clark, C. M., Nunnari, J., Pirri, J. K., & Alkema, M. J. (2011). The C. elegans touch response facilitates escape from predacious fungi. *Current Biology*, *21*(15), 1326–1330. https://doi.org/10.1016/j.cub.2011.06.063

Martin, J. R., Faure, P., & Ernst, R. (2001). The power law distribution for walking-time intervals correlates with the ellipsoid-body in Drosophila. *Journal of Neurogenetics*, *15*(3–4), 205–219. https://doi.org/10.3109/01677060109167377

Martin, J. R., Rogers, K. L., Chagneau, C., & Brûlet, P. (2007). In vivo Bioluminescence Imaging of Ca2+ Signalling in the Brain of Drosophila. *PLOS ONE*, *2*(3), e275. https://doi.org/10.1371/JOURNAL.PONE.0000275

Martin, K. A. C. (1994). A brief history of the "feature detector." *Cerebral Cortex*, *4*(1), 1–7. https://doi.org/10.1093/cercor/4.1.1

Martin, R. J., Robertson, A. P., Buxton, S. K., Beech, R. N., Charvet, C. L., & Neveu, C. (2012). Levamisole receptors: A second awakening. *Trends in Parasitology*, *28*(7), 289–296. https://doi.org/10.1016/j.pt.2012.04.003

Maye, A., Hsieh, C. H., Sugihara, G., & Brembs, B. (2007). Order in spontaneous behavior. *PLoS ONE*, *2*(5). https://doi.org/10.1371/journal.pone.0000443

McCulloch, W. S., & Pitts, W. (1943). A logical calculus of the ideas immanent in nervous activity. *The Bulletin of Mathematical Biophysics*, *5*(4), 115–133. https://doi.org/10.1007/BF02478259

Mellem, J. E., Brockie, P. J., Madsen, D. M., & Maricq, A. V. (2008). Action potentials contribute to neuronal signaling in C. elegans. *Nature Neuroscience*, *11*(8), 865–867. https://doi.org/10.1038/nn.2131

Meng, J., Ahamed, T., Yu, B., Hung, W., Mouridi, S. E., Wang, Z., Zhang, Y., Wen, Q., Boulin, T., Gao, S., & Zhen, M. (2024). A tonically active master neuron modulates mutually exclusive motor states at two timescales. *Science Advances*, *10*(15), eadk0002. https://doi.org/10.1126/SCIADV.ADK0002

Miall, R. C., Malkmus, M., & Robertson, E. M. (1996). Sensory prediction as a role for the cerebellum. *Behavioral and Brain Sciences*, *19*(3), 466–467. https://doi.org/10.1017/S0140525X00081796

Mori, H., Ashida, K., Shidara, H., Nikai, T., Hotta, K., & Oka, K. (2019). Serotonin modulates behavior-related neural activity of RID interneuron in Caenorhabditis elegans. *PLoS ONE*, *14*(12), 1–10. https://doi.org/10.1371/journal.pone.0226044

Musall, S., Kaufman, M. T., Juavinett, A. L., Gluf, S., & Churchland, A. K. (2019). Single-trial neural dynamics are dominated by richly varied movements. *Nature Neuroscience*, *22*(10), 1677–1686. https://doi.org/10.1038/s41593-019-0502-4

Nakai, J., Ohkura, M., & Imoto, K. (2001). A high signal-to-noise Ca2+ probe composed of a single green fluorescent protein. *Nature Biotechnology 2001 19:2*, *19*(2), 137–141. https://doi.org/10.1038/84397

Neuringer, A. (2004). Reinforced variability in animals and people: Implications for adaptive action. *American Psychologist*, *59*(9), 891–906. https://doi.org/10.1037/0003-066X.59.9.891

Nichols, A. L. A., Eichler, T., Latham, R., & Zimmer, M. (2017). A global brain state underlies C. Elegans sleep behavior. *Science*, *356*(6344), 1247–1256. https://doi.org/10.1126/science.aam6851

Niell, C. M., & Stryker, M. P. (2010). Modulation of Visual Responses by Behavioral State in Mouse Visual Cortex. *Neuron*, *65*(4), 472–479. https://doi.org/10.1016/j.neuron.2010.01.033

Nizami, L. (2019). Information Theory is Abused in Neuroscience. *Cybernetics and Human Knowing*, *26*(4), 47–97.

Noudoost, B., Chang, M. H., Steinmetz, N. A., & Moore, T. (2010). Top-down control of visual attention. *Current Opinion in Neurobiology*, *20*(2), 183–190. https://doi.org/10.1016/j.conb.2010.02.003

Oda, S., Toyoshima, Y., & De Bono, M. (2017). Modulation of sensory information processing by a neuroglobin in Caenorhabditis elegans. *Proceedings of the National Academy of Sciences of the United States of America*, *114*(23), E4658–E4665. https://doi.org/10.1073/pnas.1614596114

Ölveczky, B. P., Andalman, A. S., & Fee, M. S. (2005). Vocal Experimentation in the Juvenile Songbird Requires a Basal Ganglia Circuit. *PLOS Biology*, *3*(5), e153. https://doi.org/10.1371/JOURNAL.PBIO.0030153

O'Regan, K., & Noë, A. (2001). A sensorimotor account of vision and visual experience. *Behavioural and Brain Sciences*, *24*(5), 939–973.

O'Regan, J. K. (2011). Why red doesn't sound like a bell: Understanding the feel of consciousness. Oxford University Press.

Ouellette, M. H., Desrochers, M. J., Gheta, I., Ramos, R., & Hendricks, M. (2018). A gate-and-switch model for head orientation behaviors in Caenorhabditis elegans. *ENeuro*, *5*(6), 1–13. https://doi.org/10.1523/ENEURO.0121-18.2018

Parker, G. H. (1919). The elementary nervous system. *The Elementary Nervous System, by G.H. Parker ... 53 Illustrations.* https://doi.org/10.5962/BHL.TITLE.1880

Pantin, C. F. A. (1956). The origin of the nervous system. *Pubblicazioni della Stazione Zoologica di Napoli*, *28*, 171–181.

Passano, L. M., & Hutchinson, G. E. (1963). PRIMITIVE NERVOUS SYSTEMS. *Proceedings of the National Academy of Sciences of the United States Of*, *50*, 306–313. https://doi.org/10.1073/PNAS.50.2.306

Pavans De Ceccatty, M. (1974). The origin of the integrative systems: a change in view derived from research on coelenterates and sponges. *Perspectives in Biology and Medicine*, *17*(3), 379–390.

Pereira, L., Kratsios, P., Serrano-Saiz, E., Sheftel, H., Mayo, A. E., Hall, D. H., White, J. G., LeBoeuf, B., Garcia, L. R., Alon, U., & Hobert, O. (2015). A cellular and regulatory map of the cholinergic nervous system of C. Elegans. *ELife*, *4*(DECEMBER2015), 1–46. https://doi.org/10.7554/eLife.12432

Persson, A., Gross, E., Laurent, P., Busch, K. E., Bretes, H., & de Bono, M. (2009). Natural variation in a neural globin tunes oxygen sensing in wild Caenorhabditis elegans. *Nature*, *458*(7241), 1030–1033. https://doi.org/10.1038/nature07820

Pfeifer, R., & Bongard, J. (2007). *How the body shapes the way we think*. MIT Press.

Pierce-Shimomura, J. T., Morse, T. M., & Lockery, S. R. (1999). The fundamental role of pirouettes in Caenorhabditis elegans chemotaxis. *Journal of Neuroscience*, *19*(21), 9557–9569. https://doi.org/10.1523/jneurosci.19-21-09557.1999

Piggott, B. J., Liu, J., Feng, Z., Wescott, S. A., & Xu, X. Z. S. (2011). The neural circuits and synaptic mechanisms underlying motor initiation in C. elegans. *Cell*, *147*(4), 922–933. https://doi.org/10.1016/j.cell.2011.08.053

Pokala, N., Liu, Q., Gordus, A., & Bargmann, C. I. (2014). Inducible and titratable silencing of Caenorhabditis elegans neurons in vivo with histamine-gated chloride channels. *Proceedings of the National Academy of Sciences of the United States of America*, *111*(7), 2770–2775. https://doi.org/10.1073/PNAS.1400615111/SUPPL_FILE/SM02.AVI

Portugues, R., Feierstein, C. E., Engert, F., & Orger, M. B. (2014). Whole-brain activity maps reveal stereotyped, distributed networks for visuomotor behavior. *Neuron*, *81*(6), 1328–1343. https://doi.org/10.1016/J.NEURON.2014.01.019

Poulet, J. F. A., & Hedwig, B. (2002). A corollary discharge maintains auditory sensitivity during sound production. *Nature*, *418*(6900), 872–876. https://doi.org/10.1038/nature00919

Poulet, J. F. A., & Hedwig, B. (2003). A corollary discharge mechanism modulates central auditory processing in singing crickets. *Journal of Neurophysiology*, *89*(3), 1528–1540. https://doi.org/10.1152/jn.0846.2002

Poulet, J. F. A., & Hedwig, B. (2006). The cellular basis of a corollary discharge. *Science*, *311*(5760), 518–522. https://doi.org/10.1126/science.1120847

Poulet, J. F. A., & Hedwig, B. (2007). New insights into corollary discharges mediated by identified neural pathways. *Trends in Neurosciences*, *30*(1), 14–21. https://doi.org/10.1016/j.tins.2006.11.005

Powers, W. T. . (19892). *Living control systems : selected papers of William T. Powers*. 300.

Prevedel, R., Yoon, Y. G., Hoffmann, M., Pak, N., Wetzstein, G., Kato, S., Schrödel, T., Raskar, R., Zimmer, M., Boyden, E. S., & Vaziri, A. (2014). Simultaneous whole-animal 3D imaging of neuronal activity using light-field microscopy. *Nature Methods*, *11*(7), 727–730. https://doi.org/10.1038/nmeth.2964

Raizen, D. M., Zimmerman, J. E., Maycock, M. H., Ta, U. D., You, Y. J., Sundaram, M. V., & Pack, A. I. (2008). Lethargus is a Caenorhabditis elegans sleep-like state. *Nature*, *451*(7178), 569–572. https://doi.org/10.1038/nature06535

Ramot, D., Johnson, B. E., Berry, T. L., Carnell, L., & Goodman, M. B. (2008). The parallel worm tracker: A platform for measuring average speed and drug-induced paralysis in nematodes. *PLoS ONE*, *3*(5), 6–12. https://doi.org/10.1371/journal.pone.0002208

Rao, R. P. N., & Ballard, D. H. (1999). Predictive coding in the visual cortex: A functional interpretation of some extra-classical receptive-field effects. *Nature Neuroscience*, *2*(1), 79–87. https://doi.org/10.1038/4580

Raviola, E., & Mazzarello, P. (2011). The diffuse nervous network of Camillo Golgi: Facts and fiction. *Brain Research Reviews*, *66*(1–2), 75–82. https://doi.org/10.1016/j.brainresrev.2010.09.005

Requarth, T., & Sawtell, N. B. (2011). Neural mechanisms for filtering self-generated sensory signals in cerebellum-like circuits. *Current Opinion in Neurobiology*, *21*(4), 602–608. https://doi.org/10.1016/j.conb.2011.05.031

Reviewed, P. (2004). The emulation theory of representation : Motor control , imagery , and perception. *Behavioral and Brain Sciences*, 377–442.

Reynolds, J. H., & Chelazzi, L. (2004). Attentional modulation of visual processing. *Annual Review of Neuroscience*, *27*, 611–647. https://doi.org/10.1146/annurev.neuro.26.041002.131039

Riedl, J., Fieseler, C., & Zimmer, M. (2022). Tyraminergic corollary discharge filters reafferent perception in a chemosensory neuron. *Current Biology*, *32*(14), 3048-3058.e6. https://doi.org/10.1016/j.cub.2022.05.051

Roberts, W. M., Augustine, S. B., Lawton, K. J., Lindsay, T. H., Thiele, T. R., Izquierdo, E. J., Faumont, S., Lindsay, R. A., Britton, M. C., Pokala, N., Bargmann, C. I., & Lockery,

S. R. (2016). A stochastic neuronal model predicts random search behaviors at multiple spatial scales in C. elegans. *ELife*, *5*, e12572. https://doi.org/10.7554/ELIFE.12572

Rogers, C., Persson, A., Cheung, B., & Bono, M. De. (2006). *Behavioral Motifs and Neural Pathways Coordinating O 2 Responses and Aggregation in C . elegans*. 649–659. https://doi.org/10.1016/j.cub.2006.03.023

Rolls, E. T., & Deco, G. (2010). The Noisy Brain: Stochastic Dynamics as a Principle of Brain Function. *The Noisy Brain: Stochastic Dynamics as a Principle of Brain Function*, 1–316. https://doi.org/10.1093/ACPROF:OSO/9780199587865.001.0001

Rothermel, M., Carey, R. M., Puche, A., Shipley, M. T., & Wachowiak, M. (2014). Cholinergic inputs from basal forebrain add an excitatory bias to odor coding in the olfactory bulb. *Journal of Neuroscience*, *34*(13), 4654–4664. https://doi.org/10.1523/JNEUROSCI.5026-13.2014

Ruach, R., Ratner, N., Emmons, S. W., & Zaslaver, A. (2023). The synaptic organization in the Caenorhabditis elegans neural network suggests significant local compartmentalized computations. *Proceedings of the National Academy of Sciences of the United States of America*, *120*(3), e2201699120. https://doi.org/10.1073/PNAS.2201699120/SUPPL_FILE/PNAS.2201699120.SD04.CSV

Sabarathinam, S., Thamilmaran, K., Borkowski, L., Perlikowski, P., Brzeski, P., Stefanski, A., & Kapitaniak, T. (2013). Transient chaos in two coupled, dissipatively perturbed Hamiltonian Duffing oscillators. *Communications in Nonlinear Science and Numerical Simulation*, *18*(11), 3098–3107. https://doi.org/10.1016/j.cnsns.2013.04.002

Salazar Thula, O. Y. (2024). Neuronal mechanisms implementing a hierarchy of rhythmic movements in C. elegans [Doctoral dissertation, University of Vienna]. https://doi.org/10.25365/thesis.72852

Salkoff, D. B., Zagha, E., McCarthy, E., & McCormick, D. A. (2020). Movement and Performance Explain Widespread Cortical Activity in a Visual Detection Task. *Cerebral Cortex*, *30*(1), 421–437. https://doi.org/10.1093/cercor/bhz206

Schaffer, E. S., Mishra, N., Whiteway, M. R., Li, W., Vancura, M. B., Freedman, J., Patel, K. B., Voleti, V., Paninski, L., Hillman, E. M. C., Abbott, L. F., & Axel, R. (2023). The spatial and temporal structure of neural activity across the fly brain. *Nature Communications*, *14*(1). https://doi.org/10.1038/s41467-023-41261-2

Schmitt, C., Schultheis, C., Husson, S. J., Liewald, J. F., & Gottschalk, A. (2012). Specific Expression of Channelrhodopsin-2 in Single Neurons of Caenorhabditis elegans. *PLoS ONE*, *7*(8). https://doi.org/10.1371/journal.pone.0043164

Schnell, B., Weir, P. T., Roth, E., Fairhall, A. L., & Dickinson, M. H. (2014). Cellular mechanisms for integral feedback in visually guided behavior. *Proceedings of the National Academy of Sciences of the United States of America*, *111*(15), 5700–5705. https://doi.org/10.1073/pnas.1400698111

Schrödel, T., Prevedel, R., Aumayr, K., Zimmer, M., & Vaziri, A. (2013). Brain-wide 3D imaging of neuronal activity in Caenorhabditis elegans with sculpted light. *Nature Methods*, *10*(10), 1013–1020. https://doi.org/10.1038/nmeth.2637

Schröder, S., Steinmetz, N. A., Krumin, M., Pachitariu, M., Rizzi, M., Lagnado, L., Harris, K. D., & Carandini, M. (2019). Retinal outputs depend on behavioural state. *BioRxiv*, 638049. https://doi.org/10.1101/638049

Shen, C., & Powell-Coffman, J. A. (2003). Genetic Analysis of Hypoxia Signaling and Response in C. elegans. *Annals of the New York Academy of Sciences*, *995*(1), 191–199. https://doi.org/10.1111/J.1749-6632.2003.TB03222.X

Shen, Y., Wen, Q., Liu, H., Zhong, C., Qin, Y., Harris, G., Kawano, T., Wu, M., Xu, T., Samuel, A. D. T., & Zhang, Y. (2016). An extrasynaptic GABAergic signal modulates a

pattern of forward movement in Caenorhabditis elegans. *ELife*, *5*(MAY2016), 1–25. https://doi.org/10.7554/eLife.14197

Sherrington, C. S. (2012). The integrative action of the nervous system. *The Integrative Action of the Nervous System.* https://doi.org/10.1037/13798-000

Skora, S., Mende, F., & Zimmer, M. (2018). Energy Scarcity Promotes a Brain-wide Sleep State Modulated by Insulin Signaling in C. elegans. *Cell Reports*, *22*(4), 953–966. https://doi.org/10.1016/j.celrep.2017.12.091

Smythies, J. R. (John R. (2002). *The dynamic neuron : a comprehensive survey of the neurochemical basis of synaptic plasticity*. 150. https://books.google.com/books/about/The_Dynamic_Neuron.html?id=g3tXngEACAAJ

Sorribes, A., Armendariz, B. G., Lopez-Pigozzi, D., Murga, C., & de Polavieja, G. G. (2011). The Origin of Behavioral Bursts in Decision-Making Circuitry. *PLOS Computational Biology*, *7*(6), e1002075. https://doi.org/10.1371/JOURNAL.PCBI.1002075

Sperry, R. W. (1950). Neural basis of the spontaneous optokinetic response produced by visual inversion. *Journal of Comparative and Physiological Psychology*, *43*(6), 482–489. https://doi.org/10.1037/H005547

Spratling, M. W. (2010). Predictive Coding as a Model of Response Properties in Cortical Area V1. *Journal of Neuroscience*, *30*(9), 3531–3543. https://doi.org/10.1523/JNEUROSCI.4911-09.2010

Steinmetz, N. A., Zatka-Haas, P., Carandini, M., & Harris, K. D. (2019). Distributed coding of choice, action and engagement across the mouse brain. *Nature*, *576*(7786), 266–273. https://doi.org/10.1038/s41586-019-1787-x

Stephenson, R., & Lewis, V. (2011). Behavioural evidence for a sleep-like quiescent state in a pulmonate mollusc, Lymnaea stagnalis (Linnaeus). *Journal of Experimental Biology*, *214*(5), 747–756. https://doi.org/10.1242/jeb.050591

Straka, H., Simmers, J., & Chagnaud, B. P. (2018). A New Perspective on Predictive Motor Signaling. *Current Biology*, *28*(5), R232–R243. https://doi.org/10.1016/j.cub.2018.01.033

Stringer, C., Pachitariu, M., Steinmetz, N., Reddy, C. B., Carandini, M., & Harris, K. D. (2019). Spontaneous behaviors drive multidimensional, brainwide activity. *Science*, *364*(6437). https://doi.org/10.1126/science.aav7893

Suga, N., & Schlegel, P. (1972). Neural attenuation of responses to emitted sounds in echolocating bats. *Science*, *177*(4043), 82–84. https://doi.org/10.1126/science.177.4043.82

Suga, N., & Shimozawa, T. (1974). Site of Neural Attenuation of Responses to Self-Vocalized Sounds in Echolocating Bats. *Science*, *183*(4130), 1211–1213. https://doi.org/10.1126/SCIENCE.183.4130.1211

Sulston, J. E., & Horvitz, H. R. (1977). Post-embryonic cell lineages of the nematode, Caenorhabditis elegans. *Developmental Biology*, *56*(1), 110–156. https://doi.org/10.1016/0012-1606(77)90158-0

Thompson, E. (2007). Mind in life: Biology, phenomenology, and the sciences of mind. Harvard University Press.

Todorov, E. (2004). Optimality principles in sensorimotor control. *Nature Neuroscience*, *7*(9), 907–915. https://doi.org/10.1038/nn1309

Todorov, E. (2006). Optimal Control Theory. *Bayesian Brain*.

Tsalik, E. L., & Hobert, O. (2003). Functional mapping of neurons that control locomotory behavior in Caenorhabditis elegans. *Journal of Neurobiology*, *56*(2), 178–197. https://doi.org/10.1002/neu.10245

Tumer, E. C., & Brainard, M. S. (2007). Performance variability enables adaptive plasticity of 'crystallized' adult birdsong. *Nature 2007 450:7173*, *450*(7173), 1240–1244. https://doi.org/10.1038/nature06390

Uzel, K., Kato, S., & Zimmer, M. (2022). A set of hub neurons and non-local connectivity features support global brain dynamics in C. elegans. *Current Biology : CB*, *32*(16), 3443-3459.e8. https://doi.org/10.1016/J.CUB.2022.06.039

van Voorhies, W. A., & Ward, S. (2000). Broad oxygen tolerance in the nematode Caenorhabditis elegans. *Journal of Experimental Biology*, *203*(16), 2467–2478. https://doi.org/10.1242/JEB.203.16.2467

Varshney, L. R., Chen, B. L., Paniagua, E., Hall, D. H., & Chklovskii, D. B. (2011). Structural properties of the Caenorhabditis elegans neuronal network. *PLoS Computational Biology*, *7*(2). https://doi.org/10.1371/journal.pcbi.1001066

Von Holst, E., & Mittelstaedt, H. (1950). Das Reafferenzprinzip - Wechselwirkungen zwischen Zentralnervensystem und Peripherie. *Die Naturwissenschaften*, *37*(20), 464–476. https://doi.org/10.1007/BF00622503

Vorster, A. P., & Born, J. (2015). Sleep and memory in mammals, birds and invertebrates. *Neuroscience and Biobehavioral Reviews*, *50*, 103–119. https://doi.org/10.1016/j.neubiorev.2014.09.020

Wang, Y., Zhang, X., Xin, Q., Hung, W., Florman, J., Huo, J., Xu, T., Xie, Y., Alkema, M. J., Zhen, M., & Wen, Q. (2020). Flexible motor sequence generation during stereotyped escape responses. *ELife*, *9*, 1–27. https://doi.org/10.7554/eLife.56942

Ward, S., Thomson, N., White, J. G., & Brenner, S. (1975). Electron microscopical reconstruction of the anterior sensory anatomy of the nematode caenorhabditis elegans. *Journal of Comparative Neurology*, *160*(3), 313–337. https://doi.org/10.1002/cne.901600305

Ware, R. W., Clark, D., Crossland, K., & Russell, R. L. (1975). The nerve ring of the nematode Caenorhabditis elegans: Sensory input and motor output. *Journal of Comparative Neurology*, *162*(1), 71–110. https://doi.org/10.1002/cne.901620106

Webb, B. (2004). Neural mechanisms for prediction: Do insects have forward models? *Trends in Neurosciences*, *27*(5), 278–282. https://doi.org/10.1016/j.tins.2004.03.004

Weber, K. P., De, S., Kozarewa, I., Turner, D. J., Madan Babu, M., & de Bono, M. (2010). Whole genome sequencing highlights genetic changes associated with laboratory domestication of C. elegans. *PLoS ONE*, *5*(11). https://doi.org/10.1371/journal.pone.0013922

White, J. G., Southgate, E., Thomson, J. N., & Brenner, S. (1986). The structure of the nervous system of the nematode C. elegans. *Philosophical Transactions of the Royal Society of London - Series B: Biological Sciences*, *314*(1228), 1–340. http://rstb.royalsocietypublishing.org/content/315/1174/305.abstract

Wicks, S. R., & Rankin, C. H. (1996). The integration of antagonistic reflexes revealed by laser ablation of identified neurons determines habituation kinetics of the Caenorhabditis elegans tap withdrawal response. *Journal of Comparative Physiology - A Sensory, Neural, and Behavioral Physiology*, *179*(5), 675–685. https://doi.org/10.1007/BF00216131

Wolpert, D. M., & Miall, R. C. (1996). Forward Models for Physiological Motor Control. *Neural Networks*, *9*(8), 1265–1279.

Zeigler, H. P., & Gallistel, C. R. (1981). The Organization of Action: A New Synthesis. *The American Journal of Psychology*, *94*(1), 190. https://doi.org/10.2307/1422362

Zheng, Y., Brockie, P. J., Mellem, J. E., Madsen, D. M., & Maricq, A. V. (1999). Neuronal Control of Locomotion in C. elegans Is Modified by a Dominant Mutation in the GLR-1

Ionotropic Glutamate Receptor. *Neuron*, *24*(2), 347–361. https://doi.org/10.1016/S0896-6273(00)80849-1

Zimmer, M., Gray, J. M., Pokala, N., Chang, A. J., Karow, D. S., Marletta, M. A., Hudson, M. L., Morton, D. B., Chronis, N., & Bargmann, C. I. (2009). Neurons Detect Increases and Decreases in Oxygen Levels Using Distinct Guanylate Cyclases. *Neuron*, *61*(6), 865–879. https://doi.org/10.1016/j.neuron.2009.02.013

Zipser, B., & Bennett, M. V. L. (1976). Interaction of electrosensory and electromotor signals in lateral line lobe of a mormyrid fish. *Https://Doi.Org/10.1152/Jn.1976.39.4.713*, *39*(4), 713–721. https://doi.org/10.1152/JN.1976.39.4.713